Conformational behavior and aggregation of amyloid beta peptides: Molecular Dynamics simulation studies

Dissertation

zur Erlangung des Grades eines
Doktor der Naturwissenschaften
(Dr. rer. nat.)

eingereicht beim
Fachbereich Chemie der Technische Universität Dortmund

vorgelegt von

M.Sc. (Bioinfo) Raghunadha Reddy Burri
Guntur, India

Dortmund, 2008

Erstgutachter:	Prof. Dr. A. Geiger
Zweitgutachter:	Prof. Dr. R. Winter
Tag der mündlichen Prüfung:	

I dedicate this dissertation to my wonderful, awesome and precious parents
Burri Srinivasa Reddy and Burri Venkataramma.

Acknowledgement

It is a great pleasure for me to acknowledge all the people who helped me to accomplish this dissertation. First and foremost, I wish to express my deep felt gratitude towards my supervisor, Prof. Dr. Alfons Geiger, for giving me an opportunity to work in their group. I am indebted for his advice, encouragement, easy accessibility and freedom for work which helped me to explore new ideas and to complete the work. I also thank Prof. Dr. Roland Winter for his helpful suggestions and nice discussions in group meetings. *Thank you for being wonderful teachers!*

I am grateful to my coworkers, who ensured a technically stimulating, creative and pleasant working environment and helped in technical and non-technical matters. My special thanks to Dr. Ivan Brovchenko for his erudite assistance, which was in the completion of my work. *Thank you very much Ivan!* Oftenly, I had very nice discussions with Dr. Dietmar Paschek, Dr. Alla Oleinikova and other coworkers on technical and non-technical issues through which I learnt many things. *Thank you all for giving nice company!* I thank International Max-Planck Research School in Chemical Biology (IMPRS-CB) for providing me fellowship and for generous travel grants. I am grateful to IMPRS-CB faculty members for their valuable teaching and practical courses. My sincere thanks to Anneliese Ahlke and Dr. Jutta Rötter for their help in all administrative work. *Danke schön Frau Ahlke und Jutta!* I also appreciate generous computing time from LiDO.

I am thankful to my friends Vasu, Lalitha, Sunil, Rama (and his family) and Siva for taking my care during their stay in Germany, which made me feel like home. Many thanks to other friends in Dortmund, who made my stay enjoyable and IMPRS-CB students for their best wishes.

I would like to thank my parents, aunt, uncle, brothers, sister and grandmother for their blessings and nephews for their wishes without which it would have been difficult to complete the work.

Finally, I am thankful to those who have assisted me directly or indirectly in the completion of this work. Their assistance is invaluable and shall always be held in high regards.

Contents

1 Introduction **1**

2 Review **7**

2.1 Structure and conformational behavior of proteins 7

2.1.1 Aminoacids 7

2.1.2 Secondary structure of proteins 8

2.1.3 Dominant forces in conformational behavior of protein 12

2.2 Fibrilization and structure of amyloid fibrils 14

2.3 Conformational behavior and aggregation of amyloid β-peptides . . . 18

3 Aim of the Present Work **23**

4 Simulation Methods **27**

4.1 Molecular Dynamics simulation techniques 28

4.1.1 Periodic Boundary Conditions 29

4.1.2 Constraint Dynamics 29

4.1.3 Canonical NPT and NVT ensembles 30

4.1.4 Replica Exchange Molecular Dynamics (REMD) simulations . 31

4.2 Force fields 33

4.3 Computer simulations of protein folding 37

4.4 Computer simulations of peptide aggregation 38

5 Temperature-induced conformational changes of amyloid β-peptide and peptide fragments in water 41

5.1 Temperature-induced conformational changes of Aβ_{42} peptide 41

5.1.1 Model system 42

5.1.2 Conformational behavior of Aβ_{42} 43

5.1.3 Properties of water in hydration shell of Aβ_{42} 49

5.1.4 Intrinsic thermal expansivity of Aβ_{42} protein 54

5.2 Temperature-induced conformational changes of Aβ_7 fragments 61

5.2.1 Model System 61

5.2.2 Conformational behavior of Aβ_7 and Aβ_{7g} peptide 63

5.2.3 Intrinsic thermal expansivity of Aβ_7 and Aβ_{7g} peptides 67

5.3 Conclusions 69

6 Aggregation of Aβ_7 peptides in water 75

6.1 Dimer of Aβ_7 peptides 75

6.2 Tetramer of Aβ_7 peptides 79

6.3 Hexamer of Aβ_7 and Aβ_{7g} peptides 84

6.4 Decamer of Aβ_7 peptides 90

6.5 Conclusions 92

7 Fibril growth in Aβ_7 peptide system **97**

7.1 Results 98

7.2 Conclusions 107

8 Fibril growth in Aβ_{7g} peptide system **109**

8.1 Model System 109

8.2 Results 111

8.3 Conclusions 122

9 Temperature dependence of Aβ_7 and Aβ_{7g} peptides aggregations: REMD simulation study **125**

9.1 Decamer of Aβ_7 peptides 127

9.2 Decamer of Aβ_{7g} peptides 130

9.3 Conclusions 132

Summary **134**

Zusammenfassung **137**

References **140**

Curriculum Vitae **157**

Chapter 1

Introduction

The function of proteins is directly related to their shape, as the surface features of the protein create binding sites that are highly specific. The conformational behavior determines the shape or structure of the proteins. The conformation of a biomolecule may be characterized by various structural properties, such as its secondary structure, radius of gyration, volume, etc. Accordingly, the temperature dependence of these properties gives information about the temperature and character of conformational transitions. Some properties may change gradually and some other sharply when crossing a temperature-induced conformational transition. It is not clear in advance, which property is the most adequate order parameter of this transition. Therefore, it is important to find parameters most sensitive to the conformational changes of a biomolecule.

The volume of a biomolecule and its thermal expansivity may be those properties, which are highly sensitive to conformational transitions [1]. Pressure perturbation calorimetric experimental studies of staphylococcal nuclease (SNase) [2, 3], aminoacids [4] and elastin-like peptides [5] show that the apparent thermal expansion coefficient α^{app} of the biomolecules is about $+10^{-4}$ to $+10^{-3}$ K^{-1}. Below the temperature of unfolding, α^{app} typically decreases upon heating. At and above this temperature, the behavior of α^{app} changes qualitatively: it may show a minimum, become constant or may even slightly increase upon further heating. The apparent volume of a biomolecule as well as its apparent expansion coefficient include contributions from both the biomolecule itself (intrinsic part) and from hydration water. We may expect that the conformational properties of a biomolecule may be reflected in the volumetric properties of both, the biomolecule and of its hydration water. An attempt to extract the intrinsic thermal expansivity of a biomolecule in liquid water from experimental data [6] suffers from the lack of information about the temperature dependence of the properties of hydration water. However, such information may be obtained in simulations and we may expect that the conformational properties of a biomolecule may be reflected in the expansivity of both, the biomolecule and of its hydration water.

Clustering of water molecules in the hydration shell of a biomolecule seems to be closely related to its conformational behavior [7, 8, 9, 10]. Polymorphic transitions of DNA from the A- to the biologically relevant B-form occurs close to the hydration level, where a spanning H-bonded water network forms at the DNA surface via a percolation transition [8, 9]. At full hydration, this spanning network breaks upon heating at some temperature. For fully hydrated SNase and elastin-like peptides, this break occurs approximately at temperatures, where these molecules undergo conformational transitions [7, 10]. Therefore, an analysis of water clustering and percolation in the hydration shell of the biomolecule at various temperatures may give additional information about the conformational transition and its origin.

Misfolding or errors in folding can occur when the hydrophobic side chains of partially folded proteins are exposed to the aqueous environment. These hydrophobic regions bind to similar surfaces on neighboring proteins in order to shield themselves from the aqueous environment [11]. As such the proteins bind to form dimers, trimers, and higher order aggregates. In certain cases the new structure or lack of structure (aggregate structure) gives the protein possibly a new pathogenic function [12]. Some of the important aggregation diseases are Alzheimer's disease (AD), Parkinson disease and type II diabetes. Upon aggregation, certain proteins form fibrillar structures that have been implicated as necessary pathogenic factors [13]. The mechanisms of aggregation of polypeptide chains that lead to the formation of fibrillar structures are largely unknown. Understanding the events of the aggregation of a protein may lead to the understanding of the mechanisms of fibrillogenesis process. In addition, knowledge about the molecular mechanisms underlying any disease provides a possibility to design prevention or a cure [14].

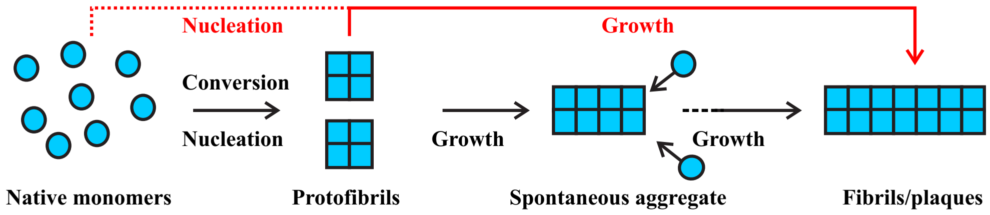

Figure 1.1: *Schematic representation of nucleation and growth.*

Experimental studies of fibril formation and growth have led to a number of views on amyloidogenesis [15, 16, 17]. One view suggests that the unstructured monomers in solution cluster and form nuclei. Once the cluster reaches a critical size, the nucleus forms a fibril which then grows to form full-length fibrils by the addition of monomers to the existing fibril ends [18]. Subsequently, the amyloid peptide monomer/dimer may add directly to existing protofibrils and fibrils [19, 20]. It has been demonstrated that the process of growth of existing fibrils through the process of monomer binding to fibril ends can be studied independently of the process of nucleation, or association of protofibrils (Figure 1.1, black path). Alternatively, intermediate peptide, "protofibrils", are formed and associate end-to-end or laterally to form fibrils as shown in Figure 1.1 (red path). This view may be augmented by the possibility that monomers associate to form micelles and that those micelles may convert to fibril nuclei upon reaching a critical size [21].

Kinetic studies have supported the view that fibrillogenesis occurs in two distinct stages- nucleation and growth of fibers. The nucleation stage is a series of thermodynamically unfavorable steps leading to the creation of a stable nucleus. The size of the nucleus is not clear at present [22]. However, through their carefully designed experiments, Maggio and coworkers have been able to analyze the kinetics of the association and reorganization steps separately by introducing what they call a transition state intermediate of the peptide [19, 20]. The term transition state refers to a metastable intermediate rather than the typically unstable activated transition state that appears in the transition state theory of activated processes. In demonstrating that fibril growth occurs by a process of monomer diffusion to the fibril end and subsequent reorganization of the aggregates, raise questions about the elementary molecular kinetic events of fibril growth [19, 20, 22]. The fibril growth is a fundamental characteristic of the fibrillogenesis process. It varies with solution conditions such as ionic strength and temperature [20]. These studies of the full length amyloid β-peptide (Aβ) show a strong temperature dependent peptide growth [20]. It can also be altered by chemical reagents capable of binding to the Aβ monomer itself or to a fibril end [23]. A quantitative determination of the effect of fibrillogenesis conditions on the growth rate provides valuable hints to understanding the molecular mechanism of fibril growth. As such, fibril formation is an appealing subject for computational studies and thus an ideal probe for understanding the early steps of aggregation at an atomic level by computer simulations.

The central role of fibrillar Aβ in AD pathogenesis suggests that therapeutic approaches focused on the fibrillogenesis process would be highly promising. It is evident that Aβ deposition is a central event in the pathological cascade, but why does the E22G Arctic mutation lead to AD, whereas the E22Q, E22K, A21G and

D23N mutations lead to a different clinical phenotype, is a query to be resolved [24]. The answer lies within the Aβ sequence. The KLVFFA motif at position 16–21 in the Aβ protein is central in the fibrillization process [25]. Disease related mutations at position 21–23 in Aβ are located close to the central hydrophobic core ($L_{17}VFFA_{21}$) region and could therefore affect the conformation of the peptide and its fibrillization process. The central hydrophobic core sequence influencing the peptide topology is the critical determinant for aggregation into intermediate structures, pathways and kinetics of the Aβ peptide fragment [26].

The research which I will describe in this thesis address this currently unsolved problem. In this thesis we have taken the Aβ_{1-42} (Aβ_{42} hereafter) and the seven residue peptide N-acetyl-KLVFFAE-NH_2, called Aβ_{16-22} (Aβ_7 hereafter) and representing residues $16-22$ of the full length Aβ peptide. This peptide is of particular interest since four disease-causing mutations occur in this region, having a positive charged residue at the N-terminus (K16), and a negative charged residue at the C-terminus (E22) [27]. Results from solid-state NMR and isotope-edited infrared spectroscopic technique show that the peptide adopts a β-sheet structure within the fibrils and, more specifically, an antiparallel [28, 29]. Aβ_7 is also one of the shortest reported amyloidogenic sequences and is highly amenable to modeling studies due to its small size.

On the theoretical side, several workers are attempting to apply techniques from the protein folding arsenal to understand protein aggregation. In particular, computer simulation is the method of choice to study processes that are dangerous, costly, or even impossible to carry out experimentally, and that are of microscopic nature and thereby partially inaccessible to detailed observation. Molecular dynamics (MD) simulations, in which Newton's equations of motion are integrated to reproduce the time evolution (trajectory) of the atoms and molecules in a system, are widely used to study dynamic processes in biomolecular systems at atomic resolution [30]. The simulation of aggregation is useful because it allows us to understand the aggregation process at a truly molecular level. In addition to the possible medical breakthroughs that such multidisciplinary studies can lead to, there is a growing possibility of understanding the mechanisms of amyloid formation that can have wide impact in field of basic computational biology.

Outline of Thesis

This thesis describes the researches on the temperature-induced conformational behavior and aggregation behavior of the amyloid peptide Aβ_{42} and its fragments. Volumetric properties and the role of hydration water are analysed by molecular dynamic simulations of peptides in explicit water. Below, the summary of the remaining chapters, of this thesis is given.

Chapter 2 contains some general review of the structural and conformational behavior of protein and aggregation.

The aim of my thesis is formulated in **chapter 3**.

Chapter 4 contains some general overview of the computational techniques used and addressed in the simulations, and gives an overview of the biomolecular simulations.

The conformational behavior of the Aβ_{42}, Aβ_7 peptide and Arctic mutation of Aβ_7 (Aβ_{7g}), their intrinsic thermal expansivities and hydrational properties are analyzed in **chapter 5**.

The conformational behavior of the Aβ_7 and Aβ_{7g} peptide aggregations, their intrinsic thermal expansivities and hydrational properties are analyzed in **chapter 6**.

In **chapter 7**, the mechanism of monomer / fibril association and reorganization of amyloid fibrils is studied.

The effect of mutation on fibril growth is analyzed in **chapter 8**.

The temperature dependence of Aβ_7 and Aβ_{7g} peptide aggregations is studied in **chapter 9**, using Replica Exchange Molecular Dynamics (REMD) simulations.

Chapter 10: The main results of the thesis are formulated in summary.

Chapter 2

Review

2.1 Structure and conformational behavior of proteins

2.1.1 Aminoacids

The basic monomeric unit of a protein is an amino acid. There are twenty naturally occurring amino acids. Their names are commonly abbreviated with either a three-letter code or a one-letter code as shown in Table 2.1. Depending upon the chemical structure of the side chain, the amino acids are divided into two different major classes (See at Table 2.1). The first class comprises those with hydrophobic side chains (non-polar) eg. Ala(A), Val(V), Leu(L), Phe(F), etc. The second class comprises of amino acids having hydrophilic side chains (polar) that are either charged (Lys(K), Glu(E), Asp(D) and Arg(R)) or uncharged (Gln(Q), His(H), etc). The amino acid glycine(G), the simplest of all the twenty amino acids, has only a hydrogen atom as the side chain [31].

The primary structure of a protein is formed by peptide bond between the amino acids. A peptide bond is formed when the carboxy group of the first amino acid condenses with the amino group of the next to eliminate water. This process is repeated until the whole polypeptide chain is synthesized. Along the polypeptide chain, the amino group of first amino acid and the carboxy group of the last amino acid still remain intact. Thus the chain is generally referred as to run from amino(N) terminus to carboxy(C) terminus. The formation of a succession of peptide bonds

Amino acid			**Side chain**	**Amino acid**			**Side chain**
Aspartic acid	Asp	D	negative	Alanine	Ala	A	nonpolar
Glutamic acid	Glu	E	negative	Glycine	Gly	G	nonpolar
Arginine	Arg	R	positive	Valine	Val	V	nonpolar
Lysine	Lys	K	positive	Leucine	Leu	L	nonpolar
Histidine	His	H	positive	Isoleucine	Ile	I	nonpolar
Asparagine	Asn	N	Uncharged	Proline	Pro	P	nonpolar
Glutamine	Gln	Q	Uncharged	Phenylalaine	Phe	F	nonpolar
Serine	Ser	S	Uncharged	Methionine	Met	M	nonpolar
Threonine	Thr	T	Uncharged	Tryptophan	Trp	W	nonpolar
Tyrosine	Tyr	Y	Uncharged	Cysteine	Cys	C	nonpolar
POLAR AMINO ACIDS				**NONPOLAR AMINO ACIDS**			

Table 2.1: *Amino acids code and their side chain properties.*

generates a ”main chain” or ”backbone” from which various ”side chains” project outwards. Thus main chain atoms of a polypeptide chain are the carbon atom $C\alpha$, to which the side chains, NH group, and the carbonyl group C=O are attached. The side chain, which is attached as the fourth valency to the $C\alpha$, is the only difference in various amino acids. These units are called residues and are linked into a polypeptide chain by peptide bonds between C atom of one residue and nitrogen atom of the next. The properties of the peptide bond and the amino acid side chains confer a high degree of conformational flexibility to the protein structure, resulting in different possible conformations from a single polypeptide chain [32].

2.1.2 Secondary structure of proteins

During the conformational dynamics of the protein, different sets of residues come in close proximity to each other in various possible conformations for the same polypeptide chain. A finely tuned balance of hydrophobic and Coulombic forces among the different parts of the polypeptide backbone, the side chains and the solvent is required to maintain correct folding [33]. Sometimes, however, subtle changes in the equilibrium of these forces leads to aggregation of proteins. Surprisingly small changes may produce remarkably different outcomes- a point mutation as seemingly innocuous as glycine-to-alanine renders superoxide dismutase aggregation-prone [34]; bovine serum albumin is destabilized against thermal unfolding in the presence of high concentrations of chaotropic salts but stabilized at low chaotrope concentrations [35].

Conformation of secondary structure

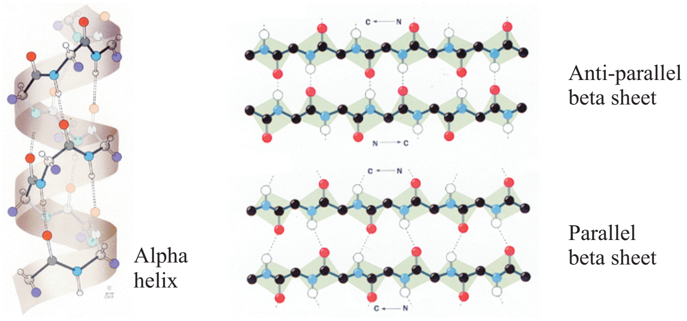

Figure 2.1: *Protein structure α-helix and β-sheet (parallel and antiparallel) [32].*

Proteins exhibit multiple structural levels. The basic level is its primary structure formed by the peptide bonds which serves as the backbone for the protein. It is simply the order of its amino acids. The secondary structure refers to certain common repeating structures found in proteins. There are two types of secondary structures: α-helix and β-sheet. Multivalent hydrogen bonding in the polyamide backbone stabilizes the secondary structural elements and gives rise to the familiar α-helix and β-sheet (Figure 2.1). An α-helix is a tight helix formed within the polypeptide chain. The polypeptide main chain makes up the central structure, and the side chains protrude out from the helix. The CO-group of one amino acid (n) is bonded to the NH-group of 4^{th} amino acid via hydrogen bond (n+4). In this manner CO-NH group forms the backbone of α-helices. α-helices are most commonly made up of hydrophobic amino acids, because hydrogen bonds are generally the strongest attraction possible between such amino acids. α-helices are found in almost all proteins to various extents. The β-sheet is the second form of regular secondary structure in proteins, consisting of β-strands connected laterally by three or more hydrogen bonds, forming a generally twisted, pleated sheet (Figure 2.1). A β-strand is a stretch of amino acids typically 5–10 amino acids long whose peptide backbones are almost fully extended. Because peptide chains have directionality conferred by their N-terminus and C-terminus, β-strands too can be said to be directional (Figure 2.1). They are usually represented in protein topology diagrams by an arrow pointing toward the C-terminus. Adjacent β-strands can form hydrogen bonds in antiparallel, parallel, or mixed arrangements. The association of β-sheets has been implicated in the formation of protein aggregates and fibrils observed in many human diseases, including Alzheimer's disease and mad cow disease.

The tertiary structure is formed by the assembly of secondary structural elements along with turns and loops into a three dimensional arrangement. The tertiary structure mainly has a hydrophobic core with charged residues on the surface of the protein that determines its biological activity and is thus responsible for its biological function. Tertiary structures of proteins (independent folding chains) can still assemble themselves under physiological conditions in order to perform specific functions. These are termed as quaternary structure.

Ramachandran plot

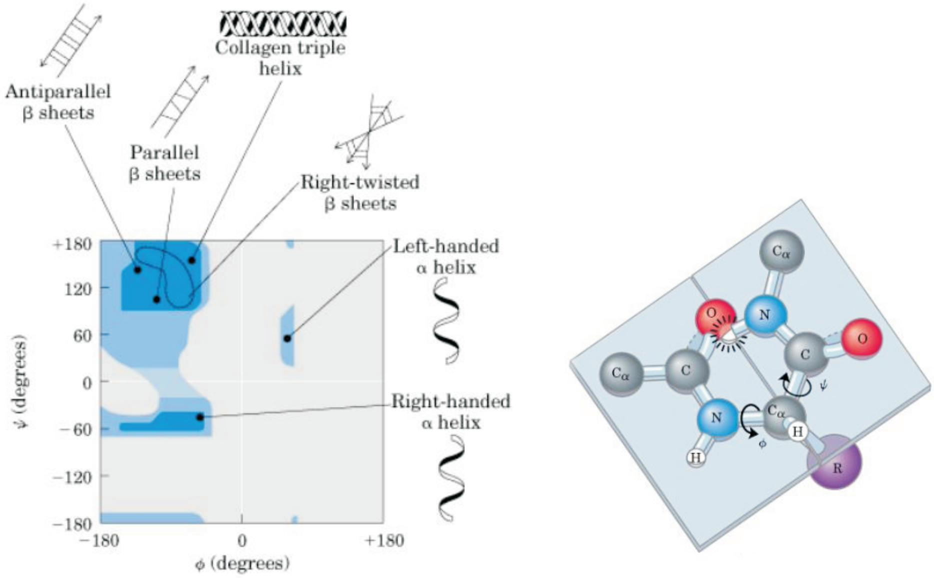
Collagen triple helix
Antiparallel β sheets
Parallel β sheets
Right-twisted β sheets
Left-handed α helix
Right-handed α helix
+180
120
60
0
−60
−120
−180
ψ (degrees)
−180
0
+180
ϕ (degrees)
Cα
N
O
C
O
C
Cα
N
H
Cα
H
R
ψ
ϕ

(a) (b)

Figure 2.2: *(a) A Ramachandran plot describes allowable conformation. (b) Peptide planes of polypeptide chain [32].*

The folding pattern of the polypeptide chain can also be described in terms of angles of internal rotation around the bonds in the main chain. The bonds in the polypeptide backbone between N and $C\alpha$ and between the $C\alpha$ and C are single bonds. Internal rotations around these bonds are not restricted by the electronic structure of the bond, but only by possible steric collisions in the conformations produced. In contrast, the peptide bond itself has a partial double bond character, with restricted internal rotation [36]. This means that the NH and CO along with the two $C\alpha$ does always remain in a peptide plane (See in Figure 2.2(b)).

The main chain conformation of each residue is determined by two angles ϕ and ψ. The dihedral angle around the bond N-$C\alpha$ is known as ϕ and the dihedral angle around the bond $C\alpha$-C is known as ψ (See in Figure 2.2(b)). As ϕ involves a previous amino acid and ψ involves the next, the first amino acid and the last amino acid in the polypeptide chain have only one angle of rotation (ψ and ϕ respectively). Ramachandran first plotted the "allowed" regions in a graph of ϕ and

ψ [37]. The plot is generally known as the Ramachandran plot, shown in Figure 2.2(a). Thus these angles allow only certain conformations. Some combinations of ϕ and ψ produce sterically disallowed conformations. There are two major allowed regions correspond to the two major types of secondary structures found in proteins, one around $\phi = -57$, $\psi = -47$ (denoted Right-handed α-helix) and the around $\phi = -125$, $\phi = +125$ (denoted β-sheet) with a neck like region between them.

Energy landscape for protein folding

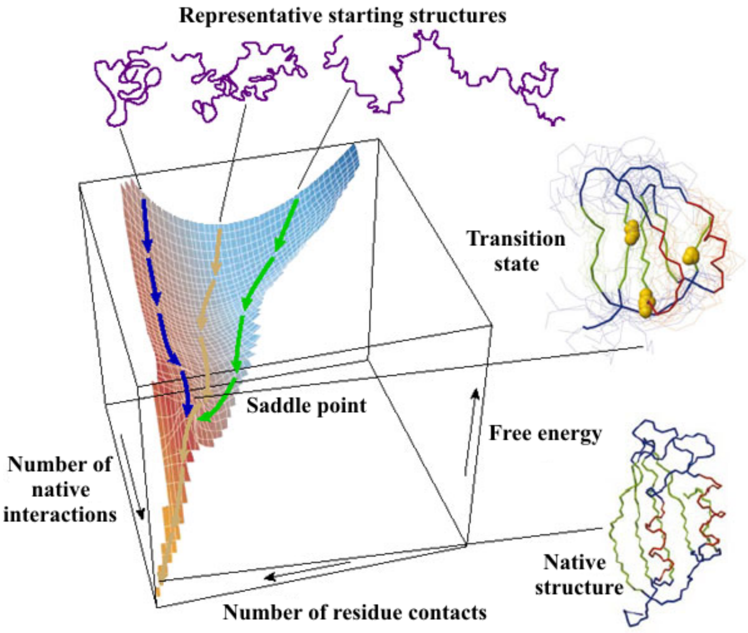
Representative starting structures
Transition state
Saddle point
Free energy
Number of native interactions
Native structure
Number of residue contacts

Figure 2.3: *Energy landscape for protein folding. The landscape on which a protein folds is often compared with a 'funnel' [13].*

The landscape perspective explains the process of reaching a global minimum in free energy (satisfying Anfinsen's experiments) by multiple folding routes on funnel-like energy landscapes [38]. The main idea behind the folding landscape is that it resembles a funnel but to some extent is rugged, i.e. with traps in which the protein can reside along the folding pathway. In the early stages of folding the funnel guides the inherent fluctuations in the conformation of an unfolded or incompletely folded polypeptide chain enabling even the residues that are highly separated in the amino-acid sequence to come into contact with one another. Since, on an average, the native-like interactions between residues are more stable than the non-native ones, they are more persistent and thus the polypeptide chain is able to find its lowest-energy structure by a process of "trial and error". Moreover, if the energy surface or 'landscape' has the right shape (see Figure 2.3) only a small number of all possible conformations needs to be sampled by any given protein molecule during its transition from a random coil to a native structure [39, 40]. Because the landscape is encoded by the amino-acid sequence, natural selection has enabled proteins to evolve so that they are able to fold rapidly and efficiently. These ideas are stimulating the investigation of the most elementary steps in the folding process by both experimental and theoretical procedures [13].

2.1.3 Dominant forces in conformational behavior of protein

A basic property of the protein is its ability to change its structural and conformational behavior. This is because many of the stabilizing interactions involve parts of the protein that are very distant in the polypeptide chain, but brought into special proximity by the folding process. Proteins are only marginally stable, and achieve stability only within narrow ranges of conditions of solvent and temperature. Tertiary and quaternary structures arise primarily from the forces among these side chains. The burial of hydrophobic side chains is of particular importance, but Coulombic interactions, including salt bridges between acids and bases, disulfide bond formation, dipole-ion interactions which occur between tyrosine and charged side chains, also contribute to protein folding and structural stability [41].

Hydrogen bonds

In the case of hydrogen bonds a hydrogen atom with a large positive partial charge interacts with an atom with a large negative partial charge. The opposite charges attract each other and the hydrogen atom, which is covalently bound to the "hydrogen bond" donor atom, comes very close to the "hydrogen bond" acceptor atom with its lone pairs. The strength of the hydrogen bond is dependent on the distance between the donor and acceptor atoms, which in turn is dependent on their electronegativities. The standard hydrogen bond between the donor and acceptor atoms is of the order of 0.26 - 0.35 nm. Hydrogen bonding between amino acids in a linear protein molecule determines the way it folds up into its functional configuration. The standard secondary structures, α-helices and β-sheets, are achieved by the formation of hydrogen bonds by the main chain atoms. Backbone hydrogen bonds are critical for forming stable secondary structures.

Hydrophobic interactions

Hydrophobic interactions are one of the most important forces that will cause the linear polypeptide to fold into a ordered structure in water. In particular, it is the interaction between hydrophobic residues. In native structures of the protein in the aqueous environment, the hydrophobic residues bury themselves in the interior and charged residues come to the surface. The aggregation of the hydrophobic surfaces gives the tightly packed core of a protein.

Electrostatic interactions

Electrostatic interactions play a important role in the conformational behavior of proteins, as many proteins contain polar and charged groups. Electrostatic interactions affect and are affected by the structural and conformational behavior of the proteins. The conformational behavior of protein implies movement of atoms, residues, and fragments of the protein with respect to one another. Most important is these involve changes in both hydrophobic and electrostatic interactions. The electrostatic contribution to the free-energy change upon salt-bridge formation.

Van der Waals forces and dense packing of protein interiors

The packing of atoms in protein interiors is important for their conformational stability. The cohesion of ordinary substances shows the existence of attractive forces between atoms and molecules. There must be limits to how far the matter can be compressed so as to avoid total collapse. This confirms the presence of repulsive force as well at short range. The most general type of interatomic force, the van der Waals force, reflects this principle: The nearer the atoms, the stronger the attractive force, until the atoms are in contact, at which the forces become repulsive and strong. Therefore to maximize the total cohesive force, as many atoms as possible must be brought as close as possible. The requirement for dense packing imposes a requirement for the structure in the interior of the protein. This produces a fit of the elements of secondary structure packed together in protein interiors.

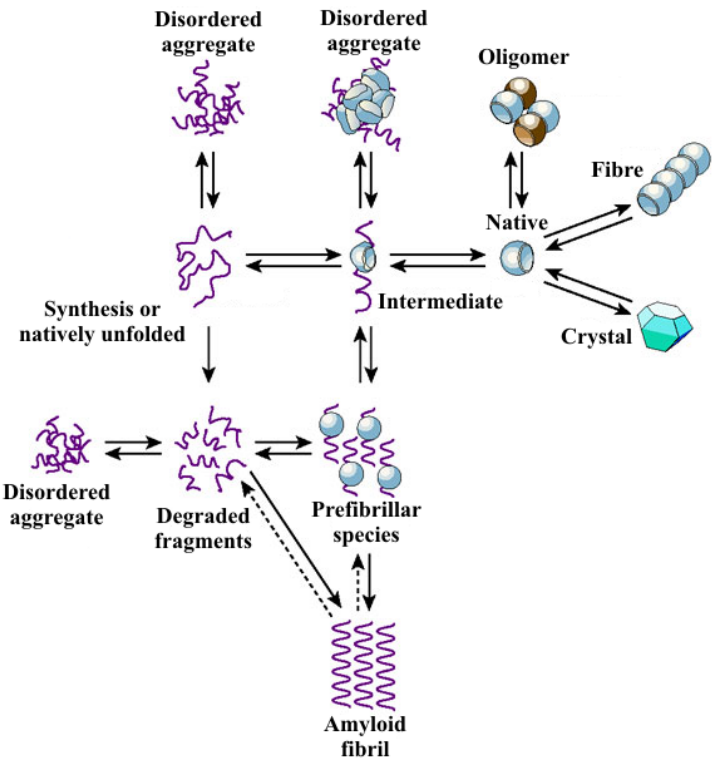
Disordered aggregate
Disordered aggregate
Oligomer
Fibre
Native
Synthesis or natively unfolded
Intermediate
Crystal
Disordered aggregate
Degraded fragments
Prefibrillar species
Amyloid fibril

Figure 2.4: *Aggregate formation during protein folding: Schematic representation of the current understanding of molecular mechanisms involved in fibril formation [14].*

2.2 Fibrilization and structure of amyloid fibrils

According to a recent hypothesis in protein folding theory, the conformational properties of a protein and the possibility of forming self-assembled supramolecular structures can be considered in terms of the relative stability of a multitude of states that are accessible to such structures [14]. In its monomeric state, the protein is assumed to fold from its highly disordered unfolded state through a patially structured intermediate to a globular native state. The native state can form aggregated species, the most ordered of which is a three dimensional crystal as shown in figure 2.4, whilst preserving its overall structure. The unfolded and partially folded states can form aggregated species that are frequently highly disordered, but amyloid fibrils can form through a nucleation and growth mechanism. There is evidence that this process occurs most readily from partially folded intermediate states of proteins [13]. This is illustrated in Figure 2.4. The state of a protein that is adopted under specific conditions depends on the relative thermodynamic stabilities of the various accessible conformations and on the kinetics of their interconversion (Figure 2.4). Amyloid fibrils are just one of the types of aggregate that can be formed by proteins, although a significant feature of this particular species is that its highly organized hydrogen-bonded structure is likely to give it unique kinetic stability. Thus, once formed, such aggregates can persist for long periods, allowing a progressive build-up of deposits in tissue, and indeed enabling seeding of the subsequent conversion of additional quantities of the same protein into amyloid fibrils [13].

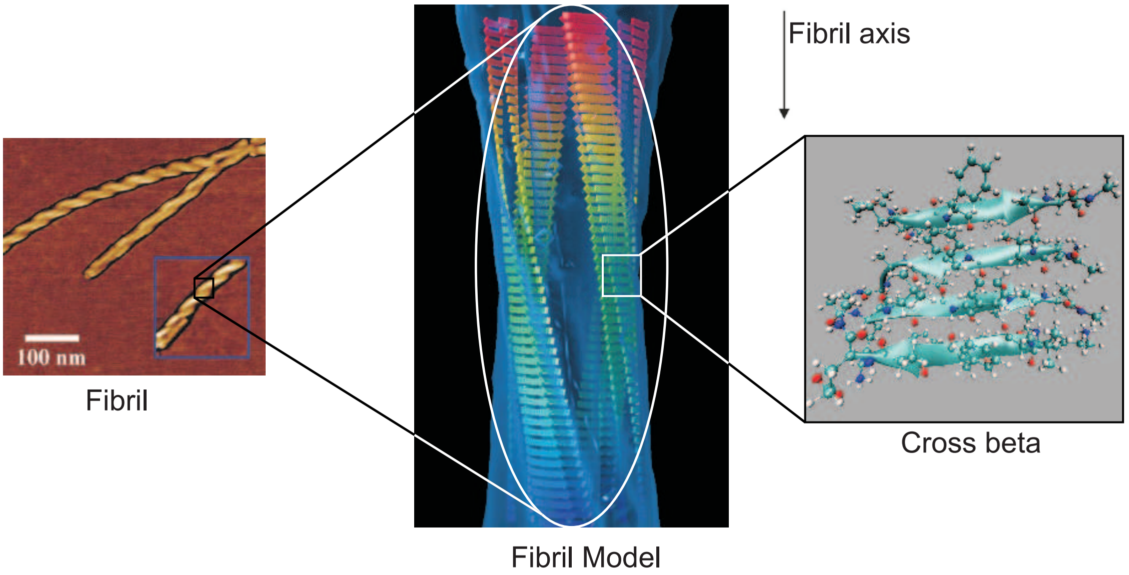

Figure 2.5: *(a) Image of fibrils obtained by Atomic Force Microscopy (AFM) (b) Conceivable schematic β-strand arrangement and protofilament assembly in an amyloid fibril (c) Cross β-sheet [42].*

The different amyloidogenic proteins or peptides do not share any sequence homology or common structure, but the amyloid oligomers/fibrils share a general "cross-β" structure, underscoring the similarity of the underlying physical mechanisms. Although tremendous efforts and progress have been made, including the advent of anti-amyloid agents, the early stage formation of the soluble oligomers and subsequent fibril growth processes remain poorly understood [43, 28]. However, standard structure determination methods simply do not work for the average protein aggregate; the aggregates are not sufficiently ordered and homogeneous to produce high-quality crystals for X-ray structure determination, and solution-phase NMR is untenable because the aggregates become insoluble at the high concentrations required. The structure of amyloid fibrils is not known in atomic detail, but there is ample evidence from X-ray diffraction and solid-state NMR studies that the core of the typical amyloid fibril is composed of β-sheets whose strands run perpendicular to the fibril axis [42]. Thus the fibril axis is oriented parallel to the direction of the backbone hydrogen bonds as shown in Figure 2.5. The β-sheet structures are the core of protofilaments which form the amyloid fibrils. High-resolution electron microscopy studies suggested that the amyloid fibrils are composed of three to six such protofilaments [44].

Under appropriate circumstances, amyloidogenic proteins may oligomerize into prefibrillar assemblies. Such circumstances can be satisfied by extreme conditions of pH and temperature or partial proteolysis for non-disease proteins, whereas destabilizing mutations on disease proteins can induce such transition even under physiological conditions. The intrinsic effect of specific mutations on the rate of aggregation can be correlated to a remarkable extent with the changes in simple physicochemical properties such as hydrophobicity, secondary structure propensity and charge [45].

Concerning above sections, amyloid fibrils share hallmarking common properties, including a similar fibrillar, microscopic morphology (i.e. bundles of straight, rigid fibrils ranging in width from 3 to 15 nm and in length from 100 to 1600 nm [46, 42]). Tentatively, one can say that hydrophobic collapse is one of the most important driving forces making the intermolecular β-sheets the most common component of aggregates. Amyloid formation is favored whenever ”allowed intermolecular interactions” between polypeptide backbones overrule specific intramolecular native side-chain contacts within a folded protein. Hence, many proteins, perhaps all, are potentially able to form amyloid fibrils under certain conditions [45, 47]. In other words, the formation of amyloid presents an alternative process to the native folding conformational struggle of a polypeptide chain in order to: (i) reduce its hydrophobic accessible surface area, (ii) saturate hydrogen bonding, and (iii) reach an alternative “non-native” global free energy minimum. Therefore, subsequent stages of hierarchical amyloid formation may be expected to enhance the burial of hydrophobic residues and the formation of energetically favorable hydrogen bonds.

Diseases

Amyloidoses comprise over 20 different diseases. The family of these diseases may be divided into two major groups (Table 2.2) - one which leads to neurodegeneration and one that does not. The neurodegenerative diseases caused by misfolding in turn, consist of a wide variety of syndromes, including well-known diseases as Alzheimer’s disease, Parkinson’s diseases, Huntington’s diseases etc (Table 2.2) [48]. These diseases are also called as neurodegenerative amyloid-related disorders [45]. Among the nonneurodegenerative diseases one may mention the systemic amyloidosis and the more localized type II diabetes. The molecular basis of diseases that are associated with fibrillar amyloid aggregates is not yet fully understood. In these disorders, specific peptides aggregation, often as a result of mutations, and give rise to protein aggregation. Although amyloid is known to be toxic [49], there is considerable debate over its role in disease [12]. It is widely thought that the oligomeric precursors to amyloid may be substantially more toxic than amyloid itself [43]. It has been suggested that nearly all proteins have the ability to form amyloid under certain conditions [43]. Even if this is the case, fibrils are likely to play an important role, either as reservoirs or sinks of toxic oligomers. Once the amyloid structure has been determined, the rational design of new drugs may be possible (e.g. peptide mimetics) [50].

Disease	**Disease proteins**	**Characteristic pathology**
Neurodegenerative misfolding diseases		
Alzheimer's disease	Amyloid β-protein and hyperphosphorylated tau	Extracellular plaques; Tangles in neuronal cytoplasm
Parkinson's disease	α-synuclein	Lowy body formation
Creutzfeldt-Jakob disease	Prion protein (PrP^{sc})	Spongiform degeneration; extracellular plaques; amyloid inside and outside neurons
Huntington's (polyglutamine expansion) disease	Long glutamine stretches within certain proteins	Intranuclear inclusions and cytoplasmic aggregates
Amyotrophic lateral sclerosis (ALS)	Superoxide dismutase	Neuronal cytoplasm
Non-Neurodegenerative misfolding diseases		
Type II diabetes	IAPP (amylin)	Islet cells of the pancreas

Table 2.2: *Some human conformational diseases caused by protein deposits [48].*

Aggregated proteins do not share a common size, sequence or secondary structure, yet the mature fibrils appear to share similarity in forming highly organized multimolecular morphology and mechanisms of toxicity [14]. Upon aggregation and membrane interaction the peptide undergoes a conformational change towards a β-rich structure which builds up the fibrils. These amyloid fibrils are considered as the typical histopathological landmark of Alzheimer's disease (AD) [51], that get deposited in the brain causing severe dementia and eventually death. AD is a progressive disease known generally as senile dementia. The disease falls into two categories, namely late onset and early onset. One form of this latter AD type runs in families and it is known as familial AD. Both types of AD are characterized by two types of lesions in the brain: senile plaques and neurofibrillary tangles. Senile plaques are areas of disorganized neuropil up to 150 mm across [48]. Extracellularly the fibrils are formed mainly by the amyloid β-peptide (Aβ) [48]. Extracellular Aβ peptide deposition is thought to be intimately associated with the AD. Neurofibrillary tangles are intracellular deposits consisting of two filaments twisted about each other in pairs. Intracellularly the tau-protein forms amyloid fibrils. This disease affects approximately 10% of all humans at 65 years of age and 50% of all those who have reached 85 years [52].

2.3 Conformational behavior and aggregation of amyloid β-peptides

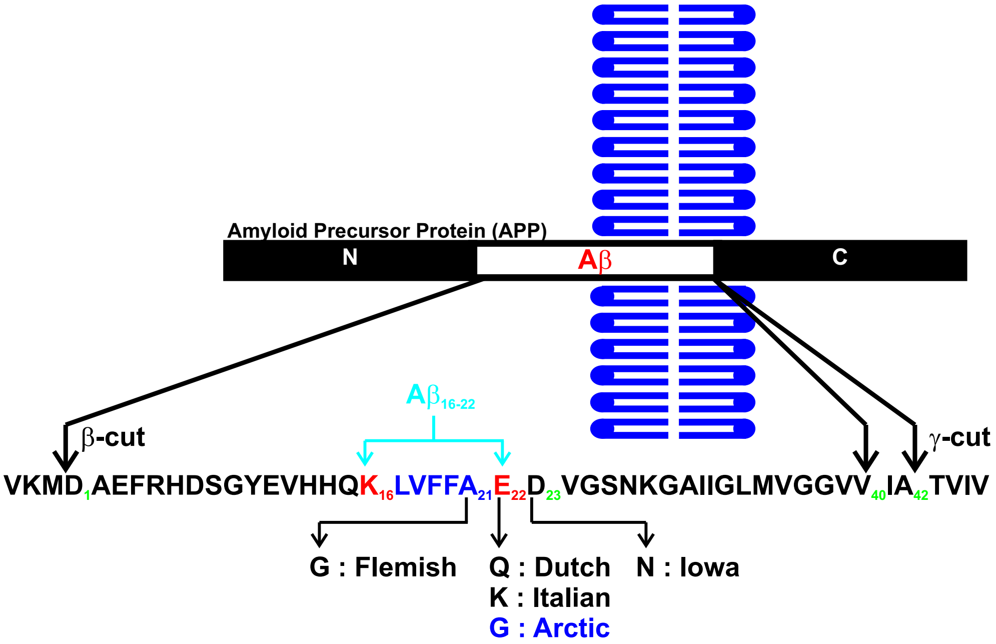
Amyloid Precursor Protein (APP)
N
Aβ
C
Aβ16-22
β-cut
γ-cut
VKMD1AEFRHDSGYEVHHQK16LVFFA21E22D23VGSNKGAIIGLMVGGVV40IA42TVIV
G : Flemish
Q : Dutch
K : Italian
G : Arctic
N : Iowa

Figure 2.6: *Schematic picture of Aβ inserted into a biological membrane. The Aβ_{16-22} peptide contains a central hydrophobic segment. This segment also contains familial disease-related mutants, which have been mapped by mutagenesis experiments.*

Amyloid β-peptide also referred to as Aβ is a highly aggregating small polypeptide having a molecular weight of approximately 4,500 Da. This peptide is a cleavage product of a much larger precursor protein referred to as amyloid precursor protein (APP), the Aβ peptide comprises 39–42 amino acids. There are at least five distinct isoforms of APP: 563, 695, 714, 751, and 770 amino acids, respectively [53]. The Aβ peptide segment comprises approximately half of the transmembrane domain and approximately the first 28 amino acids of the extracellular domain of an APP isoform (Figure 2.6). APP is a transmembrane protein which is ubiquitously expressed in all parts of the body, but shows predominant expression in the brain [24]. APP probably has two main metabolic pathways; one non-amyloid-forming and one amyloid-forming pathway. The amyloid forming non-normal pathway produces the Aβ polypeptide which is prone to form dense amyloidogenic aggregates that are resistant to proteolytic degradation and removal [45].

In AD brains, the Aβ peptide forms virtually insoluble amyloid fibrils that accumulate into senile plaques [45]. The cleaved Aβ peptide has the sequence as shown in Figure 2.6. The most common Aβ form in plasma comprises 40 amino acids (Aβ_{1-40}), but an Aβ comprising 42 amino acids (Aβ_{1-42}) is the most common form in plaques. This longer form tends to aggregate more rapidly and it is believed that it is more pathogenic than Aβ_{1-40} [54, 21]. Mainly, the Aβ peptide is in random coil conformation at these conditions and there is no significant difference in structure between the 40 and 42 residue long fragments. Experimentally, there is a distinct difference in oligomerization pathways of Aβ_{1-40} (Aβ_{40} hereafter) and Aβ_{1-42} (Aβ_{42} hereafter) [55]. Aβ_{42} is one of the major components of amyloid plaques. This peptide is highly insoluble in water. Experiments *in vitro* evidence the upper limit of the critical concentration of Aβ_{42} in water in the low micromolar range [21]. In the presence of 20 % of trifluoroethanol in water, peptide aggregates are observed after 10 days, when the concentration of Aβ_{42} is in nanomolar range [56]. Aβ_{42} is soluble and has predominantly α-helical conformation in some organic solvents (trifluoroethanol, hexafluoroisopropanol) [56, 57]. Upon addition of water, the solubility of Aβ_{42} decreases in a drastic way and formation of fibril aggregates complicates analysis of the secondary structure of an isolated Aβ_{42} peptide. Circular dichroism (CD) studies evidence mainly a disordered structure of Aβ_{42} in water with noticeable content of β-sheets and only a small amount of α-helices [56, 57]. Presumably, this reflects the structure of the peptide in its aggregated (fibrillar) phase, whereas the conformation of a single Aβ_{42} peptide in water is not clear. Other Aβ peptides exhibit a similar conformational behavior in water and in apolar solvents [58].

Higher solubilities of some of the peptides allowed studies of the concentration and temperature dependence of their secondary structure and to approach the monomeric state more closely. The Aβ_{40} peptide shows temperature-induced changes of the CD spectra upon heating from 0 to 37 °C, which evidence an increasing β-structure content [59]. These changes do not depend on the peptide concentration and, therefore, may be attributed to the properties of the monomer. The solubility of the Aβ_{12-28} peptide decreases upon heating and the CD spectra evidence the change of the secondary structure from a random coil-like structure with noticeable amount of polyproline-II helices toward a β-sheet like structure [60]. Qualitatively similar changes of the CD spectra upon heating were obtained for several other Aβ peptides in water, including the Aβ_{40} peptide [61]. The peptides Aβ_{10-35} [62] and Aβ_{1-28} [63] show a collapsed coil structure in water and an extensive β-sheet structure appears upon aggregation, only. A decrease of the Aβ_{25-35}

peptide concentration causes a decrease of β-sheet structure (presumably due to the suppression of aggregation) and facilitates disordered structures and β-turns, which may reflect the conformation of a single peptide in water [64].

In vitro experiments using, photo-induced cross-linking of unmodified proteins, size-exclusion chromatography, dynamic light scattering, circular dichroism spectroscopy, and electron microscopy showed that Aβ exists as monomers, dimers, trimers, tetramers, and larger oligomers in rapid equilibrium [19, 20, 55]. The Aβ distribution is multimodal, displaying a prominent peak of pentamers/hexamers and smaller peaks of dodecamers and octadecamers [55]. The conformation of Aβ is environment dependent. In aqueous solution, Aβ exists mainly as a random coil [65]. It has been suggested that Aβ is not toxic in a non-aggregate form, but becomes detrimental after undergoing a structural transition from a random coil to a β-sheet conformation, followed by fibril formation [57]. In experimental studies regarding temperature dependence for Aβ fibril formation, revealed that a large activation free energy is required to add a monomer to the growing fibril tip [20]. The process may involve a significant increase in entropy, suggesting that a large conformational change is required for Aβ [20].

It is evident that Aβ deposition is a central event in the pathological cascade, but why does the E22G Arctic mutation lead to AD, whereas the E22Q, E22K, A21G and D23N mutations lead to a different clinical phenotype [24, 26, 66]. The Arctic Aβ_{40} peptide has been shown to aggregate faster than Aβ_{40} and to have unique aggregation properties like forming soluble aggregation intermediates, protofibrils, more rapidly and in larger quantities than Aβ_{40} [24]. Also, Arctic Aβ_{42} aggregates assembles into protofibrils and fibrils more rapidly than Aβ_{42} wild type [66]. The dramatic effect of the Arctic mutation on aggregation rate could be a result of the loss of charge, resulting from the substitution of the negatively charged glutamic acid for a glycine at position 22 [66, 67]. In contrast to the other mutations within the Aβ domain, carriers of the Arctic mutation show an early-onset of the AD clinical symptoms. Several mutations with increased aggregation rate have a loss of charge in this region. Besides the Arctic mutation, also the Dutch mutation (E22Q) [53] and Iowa mutation (D23N) [68], accelerate Aβ aggregation and have a loss of charge. The answer may lie within the Aβ sequence. The KLVFFA sequence at position 16—21 in the Aβ peptide is central in the fibrillization process [25]. Disease related mutations at position 21—23 in Aβ are located close to the central hydrophobic core ($L_{17}VFFA_{21}$) region and could therefore affect the conformation of the peptide and its fibrillization process. This central hydrophobic core (CHC) sequence influencing the peptide topology and direct folding are critical determinants of aggregation intermediate structures, pathways and kinetics of Aβ peptide fragment [26].

Aβ_{16-22} peptide fragment

Several short sequences from the full-length β-amyloid, for example, Aβ_{1-28} [69], Aβ_{9-25} [70], Aβ_{10-35} [71, 72, 73], Aβ_{16-22} [28], Aβ_{26-33} and Aβ_{34-42} [54] have been shown to form amyloid fibrils in isolation. The seven residue peptide Ace-KLVFFAE-NH$_2$ called as Aβ_{16-22} (Aβ_7 hereafter), is one of the shortest reported amyloidogenic sequences. This peptide, having a positive charged residue at the N-terminus (K16), and a negative charged residue at the C-terminus (E22), is of particular interest since four disease-causing mutations occur in this region [28]. This peptide contains the central hydrophobic core (CHC) of the Aβ peptide. Results from solid-state NMR show that the peptides adopt a β-sheet structure within the fibrils [28]. Recently, Aβ_7 peptide rearrangement has been observed from their initial state into the final antiparallel configuration, using an isotope-edited infrared spectroscopic technique in aqueous solution at the molecular level [29]. Due to its small size, it has also been studied extensively by computational chemists using molecular dynamics simulations [74, 75, 76]. These simulations usually start from a β-sheet arrangement and study its stability.

The antiparallel arrangement of β-strands has been confirmed by simulations of Aβ_7 in explicit aqueous solvent. Ma and Nussinov, in 2002, reported that the most stable conformation for an octamer of Aβ_7 is that of two parallel β-sheets, each comprising four antiparallel β-strands [76]. The antiparallel alignment was also found to be the lowest-energy conformation by Santini et al. (2004) for dimers and trimers of Aβ_7 [77, 78]. Aβ_7 may exist in a metastable conformation in aqueous solution under conditions in which Aβ_7 can aggregate [79]. Driven by hydrophobic and electrostatic interactions with concomitant conformational changes, Aβ_7 may form dimers, tetramers, and higher order species. Hydrophobic contacts in conjunction with electrostatic and hydrogen bonding interactions, have been shown to stabilize Aβ_7 peptides [74], locking them into the antiparallel β-sheet orientation. The possible role of electrostatic interactions in enhancing the stability of amyloid fibrils through salt bridges has been investigated for a number of amyloidogenic peptides [80, 81]. Thus computer simulations of simplified [82] and atomic [76, 74] models have provided useful insights into aggregates of some peptide systems. Recent computer simulations have also sought to characterize the stability of fibril like β-sheet structures [83, 27]. Although providing valuable information about the nature of the resulting fibrils, the above structural studies offer limited insight into how and why aggregation proceeds [83]. A detailed molecular mechanism of fibril formation, which takes into account both the disaggregated as well as aggregated states, has yet to emerge from such studies. The afore mentioned studies suggest, that small peptides like Aβ_7 are well suited as model systems for probing the mechanisms of fibril formation, and elongation process.

Chapter 3

Aim of the Present Work

The ultimate goal of any simulation is to characterize and predict the behavior of real systems. Whether this goal is achieved very much depends on the quality of the model used and the available computational power. No model is an exact representation of the real system. All models must be verified, normally by comparison to experimental data. In the case of simulations aimed at understanding the mechanism of peptide folding or misfolding, verification represents a significant challenge.

A primary goal of my work will be to study the volumetric and conformational properties of the Aβ_{42} peptide and their fragments in liquid water in a wide temperature range. The secondary structure and other structural characteristics of Aβ_{42} and Aβ_{16-22} (Aβ_7) are analyzed as function of temperature. The intrinsic thermal expansion coefficient of Aβ_{42} is estimated by taking into account the expansivity of hydration water. Analysis of water clustering in the hydration shell is used to characterize the thermal breaking of the spanning H-bonded water network. Finally, we discuss the mutual relation between the conformational behavior of Aβ_{42}, the thermal expansivities of Aβ_{42} and its hydration water and the clustering in the hydration water shell.

We also analyse all atom models for peptide aggregation in solution that reproduces known experimental aggregation characteristics and enables predictions of aggregation pathways and mechanism for disease proteins. In this study, we report the structure of the initial deposit (in fibril formation study), the mechanism of monomer/fibril association (in fibrils elongation study) and the nature of the reorganization, from an initially formed deposit to a well-formed fibril at various temperatures. Our efforts in MD simulations is to employ all atom models of Aβ

peptide and Aβ peptide fragments in explicit aqueous solvent. Additionally, general features of the aggregation behavior as a function of temperature and peptide concentration could be explored by using MD simulation with a variety of amyloid peptide fragments. In this study we used Aβ_7 peptide to study fibril growth mechanism. One way to understand the underlying mechanisms for aggregation, and consequently also conformational behavior, is to understand the physical interactions stabilizing and inducing structure, either the single protein or the aggregation. I have made kinetic studies in order to better understand the aggregation process of this peptide. A detailed molecular mechanism of fibril formation, which takes into account both the disaggregated as well as aggregated states, has yet to emerge from such studies.

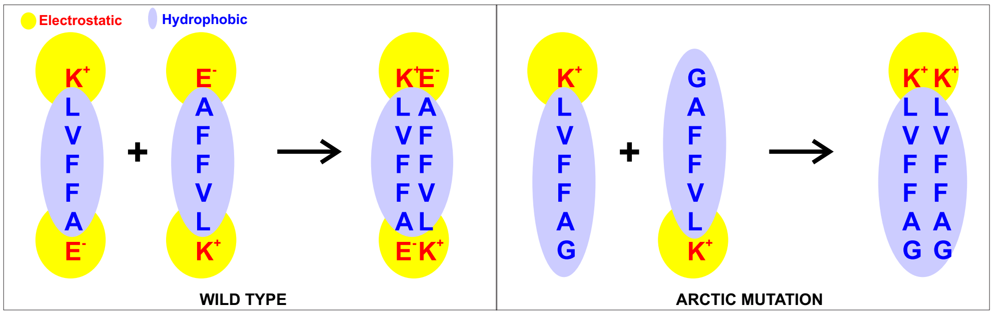

Figure 3.1: *Schematic representation for Aβ_7 wild type and arctic mutation hydration shells overlap.*

The secondary goal of my work to identify the sequence dependent properties of peptide aggregation by mutation analysis. The molecular-level perspective offered by simulations facilitates the identification of the amino acids crucial to aggregation and folding. There is evidence that evolutionary selection has tended to avoid amino-acid sequences, such as alternating polar and hydrophobic residues that favor a β-sheet structure of the type seen in amyloid fibrils [84]. Aβ_{16-22} (Aβ_7) aggregate mainly driven by hydrophobic and electrostatic interactions with concomitant conformational changes, Aβ_7 may form dimers, tetramers and/or higher order species [28]. Aβ_7 peptides may adopt an antiparallel organization by electrostatic effect and hydrophobic effect to shield hydrophobic residues from aqueous solvents. Destructive overlap of hydrophobic and hydrophilic hydration shells is depicted in Figure 3.1. The effects of electrostatically enhanced hydrophobic interactions are of major importance in many processes in aqueous solution such as protein folding, aggregation and molecular recognition. In order to resolve this discrepancy (antiparallel or parallel?) and to probe the effects of electrostatic interactions on Aβ_7 peptide aggregation, we simulated Arctic mutant (E22G) peptide in aqueous solution as wild-type. The dramatic effect of the Arctic mutation on aggregation could be a result of the loss of saltbrige (between K and E) or charge, resulting from the substitution of the negatively charged glutamic acid for a glycine at position 22, we expected that more parallel orientation then wild-type as shown in Figure 3.1. Although Arctic mutations of Aβ associated with AD are relatively rare and lead to a different clinical phenotype, detailed studies of these mutations may prove critical for gaining important insights into the mechanism(s) of Aβ aggregation and AD. At this point, little is known about the mechanism of fibrillization, particularly if different mechanisms can lead to the familiar amyloid structure.

While we are using our systems in different temperatures it is privilege to apply Replica Exchange Molecular Dynamics (REMD) algorithm. The REMD method consists of several identical copies of the system, or replicas, being simulated in parallel over range temperatures [85, 86]. This is an efficient way to simulate complex systems at different temperatures. It offers a much-improved approach for determining oligomer distributions relevant to aggregation. We also used REMD to study Aβ_7 peptide and Arctic mutant peptide aggregation at atomic level in explicit aqueous solution.

Chapter 4

Simulation Methods

Biomolecular systems are dynamic systems, with the atoms in constant motion. These movements are correlated and may be essential for biological function. We carry out biomolecular simulations in the hope to understand the properties of assemblies of peptides in terms of their structure and the microscopic interactions between them. Computer simulations act as a bridge (see Figure 4.1) between theory and experiment [87]. We can test a theory by conducting a simulation using the same model. Alternatively we can test the model by comparing with experimental results. We may also carry out simulations on the computer that are difficult or impossible in the laboratory (for example, working at extreme temperature or pressure). This serves as a complement to conventional experiments, enabling us to learn something new, something that cannot be found out in other ways [88].

There are two main approaches in performing molecular simulations: the deterministic (Molecular Dynamics) and the stochastic (Monte Carlo). Additionally, there are a whole range of hybrid techniques which combine features from both, for example Replica Exchange Molecular Dynamics (REMD) simulations [89, 90]. The choice of the simulation method depends on the system and properties under study. Molecular dynamics (MD) is more appropriate when calculating time dependent quantities such as transport coefficients while Monte Carlo (MC) is most appropriate to investigate systems in certain ensembles. The two methods also differ in their ability to explore the conformational space [91]. The ability of MC method is to make non-physical moves can significantly increase the capacity to explore the phase space while MD might not be able to cross barriers between the conformations sufficiently often to ensure the correct statistical sampling. Thus MD can be very useful in exploring local phase space whereas MC method may be more effective for

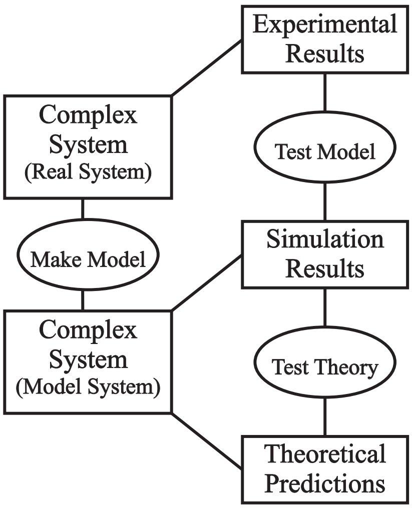
Experimental Results
Complex System (Real System)
Test Model
Make Model
Simulation Results
Complex System (Model System)
Test Theory
Theoretical Predictions

Figure 4.1: *Simulations as a bridge between theory and experiment.*

wider conformational changes [41, 92]. MD may require large computational costs, but can ultimately yield detailed dynamic information such as folding / aggregation pathways and rates of conformational changes.

4.1 Molecular Dynamics simulation techniques

The molecular dynamics method was first introduced by Alder and Wainwright in the late 1950's [93, 94] to study the interactions of hard spheres. Many important insights concerning the behavior of simple liquids emerged from their studies. The next major advance was in 1964, when Rahman carried out the first simulation using a realistic potential for liquid argon [95]. The first molecular dynamics simulation of a realistic system was done by Rahman and Stillinger in their simulation of liquid water in 1974 [96]. The first protein simulations appeared in 1977 with the simulation of the bovine pancreatic trypsin inhibitor [97] and made many other important methodological contributions in MD. Today in the literature, one routinely finds molecular dynamics simulations of solvated proteins [86], protein-DNA [98], protein-protein complexes [99] as well as lipid systems [100] addressing a variety of issues including the thermodynamics of ligand binding and the folding of small proteins [101].

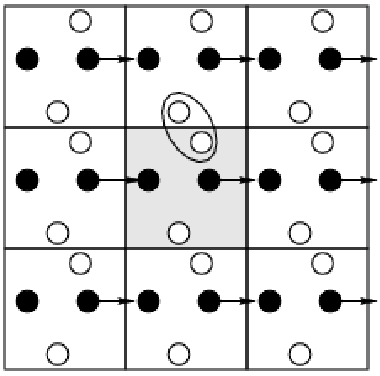

Figure 4.2: *A schematic representation of periodic boundary conditions in two dimensions. The black particle leaves the central box by leaving a through right-hand boundary, and consequently re-enters through the left-hand boundary. The two white particles interact through the boundary.*

4.1.1 Periodic Boundary Conditions

In view of the fact that the system size is small, a cluster of particles will have a lot of unwanted boundaries with its environment. By using periodic boundary conditions, one avoids real phase boundaries. This idea is represented in Figure 4.2. In this approach, the original box containing a solute and solvent molecules is surrounded with identical images of itself, i.e., the positions and velocities of corresponding particles in all of the boxes are identical. Moreover, particles interact with “images” of other particles in all replica boxes. The common approach is to use a cubic or rectangular parallelepiped box, but other shapes are also possible (e.g., truncated octahedron). By using this approach, it is possible to obtain an effect on an infinite sized system. The particle (usually a solvent molecule) which escapes the box on the right side, enters it on the left side, due to periodicity. A very good pictorial description of the method can be found in the textbooks [102, 30, 41, 92].

4.1.2 Constraint Dynamics

The constraint dynamics is handled by the SHAKE algorithm [103]. The SHAKE method allows one to consider atomic connectivity without harmonic bonds. Valence bonds vibrate at high frequency and impose a small integration time-step to a simulation. This method allows us to use larger time steps (e.g., from 1 fs to 2 fs). Consider two atoms bonded to each other at a fixed distance, a. The equality is usually written down in the form of a holonomic constraint:

$$r_k^2 - a_k^2 = 0 \tag{4.1}$$

In a constrained system, the coordinates of the particles are not independent of each other, and the equations of motion in each of the coordinate directions are related. The constraint forces lie along the bonds at all times. For each constrained bond, there are two equal, but opposite forces on the two atoms that comprise the bond, and therefore no energy is put into the system. The major advantage of this method is not the removal of a number of degrees of freedom (i.e., independent variables) from the system, but the elimination of high frequency vibrations corresponding to "hard" bond stretching interactions. In simulations of biological molecules with large conformational changes, these modes are usually of least interest, therefore their exclusion allows increasing the size of the time step, and in effect achieve a longer time range for simulations. A comprehensive introduction to SHAKE is provided in the textbook of Allen and Tildesley [102].

4.1.3 Canonical NPT and NVT ensembles

Isothermal-Isobaric (NPT) ensemble

In the isothermal-isobaric ensemble, number of atoms (N), pressure (P) and temperature (T) are conserved. In addition to a thermostat, a barostat is needed. It corresponds most closely to laboratory conditions with a flask open to ambient temperature and pressure.

Isothermal-Isochoric constant volume ensemble

In this canonical ensemble, number of atoms (N), volume (V) and temperature (T) are conserved. In NVT, the energy of endothermic and exothermic processes is exchanged with a thermostat. A variety of thermostat methods are required to add and remove energy from the boundaries of an MD system in a realistic way, approximating the canonical ensemble. Popular techniques to control temperature include the Nosé-Hoover [104] thermostat and Langevin dynamics.

4.1.4 Replica Exchange Molecular Dynamics (REMD) simulations

The replica exchange was originally created to deal with the slow dynamics of disordered spin systems. It is also called parallel tempering. The replica exchange MD (REMD) formulation [89, 90] tries to overcome the multiple-minima problem by exchanging the temperature of non-interacting replicas of the system running at several temperatures. A number of techniques have been developed to overcome kinetic trapping. Mitsutake and co-worker have provided an excellent review of these generalized ensemble methods [105]. Replica exchange is an efficient way to simulate complex systems at low temperature and is the simplest and most general form of simulated tempering [106]. Sugita and Okamoto have been the first to extend the original formulation of replica exchange into an MD-based version (REMD), testing it on the pentapeptide Metenkephalin in vacuo [90].

The basic idea of REMD is to simulate different copies (replicas) of the system at the same time but at different temperatures values. After a certain time, conformations are exchanged with a Metropolis probability. This criterion ensures that the sampling follows the canonical Boltzmann distribution at each temperature. Kinetic trapping at lower temperatures is avoided by exchanging conformations with higher temperature replicas. The acceptance rule for each state-exchange moves between two neighboring states i and j is chosen to be

$$P_{acc} \;=\; \min\{1, \exp[(\beta_i - \beta_j) \times \left(U(\vec{r}_i^{\,N}) - U(\vec{r}_j^{\,N})\right)]\}\ , \tag{4.2}$$

where $\beta = 1/k_B T$ and $U(\vec{r}_i^{\,N})$ represents the configurational energy of the system in state i.

This method is easier to apply than other generalized ensemble methods because it does not require a prior knowledge of the population distribution [107]. We focus on REMD, which has been widely used in protein folding simulations. Because the method is simple and because it is trivially parallelized in low-cost cluster environments, it rapidly gained wide application. Berne and coworkers applied this method to obtain a free energy landscape for β-hairpin folding in explicit water using 64 replicas with more than 4000 atoms [108]. With the equilibrium ensemble and the free energy landscape in hand, they reported that the β-hairpin population and the hydrogen bond probability were in agreement with experiments, and they proposed that the β-strand hydrogen bonds and hydrophobic core form together during the folding pathway.

REMD was further developed to include exchanges in multidimensional Hamiltonian space in combination with umbrella sampling [109]. It was also adapted to a heterogeneous parallel cluster by multiplexing the replicas in each temperature [110]. Paschek was added an extension of REMD approach where replicas sample a range of volumes and temperatures, which we call the VTREMD (volume–temperature REMD) approach [111] to describe pressure effects on the equilibrium helix–coil transition of an α-helical peptide [112]. Similar to temperature exchanges, they devised exchange rules for the reversible folding/unfolding of the C-terminal (41–56) fragment of protein G (GB1) with different intensive thermodynamic parameters like density and its conjugate variable, pressure [113]. Moreover, recently Paschek published his simulations from the unfolded ensemble, providing the first unbiased folding of the Trp-cage in explicit solvent. Extensive simulation uses 40 replicas(100 ns per replica) distributed over a temperature range from 280.0 to 539.7 K [86], where multiple copies (or replicas) of identical systems are simulated in parallel at different temperatures. Periodically state-exchange moves are attempted, where two neighboring replicas exchange their thermodynamic state (their temperature). The state-exchange acceptance probability P_{acc} as Eq. 4.2 has been shown to obey the detailed balance condition for an extended ensemble of canonical states [30]. The temperature spacing between each of the replicas was chosen such that the energy distributions overlap sufficiently and state exchange attempts are (on average) accepted with a 20 percent probability. Nevertheless, it suffers from one significant problem when it is applied to significantly large systems [86]. The higher the number of degrees of freedom in the system the more replicas should be used. It is not clear how many replicas should be used if a peptide or protein is simulated with explicit water. The transition probability between two temperatures depends on the overlap of the energy histograms. The histograms width depends on $1/\sqrt{N}$ (where N is the size of the system). Hence, the number of replicas required to cover a given temperature range increases with the size. As can be inferred from the examples described above [114](82 replicas for protein A versus 16 for Met-enkephalin), the major drawback of the original REMD is the dependence of the number of replicas on the degrees of freedom f in the system. To obtain a reliable result, each pair of adjacent replicas must have overlapping energy distributions [90].

The REMD methodology [90, 115] was shown to be an effective technique to sample the conformational space of short peptides in explicit solvent. This is an efficient way to simulate complex systems at different temperatures and is the simplest and most general form of simulated tempering [89]. It offers a much-improved approach to determining the oligomer distributions relevant to aggregation [116]. García and co-workers found multiple basins in the free energy landscape and concluded that

Aβ_{16-22} can form other stable configurations aside from parallel and antiparallel dimmers [116]. Meinke and Hansmann[117] also observe for a system of six β-amyloid fragment peptides (without explicit water) above 400 K a strong increase of R$_G$ but do not observe a temperature minimum. Recently, Paschek published such simulations, providing the first unbiased folding of the Trp-cage in explicit solvent using 40 replicas (100 ns per replica) [86]. REMD was implemented with a constant volume and a fixed number of atoms. Taking Paschek et al. work as a reference [86], we used REMD to study Aβ_{16-22} peptides aggregation at atomic level in explicit aqueous solution [118].

4.2 Force fields

In molecular dynamics (MD), successive configurations of the system are generated by integrating Newton's second law or the equation of motion (The motion of the atoms due to the forces acting on them follows Newton's equations of motions. The integration of Newton's equations of motion is done using the leap-frog algorithm, which is a descendent of the Verlet-Method [102].), F=ma, where 'F' is the force exerted on the particle, 'm' is its mass and 'a' is its acceleration. From knowledge of the force on each atom, it is possible to determine the acceleration of each atom in the system. Given an interaction function $V(r_1, r_2, ..., r_N)$, the force vector F on each particle is calculated as:

$$F_i = \frac{-\partial V}{\partial r_i} \tag{4.3}$$

with i =x, y or z. The position vector r is obtained as:

$$\frac{d^2 r_i}{dt^2} = \frac{F_i}{m_i} \tag{4.4}$$

From this differential equation, the set of Cartesian coordinates {r{t}} and velocities {v(t)} for all particles is generated. A trajectory that describes the positions, velocities and accelerations of the particles as they vary with time. From this trajectory, the average values of properties can be determined. The method is deterministic; once the positions and velocities of each atom are known, the state of the system can be predicted at any time in the future or the past. This can be interpreted as a statistical ensemble that will enable a macroscopic description of the behavior of the system. In molecular dynamics, the evolution of the molecular system is studied as a series of snapshots taken at very close time intervals (usually of the order of femtoseconds), those steps can be time consuming and computationally expensive. However, computers are getting faster and cheaper. Simulations of solvated proteins are calculated up to the nanosecond time scale; however, simulations into the millisecond regime have been reported.

For biomolecules, $E(r_1, r_2, ..., r_N)$ corresponds to a set of semi-empirical functions that model the effective interactions between the particles. There has been a considerable effort to develop reliable interaction functions or force fields for proteins. Typical examples are GROMOS96 43a1 [119, 120, 121, 122] and AMBER94 [123], CHARMM [124], OPLS-AA [125]. In general, these force fields depend on the functional forms and parameters used to model each interaction. Interactions are modeled by two types of physical terms: Non-bonded interactions ((fixed) charge-charge and van der Waals interactions) and bonded interactions (stretching, bending and torsions). In addition, non-physical terms to restrain and constrain the system may also be included. From the statement of the model, it is logical to argue that the quality of the interaction function chosen together with the time length of the simulation are key points that determine the accuracy of the data generated [126].

OPLS-AA force field

This force field, developed by Professor W. Jorgenson of Yale University, is probably the best one available for condensed phase simulations of peptides. All force-field equations are identical to those of authentic OPLS-AA [125]. The OPLS-AA force field or interaction function has the following form (for a complete description see Jorgensen et al. [127, 125]):

The total energy E_{tot} of a molecular system was evaluated as a sum of the following components: the nonbonded energy E_{nb}, bond stretching and angle bending terms E_{bond} and E_{angle}, and the torsional energy $E_{torsion}$.

$$E_{tot}(\theta) = E_{bond}(\theta) + E_{angle}(\theta) + E_{nb}(\theta) + E_{torsion}(\theta) \tag{4.5}$$

The nonbonded part was computed as a sum of the Coulomb and Lennard-Jones contributions for pairwise intra- and intermolecular interactions:

$$E_{nb} = \sum_{i<j} [q_i q_j e^2 / r_{ij} + 4\varepsilon_{ij}(\sigma_{ij}^{12}/r_{ij}^{12} - \sigma_{ij}^{6}/r_{ij}^{6})] f_{ij} \tag{4.6}$$

Geometric combining rules for the Lennard-Jones coefficients were employed: $\sigma_{ij} = (\sigma_{ii}\sigma_{jj})^{1/2}$ and $\varepsilon_{ij} = (\varepsilon_{ii}\varepsilon_{jj})^{1/2}$. The summation runs over all of the pairs of atoms $i < j$ on molecules i and j or i and i for the intramolecular interactions. Moreover, in the latter case, the coefficient f_{ij} is equal to 0.0 for any i–j pairs connected by a valence bond (1-2 pairs) or a valence bond angle (1-3 pairs). $f_{ij} = 0.5$ for 1,4 interactions (atoms separated by exactly three bonds) and $f_{ij} = 1.0$ for all of the other cases. The bond stretching and angle bending energies were obtained in accordance with eqs 1.5 and 1.6:

$$E_{bond} = \sum_{bonds} K_r(r - r_{eq})^2 \tag{4.7}$$

$$E_{angle} = \sum_{angles} K_\theta(\theta - \theta_{eq})^2 \tag{4.8}$$

Here the subscripts eq are used to denote the equilibrium values of the bond length r and angle θ. The last intramolecular term is for the torsional energy which is computed as follows:

$$E_{torsion} = \frac{V_1}{2}[1 + \cos(\phi + f1)] + \frac{V_2}{2}[1 - \cos(2\phi + f2)] + \frac{V_3}{2}[1 + \cos(3\phi + f3)] \tag{4.9}$$

with the summation performed over all of the dihedral angles i, where θ is the dihedral angle, V_1, V_2, and V_3 are the coefficients in the Fourier series, and f_1, f_2, and f_3 are phase angles, which are all zero for the present systems.

Comparisons to ab-initio calculations and experiment show that OPLS-AA reproduces conformational energies well for systems for which it has been specifically parameterized [128]. However, especially good results obtained for proteins from last five years. The parameters have been updated to December 1999. With the exception of improved charge, van der Waals and torsion parameters for sulfur, all parameters are native OPLS-AA. The new parameters, which use appreciably smaller charges on sulfur and which have been validated in liquid-phase simulations, significantly improve the conformational energetics of CYS and MET residues in proteins [128]. The non-bonding parameters of the OPLS force field have generally been obtained from calculations with cut-off radii $R_c = 0.95 - -1.5nm$, with the longer-range van der Waals interactions being included though correction formulae (see for example, Ref. [129]). Throughout this thesis, all systems are simulated using the OPLS-AA/L for all-atom force field parameters (GROMACS 3.2.1 /3.3 software[120, 121]).

Water Models

Water is probably the most important molecule in our relation to nature. More than 30 years ago, computer simulations of water started their road with the pioneering papers by Watts and Barker [130] and by Rahman and Stillinger [131]. A key issue when performing simulations of water is the choice of the potential model used to describe the interaction between molecules [132]. A number of different potential models have been proposed (see References [133] and [134] for a comprehensive review). It is probably fair to say that the potentials for water most commonly used in the past years have been the SPC, SPC/E [135], TIP3P [136], and TIP4P (Ref. [136]). models. Two recently proposed models, namely, TIP5P (Ref. [137]) and TIP4P/Ew [138], also give promising results and are increasingly used nowadays. The potential parameters of these models were often chosen to reproduce thermodynamic and/or structural properties of water at room temperature and pressure [132]. All these models have two common features: a Lennard–Jones (LJ) center is located on the oxygen atom and positive charges are situated on the hydrogen atoms.

In the SPC model, first proposed by Berendsen et al. [135], the geometry of the molecule does not correspond to the experimental one. The O–H bond length is assigned to 0.1 nm and the H–O–H bond angle is set to the tetrahedral value. The negative charge are located at the position of the oxygen atom. In 1987, Berendsen et al. [135] suggested that the polarization energy should be added to the internal energy of the liquid when fitting the potential parameters of the model to the vaporization enthalpy of real water. In this way Berendsen proposed a new water potential denoted as SPC/E. The geometry is the same as that of SPC, but the partial charges on H and O atoms are increased slightly. In the TIPs models of Jorgensen et al. [136] the experimental values of the O–H bond length and H–O–H bond angle are used. Differences between the different TIP models arises from the location of the negative charge. In the TIP3P model the negative charge is located on the oxygen atom. In the TIP4P model the negative charge is located on a point M which is placed at a distance d_{OM} from the oxygen along the H–O–H bisector in the direction of the positive charges as first suggested by Bernal and Fowler [139]. A new version of TIP4P, with potential parameters optimized for Ewald sums (instead of the simple truncation of the potential used in the original TIP4P) has been proposed by Horn et al. [138] This model is denoted as TIP4P/Ew. In the TIP5P model [137] two partial charges are placed at the positions of the "lone electron pairs." The geometry of the TIP5P is similar to that of the water models of the 1970s as, for instance, ST2 [96].

4.3 Computer simulations of protein folding

The simulation of peptide folding with atomic resolution has evolved remarkably during the last 10 years, i.e., from absolute skepticism on the capability of classical molecular dynamics (MD) methodology to reproduce complex biological phenomena. As such that the folding of simple oligopeptides (6–15 residues) to the seemingly realistic representation of the thermodynamics and kinetics of folding of a rapidly increasing number of polypeptides /proteins (over 40 residues) [140, 141]. From a statistical mechanical perspective the folding process may be considered as a stochastic search of the various conformations accessible to a polypeptide chain [40, 13]. A key feature in any successful folding simulation is the extent of sampling. Several techniques have been developed to address this problem such as multicanonical Monte Carlo sampling [27] and a series of different molecular dynamics techniques [76]. These MD techniques use simplified models or all-atom models.

Around 1997, however, the groups of van Gunsteren and Kollman made significant advances with somewhat different approaches, they attempted the folding of a 36-residue polypeptide, villin headpiece subdomain, in water with a phenomenally long (1 μs) simulation. The lower bound to the folding time of this polypeptide had been estimated in 10 μs [142]. This simulation time record (still the longest continuous simulation of a polypeptide in explicit solvent to date) could be achieved by the use of large supercomputing resources, an optimized parallel code developed by the same authors, and a reduced box size in combination with a simplified long-range interaction scheme. In the immediately preceding years, second generations of the most widely used force fields for biomolecular simulation had been developed [126, 125, 123]. The papers by Daura et al. [143] and Duan and Kollman [142] showed that the simulation of the folding of small proteins with atomic resolution was not a chimera but, rather, a question of time. The difficulty to access large supercomputing resources meant that, in most cases, the study of peptide folding by MD simulation was approached from extensive simulations aimed at reproducing the folding/unfolding equilibrium of small, quick folders (oligopeptides). In addition, it had become apparent that the experimentally estimated folding times depended strongly on the resolution of the technique used as well as on the model applied to interpret the data, and that actual folding times could well be shorter than estimated.

In late 1998, a paper by Schaefer et al. [144] opened new expectations on a long-debated simplifying approach, i.e., the use of (improved) implicit-solvent representations in biomolecular simulation in general and in peptide folding in particular. This level of modeling permitted a significant timescale jump and was quickly adopted by a number of groups studying peptide folding [145]. (Interestingly, it did not have a comparable impact on MD simulations of folded proteins.) The presumed correspondence between implicit- and explicit-solvent thermodynamics and kinetics is, however, a matter of active discussion [145]. In parallel to these developments, two papers prepared the terrain for two future important lines of work. On the one hand, Sugita and Okamoto [90] developed a formulation for replica-exchange MD. This built on the replica and multicanonical MonteCarlo algorithms, the latter having been already adapted to MD and later used in peptide folding simulations. In 2001, García and Sanbonmatsu [115] applied the replica-exchange MD algorithm to the study of peptide folding. Since then, this method and its derivatives [113, 86] have become standards for the study of peptide-folding thermodynamics, both in explicit- and implicit-solvent environments.

Experiments and computational simulation techniques both provide information on the details of the folding process. Current computational resources allow the simulation of peptides on a nanosecond to microsecond time-scale using all-atom models [142, 143]. All-atom models can provide an accurate description of the free energy landscape mechanism in certain circumstances. But, these models represent effective many-body interactions and/or interactions that cannot be modelled classically, therefore how reliable and universal they are remains under discussion. Another critical point is how to properly model the effect of single point mutation on peptide conformation. In this direction, two strategies have been developed: simulations in implicit solvent, which have the advantage of computational speed while compromising a detailed representation of hydrogen bond map and charge screening, and simulations in explicit solvent that (partially) include the effects of solvent. This thesis descried with explicit water but at a high computational cost even for a peptide of 42 amino acids (chapter 5 of this thesis) and aggregation process of peptide fragment. We took for further study Aβ_{16-22} as a model peptide, folding of small peptide with well defined motifs suits the requirements for such studies given the size of the molecule, the simplicity of the topology and the relatively fast rates of folding.

4.4 Computer simulations of peptide aggregation

Another major challenge for MD simulation techniques is to shed light on the formation and stability of amyloid fibrils. To be able to model amyloid fibril structures noncovalent inter-molecular interactions, within a given chemical environment, must be described with high accuracy. For example, stability of inter-peptide backbone hydrogen bonds must be reproduced under different solvation and concentration conditions. Therefore, the quality of the force field and the extent of sampling are fundamental issues in peptide aggregation simulations, as they are in peptide folding simulations. Many have used simplified models at the atomic resolution, to study the conformational preferences of the monomer or to evaluate different proposals for aggregate structure. Gupta and co-workers used multi-chain simulations of a two-dimensional lattice model [146] to study the competition between folding and aggregation. Their studies show that there is an optimum denaturant concentration in the refolding solution that maximizes refolding yield: a slightly elevated denaturant concentration destabilizes aggregation-prone intermediates relative to the native state, and thus promotes folding. Dima and Thirumalai [82] explored protein aggregation and self-propagation using Monte Carlo simulations of lattice protein models. They found that chain polymerization is consistent with template assembly, with the dimer being the minimal nucleus. Nguyen and Hall used an intermediate-resolution model to observe amyloid fibril formation by polyalanine peptides [147].

A discontinuous molecular dynamics (DMD) algorithm enabled simulations of systems containing up to 96 peptides. The simulations show that fibrillation is facilitated by the formation of disordered aggregates. These aggregates provide a high local concentration of peptide and therefore facilitate nucleation [147]. These models attempt to reduce the complexity of the problem by removing atomic detail while still hoping to capture the general aspects of the process. Such models have also been widely used in protein folding simulations but were not referred to in the previous section in part because of the current progress in the field being achieved using all-atom force fields. However, in the case of protein aggregation, which is complex and involves large time- and space-scales, coarse grained models remain an attractive option. Off-lattice coarse grained models using DMD simulations have given insight into the thermodynamics and stability of a tetrameric β-sheet complex [148].

As has been elaborated in section 2.3 several simulations of amyloidogenic peptides have been reported. Nussinov and collaborators studied possible multilayer β-sheet oligomer organizations of several peptides by high temperature molecular dynamics (MD) simulations in explicit water. These peptides include the Alzheimer's fragments $A\beta_{16-22}$, $A\beta_{16-35}$, and $A\beta_{10-35}$, [76] the NFGAIL peptide derived from the human islet amyloid protein [149]. Tiana and co-workers extended further this approach by calculating the free energies of dimers, tetramers, and octamers of the Aβ_{12-28} peptide [150]. These studies provide energetic insights into different arrangements but do not explain the assembly process. Gsponer and co-workers simulated the dynamics of the heptapeptide GNNQQNY from the yeast protein prion into trimers using the CHARMM force field and a solvent-accessible surface model [151]. They found that the preferred pathway for a trimer packed in a parallel β-sheet conformation is not associated to a downhill free energy profile because of the existence of mixed parallel-antiparallel β-sheets and parallel β-sheets with different hydrogen bond patterns.

Finally, two folding simulations on Aβ_{16-22} have yielded conflicting results on the nature of the intermediates. Obligatory α-helix intermediates were found by all-atom MD simulations on the trimer in explicit solvent [74]. Santini and Derreumaux are simulated on a dimer, based on the activation-relaxation technique (ART) and the generic OPEP (Optimized Potential for Efficient peptide structure Prediction) energy model, showed that there are multiple aggregation pathways for dimer and trimer formation but that intermediates containing 30% α-helix are not obligatory [77, 78]. In the same way as for oligomerization, different levels of description have been used to study stability of protein aggregates. Much effort has also focused on studying protofilament and fibril elongation. Other approaches have used knowledge from literature (experiment and computational study) and all-atom MD simulations in implicit [152] or explicit solvent [76, 153, 154] to suggest fibril atomic models based on thermodynamic stability. The spontaneous twisting and stabilization of protofilaments is discussed in chapter 7 and 8 of this thesis based on all-atom MD simulations with trajectories on a nanosecond time-scale.

Chapter 5

Temperature-induced conformational changes of amyloid β-peptide and peptide fragments in water

5.1 Temperature-induced conformational changes of Aβ_{42} peptide

The conformation of a single Aβ_{42} peptide and other Aβ peptides in water was intensively studied by computer simulations (see, for example, Refs. [57, 155, 156]). Typically, coil structures dominate the Aβ peptide structure and to some extent β-sheets and α-helices were also seen. However, the temperature-induced changes of the conformation of a single Aβ peptide were not studied, yet. As experimental studies of such changes are complicated by aggregation, which in turn is temperature-dependent, simulations give a unique possibility to look closely into the temperature dependent conformation and physico-chemical properties of a single Aβ peptide in water. The understanding of the conformational behavior of the monomeric state is important, as this is the starting point for peptide aggregation.

In the present section, we study the temperature-induced conformational transition of the Aβ_{42} peptide. The secondary structure and other structural characteristics of Aβ_{42} are analyzed as function of temperature. The intrinsic thermal expansion coefficient of Aβ_{42} is estimated by taking into account the expansivity of hydration water. Analysis of water clustering in the hydration shell is used to characterize the thermal breaking of a spanning H-bonded water network.

5.1.1 Model system

The Aβ_{42} peptide in a full stretched conformation (PDB ID 1z0q) [57] was placed in a cubic box with 7704 water molecules and pre-equilibrated by using 1000 steps of the steepest descent method. Electro-neutrality of Aβ_{42}, which initially had a charge -3e, was provided by distributing the neutralizing charge +3e over all Aβ_{42} atoms proportionally to the absolute values of their charges. The Gromacs software package [157] was used with the OPLS force field [125] for the Aβ_{42} peptide and the SPCE model for water. A spherical cut-off of 0.9 nm was used for the short-range intermolecular interactions; the long-range Coulombic interactions were taken into account by particle mesh Ewald summation. Molecular dynamics (MD) simulations were performed in the NPT ensemble at constant pressure $P = 1$ bar and 22 temperatures between 250 and 460 K, using the Nose-Hoover thermostat and the Parrinello-Rahman barostat. Periodic boundary conditions were applied. Simulation runs were performed with 2 fs time steps and the configuration was saved every 0.1 ps. At each temperature, the system was equilibrated during 1 ns and the subsequent 20 ns run was used for the analysis.

To characterize the conformation of the Aβ_{42} peptide we calculated its radius of gyration R_{gyr}, the solvent accessible surface area (SASA), intra-peptide hydrogen bonds and their distribution along the peptide chain. The secondary structure was determined using corresponding distributions of dihedral angles ϕ and φ in the Ramachandranan plot. A residue was considered as contributing to α-helices, when -90° $< \phi < -35^\circ$ and -70° $< \psi < -15^\circ$; to β-sheets, when -165° $< \phi < -105^\circ$ and 105° $< \psi <$ 165°; to polyproline II structures, when -105° $< \phi < -45^\circ$ and 120° $<$ $\psi <$ 180°. Residues with dihedral angles from other areas of the Ramachandran plot were attributed to disordered secondary structures (Figure 2.2(a)). The randomness of the distribution of residues with particular secondary structure along the protein chain was analyzed by the probability distribution of clusters containing S successive residues with like secondary structure. Clustering of similar residues in the peptide chain belongs to the site-percolation problem in 1D systems. In an infinite chain, the probability n_S to find S successive residues of the same kind in the case of their random (non-correlated) distribution is [158]:

$$n_S = (1 - p)^2 p^S, \tag{5.1}$$

where the occupancy probability p in the case of a biopolymer chain is the fraction of residues with some particular secondary structure. The qualitative shape of the probability distribution n_S in finite chains is similar to that in an infinite chain (Eq. 5.1), but the probabilities of clusters with small S are higher in the former case [159].

To determine the volume of the Aβ_{42} peptide in aqueous solution, we performed NPT simulations of liquid water with the same number ($N = 7704$) of water molecules, but without Aβ_{42} in the simulation box. The difference between the volumes of the two simulation boxes (with and without Aβ_{42}) was considered as the apparent volume $V^{app}(\mathrm{A}\beta_{42})$ of Aβ_{42}. The water density in the first hydration shell was calculated by counting those N_w water molecules, whose oxygens are situated closer then some distance to the nearest heavy atom of Aβ_{42}. The volume of the hydration water shell was estimated using the SASA, obtained with a probe radius of 0.14 nm.

The analysis of water clustering in hydration shells of various widths was performed similarly to previous studies [7, 160]. A water molecule was considered as belonging to the hydration shell, when the shortest distance between its oxygen atoms and the heavy atoms of Aβ_{42} does not exceed some value D, which was varied from 0.4 to 0.55 nm. Two water molecules were considered as hydrogen bonded, when the distance between their oxygens did not exceed 0.335 nm and their pair interaction energy was below -2.7 kcal/mol. At ambient conditions, these criteria yield on average about 3.3 hydrogen bonded neighbors of a water molecule in pure liquid water.

To determine the temperature, where a spanning hydrogen bonded water network breaks into an ensemble of small clusters via a percolation transition, we used the occurance probability n_S of water clusters consisting of S molecules and the probability distribution $P(S_{max})$ of the size S_{max} of the largest water cluster. The distribution n_S calculated with excluding the largest water cluster was used to determine the mean cluster size S_{mean}. The distribution $P(S_{max})$ was used to calculate the probability SP (spanning probability) to find a *spanning* water cluster, which includes most of the molecules in the hydration shell and homogeneously envelopes the peptide.

5.1.2 Conformational behavior of Aβ_{42}

The temperature dependence of the fraction of residues with some particular secondary structure defined using their dihedral angles is shown in the upper panel of Figure 5.1. The fraction p of residues with dihedral angles characteristic of α-

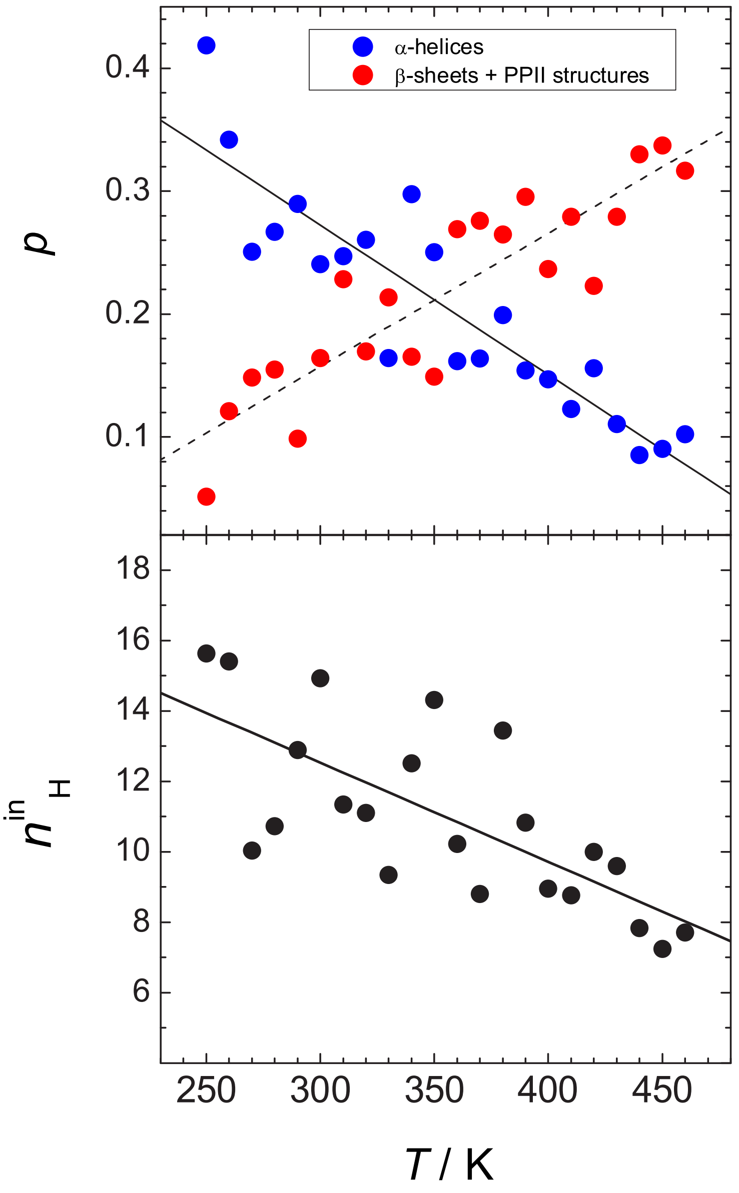

Figure 5.1: *Content p of the residues with particular secondary structure (upper panel) and average number n_H^{av} of intrapeptide H-bonds. Linear fits are shown by lines.*

helices decreases three times upon heating from 260 to about 430 K. In parallel, the corresponding values of p for β-sheets and of polyproline II structures (which are approximately equally populated) increase by about a factor of 3 upon heating. However, the total population of these three secondary structures considered is about 0.4 to 0.5 only, whereas the majority of residues exhibits some disordered structure. The probability distributions n_S of the clusters of residues with like secondary structure are shown in Figure 5.2 together with the random distributions expected for an infinite chain with the same content p. The distribution n_S of β-sheets is close to the random one at all temperatures studied. Upward deviations of n_S from Eq. 5.1 at small S are due to the finite size effect, that facilitates formation

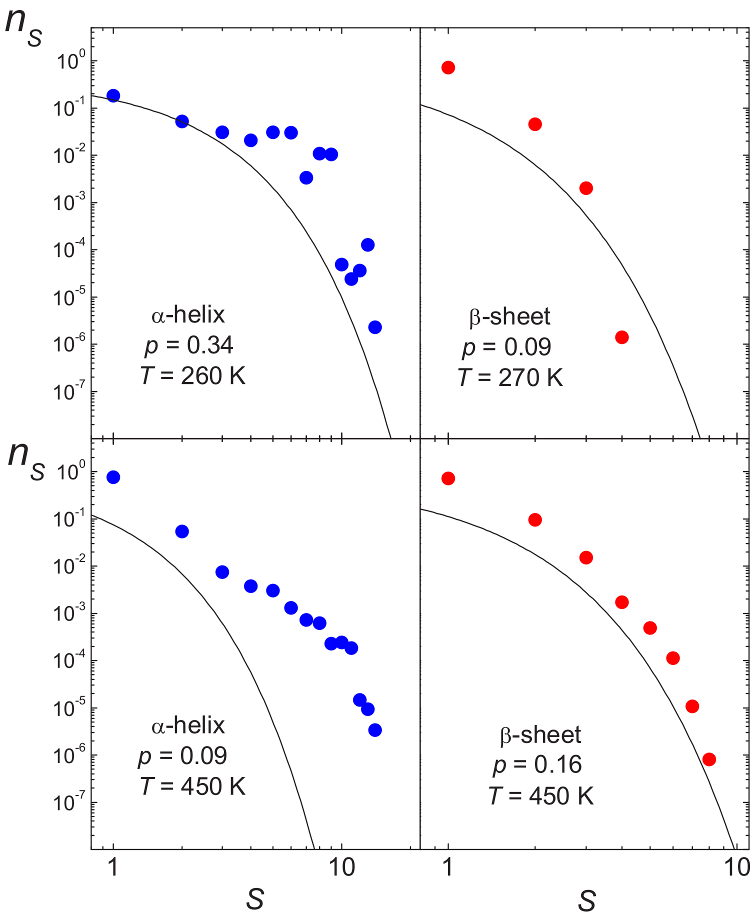

Figure 5.2: *Probability n_S to find S successive residues with the same secondary structure. Lines show n_S for a random distribution of residues in an infinite chain (Eq. 5.1) with the same content p of residues with like structure.*

of smaller clusters [159]. Similar distributions n_S were found for residues attributed to the polyproline II structure (not shown). For α-helices, the distributions n_S evidence a correlation between successive residues: there are clusters of α-helices with large S values (up to $S = 14$), which do not appear for β-sheets and polyprolines, where S does not exceed 4 at the same content p (see Figure 5.2). Besides, at all temperatures, the distribution n_S for α-helices at large S deviates strongly upwards from Eq. 5.1, indicating a trend toward cooperative "condensation" of residues, having α-helical dihedral angles.

The maps, which show the probability distribution of intrapeptide N-H...O bonds between various residues (Figure 5.3), give valuable insight in the secondary structure of Aβ_{42}. At low temperatures, most of the intrapeptide hydrogen bonds are formed between residues i and $(i + \Delta i)$ with $\Delta i = 2$, 3, 4 or 5, which are characteristic of various helices, loops and turns. Figure 5.3 evidences a high probability of such intrapeptide hydrogen bonds along four diagonal lines at $T = 260$ K, that

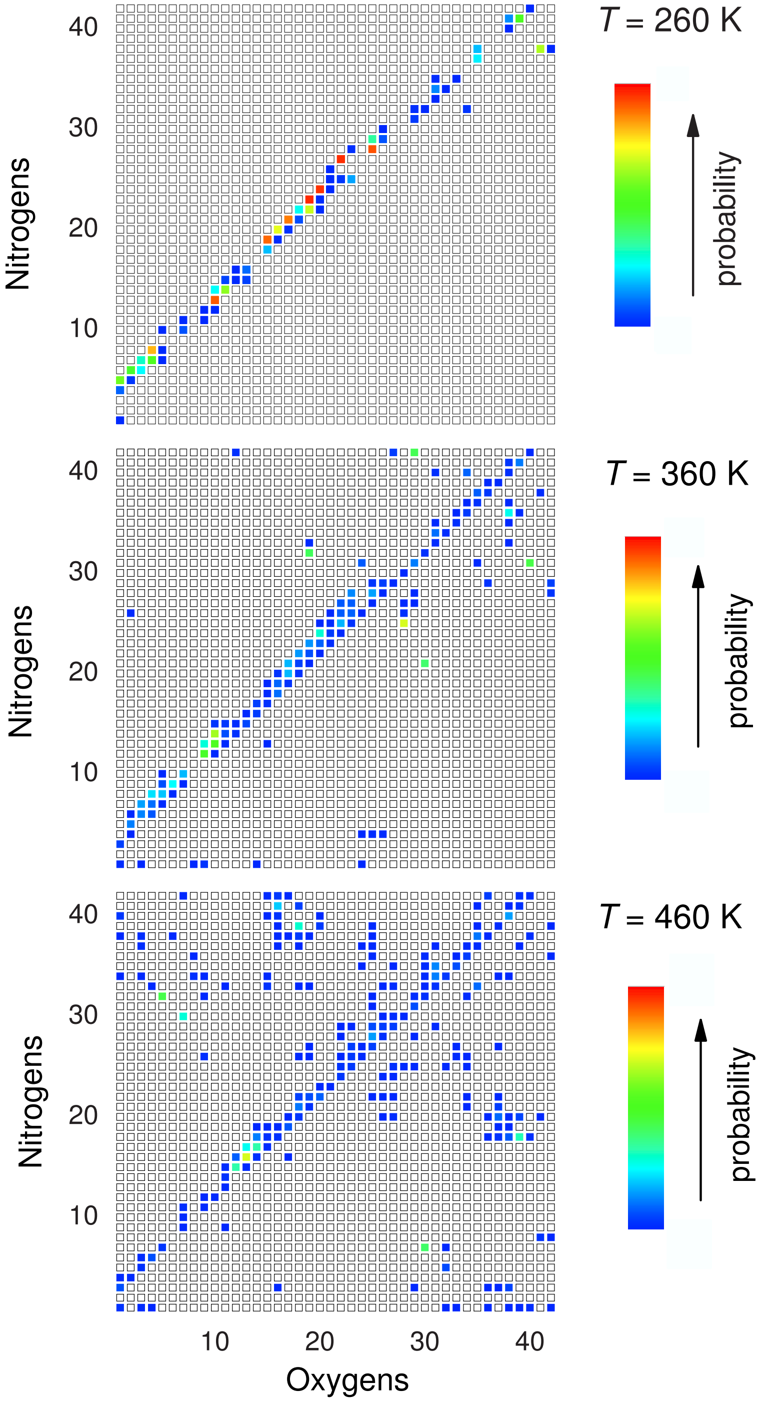

Figure 5.3: *Map of intra-peptide N-H...O hydrogen bonds of $A\beta_{42}$. The color-scale on the right-hand side indicates change of occurrence probability.*

agrees qualitatively with a high content of α-helices at low temperatures (Figure 5.1, upper panel). Upon heating, the average number of intrapeptide Hydrogen bonds decreases noticeably (see lower panel in Figure 5.1). This occurs mainly due to the break of hydrogen bonds with $\Delta i = 2, 3, 4, 5$ (not shown). Accordingly, the fraction of hydrogen bonds with $\Delta i > 5$, which correspond to β-sheets and also to

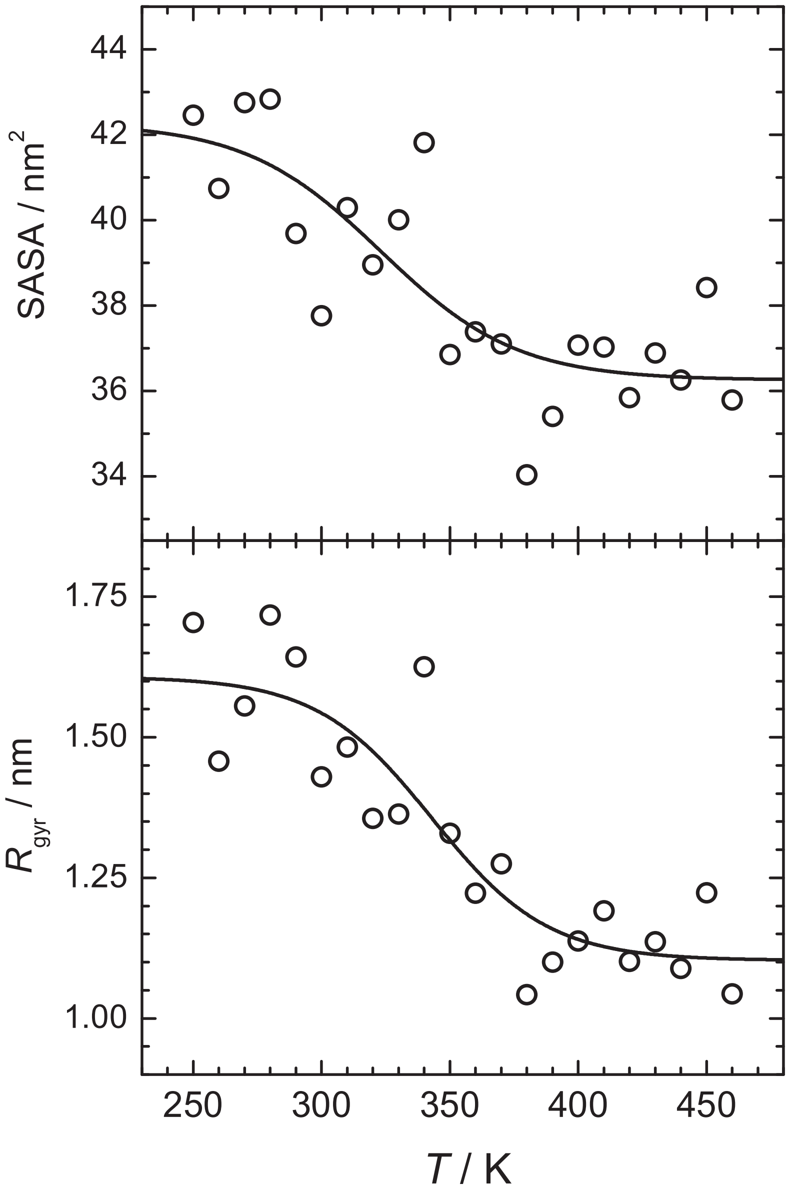

Figure 5.4: *Temperature dependence of the radius of gyration R_{gyr} and solvent accessible surface area SASA of $A\beta_{42}$. Fits to a sigmoidal function are shown by lines.*

irregular hydrogen bonds between distant residues, increases with temperature (see the case $T = 460$ K in Figure 5.3). Temperature-induced changes in the secondary structure of Aβ_{42} are rather gradual and noticeable scattering of the data points (see Figure 5.1) prevents unambiguous recognition of a conformational transition and its transition temperature.

The change of the secondary structure of Aβ_{42} is accompanied by marked changes of its geometry. The radius of gyration R_{gyr} of Aβ_{42} decreases from about 1.5 to 1.1 nm upon heating from 280 to 380 K (see lower panel in Figure 5.4). At the lowest and highest temperatures studied, some trend to saturation may be noticed in the

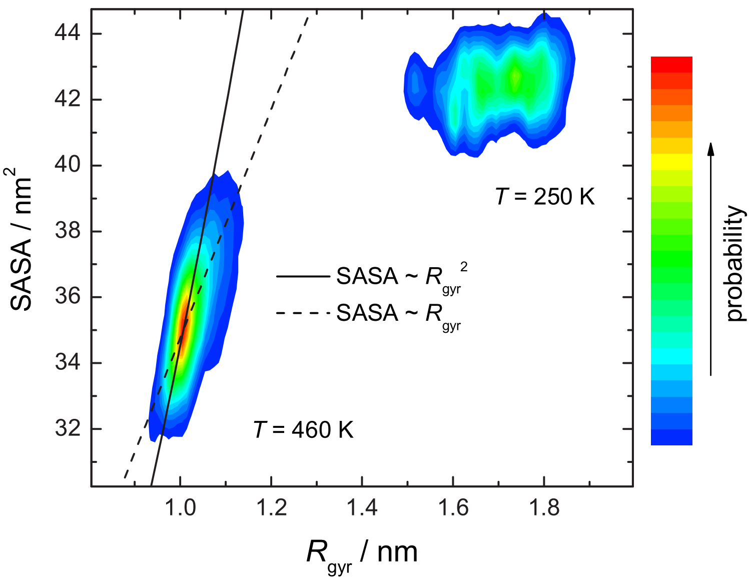

Figure 5.5: *Joint probability distribution of the solvent accessible surface area and radius of gyration of Aβ_{42} at the lowest and highest temperatures studied. The color-scale on the right-hand side indicates change of occurrence probability.*

temperature dependence of R_{gyr}. Indeed, a sigmoidal curve gives better description of $R_{gyr}(T)$ in comparison with a linear fit (mean-square deviations of the data points from the fitting line increase by about 25% in the latter case). A fit of $R_{gyr}(T)$ by a sigmoidal curve (line in lower panel of Figure 5.4) indicates an inflection point at about 340 K. A quite similar temperature behavior shows the SASA of Aβ_{42} (see upper panel in Figure 5.4). In this case, a fit to a sigmoidal function yields an inflection point at about 320 K. A joint probability distribution of R_{gyr} and SASA of Aβ_{42} allows analysis of the correlation between these two parameters (distributions for the lowest and highest temperatures studied are shown in Figure 5.5). Such correlation is practically absent for the low-temperature conformation of Aβ_{42}, which is characteristic of an extended chain. A clear correlation between SASA and R_{gyr} is found for the high-temperature conformation of Aβ_{42}. Taking into account that SASA $\sim (R_{gyr})^2$ for spherical objects and SASA $\sim R_{gyr}$ for elongated ellipsoids or cylinders, the shape of the high-temperature conformation of Aβ_{42} appears to be essentially spherical. Hence, such kind of analysis reveals that Aβ_{42} undergoes a temperature-induced transition from an extended chain-like conformation to a more compact coil conformation upon heating. The midpoint of this transition is approximately at 320 to 340 K.

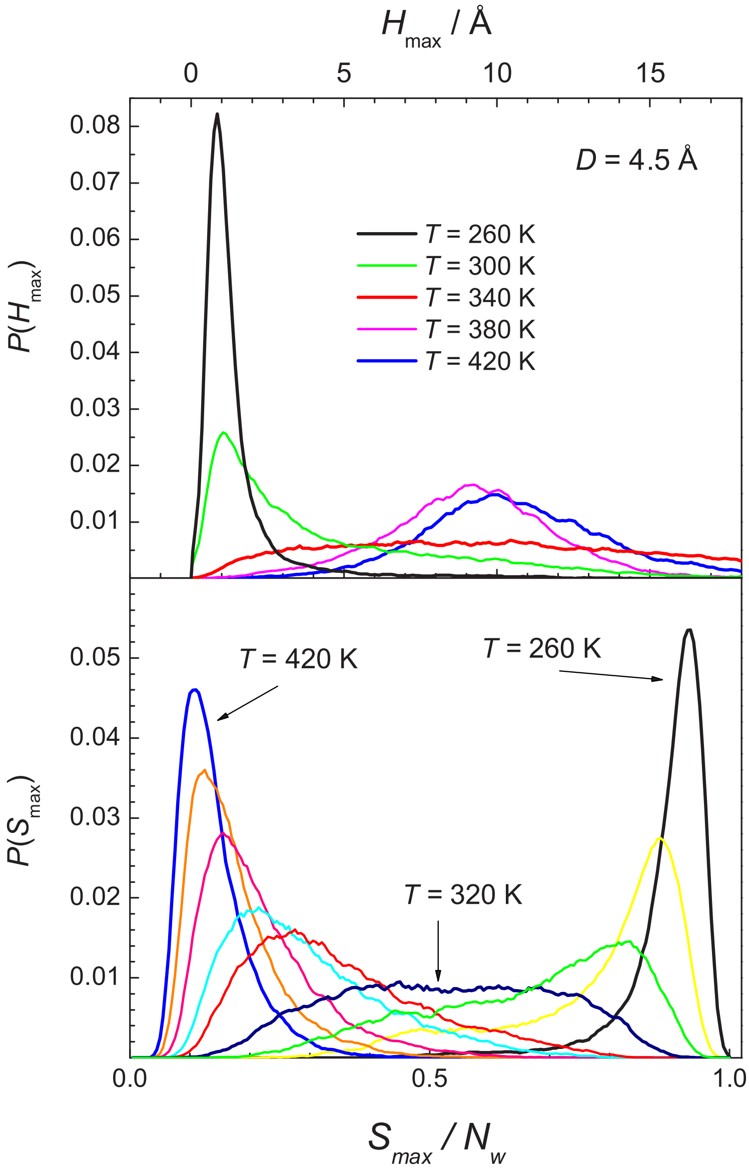

Figure 5.6: *Upper panel: Probability distribution $P(H_{max})$ of the distance H_{max} between the center of mass of Aβ_{42} and the center of mass of the largest hydration water cluster. Lower panel: Probability distribution $P(S_{max})$ of the size S_{max} of the largest water cluster, normalized by the average number N_w of water molecules in the hydration shell of width $D = 0.45$ nm.*

5.1.3 Properties of water in hydration shell of Aβ_{42}

To study the relation between the conformational transition of Aβ_{42} and the structure of hydration water, we have analyzed the clustering of hydration water at all temperatures studied. Various cluster properties were calculated in order to detect the thermal break of a spanning water network [10]. The first minimum in the density profile of liquid water near various surfaces, including biosurfaces, is located at about 0.45 nm [7]. Therefore, it is reasonable to study clustering of water molecules with their oxygens being located within the hydration shell of $D = 0.45$ nm width and some results obtained in this case are shown in Figures 5.6-5.9. In particular, the probability distributions $P(H_{max})$ [7] of the distance H_{max} between the centers of mass of Aβ_{42} and of the largest water cluster in its hydration shell are shown in the upper panel of Figure 5.6. At low temperatures, H_{max} is close to zero, indicating a homogeneous coverage of Aβ_{42} by a hydrogen bonded network of hydration water. At high temperatures, H_{max} is comparable with the radius of gyration of Aβ_{42} and a spanning network of hydration water is absent. The transition between these two qualitatively different states of hydration water is a percolation transition from a state with a majority of molecules in one spanning network to an ensemble of small clusters upon heating. The evolution of the probability distribution $P(S_{max})$ of the size S_{max} of the largest cluster of hydration water upon heating, shown in Figure 5.6, is typical for the percolation transition in finite systems. The largest water cluster includes the majority of molecules (S_{max}/N_w is close to 1) at low temperatures ($T < 320$ K) and the minority (S_{max}/N_w approaches 0) at higher temperatures.

The spanning probability *SP*, that is the probability to observe a spanning cluster of hydration water in an arbitrarily chosen configuration, can be approximately estimated as an integral of $P(S_{max})$ over $S_{max}/N_w > 0.5$ [161]. The temperature dependence of *SP*, shown in the upper panel of Figure 5.7, may be well fitted to a sigmoid with an inflection point ($SP = 50$ %) at about 320 K. This temperature marks the midpoint of the percolation transition, where spanning and non-spanning largest water clusters exist with equal probability. A true percolation threshold corresponds to some particular value of *SP*, which depends on the definition of the spanning cluster, the system dimensionality, but depends only slightly on the system size [162]. For quasi-2D percolation on the surface of a finite object, *SP* is about 95 % at the true percolation threshold [161]. Hence, a true percolation threshold of hydration water in the shell of a width of $D = 0.45$ nm is at about 280 to 290 K. This agrees with the temperature evolution of the cluster size distribution n_S (Figure 5.8). The distribution n_S at the percolation threshold should follow the unversal power law for 2D percolation (lines in Figure 5.8) in the widest range of cluster sizes S. As can be seen from Figure 5.8, this indeed happens at some temperature between 280 and 290 K.

The temperature dependence of the mean size S_{mean} [10] of water clusters in the hydration shell, calculated without the largest cluster, is shown in the lower panel of Figure 5.7. As expected, this dependence passes through a maximum when approaching the true percolation threshold upon cooling. The maximum of S_{mean}

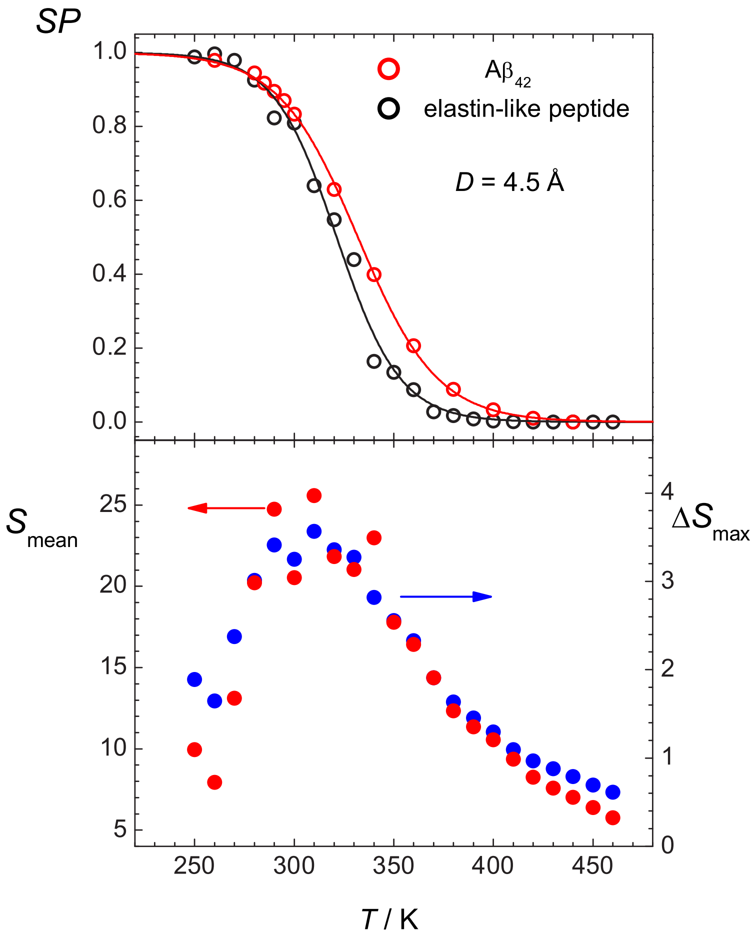

Figure 5.7: *Upper panel: Temperature dependence of the spanning probability in the hydration shell of width $D = 0.45$ nm at the surface of $A\beta_{42}$ and of an elastin-like peptide. [10] Lower panel: Temperature dependence of the mean cluster size S_{mean} and of the width ΔS_{max} of the probability distribution $P(S_{max})$ in the hydration shell of $A\beta_{42}$.*

occurs close to the midpoint of the percolation transition. Approximately at the same temperature, the probability distribution of the largest cluster $P(S_{max})$ is the widest (see Figure 5.6). The width ΔS_{max} of this distribution can be estimated as a standard deviation of S_{max} normalized by $N_w^{0.5}$ [9]. The temperature dependence of ΔS_{max} shows a maximum at about 310 to 320 K (Figure 5.7). So, the temperature dependencies of both S_{mean} and ΔS_{max} evidence the largest fluctuations of hydrogen bonding between water molecules in the hydration shell at about 310 K. The average number n_H^{av} of hydrogen bonds, which one water molecule forms in the hydration shell, is about 2.0 to 2.1 at the percolation threshold. Please note, that this value is rather universal [160] for smooth surfaces and biomolecules and it is not sensitive to the choice of the width of the hydration shell D around $A\beta_{42}$, as it can be seen from lower panel of Figure 5.9. The value of n_H^{av}, calculated for water molecules in all clusters excluding the largest one, passes through the maximum at

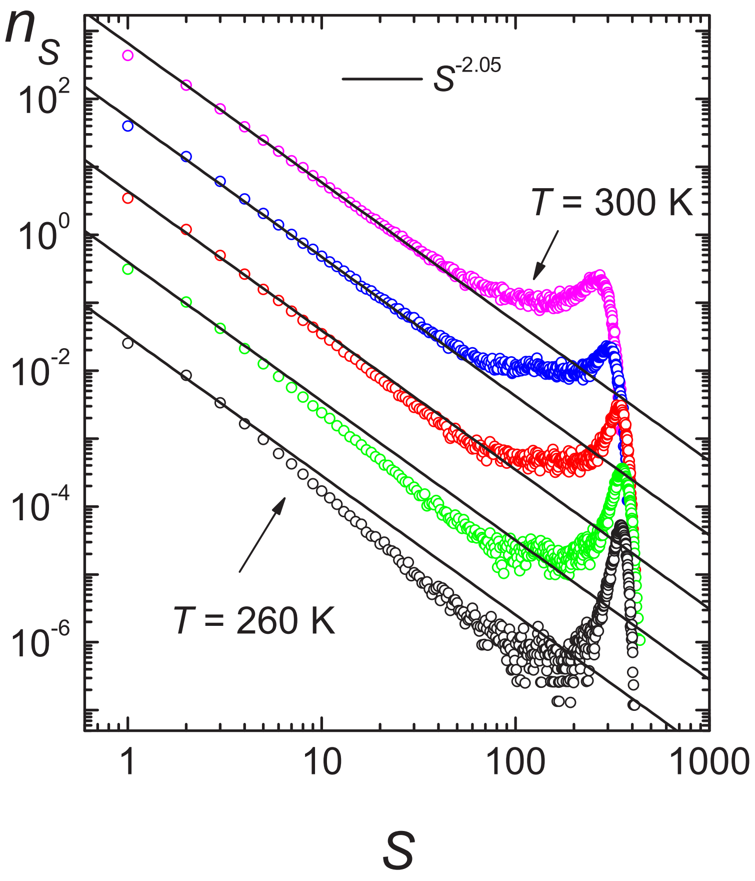

Figure 5.8: *Cluster size distribution n_S for water in the hydration shell of $A\beta_{42}$ of width D = 0.45 nm at temperatures T = 260, 270, 280, 290 and 300 K in the vicinity of the percolation transition.*

about 320 K, that is close the temperature where the mean cluster size S_{mean} has a maximum. n_H^{av} calculated within the largest water cluster only, has a rather weak temperature dependence without noticeable peculiarities.

The results presented above describe the water clustering in the first water monolayer, which includes water molecules in the shell of $D = 0.45$ nm width. Obviously, a spanning water network in thicker layers should be more stable with respect to heating. The temperatures, where the spanning probability $SP = 50$ % (midpoint of the percolation transition) and $SP = 95$ % (true percolation transition), are shown in Figure 5.10 as a function of the width D of the hydration shell analysed. Both characteristic temperatures increase with increasing D. Contrary to the water monolayer, the width of the adsorbed water bilayer depends on the kind of the adsorbing surface. The width D of the water bilayer is about 0.75 nm for smooth surfaces and should exceed at least 0.65 nm in the presense of water-surface hydrogen bonds. Extrapolation of the dependences in Figure 5.10 to higher values of D indicates that the spanning water network exists in a water bilayer in a wide range

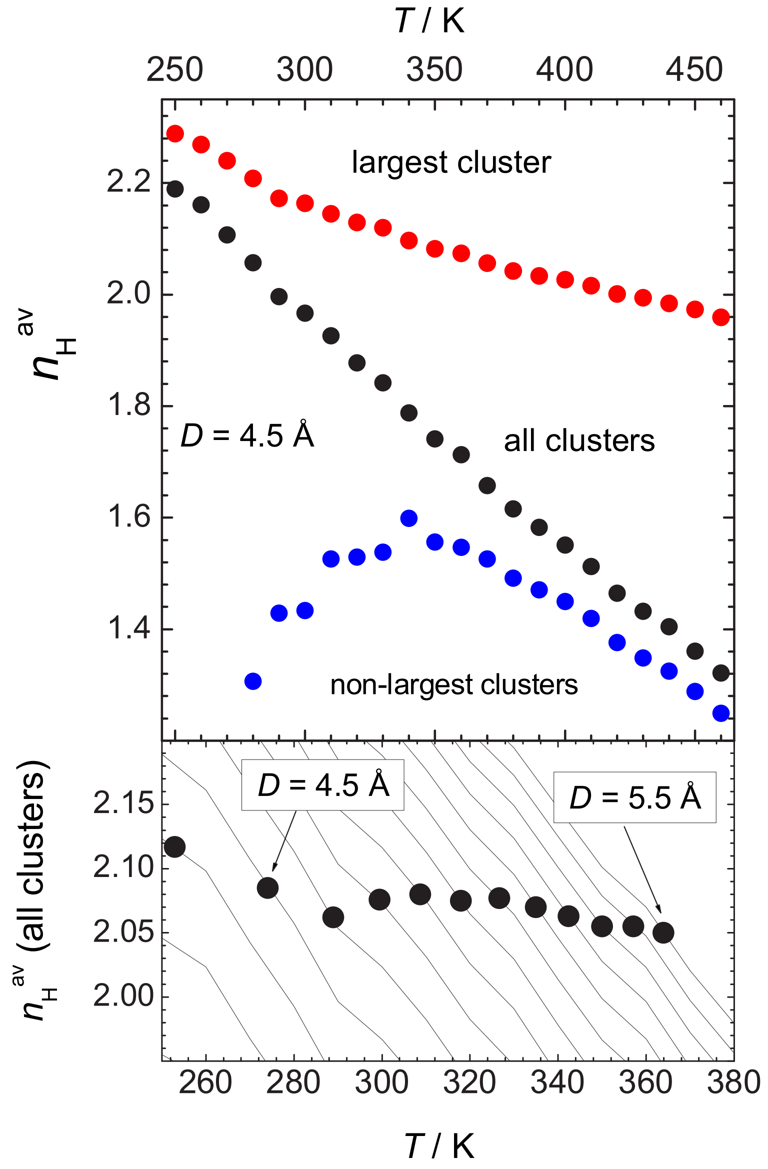

Figure 5.9: *Upper panel: Temperature dependence of the average number* n_H^{av} *of H-bonded neighbors of a water molecule in various clusters. Lower panel: Temperature dependence of* n_H^{av} *for all clusters (lines) and location of the percolation transition (solid circles) in the water shells of various widths D.*

of biologically relevant temperatures. Being in equilibrium with saturated vapor, the spanning water network in the limit $D \to \infty$ should break at the liquid-vapor critical point, which is a point of the percolation transition of physical clusters [163]. Due to the relatively low temperatures used in our constant-pressure simulations, the liquid water density is very close to its value at the liquid-vapor coexistence curve. Accordingly, the dependence of the temperature T_p, corresponding to some chosen value of SP, on the width D can be fitted by an empirical equation of the

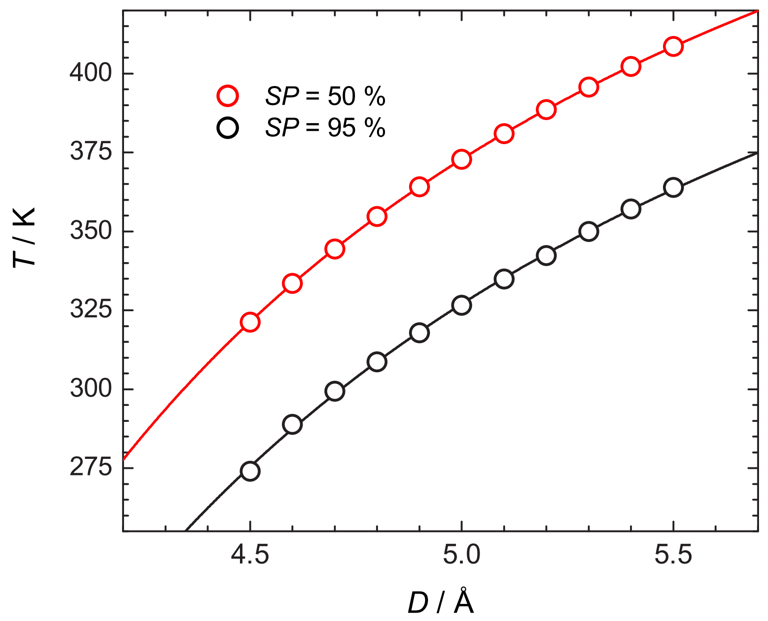

Figure 5.10: *Temperatures, corresponding to the spanning probabilities* $SP = 50\%$ *and* $SP = 95\%$ *in water shells of various widths* D*. Fits to Eq. 5.5 are shown by lines.*

form:

$$T_p = T_c^* - A/(D - D_c), \tag{5.2}$$

where D_c is a minimal possible thickness of a percolating water shell, A is a constant and T_c^* is an apparent critical temperature. The fit of the dependence for $SP = 50$ % to Eq. 5.2 gives $T_c^* \approx 604$ K and $D_c \approx 0.23$ nm. The first value is just slightly below the critical temperature of SPC/E water, estimated from the simulated liquid-vapor coexistence curve [164]. Notably, the value of the spanning probability $SP = 50$ % is close to the critical value of the wrapping probability to find an infinite cluster in 3D systems, which is about 44 % [162].

5.1.4 Intrinsic thermal expansivity of Aβ_{42} protein

The temperature dependence of the logarithm of the apparent volume $V^{app}(\mathrm{A}\beta_{42})$ of Aβ_{42} is shown in the upper panel of Figure 5.11. The derivative $\delta \ln(V)/\delta T$ is equal to the thermal expansion coefficient α. Two linear regimes with a crossover at about 320 K can be distinguished. Hence, these two linear parts of the temperature dependence of $\ln(V^{app}(\mathrm{A}\beta_{42}))$ indicate two quite different values of the thermal expansion coefficient $\alpha^{app}(\mathrm{A}\beta_{42})$ below and above 320 K. Fits to these linear dependences (blue and red lines in the upper panel of Figure 5.11) yield $\alpha^{app}(\mathrm{A}\beta_{42}) \approx$

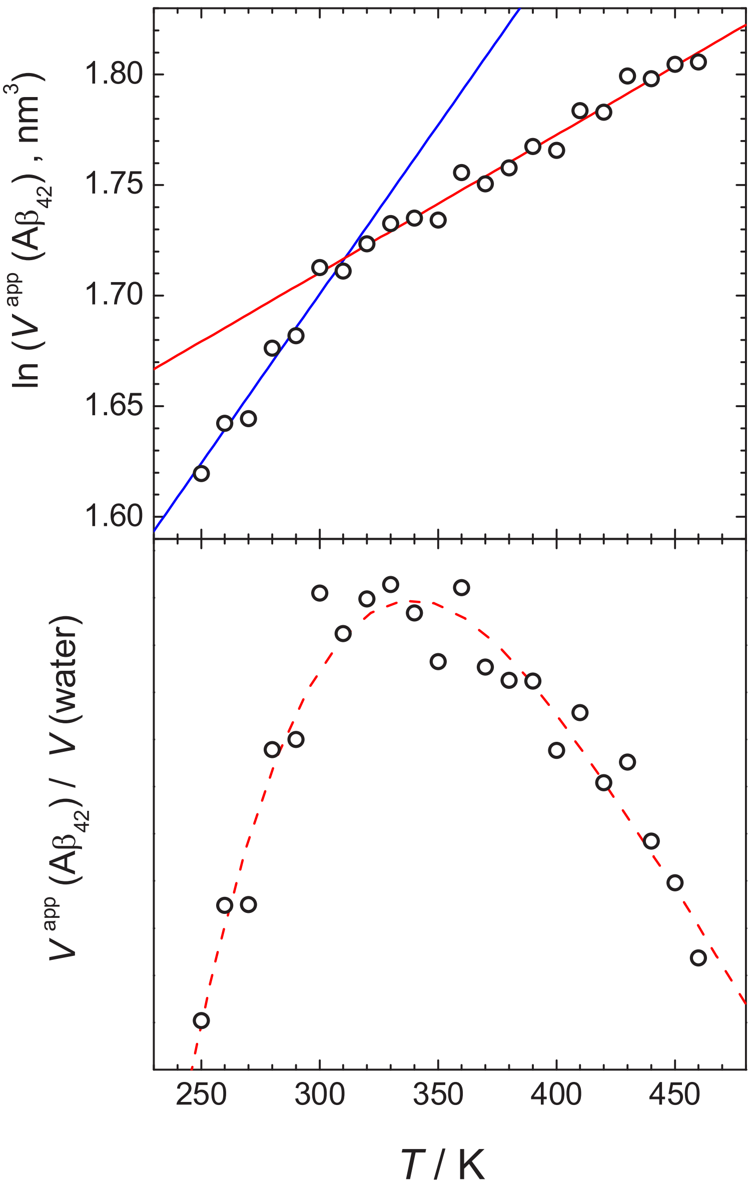

Figure 5.11: *Upper panel: Temperature dependence of ln($V^{app}(A\beta_{42})$) (circles) and linear fits in two temperature intervals (lines). Lower panel: ratio of $V^{app}(A\beta_{42})$ to the volume of some arbitrary amount of bulk liquid water. Dashed line is a guide for eyes only.*

$(1.53 \pm 0.13) \cdot 10^{-3}$ K^{-1} at $T \leq 320$ K and $\alpha^{app}(\mathrm{A}\beta_{42}) = (6.23 \pm 0.36) \cdot 10^{-4}$ K^{-1} at $T > 320$ K. The ratio of the apparent volume of Aβ_{42} to the volume of bulk liquid water (lower panel in Figure 5.11) changes with temperature non-monotonously. Upon heating, the apparent volume of Aβ_{42} increases faster than the water volume being at temperatures below ~ 340 K, and slower above ~ 340 K.

The values of the apparent thermal expansion coefficient $\alpha^{app}(\mathrm{A}\beta_{42})$, obtained by two-point differentiation of the dependence ln($V^{app}(\mathrm{A}\beta_{42})$) shown in the upper panel

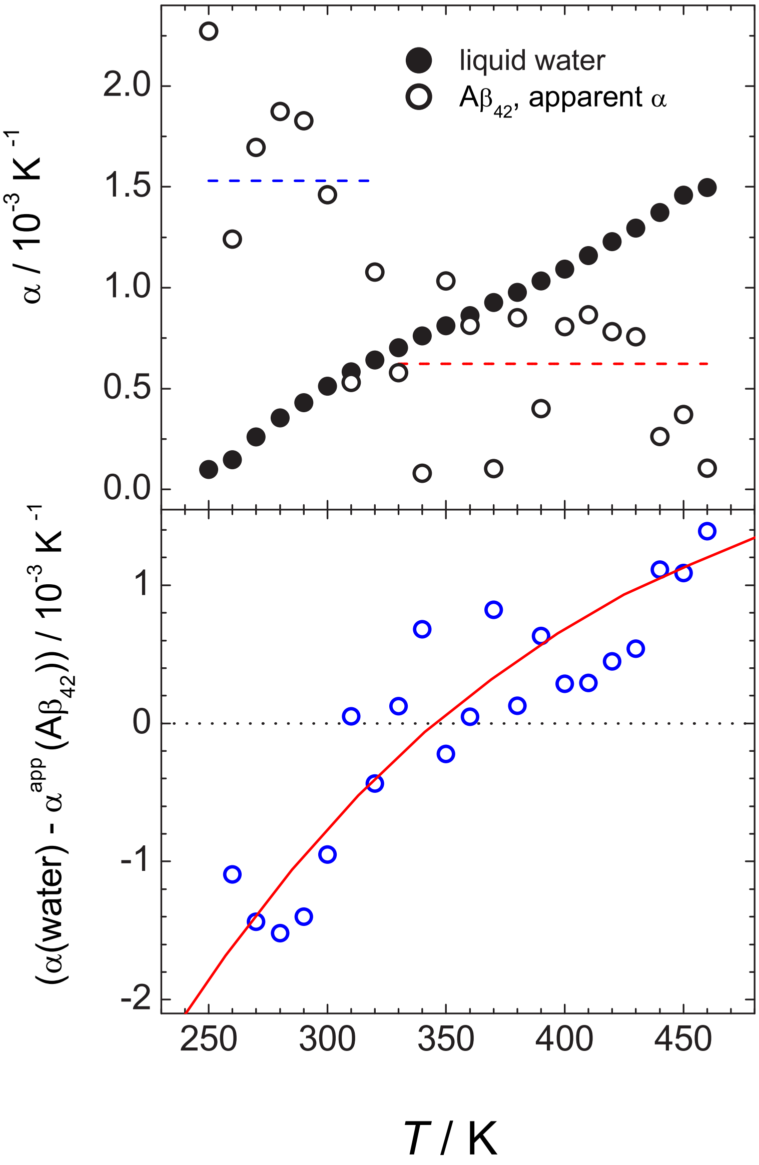

Figure 5.12: *Upper panel: Temperature dependence of the apparent thermal expansion coefficient* α *of* $A\beta_{42}$ *(open circles and dashed lines) and of bulk water (black circles). Lower panel: Temperature dependence of the difference between the apparent* α *of* $A\beta_{42}$ *and* α *of bulk water.*

of Figure 5.11, is shown by open circles in the upper panel of Figure 5.12 as a function of temperature. The two horizontal dashed lines show the values of $\alpha^{app}(\mathrm{A}\beta_{42})$, obtained from the linear fits of the same dependence at $T \leq 320$ K and $T > 320$ K, respectively. $\alpha^{app}(\mathrm{A}\beta_{42})$ obtained by differentiation noticeably decreases upon heating with a marked drop at about 320 to 350 K. Interestingly, approximately in this temperature range, $\alpha^{app}(\mathrm{A}\beta_{42})$ becomes equal to the thermal expansion coefficient of liquid water (solid circles in the upper panel of Figure 5.12). This is clearly seen when the difference $\alpha(\mathrm{water})$ - $\alpha^{app}(\mathrm{A}\beta_{42})$ is plotted as a function of temperature (lower panel in Figure 5.12).

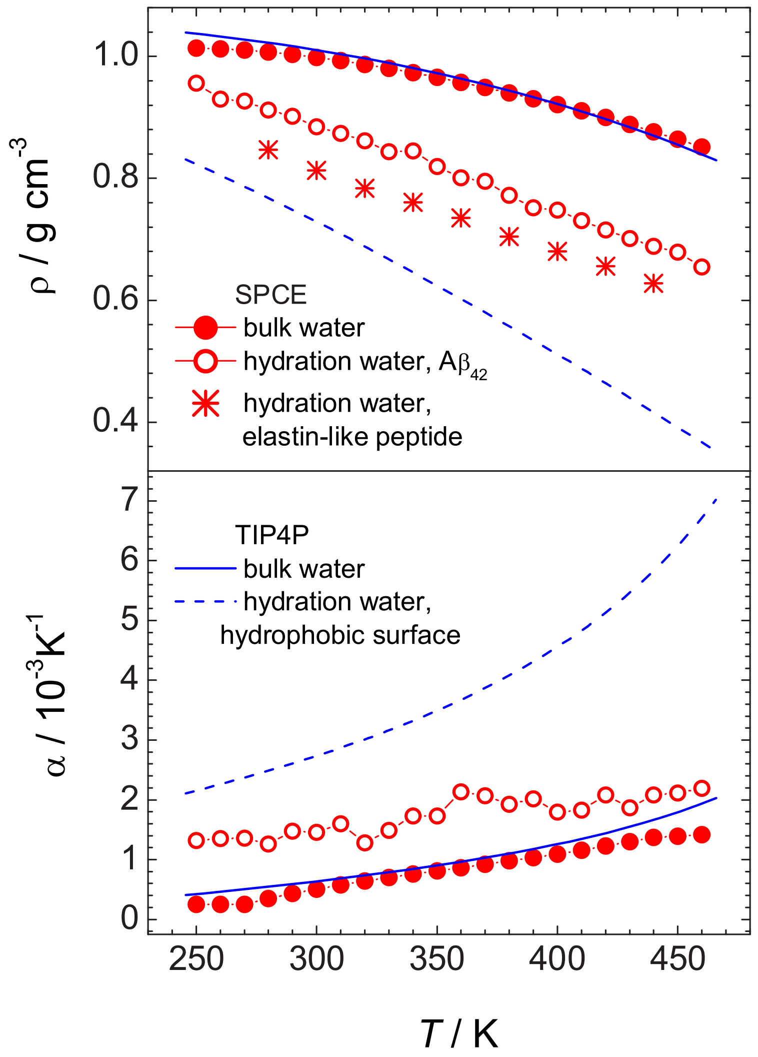

Figure 5.13: *Temperature dependence of the density (upper panel) and of the thermal expansion coefficient (lower panel) of bulk water and hydration water near Aβ_{42}, elastin-like peptide [10] and near paraffin-like surface [165] as obtained for two water models, SPC/E and TIP4P.*

The apparent volume of Aβ_{42} (or of any other object) in liquid water may be decomposed into two main contributions: the neat or intrinsic volume $V(\mathrm{A}\beta_{42})$ of Aβ_{42} and a "water defect" contribution $\Delta V(\mathrm{water})$ caused by the difference between the density of bulk and hydration water:

$$V^{app}(A\beta_{42}) = V(A\beta_{42}) + \Delta V(water). \tag{5.3}$$

The term apparent thus means that contribution due to protein-solvent interactions are included. The term intrinsic means that we are dealing with the bare protein, a property what cannot be directly measured. If we assume that the density of liquid water is affected by a protein only within some surface layer of width D and volume

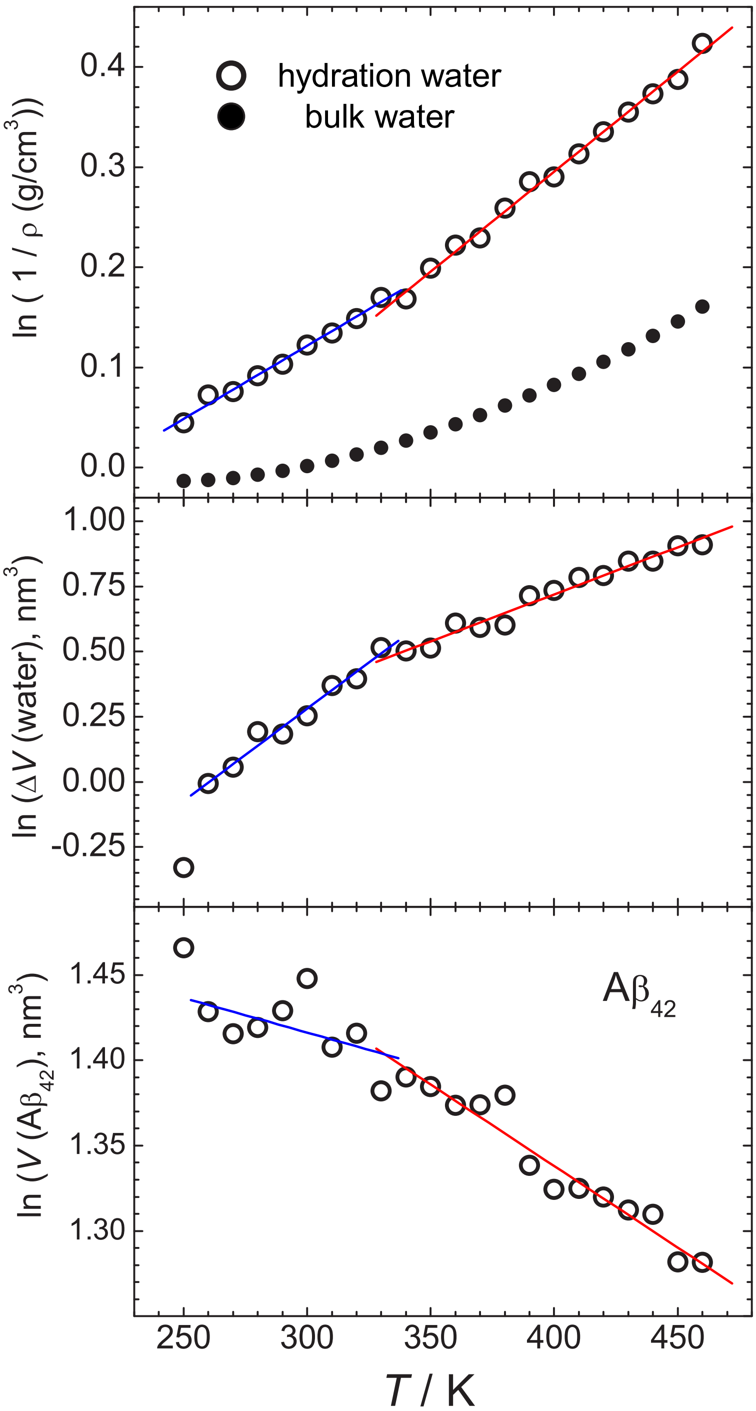

Figure 5.14: *Upper panel: Temperature dependence of ln(1/ρ) for bulk and hydration water of Aβ_{42}. Middle panel: Temperature dependence of ln(ΔV(water)), where ΔV(water) is the volume change due to the different densities of bulk and hydration water. Lower panel: Temperature dependence of ln(V(Aβ_{42})), where V(Aβ_{42}) is the intrinsic volume of Aβ_{42}. The slope of each linear dependence reflects the thermal expansion coefficient.*

V_D, then ΔV(water) is:

$$\Delta V(water) = V_D(1 - \rho_s/\rho_b), \tag{5.4}$$

where ρ_s and ρ_b are the water densities in the surface layer and in the bulk, respectively. In a first approximation, the volume of the first surface layer of water may be approximately taken as V_D = SASA$\cdot D^*$. Typically, water molecules whose oxygens are closer then $D \approx 0.45$ nm to the heavy atoms of a biomolecule may be attributed to the surface layer. The width D^* of the surface water layer is about (D - 0.15 nm), as half of the typical contact distance between water oxygen and the heavy atoms of the biomolecule (about 0.15 nm) is not accessible for the center of water oxygens. Thus, the density ρ_s of surface water is equal to $N_w \cdot m_{H_2O}/V_D$, where m_{H_2O} is the mass of a water molecule. Hence, ΔV(water) should be positive if $\rho_b > \rho_s$ and negative otherwise.

The temperature dependence of the densities ρ_b and ρ_s are compared in the upper panel of Figure 5.13. In the whole temperature interval studied, $\rho_s < \rho_b$, which indicates a pronounced depletion of the water density near the surface of Aβ_{42}. Besides, the density depletion becomes more pronounced upon heating. In fact, such situation is typical for liquid water near hydrophobic surfaces [165]. For comparison, we show the temperature dependence of the water density near a smooth surface, whose hydrophobicity is close to that of paraffin. The water density depletion is markedly stronger in the latter case, in agreement with the fact that the surface of Aβ_{42} is not as hydrophobic as paraffin.

The temperature dependence of the density of bulk and surface water may be described in the framework of the theory of critical behavior [166, 165, 167]. When *bulk* liquid is in equilibrium with saturated vapor, its density may be presented as a function of a reduced temperature $\tau = (T_c - T)/T_c$, which measures the distance to the critical temperature T_c:

$$\rho_b = \rho_c(1 + a_1\tau + a_2\tau^2 + ...) + b_1\tau^{\beta}(1 + b_2\tau^{\Delta} + ...), \tag{5.5}$$

with the critical exponents $\beta \approx 0.326$, $\Delta \approx 0.5$, ρ_c is the critical density, a_i and b_i are coefficients. Near the surface, the liquid density ρ_s obeys Eq. 5.5, however, with other values of coefficients and critical exponents. In particular, the exponent β near the surface is predicted to be about 0.8 [166]. At some distance from the surface, the liquid density is equal to the bulk value at low temperatures. Upon heating, a crossover to the surface critical behavior occurs. Intrusion of the surface critical behavior into the bulk is governed by the bulk correlation length ξ [165, 167]. The temperature dependence of the liquid density of water and Lennard-Jones fluids in the first (surface) layer follows the laws of surface critical behavior down to the freezing temperature. For fluids near weakly-attractive surfaces, the exponent β in the surface layer was found to be close to 1 [165, 167].

Near a hydrophobic surface, the density of liquid water is lower than in the bulk (see Figure 5.13, upper panel). This is caused by a missing neighbor effect, which weakens intermolecular interaction per fluid molecule near any boundary. This effect appears also in a lowering of the critical density ρ_c and, accordingly, in a much steeper decrease of the liquid density upon heating (large value of the coefficient a_1 in Eq. 5.5). Such behavior is clearly seen for the density of hydration water near the surface of Aβ_{42} as well as near an elastin-like peptide (Figure 5.13, upper panel). Accordingly, the thermal expansion coefficient α^s of surface water is larger than α^b of bulk water. The thermal expansion coefficients α^s obtained by two-point differentiation of the temperature dependence of the hydration water near Aβ_{42} and α^b are shown in Figure 5.13 (lower panel). The difference α^s - α^b remains positive in the whole temperature range studied, but the two coefficients seem to approach each other upon heating. For the strongly hydrophobic paraffin-like surface, the difference α^s - α^b grows upon heating (blue lines in the lower panel of Figure 5.13).

The temperature dependence of the inverse density $1/\rho^h$ of hydration water is shown in the upper panel of Figure 5.14 using a logarithmic scale for the vertical axis. The derivative $\delta \ln(1/\rho)/\delta T$ is equal to the thermal expansion coefficient α. This coefficient is not a constant in the temperature interval studied. Mean-square deviations of the dependence $\ln(1/\rho)(T)$ from its linear fit decreases about two times, when $\ln(1/\rho)(T)$ is fitted by two different linear fits at low and at high temperatures. This allows distinguishing of two temperature regimes with a slightly different thermal expansion coefficient of hydration water. At $T \leq 330$ K, $\alpha^s = (1.46 \pm 0.06) \cdot 10^{-3}$ K^{-1}, whereas at $T > 330$ K, $\alpha^s = (2.00 \pm 0.05) \cdot 10^{-3}$ K^{-1}. Knowledge of the surface water density at various temperatures allows calculation of ΔV(water) using Eq. 5.4 and subsequently of V(Aβ_{42}) using Eq. 5.3. The temperature dependencies of $\ln(\Delta V(\text{water}))$ and $\ln(V^{int}(\text{A}\beta_{42}))$ are shown in the middle and lower panels of Figure 5.14, respectively. Apart from the lowest temperature point at $T = 250$ K, both dependencies show two temperature regimes with a crossover at about 320 to 330 K. The intrinsic thermal expansion coefficient α^{int}(Aβ_{42}) of Aβ_{42}, estimated from the linear approximation of $\ln(V^{int}(\text{A}\beta_{42}))$ in the two temperature range, is slightly negative (α(Aβ_{42}) = -(4.1 $\pm$ 2.7)$\cdot 10^{-4}$ K^{-1}) at $T \leq 330$ K and more negative (α(Aβ_{42}) = -(9.56 $\pm$ 0.73)$\cdot 10^{-4}$ K^{-1}) at $T > 330$ K. The scattering of the data points does not allow a more detailed analysis of the temperature dependence of α^{int}(Aβ_{42}).

5.2 Temperature-induced conformational changes of Aβ_7 fragments

Many familial Alzheimer's disease (FAD) mutants of the APP protein are external to the Aβ peptide sequence and typically influence Aβ processing. A set of mutants that cluster near amino acid positions 21 through 23 in the Aβ peptide have drawn special attention to the central hydrophobic core (position 17 to 21). One of the most well-studied FAD mutant is Arctic (E22G) mutant, which has been characterized for both Aβ_{1-40} and Aβ_{1-42} both in vitro and in vivo [24, 26, 66]. A number of important computational studies have addressed the monomer conformation and oligomer assemblies of the WT and FAD mutants, both on the full length sequence as well as Aβ fragments [74, 75, 76]. We have chosen in this study to focus on the Aβ_{16-22} (Aβ_7) fragment and Arctic mutant of that fragment (Aβ_{7g}) because the best quality experimental structural data is available for this system [29, 28].

5.2.1 Model System

The initial Aβ_7 peptide has originally been modelled in the α-helix conformation, using AMBER-XLEAP program. As in the experimental study, the terminals of the Aβ_7 peptides are capped with neutral acetyl and amide groups. To reduce the unfolding time, the α-helix was converted into a random coil conformation by increasing the peptide torsion angles in the starting conformation of the simulation as shown in Figure 5.15(c) and (d). We established the prevalence of the extended conformations (random coil and β-strand) of all monomer structures. The population of α-helix peptide conformations is negligible. The Arctic E22G mutation of Aβ_7 peptide monomer (Aβ_{7g}) was modelled as the Aβ_7 peptide (Figure 5.15). We used those conformations for further study.

The Aβ_7 and Aβ_{7g} peptides in a full stretched conformation were placed in a cubic box with 848 water molecules and pre-equilibrated by using 1000 steps of the steepest descent method. Electro-neutrality of the Aβ_{7g} system, which initially had a charge +1e, was provided by replacing three water molecules with one Cl$^-$ ion. The Gromacs software package [157] was used with the OPLS force field [125] for the Aβ_7 and Aβ_{7g} peptides and the SPC/E model for water. A spherical cut-off of 0.9 nm was used for the short-range intermolecular interactions; the long-range Coulombic interactions were taken into account by particle mesh Ewald summation. Molecular dynamics (MD) simulations were performed in the NPT ensemble at constant pres-

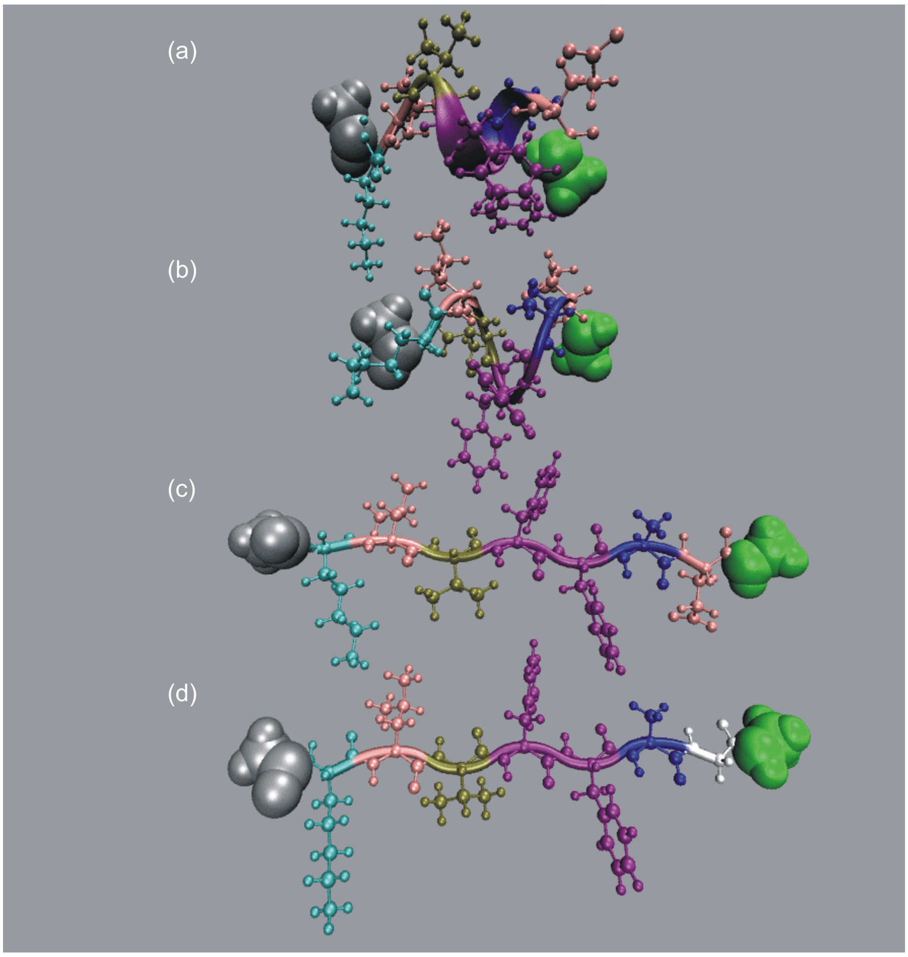

Figure 5.15: *Initial monomer conformations, (a) Monomer in α-helix conformation. (b) α-helix was converted into a random coil conformation by increasing the peptide torsion angles. (c) Initial monomer conformation for Aβ_7. (d) Initial Arctic mutation Aβ_7 peptide (Aβ_{7g}) monomer conformation.*

sure $P = 1$ bar and 8 temperatures between 285 and 460 K, using the Nose-Hoover thermostat and the Parrinello-Rahman barostat. Periodic boundary conditions were applied. Simulation runs were performed with 2 fs time steps and the configuration was saved every 0.2 ps. At each temperature, the system was equilibrated during 1 ns and the subsequent 60 ns run was used for the analysis.

To characterize the conformation of the Aβ_7 and Aβ_{7g} peptide we calculated its radius of gyration R_{gyr}, the solvent accessible surface area (SASA), intra-peptide hydrogen bonds along the peptide chain and central hydrophobic core (CHC) region. The secondary structure was determined using corresponding distributions of dihedral angles ϕ and ψ in the Ramachandranan plot. A residue was considered as contributing to α-helices, when -120° $< \phi < -30°$ and -90° $< \psi < +30°$; to β-sheets and polyproline II structures, when -180° $< \phi < -30°$ and $+90° < \psi < +180°$.

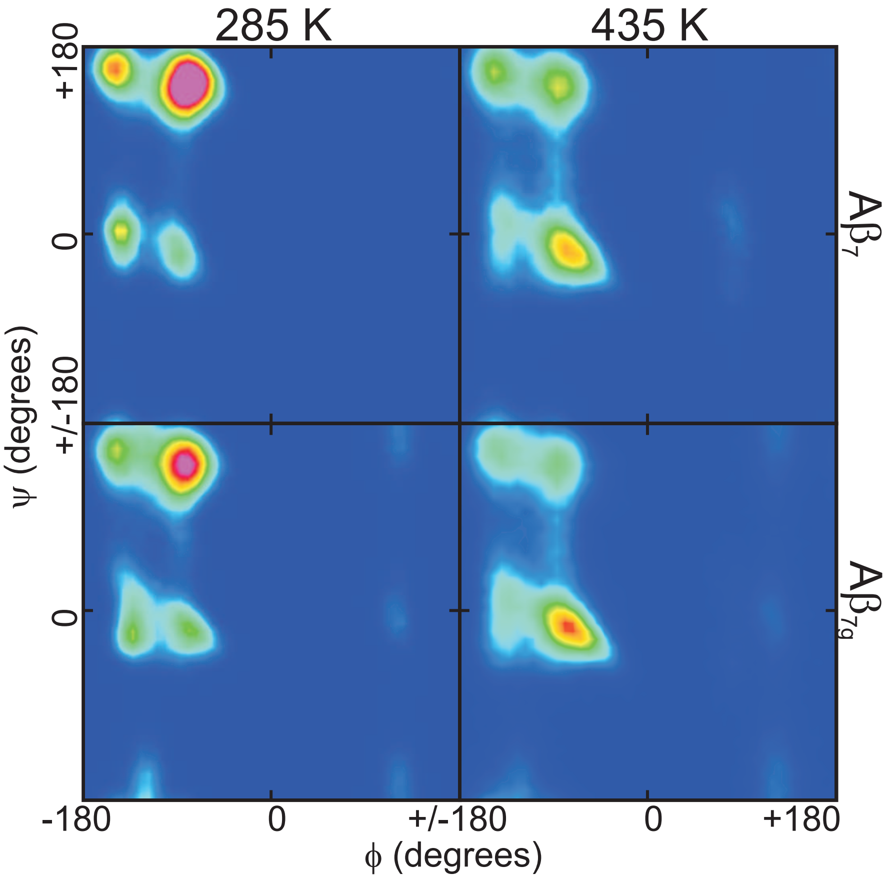

Figure 5.16: Ramachandran plots for Aβ_7 (upper panel) and Aβ_{7g} (lower panel) at low and high temperatures.

Residues with dihedral angles from other areas of the Ramachandran plot were attributed to disordered secondary structures.

5.2.2 Conformational behavior of Aβ_7 and Aβ_{7g} peptide

The temperature dependence properties of Aβ_7 and Aβ_{7g} peptide are calculated by averaging over 60 ns at the respective temperatures. The fraction of residues in both peptide systems (Aβ_7 and Aβ_{7g}) with some particular secondary structure defined by their dihedral angles, is shown in the Figure 5.16 and 5.17. The fraction of α-helices increases two times upon heating from 285 to about 460 K. In parallel, the fractions of β-sheets and of polyproline II structures decrease by about a factor of 2 upon heating. Aβ_7 peptide systems have slightly more β-strand and less α-helices content than the Aβ_{7g} peptide systems (Figure 5.17). In Figure 5.16 the Ramachandran plots of Aβ_7 (upper panel) and Aβ_{7g} (lower panel) at low and high temperatures are shown. The distributions of dihedral angles (ϕ, ψ) in the Aβ_{7g}

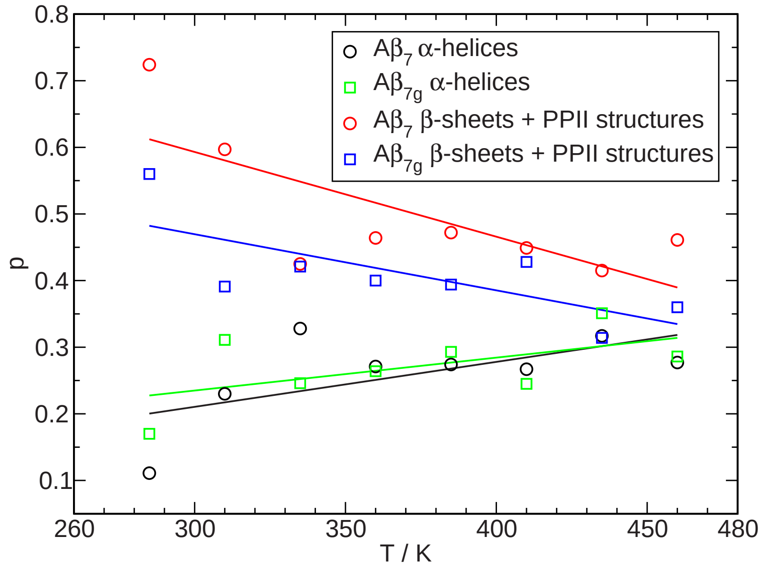

Figure 5.17: *Content p of the residues with particular secondary structure as a function of temperature. Aβ_7 and Aβ_{7g} peptide points are shown in circles and squares, respectively. Lines are linear fitted for that particular color points.*

peptide system at higher temperatures contain more α-helix conformations than the Aβ_7 peptide system (Figure 5.16). However, the total population of these three secondary structures is about 0.8 to 0.9.

The end-to-end distance decreased with increasing temperature in both monomer systems and is shown in the upper panel of Figure 5.18. As seen from quadratic fit lines, the end-to-end distance in the Aβ_7 peptide system sharply decreased upon heating from 285 to 385 K and slightly increased at higher temperatures (Figure 5.18, upper panel). Subsequently, the intrapeptide hydrogen bonds within the peptide atoms increased with temperature. The Aβ_7 system rapidly formed high number of hydrogen bonds in comparison to the Aβ_{7g} system. In the Aβ_7 system the highest number of intrapeptide hydrogen bonds are obtained at 410 K (Figure 5.18, lower panel). Interestingly, the end-to-end distances and intrapeptide hydrogen bonds in the whole temperature range are consistent with the increases fraction of α-helix and weaker propensity for β-strand conformations. Thus, various measures shows that the higher temperatures and weakening of electrostatic interactions due to the absence of negative charged residue promotes α-helices formation in monomers.

The temperature dependence of the solvent accessible surface area (SASA) and the radius of gyration (R$_{gyr}$) was calculated over the central hydrophobic core (CHC) atoms. CHC extends from residues L17 to A21 in Aβ_7 and Aβ_{7g} peptide. The value of the SASA decreased while increasing temperature in both systems. In the Aβ_7 peptide system, the SASA value sharply deceased upon heating from 285 to

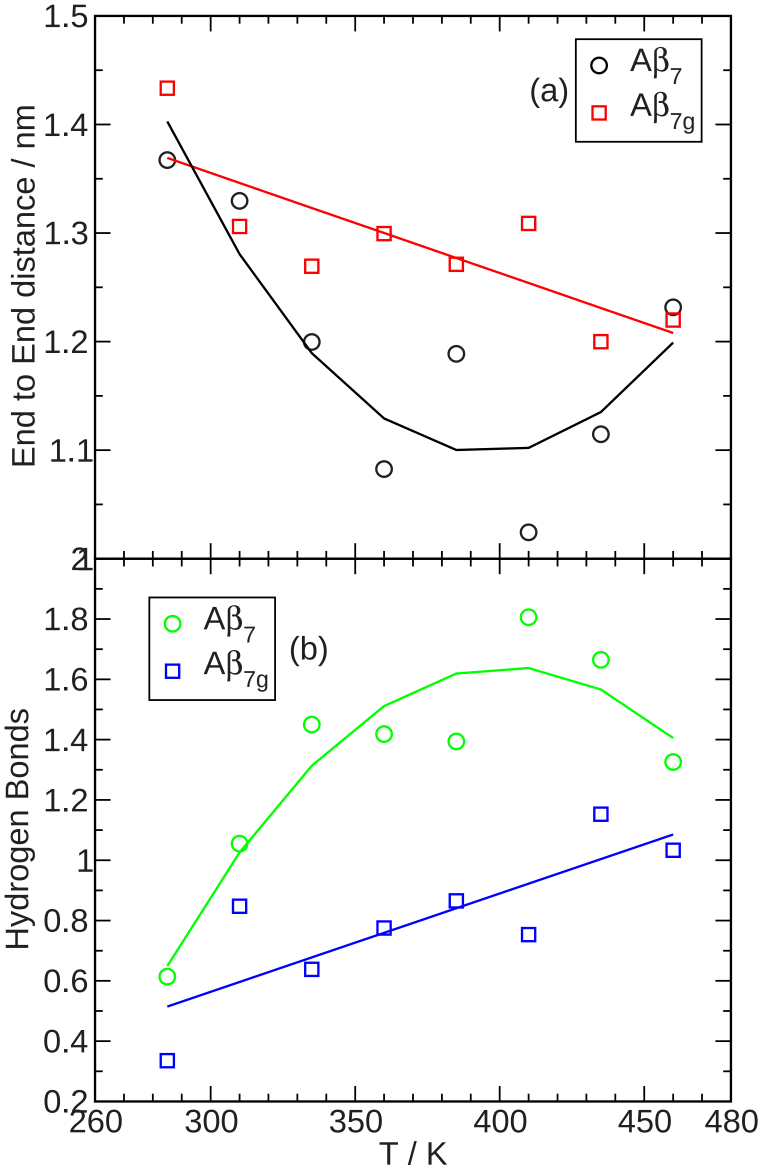

Figure 5.18: *End-to-End distance (upper panel) and number of intrapeptide Hydrogen bonds between the all residues (lower panel) as a function of temperature. Aβ_7 and Aβ_{7g} peptide points are shown in circles and squares, respectively. Lines are quadratic and linear fitted for Aβ_7 and Aβ_{7g} peptide points, respectively.*

385 K and slightly increased at higher temperatures. In the Aβ_{7g} peptide system, it also decreased with increasing temperature. Here the SASA have little higher values than in the Aβ_7 peptide system (Figure 5.19, upper panel). Subsequently, the behaviour of R$_{gyr}$ calculated from the CHC region was identical with that of SASA. The average R$_{gyr}$ value in the Aβ_7 peptide system is smaller than in the Aβ_{7g} peptide system (Figure 5.19, middle panel). In the wildtype system, the average number of hydrogen bonds calculated over the CHC region increased upon heating from 285 to 385 K and decreased at higher temperatures. In the mutant system, the

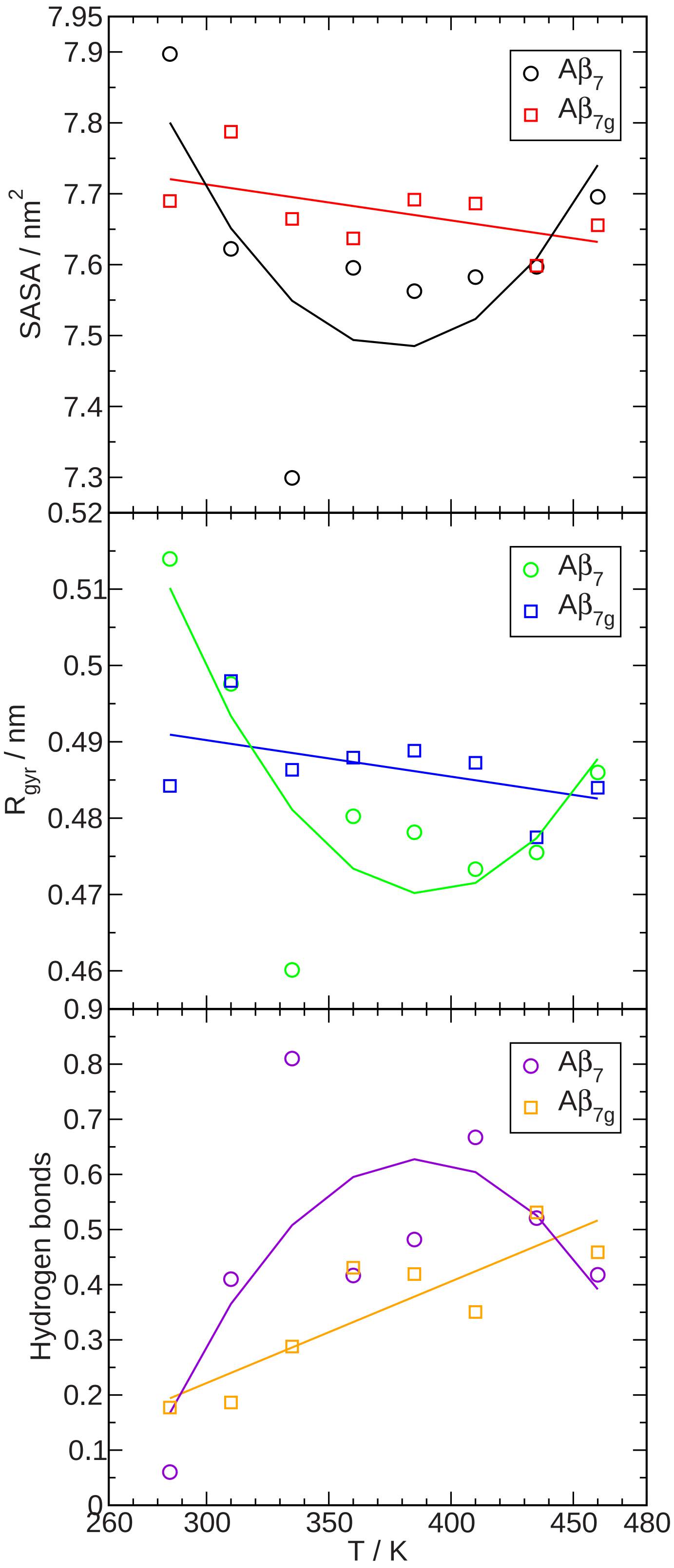

Figure 5.19: *Temperature dependence of the solvent accessible surface area SASA, radius of gyration R_{gyr} and intrapeptide hydrogen bonds between the CHC atoms of $A\beta_7$ and $A\beta_{7g}$ peptides. Fits to a quadratic and linear function are shown by lines.*

hydrogen bonds increased with increasing temperatures (Figure 5.19, lower panel). Thus, various measures show that the Aβ_7 system has stronger thermal effects than the Aβ_{7g} system.

5.2.3 Intrinsic thermal expansivity of Aβ_7 and Aβ_{7g} peptides

The temperature dependence of the apparent volume V^{app} of Aβ_7 and Aβ_{7g} are shown in the upper panel of Figure 5.20, using a logarithmic scale for the vertical axis. Both monomer systems shown similar temperature dependence. Two linear regimes with a crossover at about 385 K can be distinguished. The derivative $\delta \ln(V)/\delta T$ is equal to the thermal expansion coefficient α. Hence, these two linear parts of the temperature dependence of $\ln(V^{app})$ indicate two quite different values of the thermal expansion coefficient α^{app} below and above 385 K. Linear fits to $\ln(V^{app}(\mathrm{A}\beta_7))$ (solid and dashed lines in the upper panel of Figure 5.20(black)) yield $\alpha^{app}(\mathrm{A}\beta_7) \approx (1.66 \pm 0.07){\cdot}10^{-3}$ K^{-1} at $T \leq 385$ K and $\alpha^{app}(\mathrm{A}\beta_7) = (2.11 \pm 0.02){\cdot}10^{-3}$ K^{-1} at $T > 385$ K. Linear fits to $\ln(V^{app}(\mathrm{A}\beta_{7g}))$ (solid and dashed lines in the upper panel of Figure 5.20(red)) yield $\alpha^{app}(\mathrm{A}\beta_{7g}) \approx (2.54 \pm 0.01){\cdot}10^{-3}$ K^{-1} at $T \leq 385$ K and $\alpha^{app}(\mathrm{A}\beta_{7g}) = (1.49 \pm 0.04){\cdot}10^{-3}$ K^{-1} at $T > 385$ K. The obtained temperature dependence of the apparent thermal expansion coefficient $\alpha^{app}(\mathrm{A}\beta_{7/7g})$ (Figure 5.20, upper panel) is quite different to the dependences $\alpha^{app}(\mathrm{A}\beta_{42})$, obtained in last section. Our results indicate, that $\alpha^{app}(A\beta_7)$ is positive at low temperatures and increases upon heating. $\alpha^{app}(A\beta_{7g})$ is also positive at low temperatures and increases upon heating.

The temperature dependencies of $\ln(V^{int}(\mathrm{A}\beta_{7/7g}))$ are shown in the middle panel of Figure 5.20. The temperature dependencies show two temperature regimes (solid and dashed lines) with a crossover at about 380 to 390 K. The intrinsic thermal expansion coefficient $\alpha^{int}(\mathrm{A}\beta_7)$ of Aβ_7, is estimated from the linear approximation of $\ln(V^{int}(\mathrm{A}\beta_7))(T)$ in the two temperature range studied. Linear fits to $\ln(V^{int}(\mathrm{A}\beta_7))$ (solid and dashed lines in the upper panel of Figure 5.20(green)) yield $\alpha^{int}(\mathrm{A}\beta_7) \approx (0.16 \pm 0.063){\cdot}10^{-3}$ K^{-1} at $T \leq 385$ K and $\alpha^{int}(\mathrm{A}\beta_7) = (1.38 \pm 0.014){\cdot}10^{-3}$ K^{-1} at $T > 385$ K. The intrinsic thermal expansion coefficient $\alpha^{int}(\mathrm{A}\beta_{7g})$ of Aβ_{7g}, estimated from the linear approximation of $\ln(V^{int}(\mathrm{A}\beta_{7g}))(T)$ in the two temperature range studied. Fits to $\ln(V^{int}(\mathrm{A}\beta_{7g}))$ linear dependences (sold and dashed lines in the upper panel of Figure 5.20(blue)) yield $\alpha^{int}(\mathrm{A}\beta_{7g}) \approx (-0.16 \pm 0.034){\cdot}10^{-3}$ K^{-1} at $T \leq 385$ K and $\alpha^{int}(\mathrm{A}\beta_{7g}) = (1.71 \pm 0.002){\cdot}10^{-3}$ K^{-1} at $T > 385$ K. The obtained temperature dependence of the intrinsic thermal expansion coefficient $\alpha^{int}(\mathrm{A}\beta_{7/7g})$ (Figure 5.20, middle panel) shows that $\alpha^{int}(A\beta_7)$ is positive at low temperatures

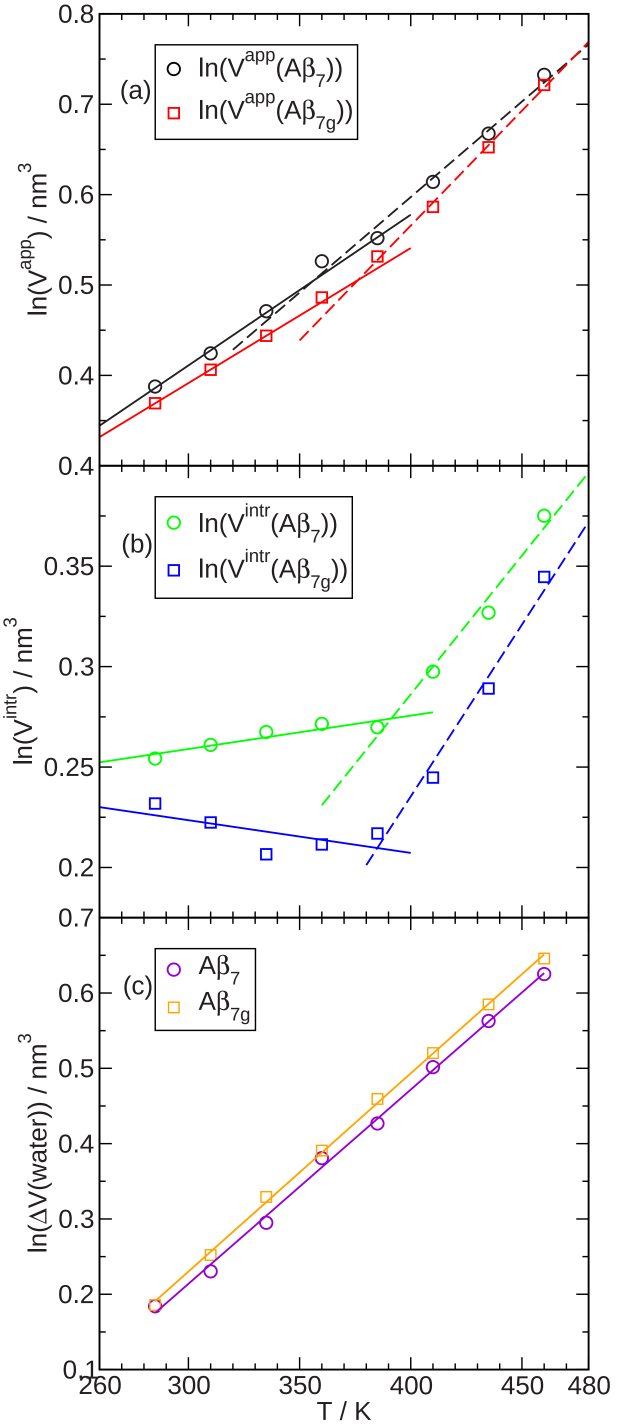

Figure 5.20: *Upper panel: Temperature dependence of* $\ln(V^{app}(A\beta_7))$ *(circles),* $\ln(V^{app}(A\beta_{7g}))$ *(squares) and linear fits in two temperature intervals. Middle panel: Temperature dependence of* $\ln(V^{int}(A\beta_7))$ *(circles),* $\ln(V^{int}(A\beta_{7g}))$ *(squares), where* $V(A\beta_7)$ *is the intrinsic volume of* $A\beta_7$*. The slope of each linear dependence reflects the thermal expansion coefficient. Lower panel: Temperature dependence of* $\ln(\Delta V(\text{water}))$*, where* $\Delta V(\text{water})$ *is the volume change due to the different densities of bulk and hydration water in the* $A\beta_7$ *and* $A\beta_{7g}$ *peptide system.*

and increases upon heating. $\alpha^{int}(A\beta_{7g})$ is slightly negative at low temperatures and increases upon heating. ΔV(water) is the volume change due to the different densities of bulk and hydration water in the Aβ_7 and Aβ_{7g} peptide system, is shown in Figure 5.20 (lower panel). This difference increases with increasing temperature.

5.3 Conclusions

By taking into account the temperature dependence of the hydration water, we determined the temperature dependence of the intrinsic volume of Aβ_{42} and its expansion coefficient α. To the best of our knowledge, this is the first estimation of an intrinsic α of a biomolecule in water. In crystals, α of biomolecules is small ($\sim 10^{-4}$) and positive [168]. However, Aβ_{42} in solution shows a negative expansion coefficient, i.e., it contracts and becomes more densely packed upon heating. Moreover, our preliminary results show that also the elastin-like peptide, studied in Ref. [10], has a negative α, whose absolute value is about two times larger than α of Aβ_{42}.

A negative expansion coefficient of a biomolecule may be related to the entropic character of its elasticity. Generally, noncrystalline (amorphous) macromolecular and biomolecular [169, 170, 171] substances show a rubber-like elastic behavior at temperatures well above their glass temperature [172]. Rubber elastic behavior originates from a decrease of entropy upon elongation of a polymer chain due to the decreasing number of available configurations. The increase of entropy upon heating enhances those contractive forces, thus leading to a negative expansion coefficient of rubber elastic bodies. It was shown recently [10], that a single elastin-like peptide in water exhibits a distribution of the end-to-end distances close to one of an ideal random coil with a purely entropic elasticity. This explains the strongly negative thermal expansion coefficient of elastin-like peptides. The weaker thermal contraction of Aβ_{42} may indicate its slightly more ordered conformation. The change of its expansion coefficient with temperature (lower panel in Figure 5.14) evidences that it becomes more disordered at the conformational transition.

Another well-known example of a substance with a negative thermal expansion is neat liquid water at temperatures below about 4°C [173]. This behavior originates from the presence of tetrahedrally ordered water molecules, which can be packed in a low-density substance only, if their tetrahedricity is preserved. Upon heating, the fraction of such water molecules decreases, thus causing densification of liquid water (this explanation is known since the 19th century [174, 175]). In analogy, we may assume that the anomalous (negative) expansivity of a biomolecule may also originate, at least partially, from a decrease of intramolecular hydrogen bonding upon heating. Aβ_{42} has a mainly random coil-like conformation with some number of intrapeptide hydrogen bonds, which prevent close packing of the peptide chain. A decrease of the number of such bonds should help to pack the peptide more tightly. As a consequence, also the defect or void volume will be diminished at higher temperatures. Indeed, the average - irrespective of accompanying conformational changes - number of intrapeptide hydrogen bonds of Aβ_{42} decreases from about 15 at 250 K to about 13 at T_t and to about 8 at 460 K. A similar behavior is observed for the elastin-like peptide, where this number decreases from about 7 to 5.5 upon heating from 280 to 440 K. As in the case of supercooled water, the collapse of more open structures upon heating may be strong enough to overcome conventional thermal expansion and to provide negative intrinsic thermal expansion coefficients.

The obtained temperature dependence of the apparent thermal expansion coefficient $\alpha^{app}(\mathrm{A}\beta_{42})$ (Figure 5.12) is quite similar to the dependences $\alpha^{app}(T)$, obtained for various biomolecules experimentally [2, 3, 4, 5]: α^{app} is positive at low temperatures and decreases upon heating. Our results indicate, that such behavior of α^{app} reflects mainly the specific temperature behavior of "water defects", that account for the different temperature dependences of the volumetric properties of bulk and hydration water (Eq. 5.4). Large positive values of α^{app} at low temperatures are due to the fact that the thermal expansion coefficient of hydration water essentially exceeds the bulk value. This difference decreases with temperature, as the thermal expansion coefficients of bulk and hydration water approach each other (Figure 5.13). However, this does not explain the noticeable change of the apparent volumetric properties in a rather narrow temperature interval near 320 K (see upper panel in Figure 5.11). This behavior may originate from the specific intrinsic properties of Aβ_{42} and/or from the specific properties of hydration water.

The Aβ_{42} peptide exhibits an essentially disordered conformational structure at all temperatures studied. Residues with like secondary structure are distributed almost randomly along the peptide chain (Figure 5.12) and only for residues, having α-helical dihedral angles, some trend toward "condensation" can be noticed. Such disordered structure is quite similar to the one of elastin-like peptide [10]. Upon heating, Aβ_{42} loses elements of secondary structure, characterized by intrapeptide hydrogen bonds with $\Delta i = 2$, 3, 4 and 5 (such as α-helices) and adopts β-like structures (Figures 5.1, 5.3). The same trend is seen in the experimental studies of the amyloid β-beta peptides in water (see Review). Geometrical analysis evidences that the Aβ_{42} peptide is an extended chain at low temperatures and is a relatively compact coil at higher temperatures (see Figure 5.21). Such temperature behavior

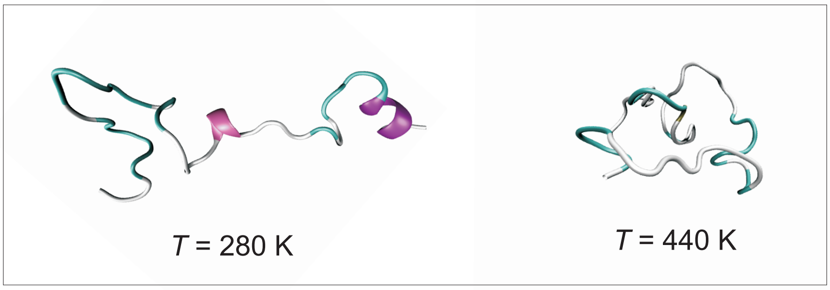

Figure 5.21: *Typical configurations of Aβ_{42} below and above the temperature of the conformational transition ($T_t \approx$ 325 K).*

is opposite to the one of elastin-like peptide [10]. Note, that despite these qualitative differences, both peptides show a negative thermal expansivity. Probably, the randomness of the distribution of the secondary structure elements along the chain and the decreasing number of intrapeptide hydrogen bonds upon heating are the key factors that cause the negative thermal expansivity of these peptides. Mainly positive thermal expansivity of Aβ_7 peptides (Figure 5.20) should be attributed to the fact that, upon heating, number of intrapeptide hydrogen bonds as well as α-helical content increases (Figures 5.17 and 5.18). We may conclude, that α-helical structures are more "solid-like", in comparison with β-sheets and PPII structures, and provide solid-like, i.e. positive thermal expansivity.

The temperature dependence of the density ρ_b of bulk liquid water and the densities ρ_h of hydration water near various surfaces are compared in Figure 5.22. In the whole temperature interval studied, $\rho_h < \rho_b$, which indicates a pronounced depletion of the water density near the surface of Aβ_{42}, Aβ_7 and Aβ_{7g}. For comparison, we show the temperature dependence of the hydration water density near silica and carbon surfaces. As can be seen from Figure 5.22 the hydrophobicity of the surfaces of the studied β-peptides is in between silica and carbon surfaces. The density of hydration water near the Aβ_7 surface is higher than in the case of Aβ_{42}. This is in agreement with the fact that the surface of Aβ_7 is not as hydrophobic as the Aβ_{42} surface. The Arctic mutation of Aβ_7 causes a weakening of water-peptide electrostatic interactions due to the absence of negative charged residue and promotes a slightly more hydrophobic surface, that is clearly seen in Figure 5.22.

The change of the apparent volumetric properties of the Aβ_{42} peptide at about 320 K may originate from its temperature-induced conformational transition. No clear

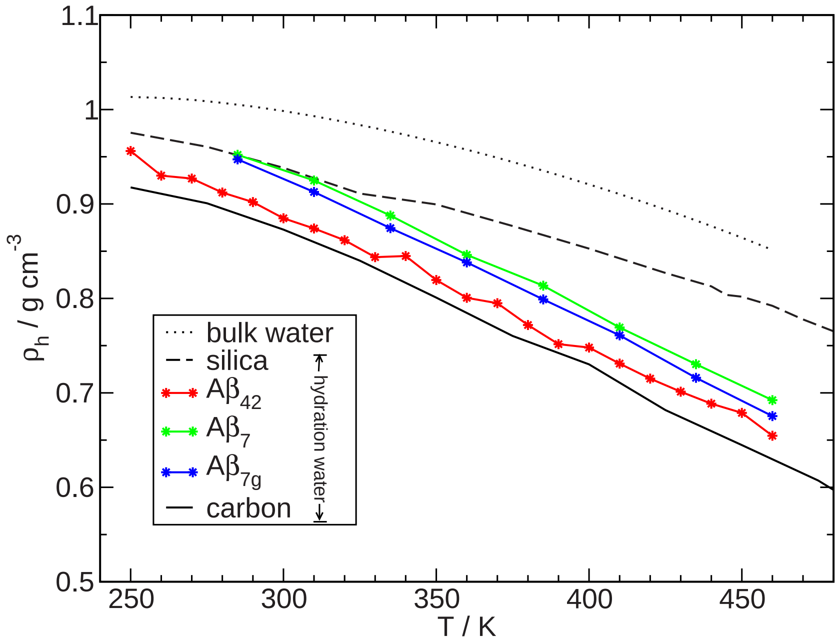

Figure 5.22: *Temperature dependence of the density of bulk water and hydration water near silica, $A\beta_{42}$, $A\beta_7$, $A\beta_{7g}$, and near carbon surface.*

evidences of such transition can be seen from the behavior of the secondary structure content (Figure 5.1) and only a rather gradual transition with a midpoint at about 320 to 340 K can be seen in the behavior of geometrical parameters (Figure 5.4). We may expect that the volumetric properties are more sensitive to the temperature-induced conformational changes of such disordered peptide, as $A\beta_{42}$. These changes are not clearly seen in the temperature dependence of the intrinsic volume of $A\beta_{42}$ (lower panel in Figure 5.14) due to the strong scattering of the data points and further studies are necessary to clarify the sensitivity of the intrinsic volume of a peptide to its conformational changes. However, slight changes of the expansivity of hydration water at about 330 K may simply reflect the fact that the peptide surface becomes slightly more hydrophobic above this temperature due to some conformational changes. The decrease of the solubility of $A\beta_{42}$ upon heating corroborates this idea. If the latter explanation is correct, we may conclude that, at least for disordered peptides, the thermal expansivity of hydration water may be a more adequate order parameter of the conformational transition than, for example, the radius of gyration or the secondary structure content.

Alternatively, the change of the apparent volumetric properties of the $A\beta_{42}$ peptide at about 320 K may originate solely from the intrinsic temperature behavior of hydration water. Below this temperature, hydration water forms an extended hydrogen bonded network, which includes most of the water molecules in the hydration shell, whereas, at higher temperatures, only small hydrogen bonded clusters are present in the hydration shell. The percolation transition between these two qualitatively different states occurs in a rather narrow temperature interval (Figure 5.7). Hence, the thermal expansion of hydration water may differ in these two states, being higher for the more disordered one. To support this explanation, the thermal expansion coefficient of hydration water should be studied in detail for surfaces with various strengths of the temperature-independent water-wall interaction.

Interestingly, the conformational transition of both peptides (the $A\beta_{42}$ and elastin-like peptides) occurs when the spanning network of their hydration water breaks upon heating. As can be seen from the upper panel of Figure 5.7, the temperatures of this break are close for these two peptides. The difference in the temperature dependence of the spanning probability appears in a small ($\sim$10 K) shift of the inflection point and in a notable difference of the sigmoid width, which is naturally to attribute to the difference in peptide sizes (the SASA of $A\beta_{42}$ is about two times larger). The similarity of the behavior of hydration water at the surfaces of the two different peptides may originate from a rather close level of the hydrophobicity of their surfaces (ca. 50% hydrophobic residues in both cases). This can be seen from the upper panel of Figure 5.13, where the densities of hydration water of these two peptides are compared: The surface of the elastin-like peptide is only slightly more hydrophobic. We may assume, that - owing to the strong coupling of the protein and hydration water ("slaving effect") - the thermal break of the spanning network of hydration water provokes (or speeds up) conformational changes of a peptide. However, the character of these changes seems to be governed by the chemical structure of the peptide. Further studies are needed to clarify the relation between the peptide structure (amino acid sequences) and the temperature of the percolation transition of hydration water on its surface. This includes both the effect of peptide hydrophilicity/hydrophobicity on water percolation and the effect of water clustering in the hydration shell on the secondary structure and volumetric properties of the peptide.

Chapter 6

Aggregation of Aβ_7 peptides in water

A goal of this chapter is to determine the initial deposit of the free monomers. As a first step, we have characterized the temperature-induced conformational changes and volumetric properties of the Aβ_{42} peptide and peptide fragments. Thus, various measures show that the temperature promotes α-helix formation in Aβ_7 monomer. In the range from 285 to 385 K, it appears that the lowering of R$_{gyr}$, SASA and the volumetric properties of the Aβ_7 peptide provide aggregation behavior in water. Therefore we continue to study temperature dependent aggregation properties in water.

6.1 Dimer of Aβ_7 peptides

Two free Aβ_7 peptides are arranged in antiparallel orientation and initial distance of 1 nm with 848 SPC/E water molecules in cubic box with length 3.0 nm. Starting from the same configuration, eight independent simulations at constant pressure of 1 bar and 8 temperatures from 285 to 460 K with 25 K intervals were carried out. As in the monomer simulations, dimer system also were pre-equilibrated by using 1000 steps of the steepest descent method. Other simulation parameters were used as in the monomer system in the previous chapter (chapter 5). At each temperature, the system was equilibrated during 1 ns and the subsequent 50 ns run was used for the analysis. To characterize the conformation of the Aβ_7 peptide dimer we calculated its solvent accessible surface area (SASA), inter-peptide hydrogen

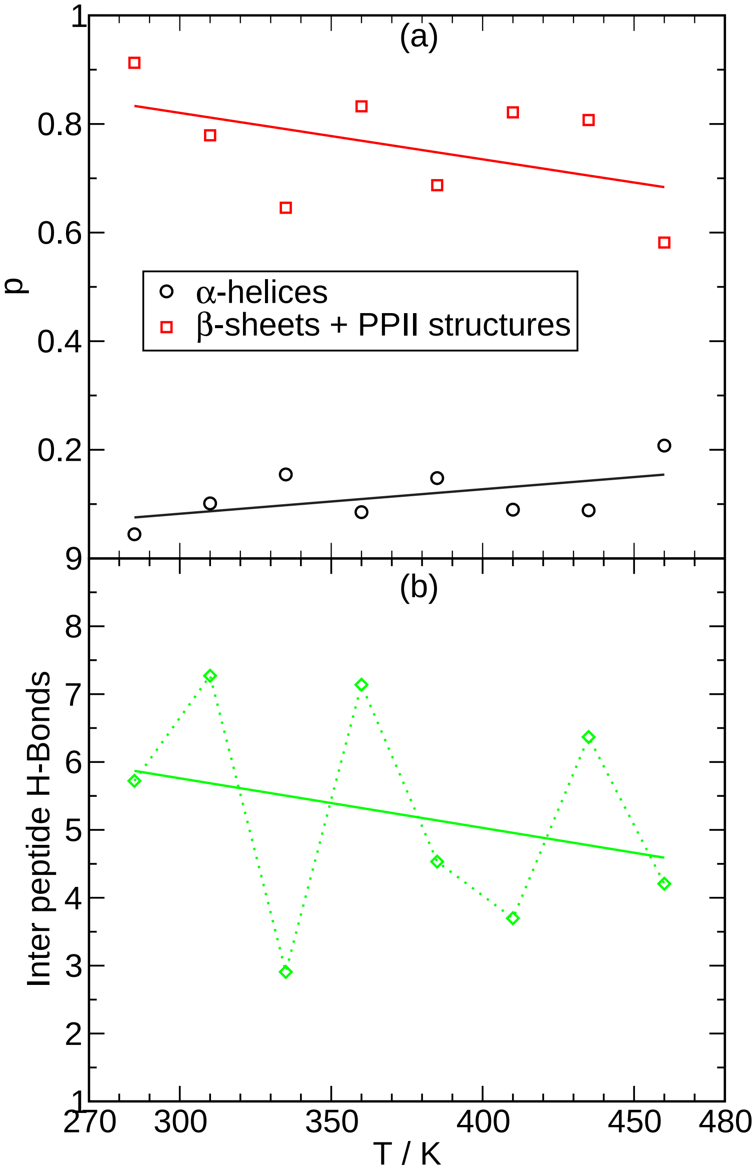

Figure 6.1: *Content p of the residues with particular secondary structure (upper panel) and average number of inter peptide Hydrogen bonds (lower panel). Linear fits are shown by lines.*

bonds along the peptide chain. The secondary structure was determined using corresponding distributions of dihedral angles ϕ and ψ in the Ramachandranan plot. A residue was considered as contributing to α-helices, when -120° $< \phi < -30°$ and -90° $< \psi < +30°$; to β-sheets and polyproline II structures, when -180° $< \phi < -30°$ and $+90° < \psi < +180°$. The volumetric properties of the dimer are calculated as in the case of the monomers in the previous chapter (chapter 5).

The fraction of residues in the dimer system with some particular secondary structure, defined using their dihedral angles, is shown in the upper panel of Figure 6.1.

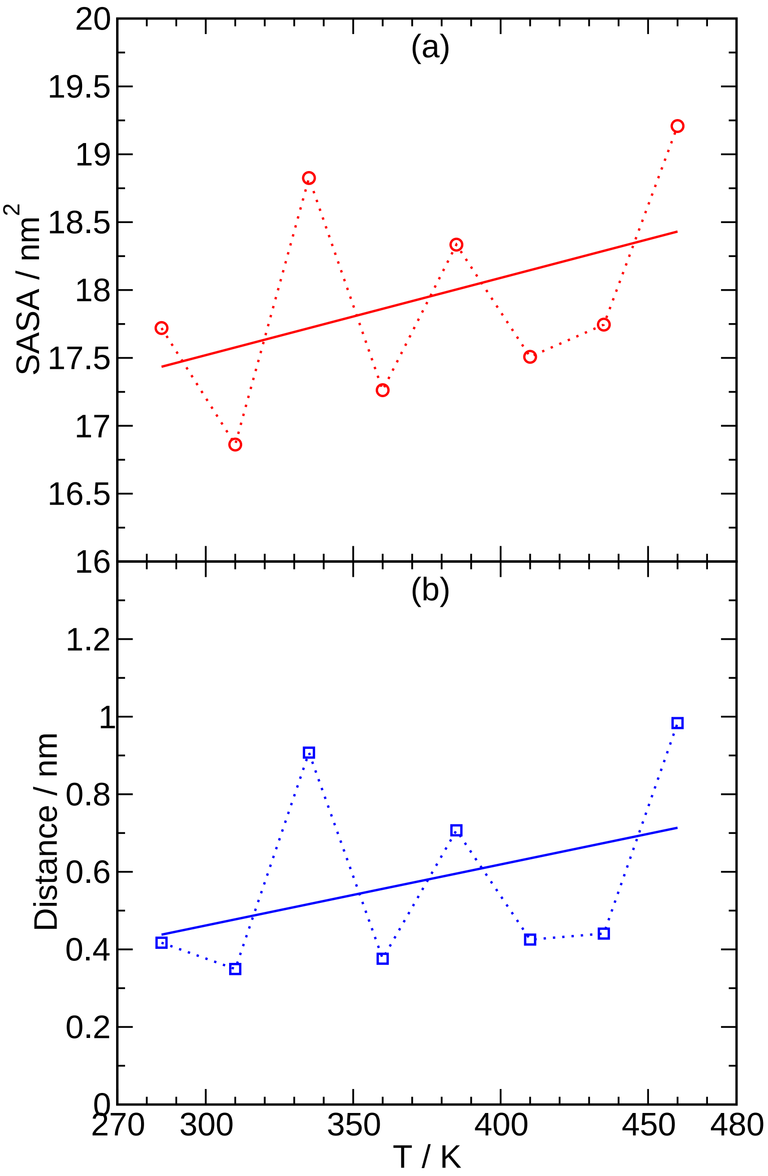

Figure 6.2: *Temperature dependence of the solvent accessible surface area SASA (upper panel) and distance between two peptides (lower panel). Fits to a linear function are shown by lines.*

The fraction of α-helices increases upon heating from 285 to about 460 K. In parallel, the fractions of β-sheets and polyproline II structures decrease upon heating. The total population of these three secondary structures considered is about 0.8 to 0.9, that show very few residues that exhibits some disordered structure. Temperature dependence of inter-peptide hydrogen bonds is spread between 3 to 7 hydrogen bonds. The linear fit of the temperature dependence shows that inter hydrogen bonds decrease with increasing temperature (Figure 6.1, lower panel).

The temperature dependence of the solvent accessible surface area (SASA) was calculated over all peptide atoms, also the distance between two peptides (center

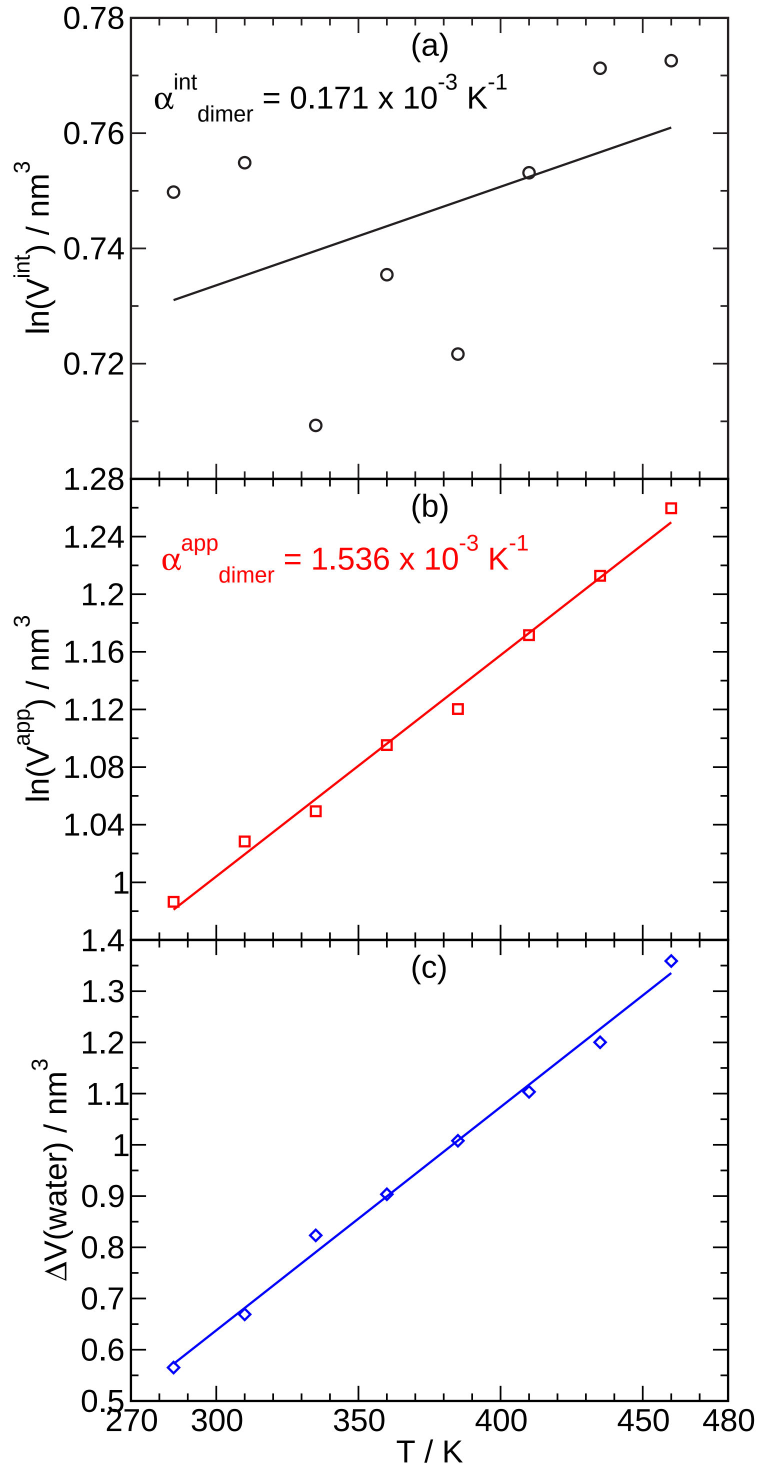

Figure 6.3: *Upper panel: Temperature dependence of* $\ln(V^{int}(\text{dimer}))$*, where V(dimer) is the intrinsic volume of two* $A\beta_7$ *peptides. Middle panel: Temperature dependence of* $\ln(V^{app}(\text{dimer}))$*, and linear fits. The slope of each linear dependence reflects the thermal expansion coefficient. Lower panel: Temperature dependence of* $\Delta V(\text{water})$*, where* $\Delta V(\text{water})$ *is the volume change due to the different densities of bulk and hydration water in the* $A\beta_7$ *peptide dimer system.*

of mass). The SASA value increased upon heating from 285 to 460 K (Figure 6.2, upper panel). Subsequently, the temperature dependence of the distance between two peptides, calculated from center of mass, was identical with SASA and inter-peptide hydrogen bonds (Figure 6.2, lower panel). Thus, measurements shows that, the dimer system is not stable in respect to the whole temperature region. The two Aβ_7 free peptides form an unstable antiparallel β-sheet. This finding is in agreement with the idea that the formation and stability of inter-peptide hydrogen bonds depend on their exposure to the solvent. Here, only emphasize, that dimer is not stable and this is reflected in Figures 6.1 and 6.2.

The temperature dependencies of $\ln(V^{int}(\text{dimer}))$ are shown in the upper panel of Figure 6.3. The derivative $\delta\ln(V)/\delta T$ is equal to the thermal expansion coefficient α. Fit to $\ln(V^{int}(\text{dimer}))$ linear dependences yield $\alpha^{int}(\text{dimer}) \approx (0.171 \pm 0.02)\cdot 10^{-3}$ K^{-1}. The obtained intrinsic thermal expansion coefficient $\alpha^{inr}(\text{dimer})$ is positive (Figure 6.3, upper panel). The temperature dependence of the apparent volume $\ln(V^{app})$ of dimer system is shown in the middle panel of Figure 6.3 using a logarithmic scale for the vertical axis. Hence, the linear part of the temperature dependence of $\ln(V^{app})$ indicate a value of the thermal expansion coefficient α^{app} from 285 to 460 K. Fit of $\ln(V^{app}(\text{dimer}))$ for a linear dependence yield $\alpha^{app}(\text{dimer}) \approx (1.536 \pm 0.014)\cdot 10^{-3}$ K^{-1} (Figure 6.3, middle panel). The obtained intrinsic thermal expansion coefficient $\alpha^{int}(\text{dimer})$ is positive as $\alpha^{int}(\text{monomer})$, obtained in previous chapter (chapter 5). $\Delta V(\text{water})$ is the volume change due to the different densities of bulk and hydration water in the Aβ_7 peptide dimer system, is shown in Figure 6.3 (lower panel). This difference increases with increasing temperature.

6.2 Tetramer of Aβ_7 peptides

In this section, we studied the aggregation of four peptides. As starting configuration form monomers are arranged antiparallel with 1976 SPC/E water molecules in a $4.0 \times 4.0 \times 4.0\,\text{nm}^3$ cubic box with about 1 nm initial distance between all peptides. Eight individual simulation runs were started from the same initial structure but with temperature intervals of 25 K from 285 K, using the Berendsen thermostat. Other simulation parameters were used as in the monomer or dimer systems. Before starting the actual simulation, an initial equilibration run of about 1 ns length was performed and the subsequent 20 ns run was used for the analysis. To characterize the conformation of the four Aβ_7 peptide cluster, we calculated its radius of gyration R_{gyr}, the solvent accessible surface area (SASA) and inter-peptide hydrogen

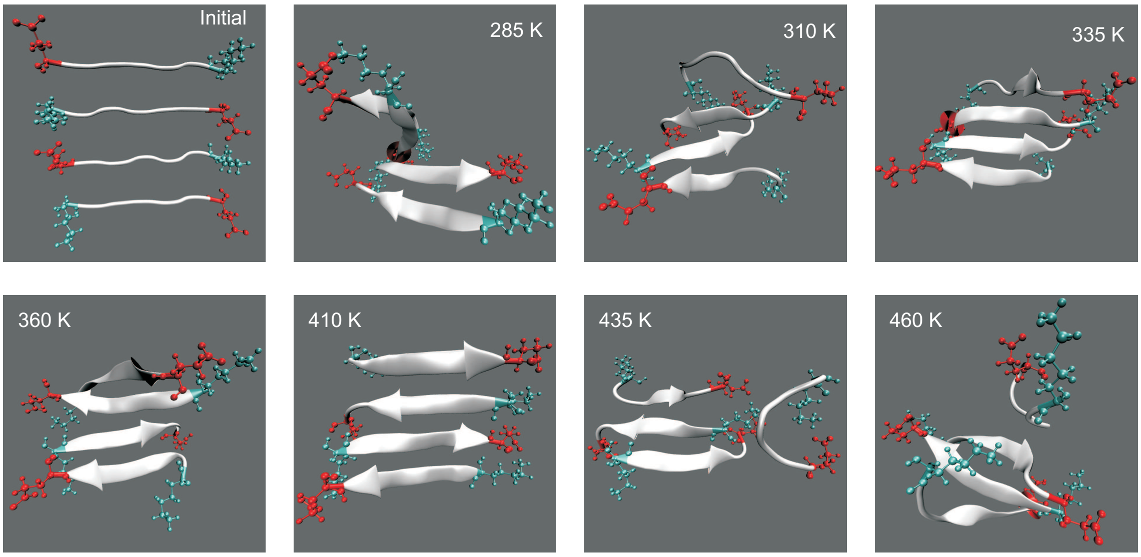

Figure 6.4: *The final snapshots of the four peptide simulation trajectories in different temperatures after 20 ns. At 410 K the most ordered fibrils are observed.*

bonds along the peptide chain. The secondary structure was determined using corresponding distributions of dihedral angles ϕ and ψ in the Ramachandranan plot. A residue was considered to belong to α-helices, β-sheets and polyproline II structures compounding to the ϕ and ψ intervals. The volumetric properties of the tetramer were also calculated as for the dimer and monomer systems.

Non-aggregated monomers have both a low α-helix and β-strand content, whereas the aggregated tetramer systems show structures with high β-sheet content, which is depended on temperature. After 20 ns the following picture emerges (Figures 6.4): at 285 K two weakly bonded antiparallel β-sheet dimers are formed. At 310 K first two antiparallel dimers are formed and then one dimer separated to form one trimer and a single monomer as shown in figures 6.4. At the temperatures between 335 and 410 K the monomeric peptides aggregate within the observation time to more or less well ordered antiparallel β-sheet tetramers. At even higher temperatures (above 435 K) the tetramer minimizes the contact surface of hydrophobic groups with water by rearranging its outer peptides (Figures 6.4). This is accompanied by the fraction of α-helices, β-sheets and number of inter peptide hydrogen bonds as shown in figure 6.5.

The fraction of residues in the tetramer system with some particular secondary structure, defined using their dihedral angles, is shown in the upper panel of Figure 6.5. The fraction of β-sheets and polyproline II structures decreased upon heating from 285 to about 460 K. Subsequently, the fraction of α-helices slightly increases upon heating (Figure 6.5, upper panel). The number of inter-peptide hydrogen

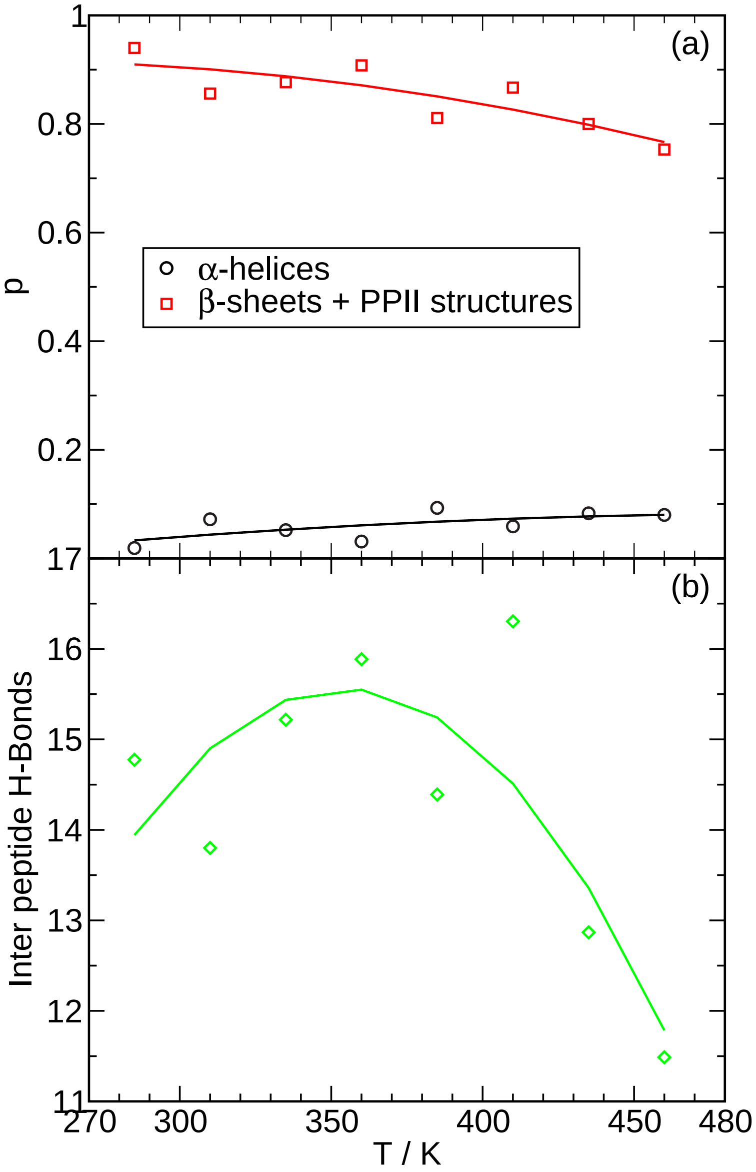

Figure 6.5: *Content p of the residues with particular secondary structure (upper panel) and average number of inter peptide hydrogen bonds (lower panel). Fits to a quadratic function are shown by lines.*

bonds increased upon heating from 285 to 360 K and sharply decreased at higher temperatures. Hence, the quadratic function fit of the temperature dependence is shown in lines in the lower panel of Figure 6.5. At higher temperatures the snapshots show more disorder states, this leads to a decreasing number of inter peptide hydrogen bonds. In other words the hydrophobicity increase with temperature leads to a cluster rearrangement to protect the hydrophobic residues from water. This is achieved by placing peptides above rather than at the ends of the β-sheet.

The temperature dependence of the solvent accessible surface area (SASA) and

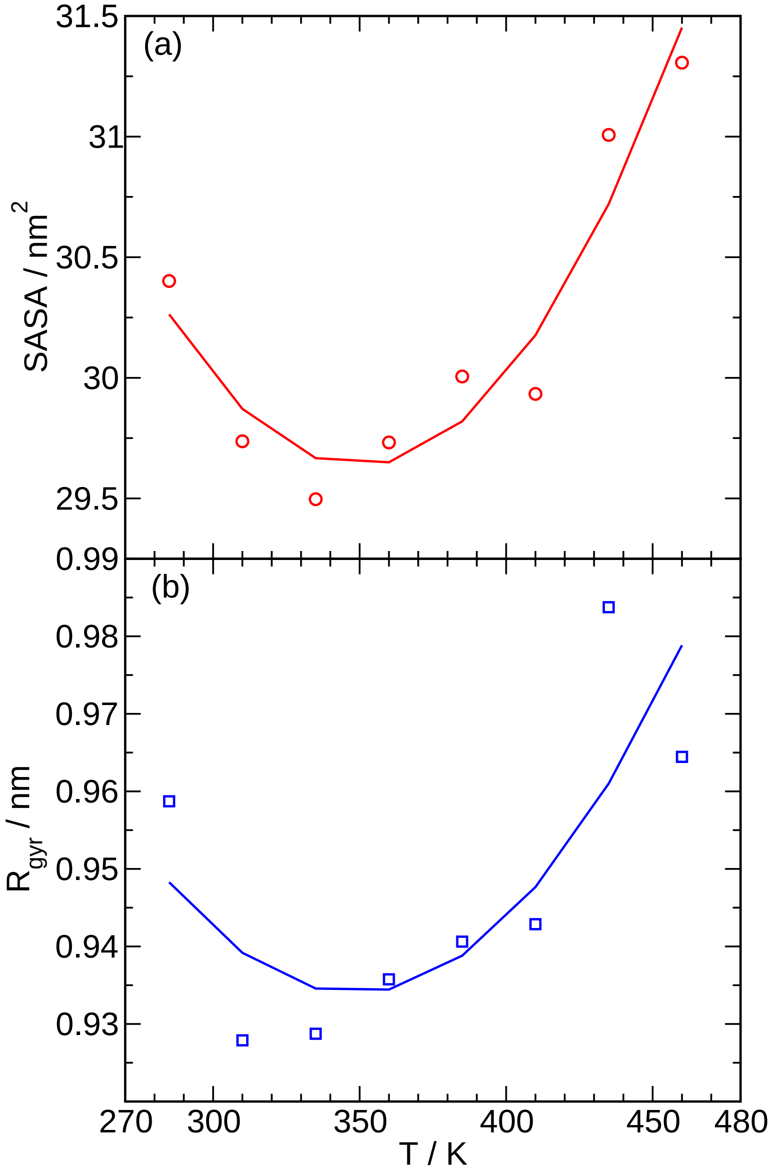

Figure 6.6: *Temperature dependence of the solvent accessible surface area SASA (upper panel) and Radius of gyration R_{gyr} (lower panel) calculated over protein atoms. Fits to a quadratic function are shown by lines.*

radius of gyration (R_{gyr}) were calculated over all peptide atoms. The SASA values deceases upon heating from 285 to 360 K and increases at higher temperatures (Figure 6.6, upper panel). The temperature dependence of R_{gyr}, calculated over all peptide atoms, showed an identical behaviour as SASA (Figure 6.6, lower panel). We may conclude that at this point the addition of more peptides does lead to an extended β-sheet and also the ordered β-sheet arrangement is stabilized by building up a second layer. As the tetramers form well-aligned four-stranded β-sheets in the temperature range from 310 K to 410 K, it appears that the four-stranded β-sheets provide a stable template for further growth of fibrillarly ordered peptide aggregates. Therefore the 360 K tetramer conformation after 20 ns has been used as a templet

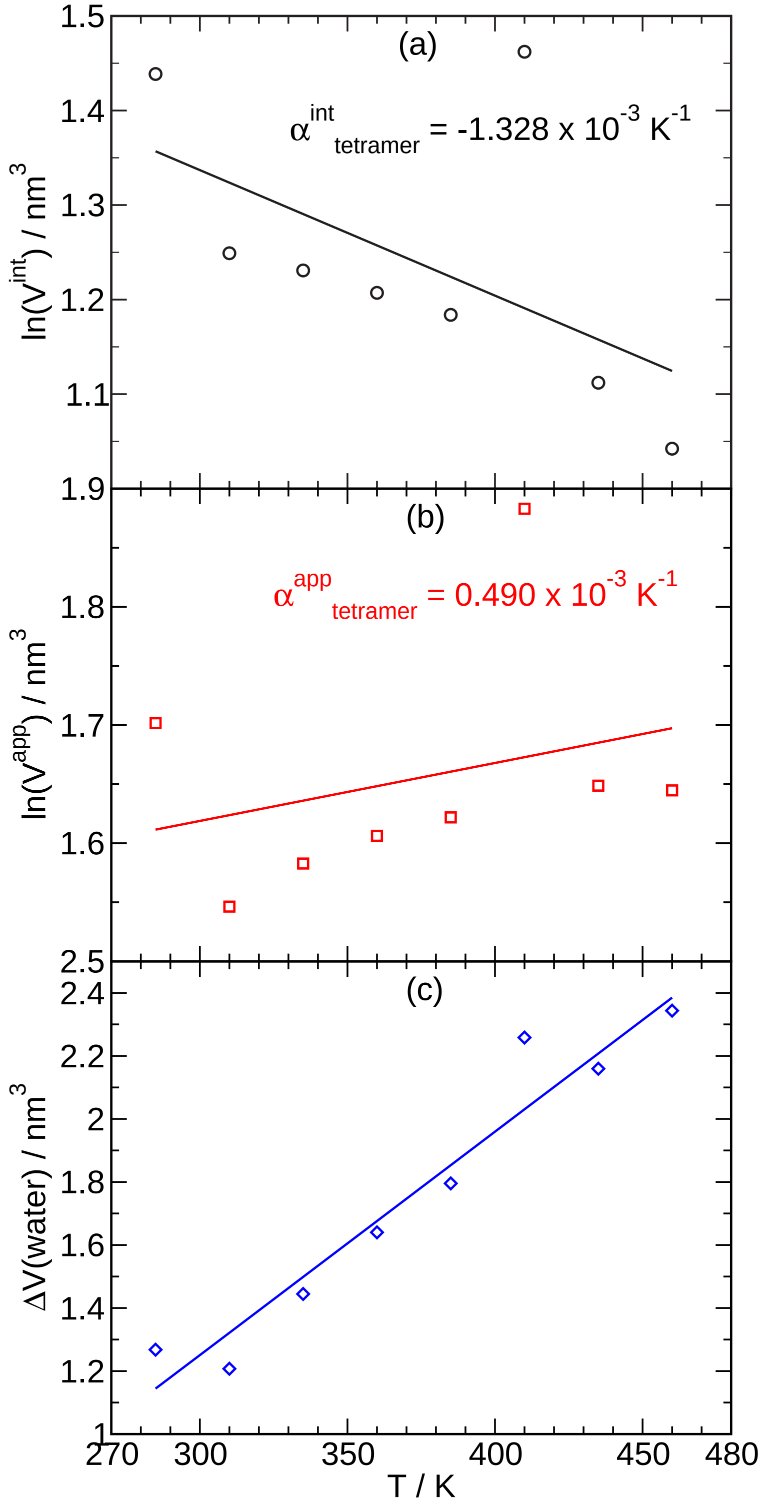

Figure 6.7: *Upper panel: Temperature dependence of ln(*V^{int}*(tetramer)), where V(tetramer) is the intrinsic volume of four* $A\beta_7$ *peptides. Middle panel: Temperature dependence of ln(*V^{app}*(tetramer)), and linear fits. Lower panel: Temperature dependence of* ΔV*(water), where* ΔV*(water) is the volume change due to the different densities of bulk and hydration water in the tetramer systems.*

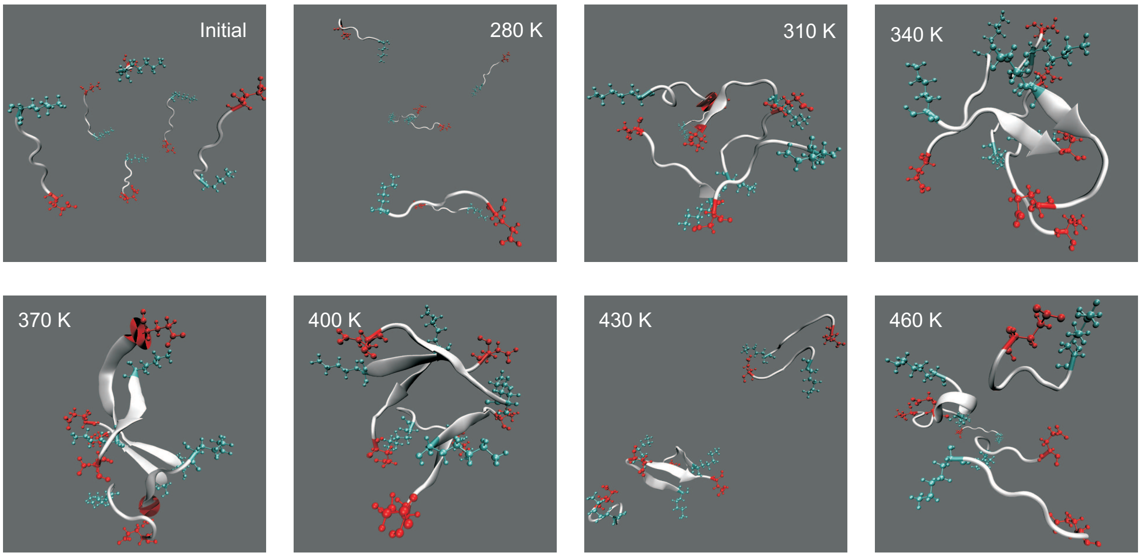

Figure 6.8: *The final snapshots of the simulation trajectories for the six Aβ_7 peptide system at 1 bar after* 80 *ns at different temperatures from 280 to* 460 *K.*

for the subsequent study of the growth process.

The temperature dependence of $\ln(V^{int}(\text{tetramer}))$ is shown in the upper panel of Figure 6.7. The derivative $\delta\ln(V)/\delta T$ is equal to the thermal expansion coefficient α. The fit of a linear dependence to $\ln(V^{int}(\text{tetramer}))$ yields $\alpha^{int}(\text{tetramer})$ $\approx(-1.328 \pm 0.022)\cdot10^{-3}$ K^{-1}. The obtained intrinsic thermal expansion coefficient $\alpha^{int}(\text{tetramer})$ is negative (Figure 6.7, upper panel). The temperature dependence of the apparent volume $\ln(V^{app})$ of the tetramer system is shown in the middle panel of Figure 6.7, using a logarithmic scale for the vertical axis. Hence, the linear part of the temperature dependence of $\ln(V^{app})$ indicates a value of the thermal expansion coefficient α^{app} from 285 to 460 K. A fit of a linear dependence to $\ln(V^{app}(\text{tetramer}))$ yields $\alpha^{app}(\text{tetramer}) \approx (0.490 \pm 0.011)\cdot10^{-3}$ K^{-1} (Figure 6.7, middle panel). The obtained intrinsic thermal expansion coefficient $\alpha^{int}(\text{tetramer})$ is negative as $\alpha^{int}(\text{A}\beta_{42})$, obtained in previous chapter (chapter 5). $\Delta V(\text{water})$ is the volume change due to the different densities of bulk and hydration water in the Aβ_7 peptide tetramer system, is shown in Figure 6.7 (lower panel). This difference increases with increasing temperature.

6.3 Hexamer of Aβ_7 and Aβ_{7g} peptides

In this section, we studied the aggregation of six peptides. For the starting configuration, six peptides are located in the center of the six planes of a 2.9 nm cube.

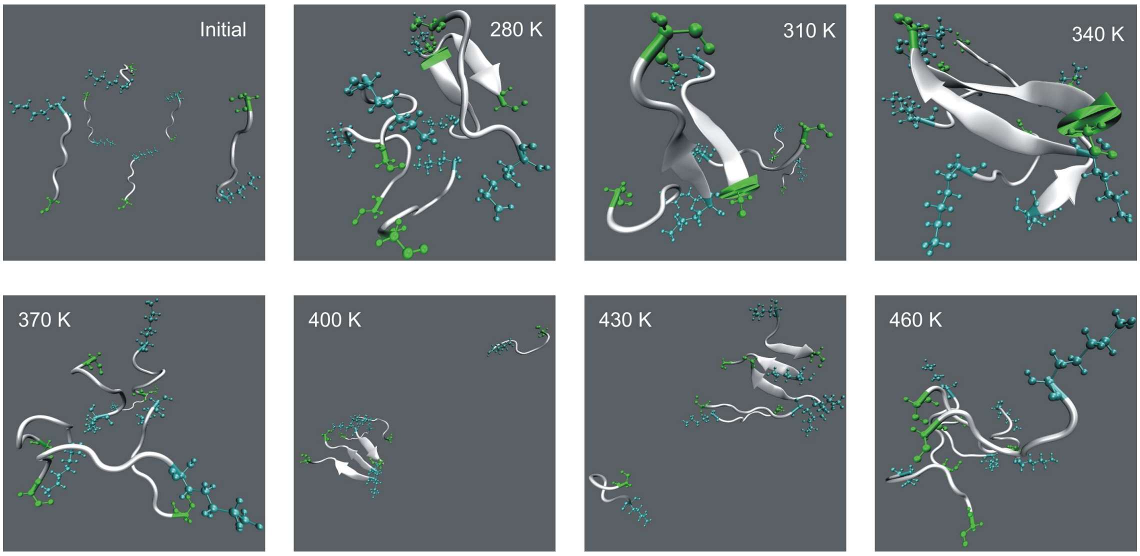

Figure 6.9: *The final snapshots of the simulation trajectories for the six Aβ_{7g} peptide system at 1 bar after* 80 ns *at different temperatures from 280 to* 460 K*.*

Every peptide was arranged parallel to cube edges and anti-parallel oriented to the opposite peptide (Figure 6.8). This separation provides sufficient space for the overall tumbling of each peptide. The whole system was maintained in the center of a $5.8 \times 5.8 \times 5.8\,\mathrm{nm}^3$ cubic box with 6094 SPC/E molecules for the wildtype system. For the mutation system, six free arctic mutation peptides (Aβ_{7g}) was maintained in the center of $5.8 \times 5.8 \times 5.8\,\mathrm{nm}^3$ cubic box with 6121 SPC/E molecules and to balance our system we added six additional Cl^- ion. Seven individual simulation runs were started from the same initial structure but with temperature intervals of 30 K from 280 K, in both systems. The other simulation parameters were used as in the dimer and tetramer systems. Before starting the actual simulation, an initial equilibration run of about 1 ns length was performed and a subsequent 80 ns run was used for the analysis. To characterize the conformation of the six peptide cluster we calculated its solvent accessible surface area (SASA) and inter-peptide hydrogen bonds along the peptide chain. The secondary structure was determined, using the corresponding distributions of dihedral angles ϕ and ψ in the Ramachandranan plot. A residue was considered to have α-helix, β-sheet and polyproline II structures using the same ϕ and ψ intervals as before. The volumetric properties of the hexamer were also calculated as in the tetramer, dimer and monomer systems.

As in the tetramer simulations, the Aβ_7 hexamer simulations show a strong temperature dependence. After 80 ns the following picture emerges (Figure 6.8): below 310 K peptides are isolated. At 310 K two weakly bonded antiparallel β-sheet dimers are formed. At 340 K first formed one antiparallel dimer. At 370 K two antiparallel dimers as shown in figure 6.8. At the temperatures between 340 and 400 K the

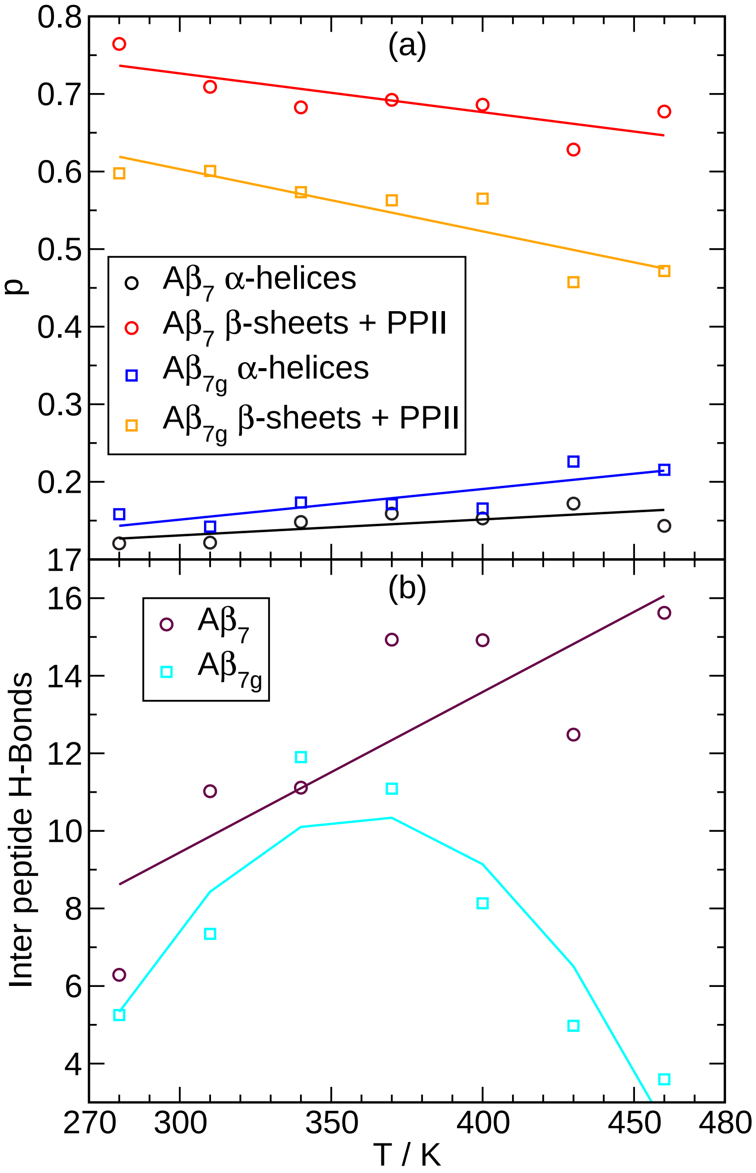

Figure 6.10: *Content p of residues with particular secondary structure (upper panel) and average number of inter peptide Hydrogen bonds (lower panel). Linear and quadratic fits are shown by lines.*

monomeric peptides aggregate within the observation time to more or less well ordered antiparallel β-sheets. At even higher temperatures (above 430 K) the Aβ_7 peptide system formed mostly disordered aggregates (Figure 6.8). On the other hand, the mutant system showed more disordered aggregates in the whole temperature ranges (Figure 6.9). This is accompanied by the fraction of α-helices, β-sheets and the number of inter peptide hydrogen bonds shown in the figure 6.10.

The fraction of residues in both hexamer systems with some particular secondary structure is shown in the upper panel of Figure 6.10. In the wildtype system, the

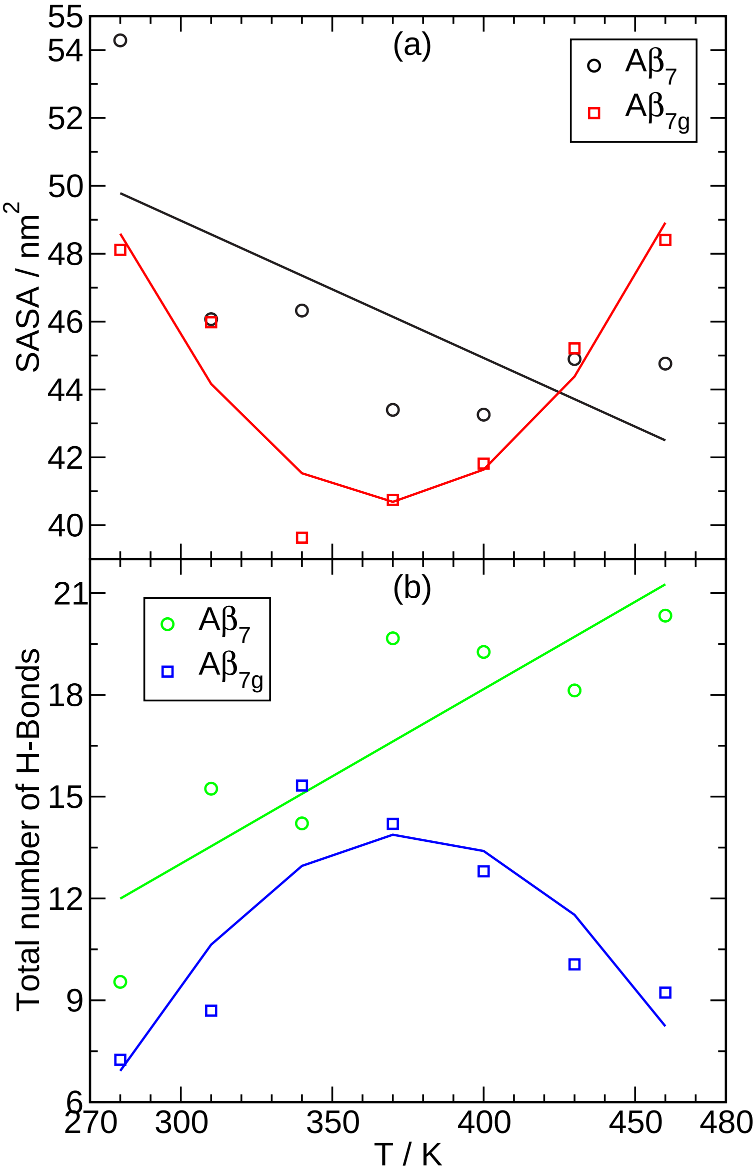

Figure 6.11: *Temperature dependence of the solvent accessible surface area SASA (upper panel) and total number of hydrogen bonds (lower panel) calculated over protein atoms. Linear and quadratic fits are shown by lines.*

fraction of β-sheets and polyproline II structures slightly decreases upon heating from 285 to about 460 K. Subsequently, the fraction of α-helices slightly increases upon heating (Figure 6.10, upper panel in circle). In the mutant system, the fraction of β-sheets and polyproline II structures also decreases upon heating from 285 to about 460 K. Subsequently, the fraction of α-helices increases upon heating (Figure 6.10, upper panel in squares). However, the total population of these three secondary structures in the wildtype system is about 0.8 to 0.9, whereas in the mutant system it is about 0.7 to 0.8. This means that the structures are more disordered in the mutant system than in the wildtype. In the wildtype system, the temperature dependence of

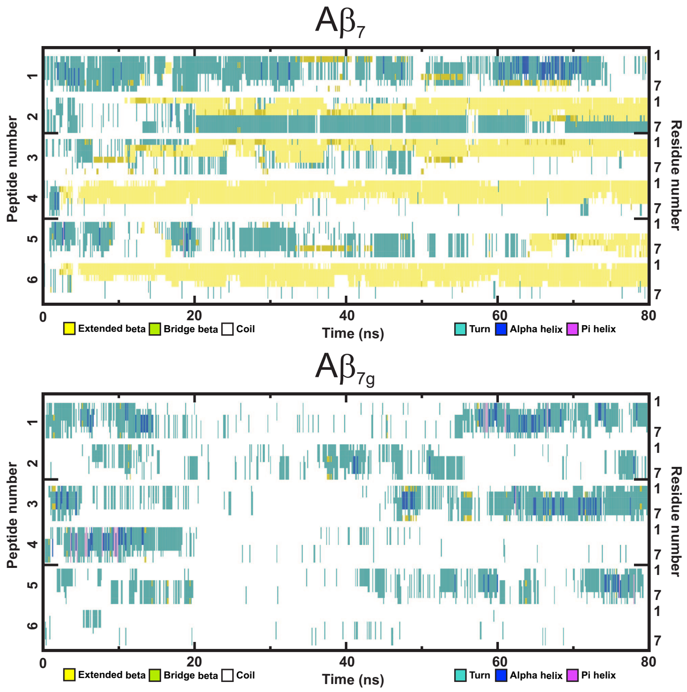

Figure 6.12: *Dynamics of the secondary structure in 80 ns simulation time at 400 K of (a) six A*β_7 *peptides (b) six A*β_{7g} *peptides, assigned according to the values of dihedral angles* ϕ *and* ψ*.* β*-strand,* α*-helix, and RC conformations are represented in yellow, blue, and white, respectively. The six A*β_7 *peptides are fast converting into a* β*-strand (see text for details).*

the inter-peptide hydrogen bonds sharply increases upon heating from 280 to 460 K. The linear fit of the temperature dependence is shown in lines (circles) in the lower panel of Figure 6.10. In the mutant system, the number of inter-peptide hydrogen bonds decreases upon heating from 340 to 460 K (Figure 6.10, lower panel, squares). The disorder of the aggregated states in the mutant system leads to a decreasing number of inter peptide hydrogen bonds. This can be explained by the fact that the E22G mutation leads to a cluster rearrangement to protect the hydrophobic residues from water.

The temperature dependence of the solvent accessible surface area (SASA) and of the total number of hydrogen bonds were calculated over all peptide atoms. In the wildtype system, the SASA values decease upon heating from 280 to 460 K (Figure 6.11, upper panel, circles). The total number of hydrogen bonds are calculated over all peptide atoms was identical with SASA (Figure 6.11, lower panel, circles). In mutant system, the SASA values are flat ended in all temperature range (Figure 6.11, upper panel, squares). We may conclude that the wildtype system shows a stronger temperature effect than the Arctic mutation. As most wildtype hexamers form well-aligned β-sheets in the temperature range from 340 K to 400 K, it appears

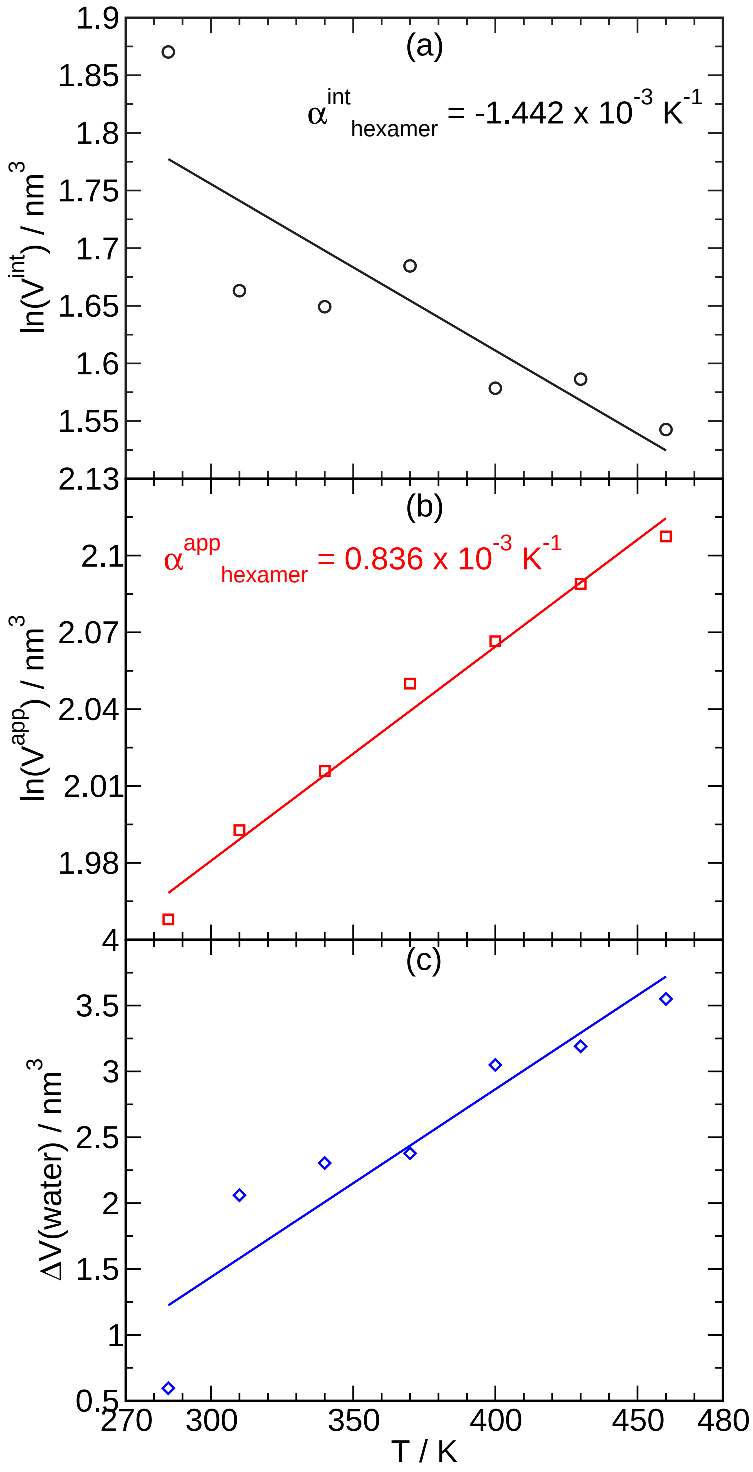

Figure 6.13: *Upper panel: Temperature dependence of* $\ln(V^{int}(\mathrm{hexamer}))$*, where* $V^{int}(\mathrm{hexamer})$ *is the intrinsic volume of the six* $A\beta_7$ *peptides cluster. Middle panel: Temperature dependence of* $\ln(V^{app}(\mathrm{hexamer}))$*, and linear fits. Lower panel: Temperature dependence of* $\Delta V(\mathrm{water})$*, where* $\Delta V(\mathrm{water})$ *is the volume change due to the different densities of bulk and hydration water in the hexamer system.*

that the temperature 400 K form more inter peptide hydrogen bonds as tetramer simulation.

The dynamics of the secondary structure at 400 K of the wildtype and mutant system at the residual level is presented in Figure 6.12. The secondary structure changes, accompanying the peptide extension, give a preliminary view recording the protofibril formation. In the wildtype system, shortly after the initial equilibration the Aβ_7 peptides adapt random coil (RC) and turn conformations (Figure 6.12a). Subsequently, dramatic increase in the β-strand content within 20 ns time is observed, indicating formation of β-sheet (Figure 6.12a). In the mutant system, the Aβ_{7g} peptides adapt RC and turn conformations (Figure 6.12b). There is no indication of ordered aggregation at 400 K (Figure 6.12b).

The temperature dependence of $\ln(V^{int}(\text{hexamer}))$ is shown in the upper panel of Figure 6.13. The derivative $\delta \ln(V)/\delta T$ is equal to the thermal expansion coefficient α. A fit of a linear dependence to $\ln(V^{int}(\text{hexamer}))$ yields $\alpha^{int}(\text{hexamer}) \approx(-1.442 \pm 0.012)\cdot 10^{-3}\ \text{K}^{-1}$. The obtained intrinsic thermal expansion coefficient $\alpha^{int}(\text{hexamer})$ is negative (Figure 6.13, upper panel). The temperature dependence of the apparent volume $\ln(V^{app})$ of the hexamer system is shown in the middle panel of Figure 6.13, using a logarithmic scale for the vertical axis. The linear part of the temperature dependence of $\ln(V^{app})$ indicates a value of the thermal expansion coefficient α^{app} from 280 to 460 K. A linear fit to $\ln(V^{app}(\text{hexamer}))$ yields $\alpha^{app}(\text{hexamer}) \approx (0.836 \pm 0.01)\cdot 10^{-3}\ \text{K}^{-1}$ (Figure 6.13, middle panel). The obtained intrinsic thermal expansion coefficient $\alpha^{int}(\text{hexamer})$ is negative as $\alpha^{int}(\text{A}\beta_{42})$ and $\alpha^{int}(\text{tetramer})$, obtained in the previous studies. $\Delta V(\text{water})$ is the volume change due to the different densities of bulk and hydration water in the Aβ_7 and Aβ_{7g} peptide hexamer systems, are shown in Figure 6.13 (lower panel). This difference increases with increasing temperature.

6.4 Decamer of Aβ_7 peptides

In this section, we studied the aggregation of ten peptides. For the starting configuration, six peptides are located in the center of the six planes of a 2.9 nm cube and at the center of cube located the ordered tetramer obtained at 360 K after 20 ns. All free six peptides are located same as hexamer system and the whole system was maintained in the center of a $5.8 \times 5.8 \times 5.8\,\text{nm}^3$ cubic box with 5900 SPC/E molecules for the decamer system. Seven individual simulation runs were started from the same initial structure but with temperature intervals of 30 K from 280 K.

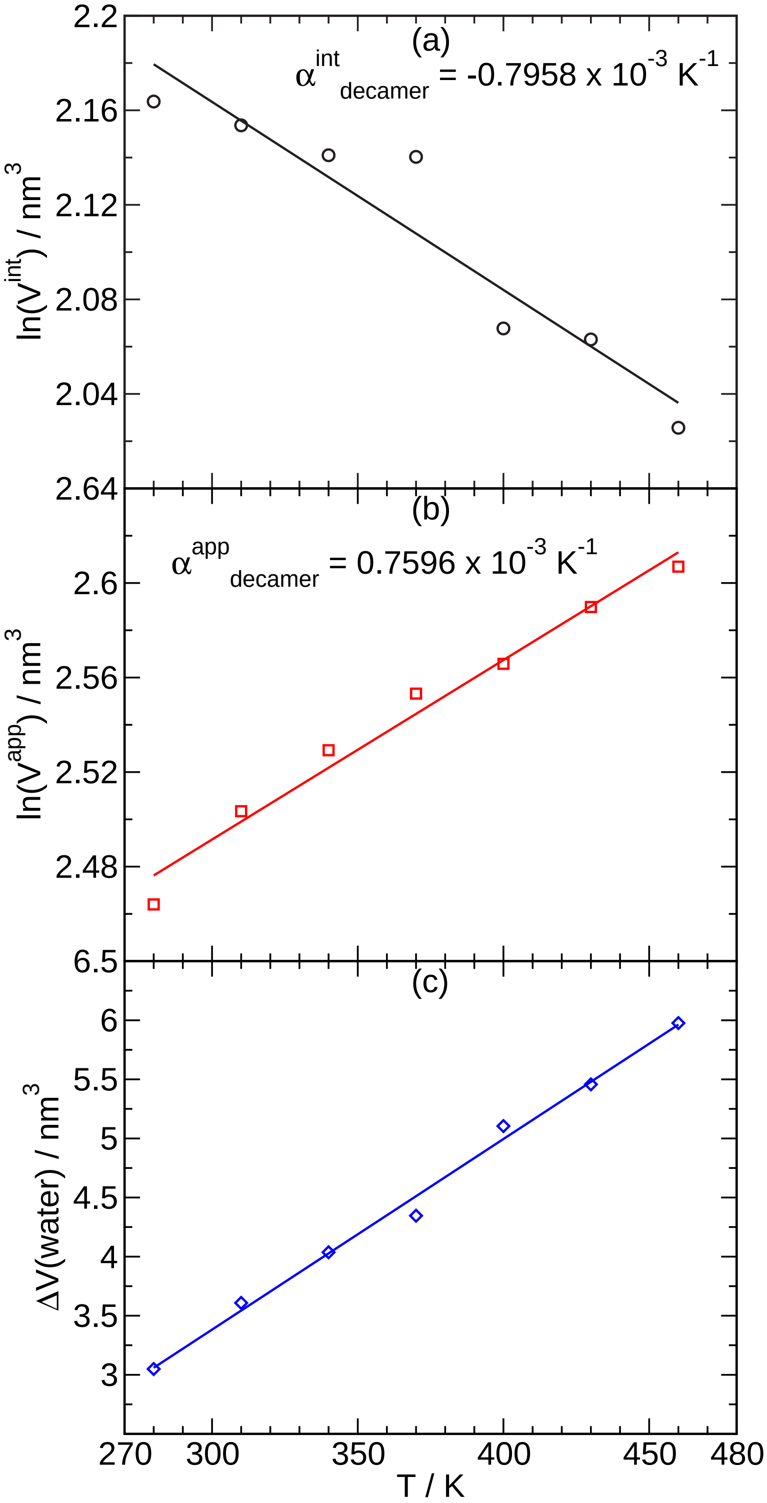

Figure 6.14: *Upper panel: Temperature dependence of* $\ln(V^{int}(\text{decamer}))$*, where V(decamer) is the intrinsic volume of ten* $A\beta_7$ *peptides cluster. Middle panel: Temperature dependence of* $\ln(V^{app}(\text{decamer}))$*, and linear fits. Lower panel: Temperature dependence of* $\Delta V(\text{water})$*, where* $\Delta V(\text{water})$ *is the volume change due to the different densities of bulk and hydration water in the decamer system.*

Other simulation parameters were used as in the tetramer or hexamer systems. Before starting the actual simulation, an initial equilibration run of about 1 ns length was performed. The subsequent 80 ns run was used for the analysis of volumetric properties. More details about the fibril growth mechanism and structural details are given in next chapters.

The temperature dependence of $\ln(V^{int}(\text{decamer}))$ is shown in the upper panel of Figure 6.14. The derivative $\delta \ln(V)/\delta T$ is equal to the thermal expansion coefficient α. The fit of a linear dependence to $\ln(V^{int}(\text{decamer}))$ yields $\alpha^{int}(\text{decamer}) \approx(-0.795 \pm 0.008)\cdot 10^{-3}$ K^{-1}. The obtained intrinsic thermal expansion coefficient $\alpha^{int}(\text{decamer})$ is negative (Figure 6.14, upper panel). The temperature dependence of the apparent volume $\ln(V^{app})$ of the decamer system is shown in the middle panel of Figure 6.14, using a logarithmic scale for the vertical axis. Hence, the linear part of the temperature dependence of $\ln(V^{app})$ indicates a value of the thermal expansion coefficient α^{app} from 285 to 460 K. A fit of a linear dependence to $\ln(V^{app}(\text{decamer}))$ yields $\alpha^{app}(\text{decamer}) \approx (0.759 \pm 0.006)\cdot 10^{-3}$ K^{-1} (Figure 6.14, middle panel). The obtained intrinsic thermal expansion coefficient $\alpha^{int}(\text{decamer})$ is negative as tetramer and hexamer system, obtained in previous section. The volume defect increases with increasing temperature (Figure 6.14, lower panel). $\Delta V(\text{water})$ is the volume change due to the different densities of bulk and hydration water in the Aβ_7 peptide decamer system, is shown in Figure 6.14 (lower panel). This difference increases with increasing temperature.

6.5 Conclusions

The dimer system exhibits an essentially disordered conformational structure at all temperatures studied. The inter peptide hydrogen bonds are distributed almost randomly along the whole temperature range and linear fits show that the hydrogen bonds decrease with increasing temperature (Figure 6.1, lower panel). In the case of the tetramer system, the quadratic function fit indicate an reversal point at about 360 K. Figure 6.5 lower panel shows that the inter peptide hydrogen bonds increase upon heating from 285 to 360 K and decrease at higher temperatures. In the hexamer system, the inter peptide hydrogen bonds increase with increasing temperature as shown in the lower panel of Figure 6.10. The SASA analysis shows the same behavior as inter peptide hydrogen bonds in all Aβ_7 peptide systems (dimer, tetramer and hexamer) and as seen in Figures 6.2, 6.5 and 6.11 (upper panel).

We may expect that the volumetric properties of peptide aggregates depend on the

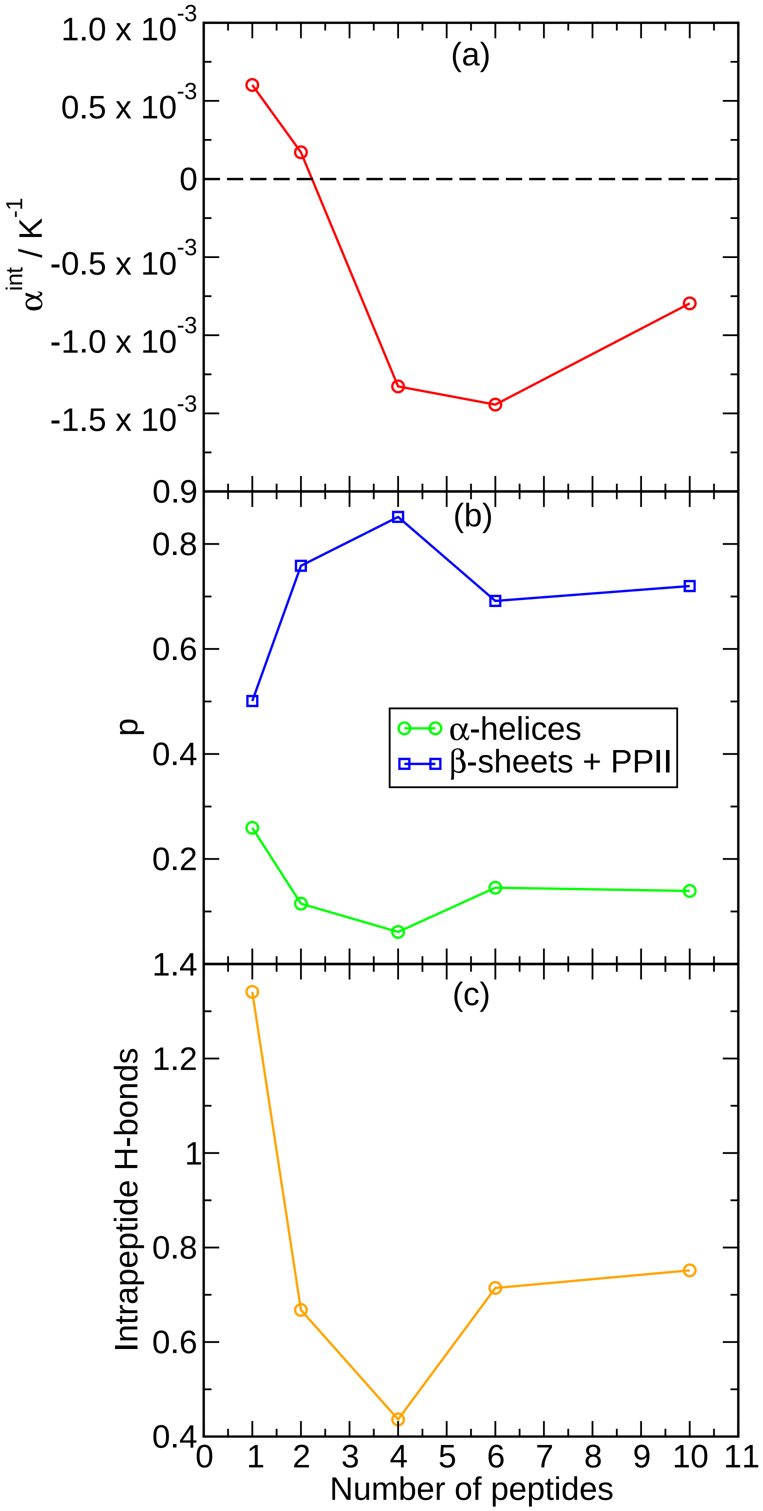

Figure 6.15: *The intrinsic thermal expansion coefficient* α^{int} *(upper panel), content* p *of the residues with particular secondary structure (middle panel) and average number of intrapeptide hydrogen bonds (lower panel) in all peptide aggregation systems. Fits to a quadratic function are shown by lines.*

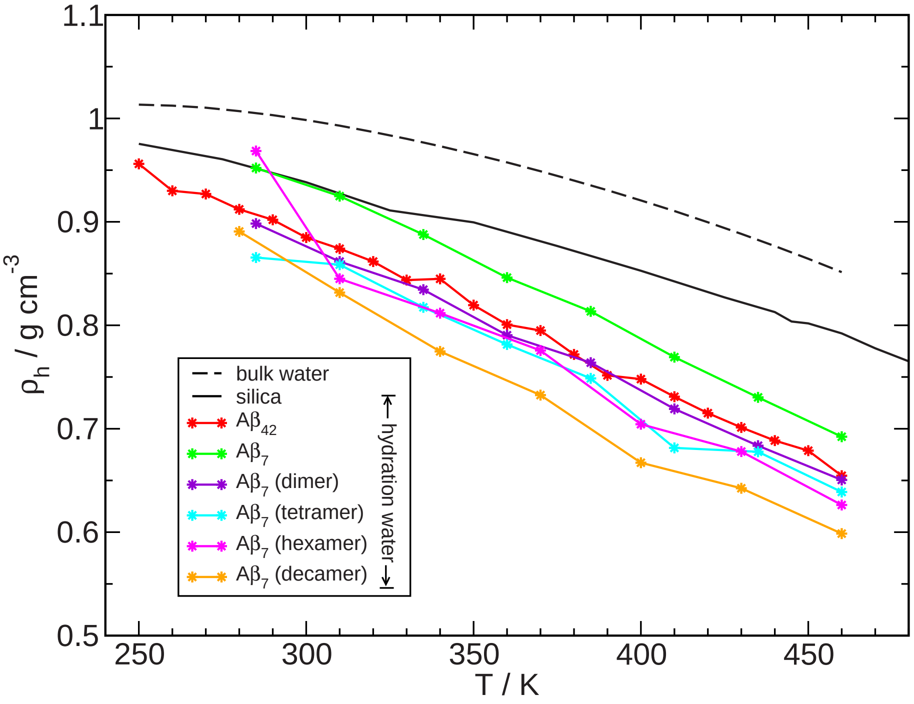

Figure 6.16: *Temperature dependence of the density of bulk water and hydration water near silica, Aβ_{42}, monomer, dimer, tetramer, hexamer and decamer of Aβ_7 peptide surface.*

number of peptides in the aggregate and on the character of aggregation. The Aβ_7 dimer system in solution shows a positive intrinsic thermal expansion coefficient similar to the Aβ_7 monomer. For the tetramer, hexamer and decamer, a thermal expansion coefficient is negative similar to the Aβ_{42} peptide. So, the expansion coefficient of peptide aggregation becomes negative with increasing number of peptides in aggregates. These changes are seen in the intrinsic thermal expansion coefficient α^{int} in different systems (Figure 6.15, upper panel). The mainly negative thermal expansivity of Aβ_7 peptide aggregates should be attributed to the decreasing the number of intrapeptide hydrogen bonds as well as to the α-helical content upon increasing the number of peptides (Figures 6.15, middle and lower panel). Further studies are necessary to clarify the sensitivity of the intrinsic volume of peptide aggregates to the character of aggregation. Probably, a high value of the inter peptide hydrogen bonds and β-sheet content are the key factors that cause the negative thermal expansivity of these peptide aggregates.

Thus, we may assume that the anomalous (negative) expansivity of the tetramer, hexamer and decamer systems may originate, at least partially, from an increase of the inter peptide hydrogen bonding upon heating. An increase of the number of inter peptide hydrogen bonds should help to increasing the β-sheet content and pack the peptides more tightly. As a consequence, also the defect or void volume will be diminished at higher temperatures. A similar behavior is observed for the

Aβ_{42} peptide, where the number of intrapeptide hydrogen bonds decreases from 250 to 460 K and similar temperature dependence was shown in thermal expansivity values (chapter 5). The temperature dependence of the density ρ_b of bulk liquid water and densities ρ_h of hydration water near various peptide cluster surfaces are compared in Figure 6.16. For comparison, we show the temperature dependence of the water density near a silica surface. Increasing the number of peptides, the peptide aggregate surface become more hydrophobic due to peptide aggregation as indicated by the decreasing density of hydration water. The water density depletion is markedly stronger in the surface of Aβ_7 decamer, which is more hydrophobic, then a carbon surface.

In this section, we have also attempted to follow the aggregation in systems of six Aβ_7 and six Aβ_{7g} peptides at different temperatures. In the mutated system the aggregated structures do not strongly depend on temperature as observed in the wildtype system. More disordered aggregates were formed at all temperatures studied with smaller SASA values (Figure 6.11, upper panel). This state is sequence dependent, since no ordered structure is found for the Arctic variant Aβ_{7g}, in agreement with the experiment [24, 26, 66, 67].

Chapter 7

Fibril growth in Aβ_7 peptide system

A goal of this chapter is to determine the conformational changes that free monomers undergo, when interacting with a preformed oligomer. As a first step, we characterized the energy minima structures achieved by a tetramer during 20 ns simulations at different temperatures (discussed in the previous chapter). The tetramer adopts a well aligned four stranded antiparallel β-sheet in the temperature range from 330 to 410 K. Since this temperature range provides a stable template for further growth of fibrillarly ordered peptide aggregates, we used the tetramer conformation after 20 ns at 360 K (mean of the temperature range) as template for the subsequent study of the growth process. In a supplementary study (also in chapter 6) we placed six free Aβ_{16-22} (Aβ_7) peptides, separated by a distance of 2.9 nm from each other with antiparallel orientation inside the simulation box. This end-to-end separation between the peptides provides sufficient space for overall tumbling of each molecule. Here also, β-strand conformations were obtained from these peptides, which adopt a collapsed coil structure as monomers in water. With these additional hexamer simulations we could verify, that the simulation results are independent of the initial placement of the Aβ_7 peptides. At 400 K the six free Aβ_7 monomers predominantly adopted the antiparallel β-sheet structures within 80 ns of simulation time.

For the fibril growth study, discussed in this chapter, we took six free peptides and placed them at a uniform distance of about 1.45 nm around the center of the ordered tetramer obtained at 360 K after 20 ns (see Figure 7.1). The 10 peptides were immersed in 5900 water molecules in a cubic box measuring $5.8 \times 5.8 \times 5.8\,\mathrm{nm}^3$. With this starting configuration, seven independent simulations were carried out at

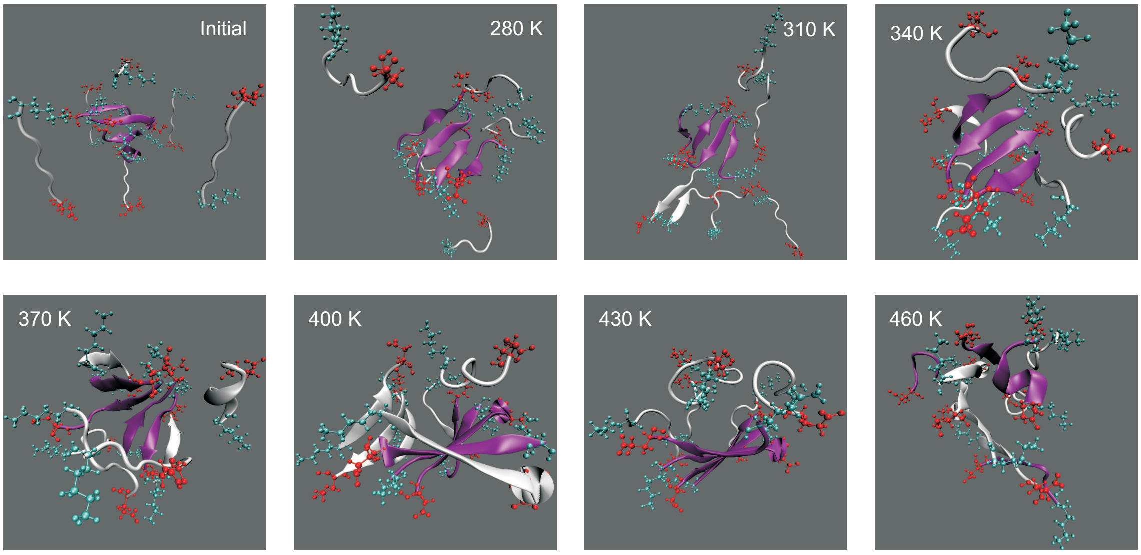

Figure 7.1: *The final snapshots of the simulation trajectories for the ten peptide system at 1 atm after 40 ns at different temperatures from 280 to 460 K. The initial ordered peptide tetramer is in purple. Additional peptides (in white) were placed around 1.45 nm away from the center of mass of the initial ordered peptide aggregate as monomer peptides and became part of the peptide aggregate during the simulations. K(+) shown in cyan and E(-) in red. The most ordered structure is obtained at 400 K.*

constant pressure of 1 atm in the temperature range between 280 to 460 K at 30 K intervals for 40 ns each. Before starting the actual simulations, we equilibrated the system for 1 ns at the above given temperatures.

7.1 Results

Figures 7.1 and 7.2 characterize the aggregates obtained from the simulation runs at different temperatures under constant pressure. Figure 7.1 illustrate the final configurations attained after 40 ns while Figure 7.2 gives the average number of hydrogen-bonds between different peptides in the form of an interaction matrix. The interaction matrix depicts the hydrogenbonds averaged over 0 to 8 ns and 8 to 40 ns in the upper and lower half of the matrix respectively, color coded according to the given scale. This reveals that within $\sim$ 8 ns the system was close to equilibrium. To get a clear picture of the final aggregates the numbering of the peptides was chosen such that the neighbouring peptides in the final conformation have consecutive numbers. The numbers given in red indicate the original tetramer, which works as nucleus for a further fibril growth (Figure 7.2). As one can see, except at the highest temperature, the nucleus shows a remarkable stability until 430 K, beyond

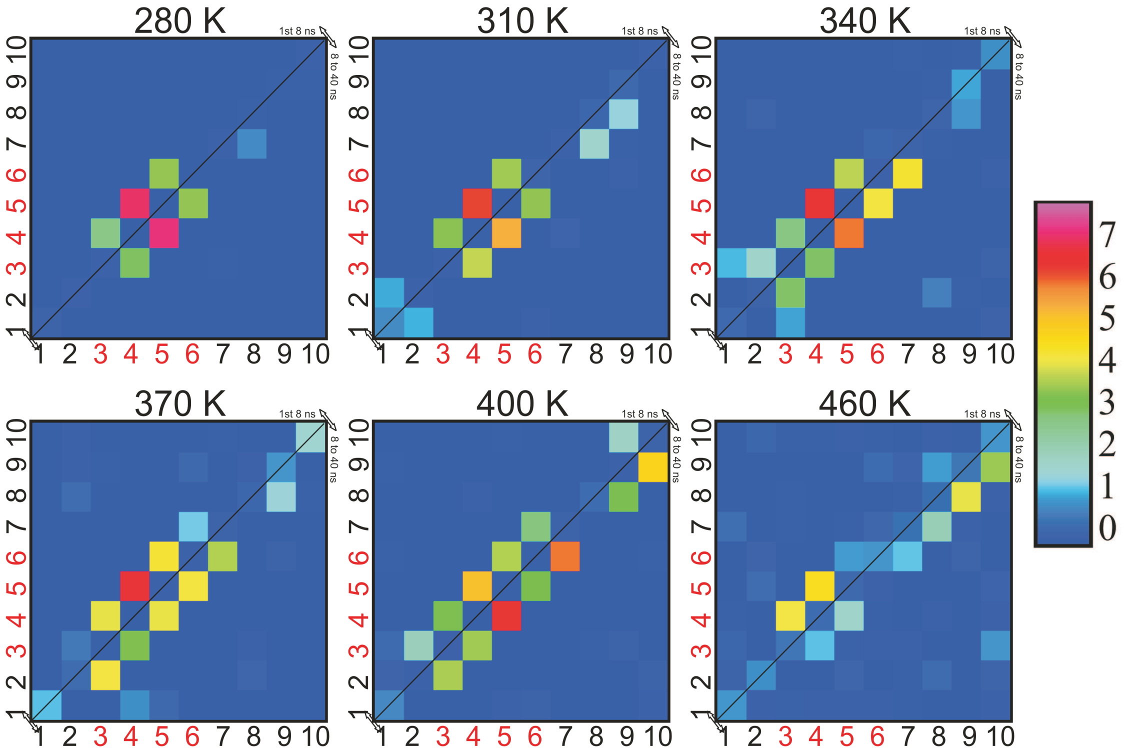

__Figure 7.2:__ Hydrogen-bond map with average number of hydrogen bonds between the peptides; upper half of the matrix averaged over first 8 ns simulation time, lower matrix averaged from 8 ns to 40 ns of the simulation trajectories. Peptides number 3 to 6 (red numbers) represent the ordered tetramer from the 360 K simulation run used in the starting configuration (see text).

which larger rearrangements occur.

At the lowest temperatures the added monomers remain isolated and adopt a collapsed coil structure. At 310 K the free peptides show short lived hydrogen bond interactions formed between each other leading to short lived isolated dimers. At 340 and 370 K two free peptides were attached to the original tetramer on both ends to form a loosely ordered hexamer, three peptides form additional hydrogen-bond interactions leading to a short lived dimer and/or a few intramolecular hydrogen-bonds. At 400 K the most pronounced aggregation occurs: two layered β-sheets, consisting of six and three peptides are formed (Figure 7.1) while one peptide is still detached, forming intramolecular hydrogen bonds. Figure 7.1 shows that at this temperature the hexameric β-sheet develops a pronounced left-handed twist and the trimer establishes a parallel sheet to sheet contact, reminiscent of the amyloid protofilament structure. At the highest temperature of 460 K the increased mobility of the molecules produced the strongest rearrangement: the original tetrameric nucleus was unstable, nevertheless an extended antiparallel β-sheet structure can be identified with a few detached monomers. The low average number of hydrogen

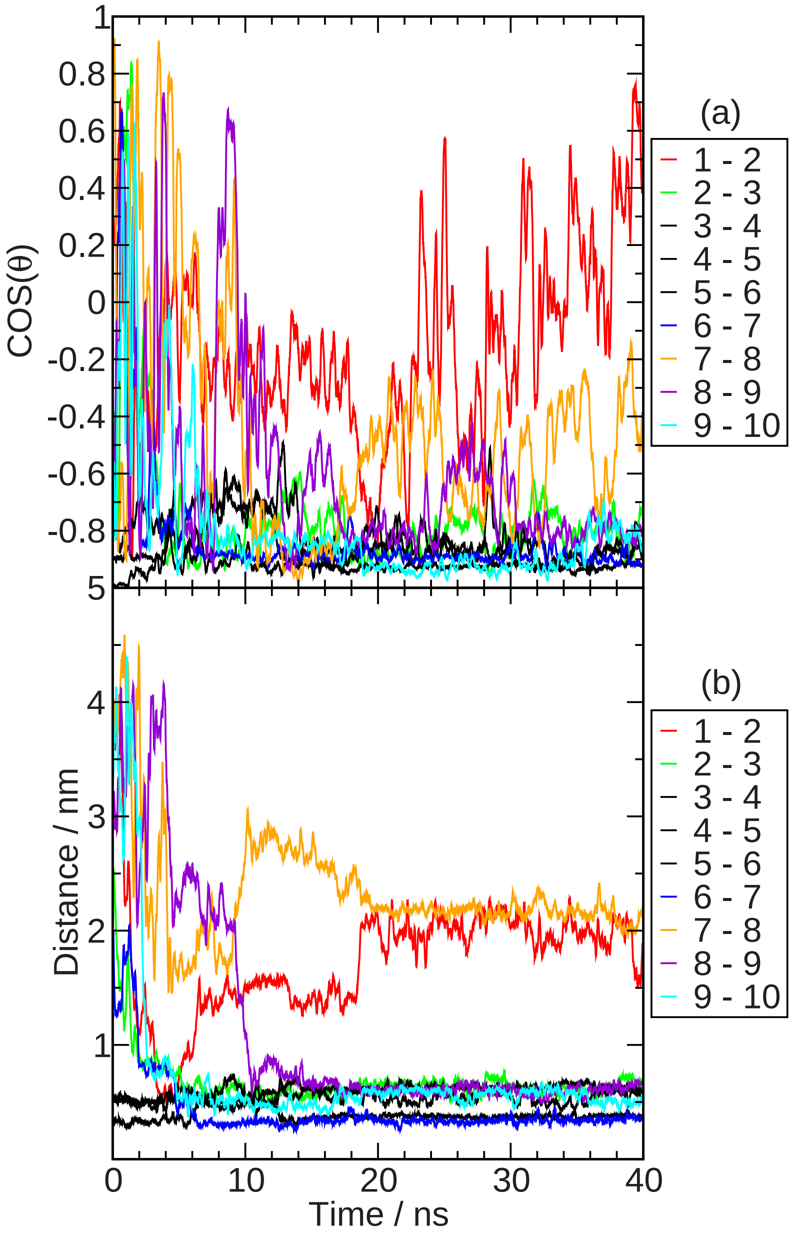

Figure 7.3: *Properties of the peptides at 400 K during the 40 ns simulation time, (a) angle, (b) distance. Peptide numbers are as in Figure 7.2 and the initial antiparallel tetramer is shown with black lines.*

bonds (Figure 7.2) at this temperature indicates a strongly dynamic system.

Figure 7.3 illustrates the formation of two layered β-sheet structures with antiparallel orientation of the peptides in more detail. The black lines indicate the original tetramer (peptides 3 to 6), which works as nucleus for a further fibril growth (Figure 7.2). Figure 7.3a indicates the time dependence of the cosines that characterize the mutual orientation of consecutive neighbouring peptide pairs going along the diagonal of the interaction matrix (Figure 7.2). The orientation vector of the peptides connects the central carbon atom (C_α) of residues L17 and A21. At 400 K,

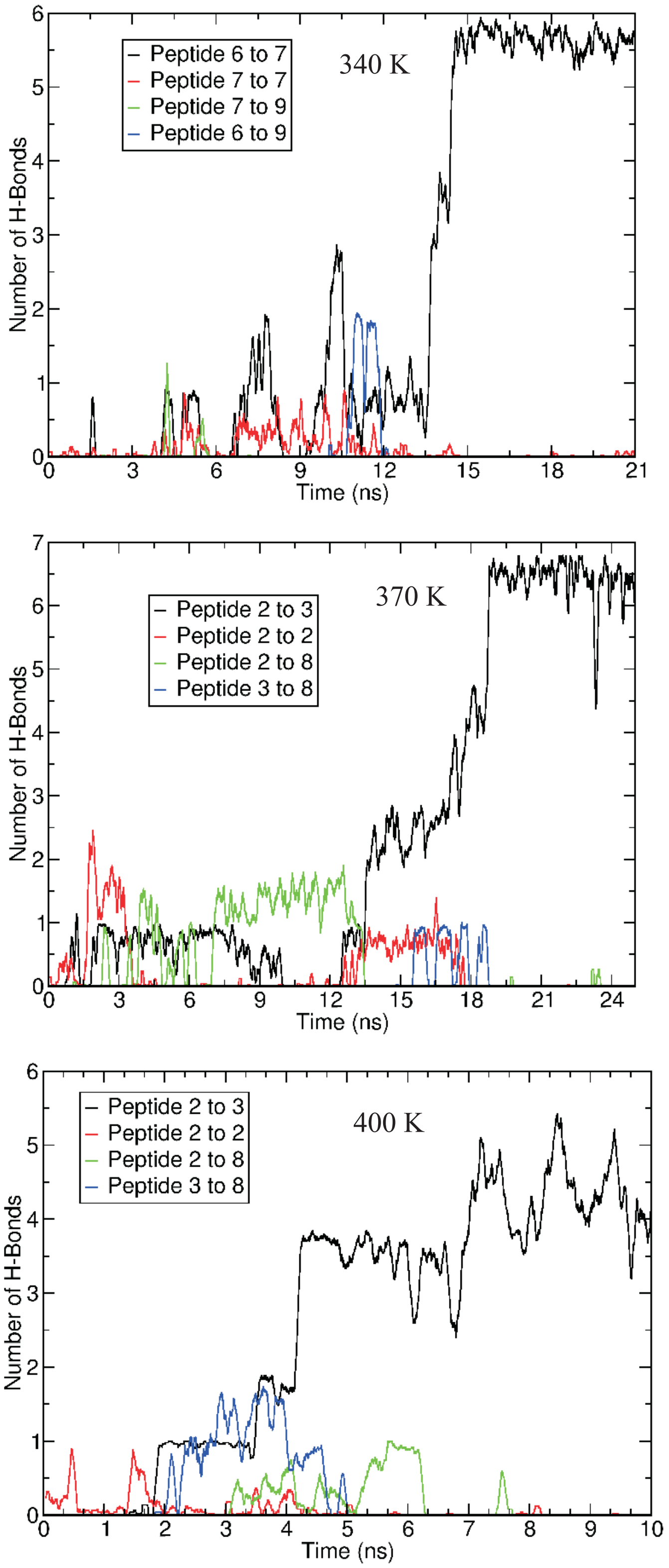

Figure 7.4: *Docking of peptide number 2 and 7 to existing β-sheet with intermediate short lived dimers. Numbers of hydrogen bonds between backbone atoms are taken to characterize the extent of dimer formation. Peptide numbers are as shown in Figure* 7.2

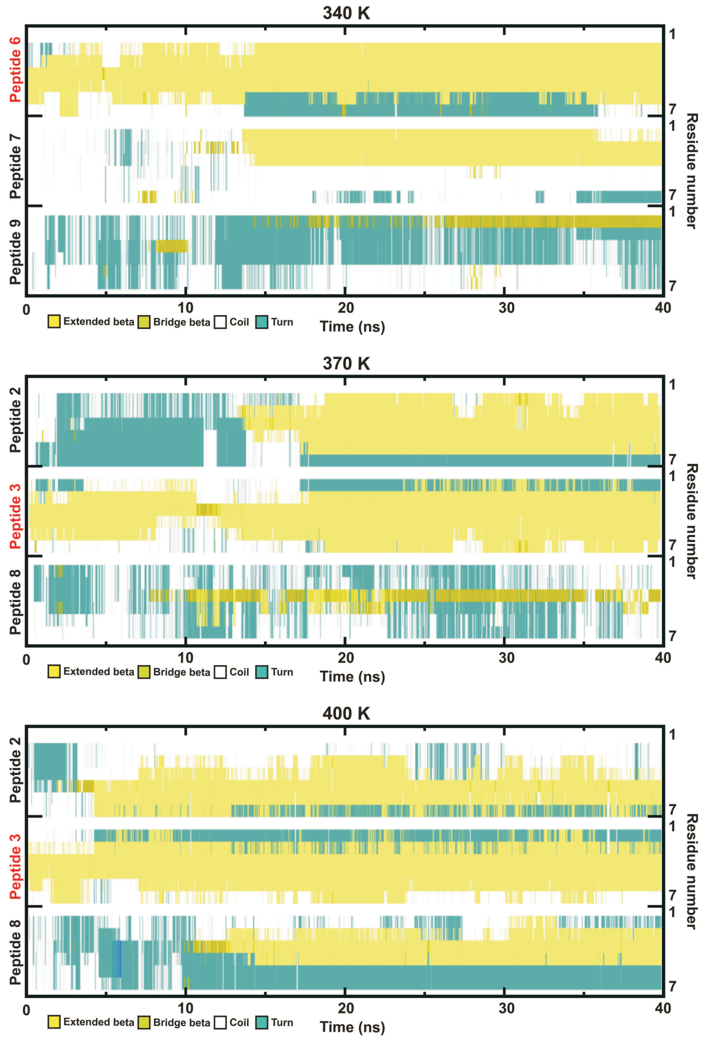

Figure 7.5: *Docking of peptide number 2 and 7 to the existing β-sheet with intermediate short lived dimers. Peptides number 3 and 6 (red numbers) represent the two sides of the ordered tetramer from the 360 K simulation run used in the starting configuration. Peptide numbers are as shown in Figure* 7.4.

all peptide pairs except pairs number 1-2 and 7-8 lie in the range of $cos(\theta) = -0.7$ to -0.9. Peptide pairs 1-2 and 7-8 show larger $cos(\theta)$ values (Figure 7.3a). The intermediate $cos(\theta)$-value of pair 7-8 is due to the fact that these two belong to the two different parallel layers (trimer and hexamer), discussed above. The fact that none of the peptide pairs showed a value of $cos(\theta) < -0.9$ indicates clearly the twist in the β-sheet (Figure 7.1(400 K)).

The distances between all consecutive peptide pairs within the trimer and the hexamer reache minima of less than 0.7 nm(measured between the center of mass) within 10 ns [Figure 7.3(b)]. The apparent bi-modal distribution of the close pair-distances can be explained by the formation of two different categories of antiparallel hydrogen bonded pairs within the β-sheet ('face to face' and 'back to back').

We observe a dominant growth mechanism, where two peptide monomers associate to form intermediate antiparallel dimers that later dissociate to attach to an existing larger ordered peptide aggregate (Figure 7.4). For example, one of the free peptides (peptide number 2 or 7) is ready for docking to the tetramer (peptides number 3 to 6) by initially undergoing a structural transition via intermolecular hydrogen bonds, the formation of intermediate dimers (green and blue lines). The red line (Figure 7.4) indicates the formation of intramolecular hydrogenbonds within the free peptides. The kinetic data presented here support a model of amyloid growth in which the depositing monomeric peptides initially need to undergo conformational changes to facilitate the docking to the tetramer. For this, the free peptides, having collapsed coil structures with intramolecular hydrogen bonds (red lines), form a reversible intermediate dimer structure (green lines) by undergoing certain conformational changes. Finally one of the peptides in the intermediate dimer detaches and docks to the tetramer (black lines) leaving behind a template for facilitating the next deposition. Only after forming a second intermediate pair (blue lines) the number of hydrogen bonds between the docking monomer and the tetramer increased strongly (Figure 7.4). At all temperatures- 340, 370, and 400 K- the formation of a intermediate dimer precedes the association of one of the monomers from the intermediate dimer with the tetramer by a growth process, as shown in Figure 7.4. While our results establish the reversibility of early dimer formation between the free peptides, they are likely to act as a critical factor in the fibril growth. We observed similar pathways during the tetramer and hexamer formation and growth processes. However,essentially the tetramer nuclei formation is the first step, followed by elongation via dimer formation in this pathway.

Figure 7.5 represents the time dependence of the secondary structure conformation of the docking monomer, which has been characterized before by the formation of hydrogen bonds with the existing tetramer. Shortly after the initial equilibration peptides 7 and 2 adapted random coil and turn conformations, which are dominant in the 340 and 370 K trajectories. Subsequently, a dramatic increase in the β-strand content (Figures 7.5) is observed, in line with the observed fibril growth. At 400 K, peptide 2 changes the secondary structure after intermediate dimer formation much faster than at the other temperatures (Figure 7.5c). These secondary structure changes accompanying the peptide extension, give a preliminary view of the oligomer elongation mechanism. The formation of hydrogen bonds with the existing tetramer is connected with a conformational change of the monomers, which then facilitates the docking to existing β-sheet structures.

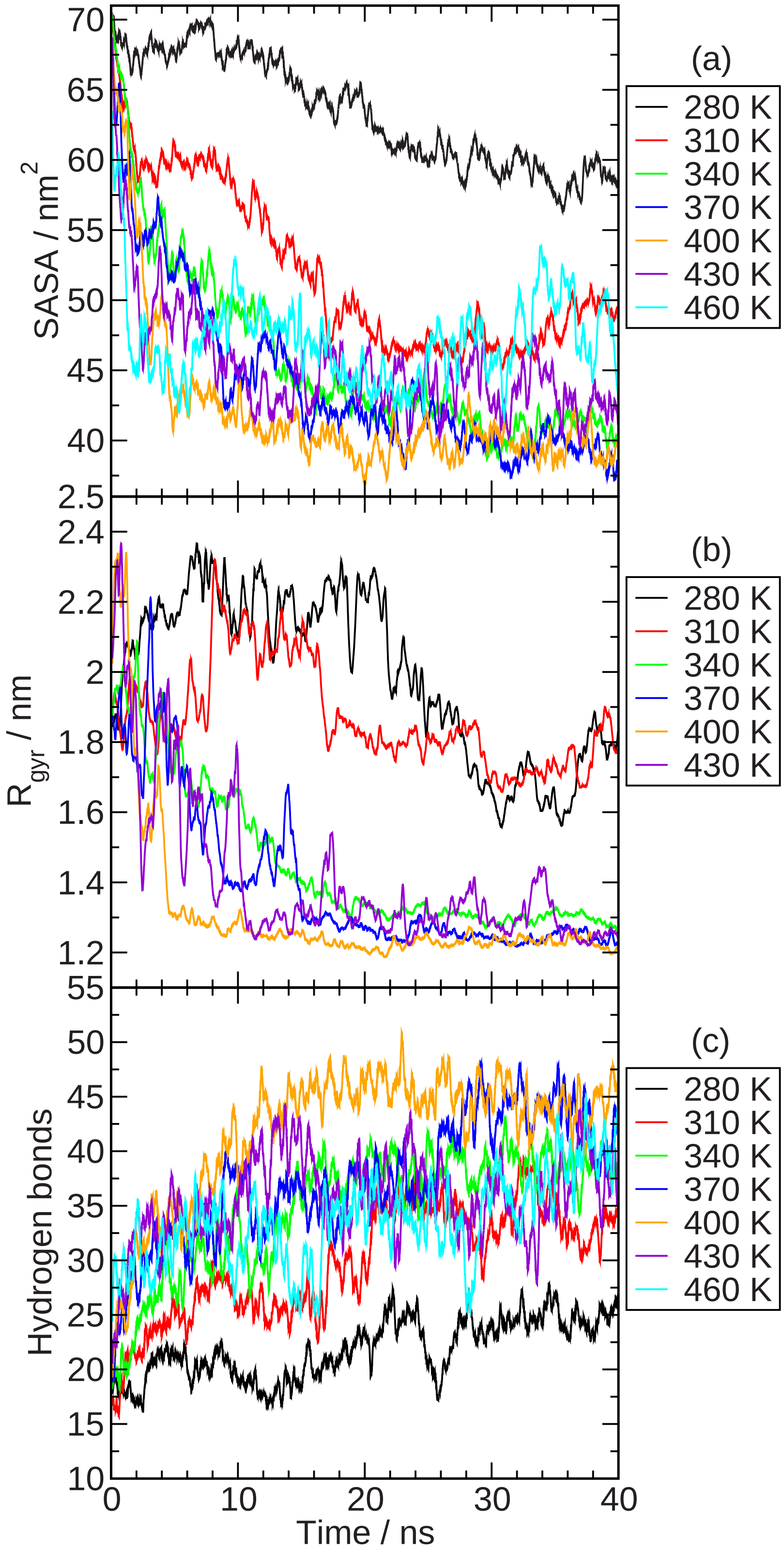

Figure 7.6: *Properties of the peptide cluster within 40 ns simulation time at different temperatures, (a) Solvent Accessible Surface area, (b) Radius of gyration R_{gyr}, and (c) Number of hydrogen-bonds calculated over protein atoms with respective time.*

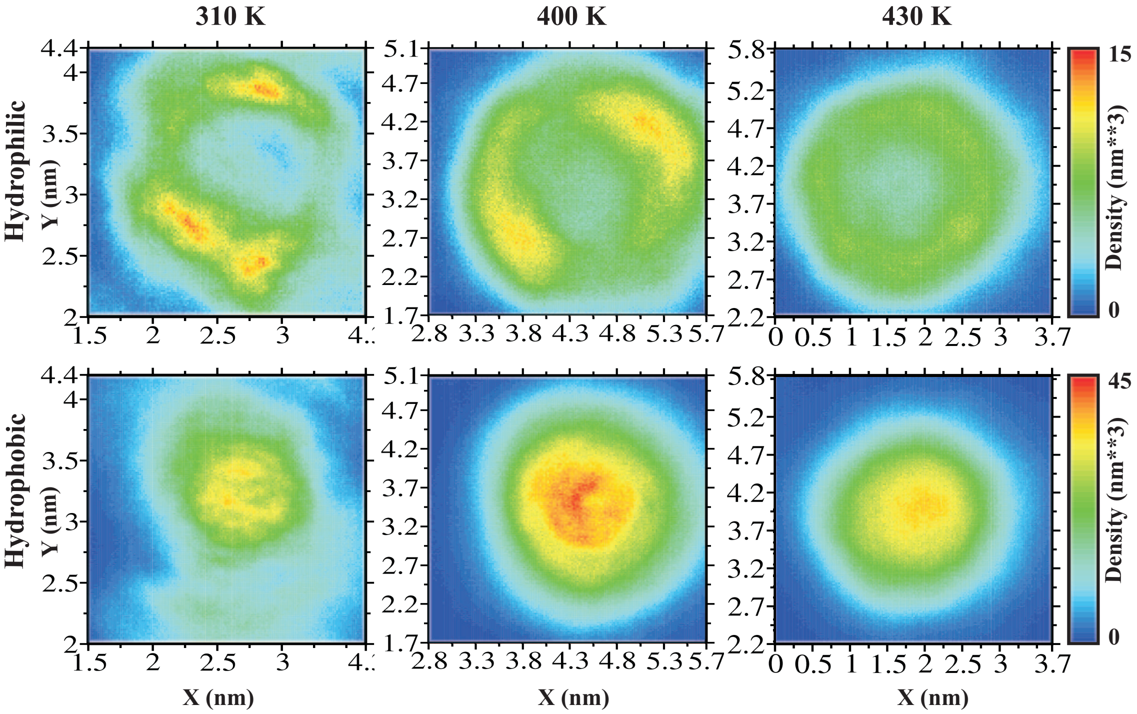

Figure 7.7: *2D Density maps (view from fibril axis) for all atoms of hydrophilic and hydrophobic residues in the simulation trajectories at 40 ns. Hydrophilic residues form a ring around hydrophobic residues at higher temperatures.*

Some other properties of the peptide cluster, the solvent accessible surface area (SASA), radius of gyration (R_{gyr}) and the average number of hydrogen bonds were calculated from the peptide backbone atoms, as a function of time at different temperatures. The R_{gyr} decreases with increasing temperature, leading to a R_{gyr} minimum at 400 K after which it increases at higher temperature (Figure 7.6a). Subsequently, SASA also shows a minimum close to 400 K (Figure 7.6(b)). The total number of peptide-peptide hydrogen bonds increases with temperature, passes through a maximum at 400 K and starts to reduce a higher temperatures (Figure7.6c).

Soreghan et al. described the essentiality of amphiphilic properties for Aβ peptides [176]. Our data also demonstrate that amphiphilicity is a significant factor in determining the organization of β-sheets in amyloid fibrils elongation. In Figure 7.7 the density distribution of the hydrophilic and hydrophobic residues (upper and lower row respectively) of the Aβ_7 peptide cluster is shown. The distributions are averaged over the whole 40 ns simulation runs. With increasing temperature, the increasing rotational dynamics of the aggregates is reflected by increasing rotational averaging (Figure 7.7). At lower temperature (at 310 K) the hydrophilic residues of the Aβ_7 peptides show maximum mass-density. With increase in temperature to 400 K, the hydrophobic residues mass-density in the interior increases while that of the

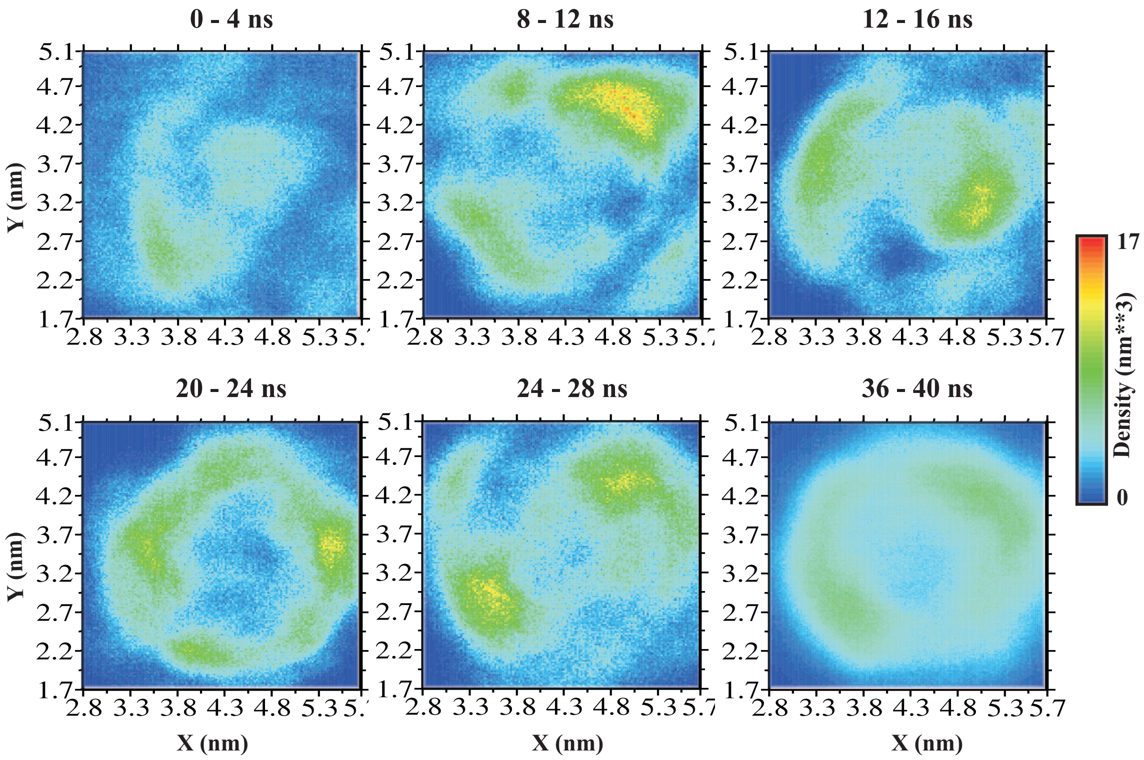

Figure 7.8: 2D Density maps (view from fibril axis) for all atoms of hydrophilic residue in the simulation trajectories in 40 *ns at* 400 *K.*

hydrophilic residues at the outside decreased (Figure 7.7). In Figure 7.8 the density distribution of the hydrophilic residues of the Aβ_7 peptide cluster at 400 K is shown. The distributions are averaged over 4 ns time sections of the simulation runs. At 400 K and higher temperatures, the density distributions reflect the increasing rotational dynamics of the aggregate (Figures 7.7). Thus, different measures show that the Aβ_7 peptides adopt an antiparallel organization due to electrostatic interaction and shield the hydrophobic residues from aqueous solvents (Figure 7.1).

While the center of our pleated β-sheet structure is hydrophobic, the ends of the sheets are hydrophilic. Electrostatic interactions and/or hydrogen bond interactions have been proposed as additional forces stabilizing the cross-β structure [177]. Consistent with the above suggestions, the fully solvated and equilibrated untwisted pleated β-sheet model shows that several polar side chains are involved in intersheet electrostatic interactions. For instance, the side chain of K16 from one monomer interacts with that of E22 from the neighboring monomer in the same layer. The side chains of these residues pack so as to optimize space filling interactions between the monomers. The side chains are in contact with those in the neighboring layer, so that a hydrophobic core is formed along the center of the pleated β-sheet. Moreover, while the center of the hydrophobic core was totally buried, the edges were solvent exposed (Figure 7.7). Hence, the hydrophobicity plays an important role in amyloid fibril formation. The buried hydrophobic core is critical in organizing the Aβ_7 aggregation and the fibril elongation. Interestingly, the twist between two neighboring monomers at lower temperatures is not necessary, because there are free monomers to protect the hydrophobic core and electrostatic interaction has taken a major role. Whereas the buried hydrophobic core could be critical in the formation of protofilaments, the exposed fraction (Figure 7.7) could play an important role in assembling the protofilaments into fibrils in a later stage. In our simulations, Aβ_7 monomers first formed antiparallel dimers at lower temperatures (from 280 to 340 K) and started elongation to ordered fibrils from 340 to 400 K. At higher temperatures (from 400 to 460 K) the twist angle between the monomers increased to protect the hydrophobic residues from water.

7.2 Conclusions

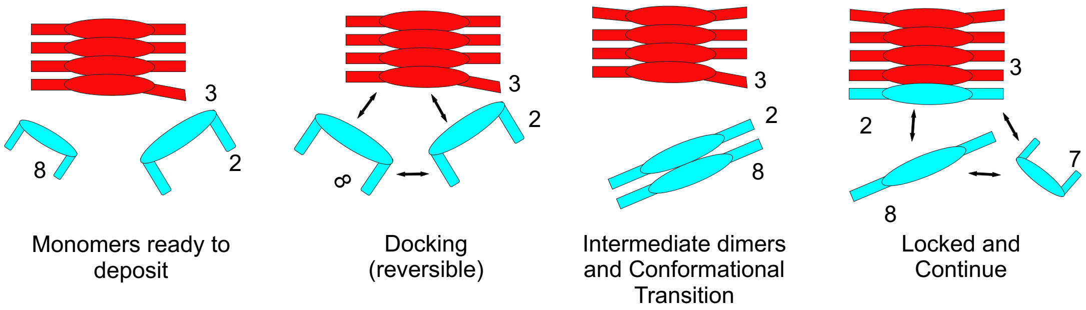
3
8
2
Monomers ready to deposit
3
2
8
Docking (reversible)
3
2
8
Intermediate dimers and Conformational Transition
3
2
7
8
Locked and Continue

Figure 7.9: *Schematic representation for docking to existing β-sheet with intermediate dimers.*

We studied a minimal oligomer size as an amyloid aggregate seed and the mechanism of seed growth with an Aβ_7 peptide model. We found that the initial Aβ_7 peptides are unstructured, which then self-assemble into aggregated structures, depending on temperature. After tetramer formation six additional free peptides were added to the fibril to deduce the monomer interaction pathways. The dominant pathway is the association of two peptide monomers to form antiparallel dimers that later disaggregate to attach one of the peptides to the existing larger ordered peptide aggregates (Figure 7.9). Thus, the formation of intermediate dimers helps to form stable association of one of the monomers from the intermediate dimer, with the tetramer by a growth process at all temperatues- 340, 370, and 400 K- as shown in Figure 7.4. While our results establish the reversibility of early dimer formation between the free peptides, they are likely to act as a critical factor in the fibril growth (Figure 7.9 gives a schematic representation).

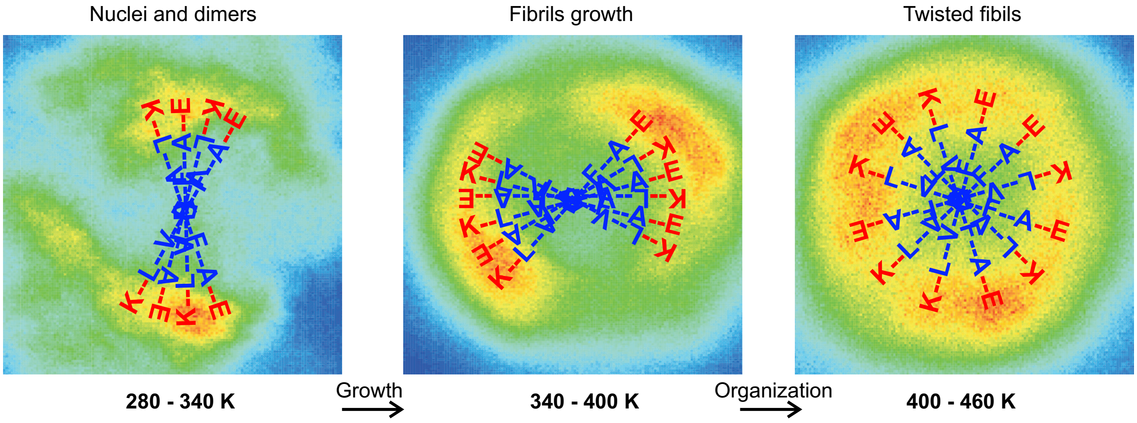

Figure 7.10: *Schematic representation for the temperature dependent elongation and reorganization of the Aβ_7 peptides. The polar residues(in red color) formed the outer wall of the fibril indicated by 2D-density map. The hydrophobic residues (in blue color) filled the inner part of the fibrils.*

The growth of the peptide aggregate is initiated by apolar - apolar atom contacts, which follow reduction of the water molecules in the primary solvation shell of the peptides and electrostatics interactions. This demonstrates that amphiphilicity is critical in determining the structural organization of β-sheets in the amyloid fibril (Figure 7.10). The twisted nature of the amyloid fibrils is likely the result of stabilizing packing interactions of the protofilaments at higher temperatures. Initially at lower temperatures polar interactions play a major role to increase the peptide density with increasing temperature. Subsequently, the fibril growth was correlated with the increasing number of peptide - peptide hydrogen bonds, which is another driving force of β-sheet elongation. Hydrophobic residues can play a role in either a parallel or an antiparallel structure. The antiparallel structure may then be favored by electrostatic interactions between the C- and N-termini of neighboring molecules in a β-sheet. The present findings indicate that the temperature dependence of fibril elongation rates can provide valuable insights into the process of monomer addition at the growing fibril tip. Addition of peptides to an existing small oligomer notably improves the order of the aggregate in which labile outer layer β-sheets were stabilized, which provides good templates for further elongation.

Chapter 8

Fibril growth in Aβ_{7g} peptide system

To study further the driving force of the Aβ_{16-22}(Aβ_7) fibrils elongation process, specific single point mutation which determine association forces and aggregation rates can be implemented. The results from the Aβ_7 fibril growth study at seven different temperatures show that the free monomers initially form anti-parallel hydrogen-bonded dimers in the lower temperature range of 280–340 K. At mid temperature range from 340 to 400 K, these dimers aggregate, to form larger structures that resemble the amyloid fibrils: twisted β-sheets formed from antiparallely oriented peptides and initiation of a self assembled second layer. The β-sheets of the two layers adopt an antiparallel peptide organization by electrostatic effects and shield hydrophobic residues from the aqueous solvent.

8.1 Model System

In the fibril formation study of chapter 6, an antiparallel arrangement of β-sheets has been confirmed in all systems. We observed the distinct roles of the hydrophobic interactions, which provide the driving force for the initial collapse, and of the electrostatic interactions, which result in the formation and stabilization of antiparallel β-sheets. Thus, we conclude that the ordered antiparallel orientation is only obtained upon the formation of salt bridges between K16 - E22. The role of electrostatic interactions (EI), in particular the salt bridge formation between negatively charged E22 and positively charged K16, was hypothesized to be important at early

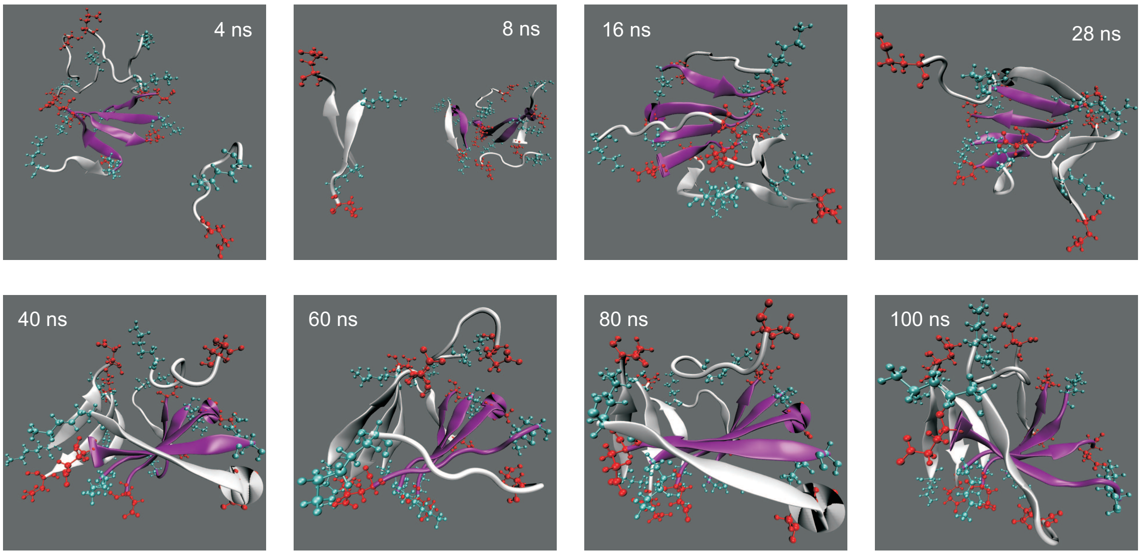

Figure 8.1: *Snapshots of the simulation trajectories for the six free Aβ_7 peptides system around a Aβ_7 tetramer at 400 K in 100 ns simulation time. K(+) shown in cyan and E(-) in red.*

stages of folding as well as at later stages of fibril formation. To probe the effects of electrostatic interactions in the aggregation process, a model system of small peptides like Aβ_7 with Arctic E22G mutation (Aβ_{7g}) is well suited. The dramatic effect of the Arctic mutation on aggregation could be a result of the loss of saltbrige (between K and E), resulting from the substitution of the negatively charged glutamic acid (E) for a neutral glycine (G) at position 22. Thus, it is reasonable to expect that EI may play an important role at intermediate stages of oligomer formation. Henceforth, we study the structural changes occurring during the aggregation due to Arctic mutation, thereby understanding the structural changes that are contributing to the formation of lager oligomers of Aβ_7.

In the starting configuration of this study, six monomeric Aβ_7 and/or Aβ_{7g} peptides were placed uniformly (in antiparallel orientation) at a distance of about 1.45 nm around the center of an ordered tetramer of Aβ_7 maintaining 2.9 nm distance between every two free peptides. The tetramer, that served as a nucleus for further growth, was obtained in an initial constant pressure simulation of four peptides at 360 K after 20 ns. All the 10 peptides where immersed in 5900 SPC/E water molecules in a $5.8 \times 5.8 \times 5.8\ \mathrm{nm}^3$ cubic box and periodic boundary conditions were applied (chapter 6). In total we performed three sets of Aβ_{7g} simulation studies in aqueous solution having different free Aβ_{7g} peptides; set1 - wildtype, having six free Aβ_7 peptides, set2 - hetero system, having three each of free Aβ_7 and Aβ_{7g} peptides, set3 - mutant system, having six free Aβ_{7g} peptides. For all the systems we maintained the same nuclei of four Aβ_7. To maintain the neutrallity of the system we replace

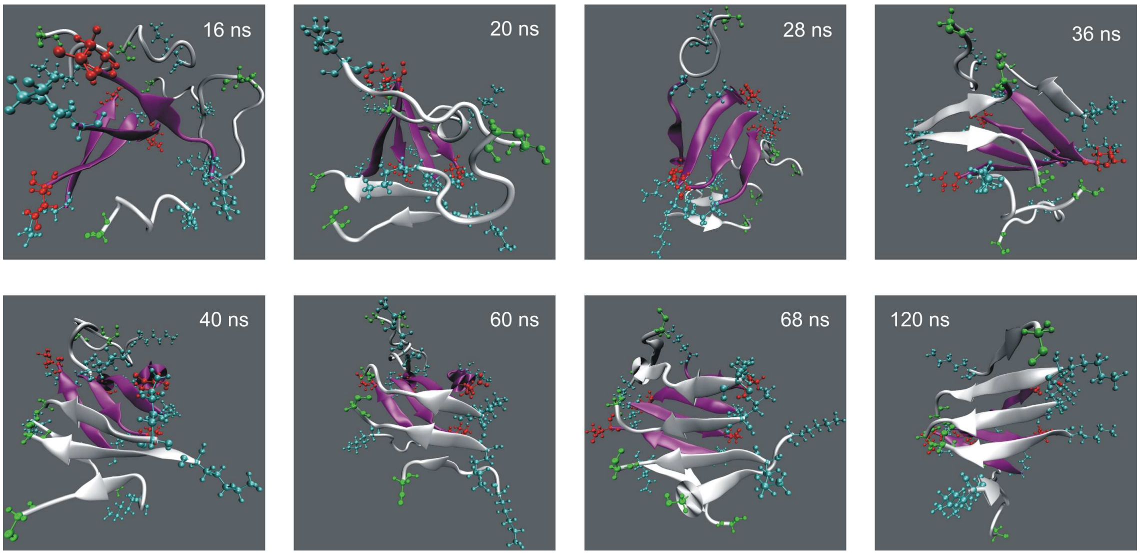

Figure 8.2: *Snapshots of the simulation trajectories for the six free Aβ_{7g} peptides around the Aβ_7 tetramer at 400 K in 100 ns simulation time. K(+) shown in cyan, E(-) in red and G(mutant) in green.*

water molecules with equivalent number of Cl^- ions, corresponding to the number of free Aβ_{7g} peptides.

8.2 Results

The wildtype system predominantly adopted a secondary structure within 40 ns, simulated at 400 K (Chapter 6). In contrast, the mutant system took more than 100 ns to attain the secondary structure. Therefore, for comparative study, we also simulated the wildtype system upto 100 ns at 400 K temperature. In this simulation study we observed that the wildtype system took 8 ns to form the first dimers, while 20 ns was taken by the mutant system (Figures 8.1, 8.2), indicating that the EI between charged molecules is strongly supporting the hydrophobic interactions. The wildtype system attained antiparallel orientation for both layers within 20 ns (Figure 8.1). In the mutant system, the first layer was the nucleus with antiparallel orientation while the second layer formed a parallel β-sheet (Figure 8.2). Interestingly, the wildtype system showed in the first layer a more significant twist than the mutant system (Figure 8.2). In the heterogeneous system, we clearly observed that two free Aβ_7 peptides first formed a antiparallel β-sheet. The remaining one free Aβ_7 peptide formed a parallel β-sheet dimer with one free Aβ_{7g} peptide while two free Aβ_{7g} peptides remained isolated (Figure 8.3).

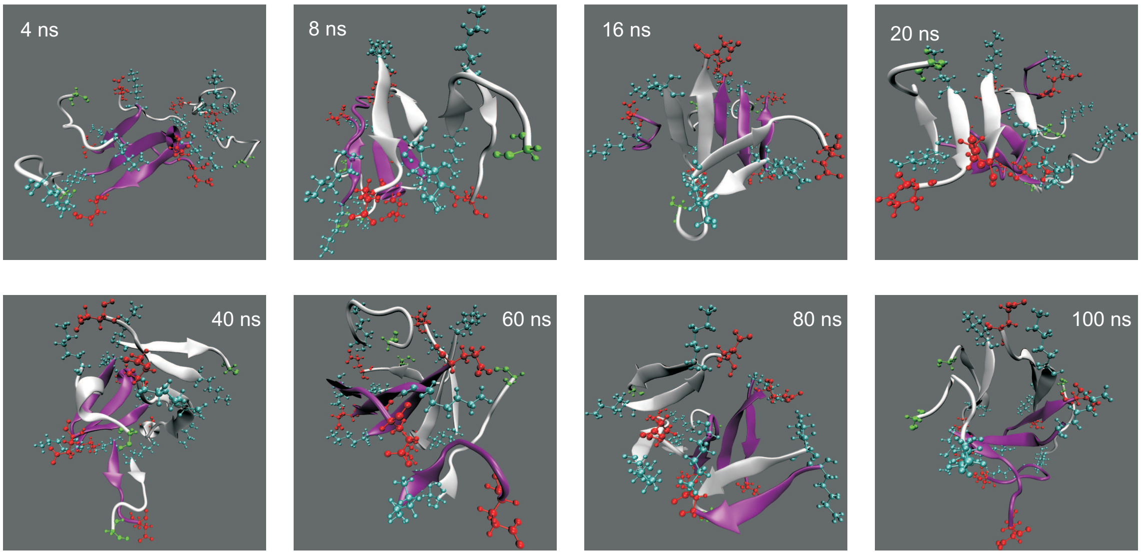

Figure 8.3: *Snapshots of the simulation trajectories for the three free Aβ_7 and three free Aβ_{7g} peptides (heterogeneous) system at 400 K in 100 ns simulation time. K(+) shown in cyan, E(-) in red and G(mutant) in green.*

The formation of two β-sheet structures with either antiparallel or parallel orientations of the peptides is illustrated in more detail in Figure 8.4. Figure 8.4 depicts the time dependence on the angle, which characterizes the mutual orientation of consecutive neighboring peptide pairs going along the matrix diagonal in Figure 8.5. The vector, which gives the orientation of the peptides, point from central carbon atom (C_α) of residue L17 to the C_α of residue A21. Though the simulations were performed for 100 ns, the last 20 ns were used for calculating angle between the neighboring peptides. Figure 8.4*a* shows that only two peptide pairs (peptide number 5-6 and 9-10) do not form antiparallel β-sheet as the valuey, the fellow falls below $\theta = 150° \pm 10°$ within the time of simulation. Note that in Figure 8.4*a* values of $\theta > 140°$ point out that the antiprallel β-sheet is more favorable in the wildtype system (also seen in Figure 8.1). Figure 8.4*b* shows that three free Aβ_{7g} peptides (number 7, 8 and 9) where forming a parallel β-sheet with a value of $\theta = 20° \pm 10°$. Two free peptides (peptide number 1 with 2 and 9 with 10), which were close to the tetrad nucleus, are attached in an antiparallel β-sheet orientation due to electrostatic interactions in the mutant system. Figure 8.4*c* representing the heterogeneous system, shows that three free Aβ_7 peptides (peptide number 6, 7 and 8) with one free Aβ_{7g} peptide (peptide number 9) where forming an antiparallel β-sheet having a value of $\theta = 140° \pm 10°$ due to electrostatic interactions. The remain two free Aβ_{7g} peptides (peptide number 1 and 10) stay isolated. In summary, the following structures have developed after 100 ns simulation time in the systems (this is also supported by the following discussions). In the wildtype system, two antiparallel β-sheets of 5 (peptides 1 to 5) and 4 (peptides 6 to 9) are formed, which have a

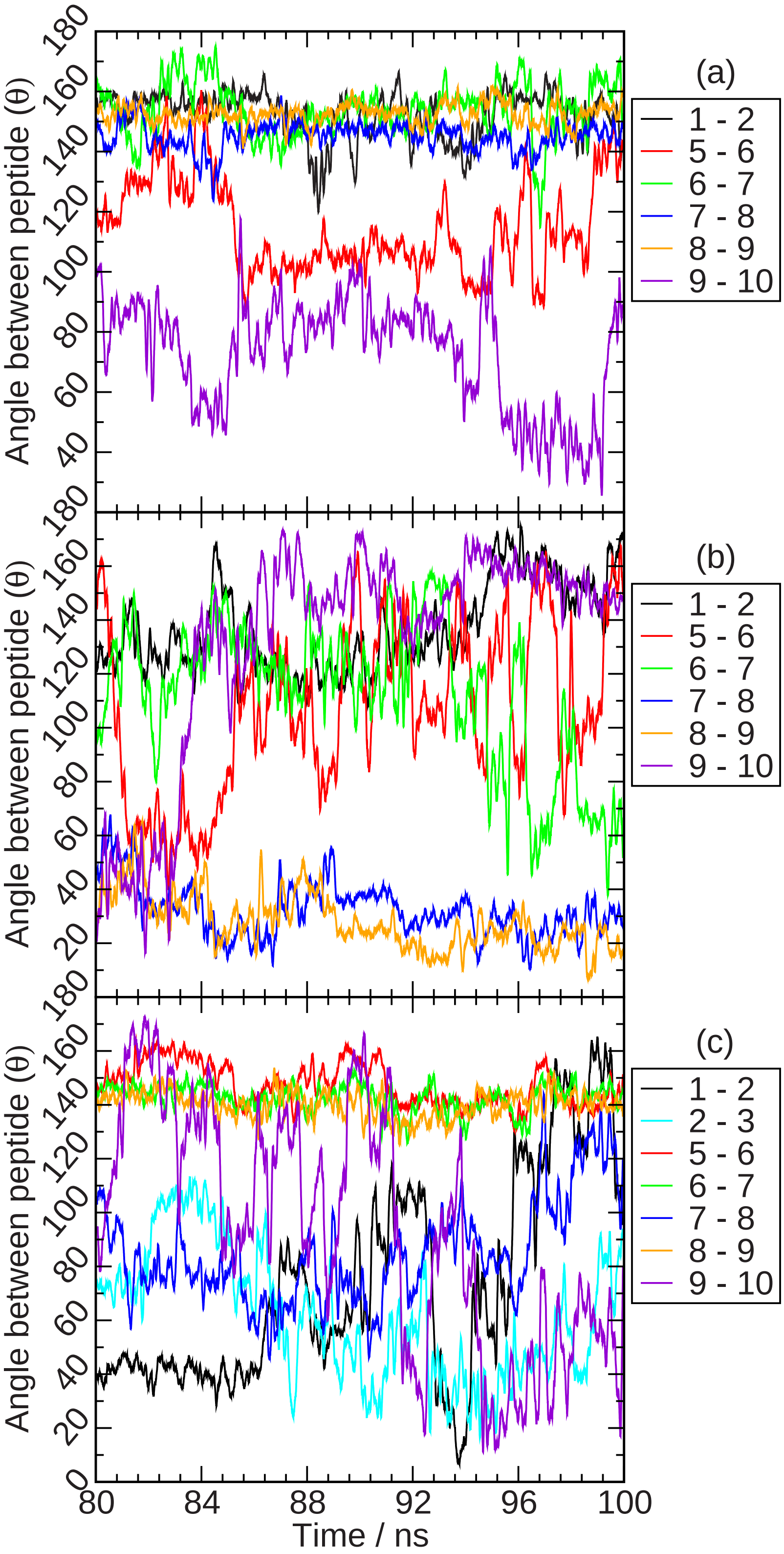

Figure 8.4: *Angle between neighbouring peptides calculated in last 20 ns simulation time at 400 K during the 100 ns simulation time, (a) Wlidtype system, (b) Mutant system and (c) Heterogeneous system. Peptide numbers are as in Figure 8.5.*

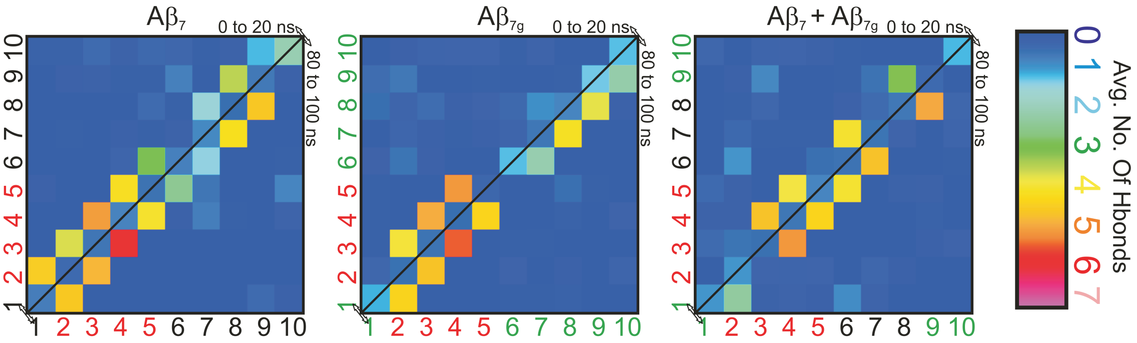

Figure 8.5: *Hydrogen-bond map with average number of hydrogen bonds between the peptides; upper half of the matrix averaged over first* 20 ns *simulation time, lower matrix averaged over last* 20 ns *of the 100 ns simulation trajectories. Peptides number 2 to 5 (red numbers) represent the ordered tetramer from the* 360 K *simulation run used in the starting configuration (see text). Free Aβ_7 and Aβ_{7g} peptide numbers are shown in black and green respectively.*

close sheet - 4 - sheet contact. When adding 6 Aβ_{7g} mutant peptides to the original tetramer of Aβ_7, the original antiparallel tetramer is extended by one antiparallely attached mutant peptide, additionally a tetramer of thru parallel at an antiparallely attached mutant peptide is formed. In the mixed system the original antiparall tetramer is extended by two wildtype peptides. Additionally a wildtype and a mutant peptide form an antiparallel dimer.

The interaction matrix represents the average number of hydrogen-bonds between the different peptides (Figure 8.5). To get a clear picture of the final aggregates the numbering of the peptides has been chosen such that neighboring peptides have consecutive numbers. The numbers given in red indicate the original tetramer nuclei (see Figure 8.5). The upper half of the matrix shows that the wildtype system formed proto-fibrils of two layers within 20 ns and remained stable even when the simulation time was extended to 100 ns (Figure 8.5a). In the mutant system only one parallel dimer formed in 20 ns additionally to the original tetramer and extended to two layers of β-sheets when simulated for 100 ns (Figure 8.5b). In the heterogeneous system the first two dimers were formed within 20 ns via strong hydrogenbond interactions (Figure 8.5c) and the original nucleus was strongly disturbed. While the other two Aβ_{7g} form a parallel β-sheet in 100 ns (see also Figure 8.3). These findings suggest that the electrostatic interactions have a major role in the initial Aβ_7 peptide aggregation. The absence of negatively charged residues at the C-terminus in the mutant or heterogeneous system leads to longer simulation times, with hydrophobic interactions as major driving force for aggregation.

The dynamics of the secondary structure at 400 K of the three systems at the resid-

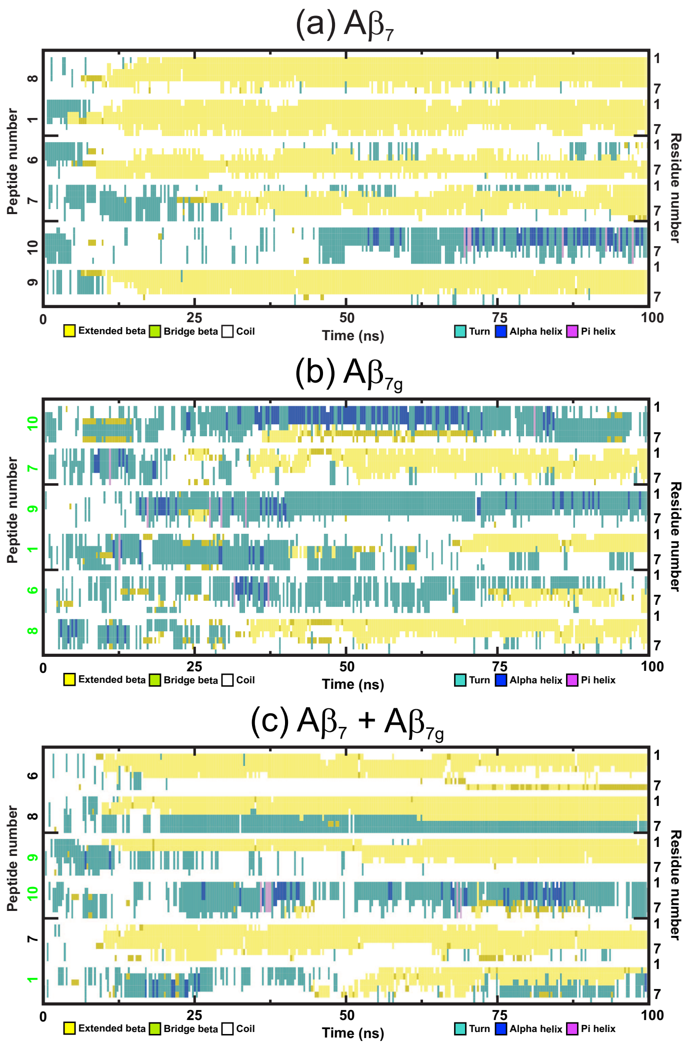

Figure 8.6: *Dynamics of secondary structure at 400 K of the added free peptides in the three systems at the residue level (same trajectory as in Figures 8.1-8.3). The secondary structure is assigned according to the values of dihedral angles ϕ and ψ. β-strand, α-helix, and RC conformations are represented in yellow, blue, and white, respectively. Free Aβ_7 peptides are fast converting into a β-strands (see text for details). Peptide numbers are as shown in Figure* 8.5.

ual level are represented in Figure 8.6. The secondary structure changes, which accompany the extension of the nucleus, gives a first view, recording the elongation mechanism of the oligomers. Shortly after initial equilibration the wildtype system adapted random coil (RC) and turn conformations (Figure 8.6a). Subsequently, a dramatic increase in the β-strand content is observed, indicating fibril growth. One free Aβ_7 peptide (number 10) forms some α-helical conformation to protect the hydrophobic core from water (shown in Figure 8.6a). Comparatively, in the mutant system, the free Aβ_{7g} peptides adopted a rather encomplete β-strand structure (Figure 8.6b). In the heterogeneous system, the three free Aβ_7 peptides (peptide

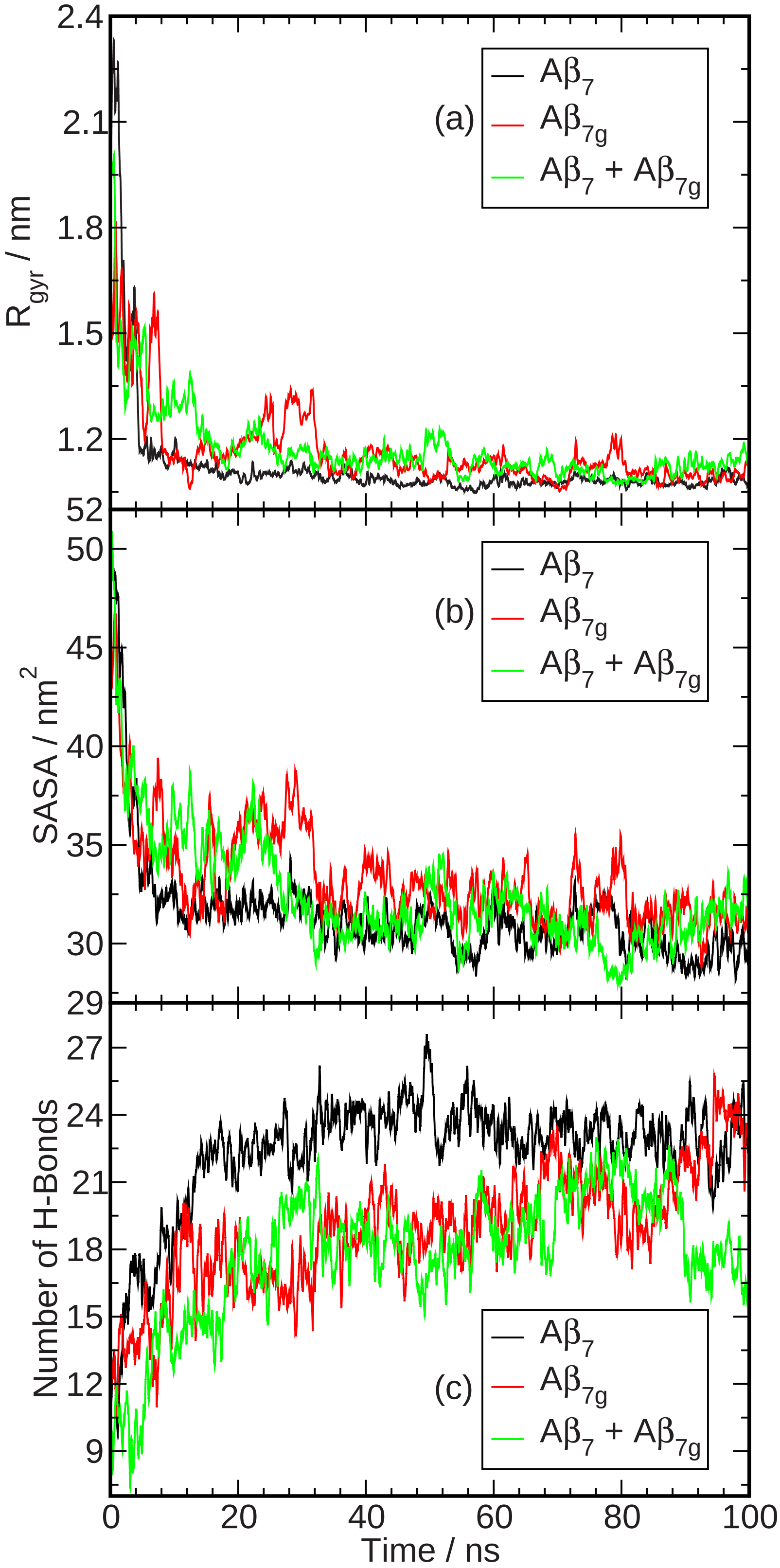

Figure 8.7: *Time dependence properties of the peptide aggregates, calculated over CHC at 400 K (a) Radius of gyration R_{gyr}, (b) Solvent accessible surface area and (c) Number of hydrogen bonds.*

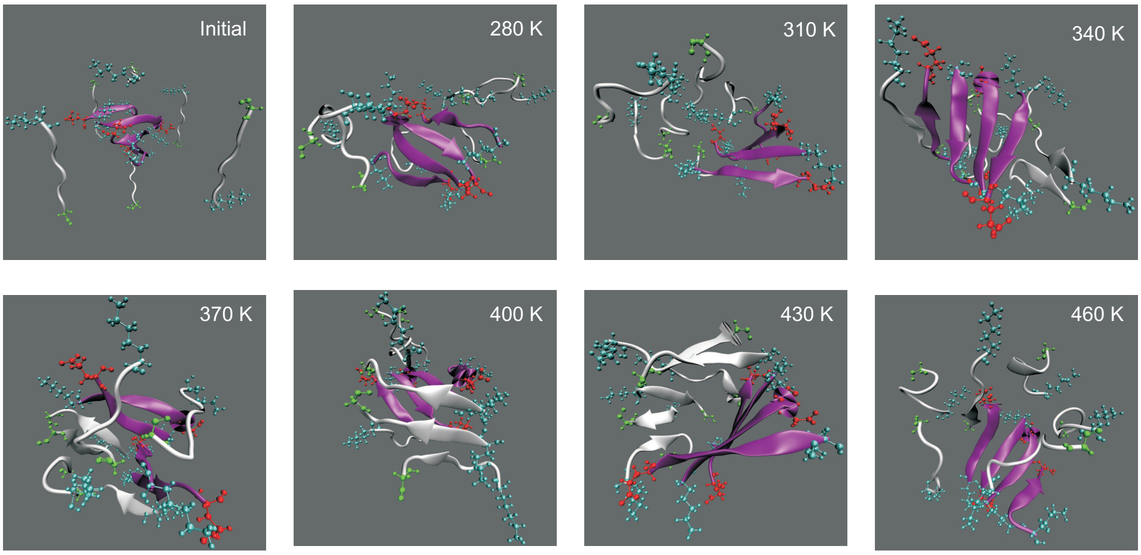

Figure 8.8: *The final snapshots of the simulation trajectories of the system with six added mutation peptides at 1 atm after* 60 *ns at different temperatures from 280 to* 460 *K. The initial ordered peptide tetramer is in purple. Additional peptides (in white) were placed around* 1.45 *nm away from the center of mass of the initial ordered peptide aggregate. K(+) shown in cyan, E(-) in red and G(mutant) in green.*

number 6, 7, and 8) are having more β-strand content than the three free Aβ_{7g} peptides (peptide number 1, 9, and 10) as shown in Figure 8.6c. The formation of β-sheets with the existing tetramer is connected with a conformational change of the monomers, which then facilitates the docking to the existing β-sheet structures. The free Aβ_7 peptide docked faster than the free Aβ_{7g} peptides (Figure 8.6).

Some other properties of the peptide aggregation, solvent accessible surface area (SASA), radius of gyration (R$_{gyr}$) and average number of hydrogenbonds were calculated over the central hydrophobic core (CHC) atoms at 400 K. The CHC is represented by the L17 to A21 residues in the Aβ_7 and Aβ_{7g} peptides. In the wildtype system SASA decreased strongly within 10 ns (Figure 8.7a). In the mutant and heterogeneous systems CHC atoms are not well protected and so SAS was comparatively higher (Figure 8.7a). Consequently, the R$_{gyr}$ calculated from the CHC region show a simulation time dependence as SASA (Figure 8.7b). The wildtype system rapidly formed a high number of hydrogen bonds in comparision to the mutant system (Figure 8.7c). Thus it confirms that the EI have an important role for the initial Aβ_7 peptide aggregation.

In the mutant and heterogeneous systems we observed the formation of β-sheets in the 400 K simulations, but at other temperatures such systems are forming mostly disordered aggregation structures. Figures 8.8 and 8.9 illustrate the final config-

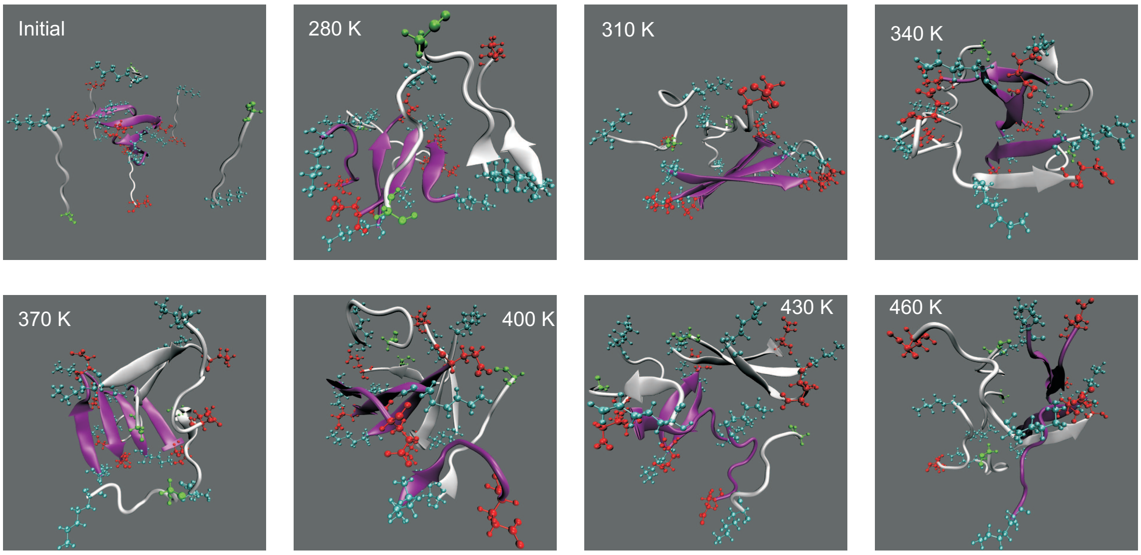

Figure 8.9: *The final snapshots of the heterogeneous system simulation trajectories after 60 ns at 1 atm at different temperatures from 280 to 460 K. The initial ordered peptide tetramer is in purple. Additional peptides (in white) were placed around 1.45 nm away from the center of mass of the initial ordered peptide aggregate. K(+) shown in cyan, E(-) in red and G(mutant) in green.*

urations of mutant and heterogeneous systems respectively. Every snapshot was attained after 60 ns at the respective temperature. In the mutation system, the final configurations at all temperatures except 400 and 430 K show disordered, droplet like aggregates. At 400 and 430 K, the mutant peptides show some ordered structure which are mostly parallel β-sheets (Figure 8.8). For the heterogeneous system, the final configurations are also shown as for the mutant system (Figure 8.9).

Some other temperature depended properties of the peptide aggregation, the solvent accessible surface area (SASA), the radius of gyration (R$_{gyr}$) and the average number of hydrogen bonds were calculated over the central hydrophobic core (CHC) of the peptides. At each temperature these value were averaged over the 60 ns simulation run. The SASA (calculated over the CHC atoms) of the wildtype system strongly decreases from about 62.5 to 44 nm^2 upon heating from 280 to 400 K and started to increase at higher temperatures (Figure 8.10a, black lines). The SASA in the mutant and heterogeneous systems show identical temperature dependence but not as strong as the wildtype system. Interestingly, the mutant and heterogeneous systems show a lower SASA than the wildtype system except at 400 K (Figure 8.10a). The R$_{gyr}$ show a quite similar temperature behavior as SASA (Figure 8.10b). The wildtype system has more hydrogen bonds than any other system (Figure 8.10c). Thus it confirms that the CHC atoms in the mutant and heterogeneous systems form disordered aggregated structures with low SASA, like droplets. In the wildtype system most

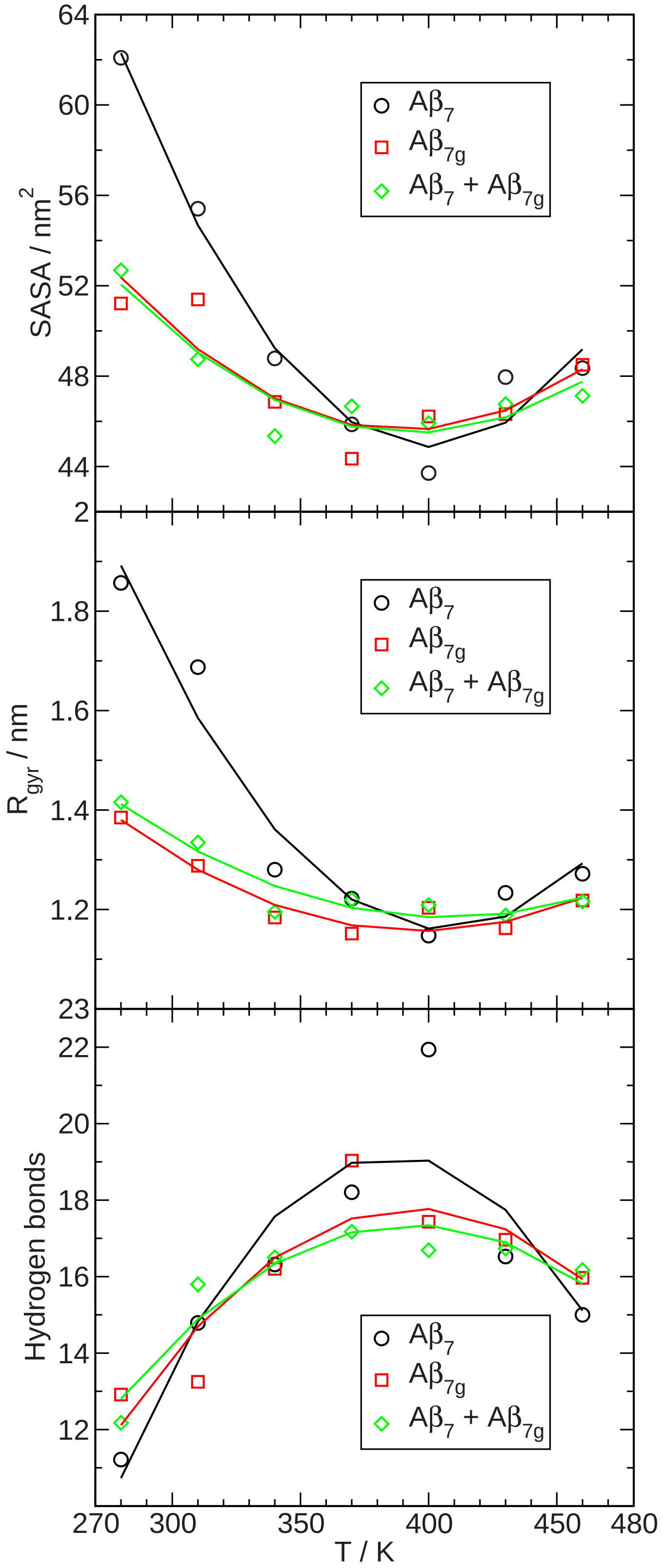

Figure 8.10: *Temperature dependent properties of aggregated systems are calculated over the CHC atoms and averaged over 60 ns time, (a) Solvent accessible surface area, (b) Radius of gyration R_{gyr}, and (c) Number of hydrogen-bonds.*

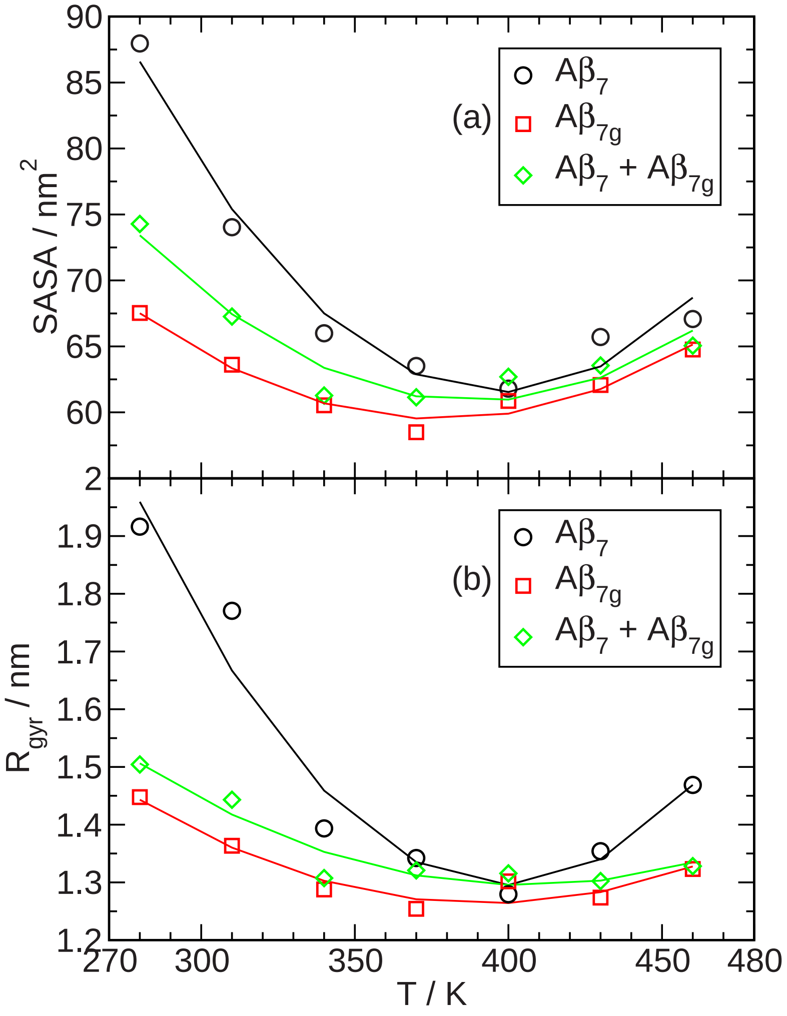

Figure 8.11: *Temperature dependence properties of the aggregated systems, calculated over all peptide atoms and averaged over 60 ns time, (a) Solvent accessible surface area, (b) Radius of gyration* R_{gyr}.

ordered aggregate structures are formed.

The SASA and R_{gyr} calculated over all peptide atoms are shown in Figure 8.11. In the wildtype system below 400 K the SASA of peptide cluster strongly decreases upon heating and starts to increase with temperature above 400 K (Figure 8.11a, black lines). The mutant system shows the lowest SASA and a fit yields a tuning point at about 370 K (Figure 8.11a, red lines). In the heterogeneous system, the SASA values are in the middle between wildtype and mutation system (Figure 8.11a, green lines). This is not observed when using CHC atoms only. A quite similar temperature behavior shows R_{gyr} (Figure 8.11b). Figure 8.12 characterizes the number of inter and total (inter+intra) hydrogen bonds between peptide cluster. The wildtype system has more inter and total hydrogen bonds than any other system (Figure 8.12). Interestingly, the mutant system shows more inter hydrogen bonds

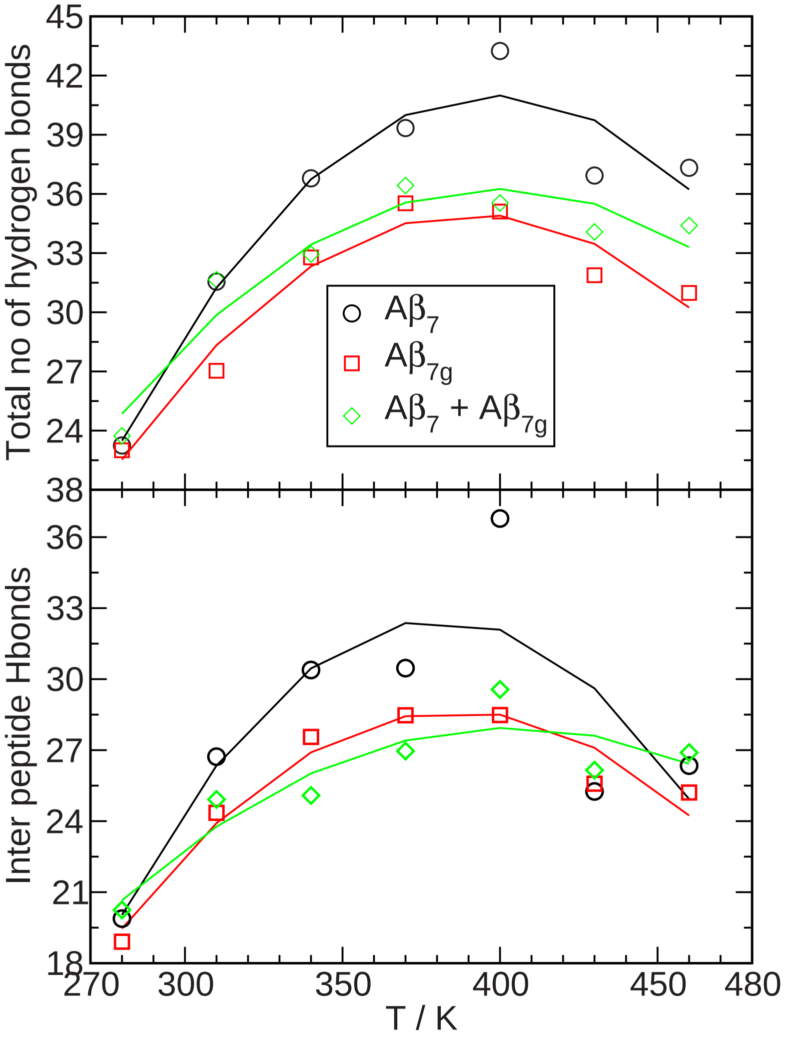

Figure 8.12: Temperature dependence hydrogen bonds of the aggregated systems are calculated over (a) Total number of hydrogen bonds and (b) Inter peptide hydrogen bonds.

than the heterogeneous system (Figure 8.12b). This confirms that the mutant and heterogeneous systems form more disordered like droplet aggregated structures with low SASA. In the wildtype system most ordered aggregate structures are formed. Thus confirms that EI have a major role for an ordered Aβ_7 peptide aggregation. In the mutant system, a negatively charged residue at the C-terminus is lacking which results in the hydrophobic interactions being the major driving force for Aβ_{7g} peptide aggregation. The heterogeneous system also formed disordered aggregates due to the hydrophobic effect, as seen in the mutant system.

8.3 Conclusions

Solid-state NMR studies utilized peptide fragments such as the A$\beta_{34\text{–}42}$ [54] and A$\beta_{16\text{–}22}$ (Aβ_7) [28, 29] containing regions which are important for amyloidosis. In both cases antiparallel β-sheet were the major structural motif. Contrarily, using longer residues, like A$\beta_{10\text{–}35}$ and the native A$\beta_{1\text{–}40}$ peptide attained parallel β-sheet structures were found [73, 72]. Thus the overall structure of the peptide aggregates depends on the Aβ peptide sequence. Nonetheless, the parallel versus antiparallel variation was a puzzle, since the shorter Aβ peptides still form classic amyloid fibrils [27, 74].

Interestingly, Meinke and Hansmann observed in MD simulations without explicit water and charges on residues both parallel and antiparallel conformations for system of six Aβ_7 peptides [117]. This is probably due to the lack of charges in their simulations. Gnanakaran and Garcia reported that Aβ_7 peptides formed antiprallel dimers due to the strong EI between the charged groups only at 275 K. However, at higher temperatures (more than 275 K) they observed parallel dimers. This means that at higher temperatures the EI was overplayed by hydrophobic interactions which leads to a higher twist of the β-sheet [116]. Gordon and coworkers took into consideration that the peptide amphiphilicity influences the parallel versus antiparallel orientation [178]. In agreement with this observation, the Aβ_7 peptide used in this study was nonamphiphilic that led to the formation of antiparallel β-sheets. This was achieved by the electrostatic interactions between oppositely charged side chains and stabilized further by the hydrogenbonds between the backbone atoms. This provides a rationale for the propensity of the amyloid-forming proteins to adopt unique fibril structures, parallel or antiparallel arrangements. We confirmed this hypothesis by simulating Aβ_7 peptide with Arctic mutation peptide (Aβ_{7g}) in aqueous solution. This effects aggregation by the loss of a saltbrige (between K and E) or charge, resulting from the substitution of the negatively charged glutamic acid (E) by a glycine (G) at position 22. The simulation results from Aβ_7 and Aβ_{7g} peptide systems served as model for investigating the role of electrostatic interactions and other factors on β-strand orientation in amyloid fibrils. Our data clearly conclude that the Aβ_7 peptide aggregates organize into micelle-like structures, in which hydrophobic regions are shielded from the aqueous environment at high temperatures.

Antiparallel β-sheets are forming faster than parallel β-sheets, suggesting that such structures inherently contain additional driving forces, provided by the electrostatic interactions, which are absent in Aβ_{7g} peptide system. The new question opens, why and how only Aβ_7 peptide systems have a twist between the peptides in ag-

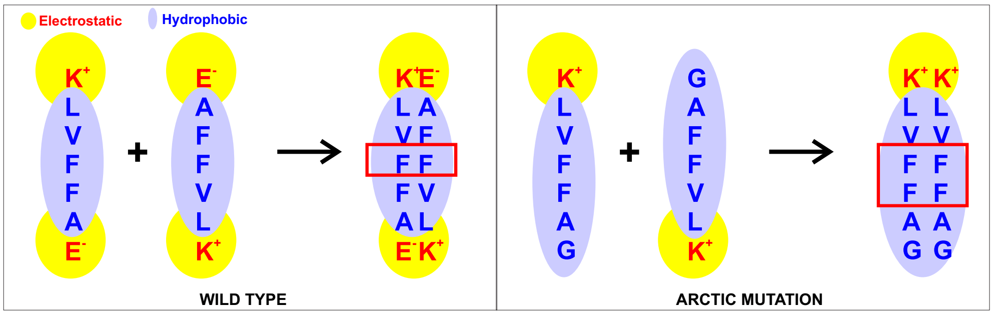

Figure 8.13: *Schematic representation for Aβ_7 (wild type) and Aβ_{7g} (arctic mutation) hydration shells overlap.*

gregation. This could be explained due to the micelle-like structures formed by β-amyloid peptides in which hydrophobic regions are shielded from the aqueous environment [176]. Protofibrillar structures may have this feature in common with micelles, though some micelle-like structures may not be on the pathway toward fibril formation [33]. The formation of β-sheet fibrillar structures may be kinetically controlled, in which case for Aβ_{7g} a parallel structure would be favored because the CHC produces a parallel alignment in a prefibrillar aggregated state of peptide. CHC has two F(Phe) residues, that leads to a strong hydrophobic interaction between the side chains of Phe (Figure 8.12). In such a scenario, the parallel β-sheet would represent a kinetically trapped intermediate, rather than the thermodynamically preferred state. Further, the aggregation of CHC may be sufficient to overcome not only intrinsically greater stability of antiparallel over parallel β-sheets but also unfavorable charge repulsions between K16 residues (Figure 8.12). In contrast, these charge interactions may favor the antiparallel orientation of Aβ_7.

Our results are consistent with a parallel β-sheet organization in Aβ_{7g} fibrils and an antiparallel organization in Aβ_7 fibrils. These data indicate that EIs significantly influence Aβ_7 peptide fibril elongation process and peptide orientation. Other factors, such as hydrophobic interactions and hydrogen bond geometry, may also be critical in the elongation process.

Chapter 9

Temperature dependence of Aβ_7 and Aβ_{7g} peptides aggregations: REMD simulation study

In the fibril elongation study of the wildtype peptide sytem at constant pressure and at seven different temperatures, the six free Aβ_7 monomers form anti-parallel hydrogen-bonded dimers in the lower temperature range of 280–340 K. In the mid temperature range from 340 to 400 K, these dimers aggregates to form larger structures that resemble the amyloid fibrils: twisted β-sheets are formed from antiparallely oriented peptides and the initiation of a self assembled second layer is observed. In the higher temperature range (from 400 to 460 K) the twist angle between the monomers increases, probably to protect the hydrophobic residues from water. The same study, when applied to the mutant system with six free Aβ_{7g} peptides did not show any twist between the peptides and did not show strong temperature dependence. Interestingly the Aβ_{7g} peptide system formed more parallel β-sheets (chapter 8). In order to study the temperature dependence of the aggregation process, Replica Exchange Molecular Dynamics (REMD) is the technique of choice. REMD is an enhanced sampling technique, based on the parallel tempering Monte Carlo method [90], where multiple copies (or replicas) of identical systems are simulated in parallel at different temperatures. Periodically, state exchange moves are attempted, where two neighboring replicas exchange their thermodynamic states (their temperature). The acceptance probability P_{acc} for each state-exchange move between two neighboring states i and j is given by Eq. 4.2. The state-exchange acceptance probability P_{acc} has been shown to obey the detailed balance condition for an extended ensemble of canonical states [86]. This is an efficient way to simulate complex systems at different temperatures and is the simplest and most general form of simulated tempering. It offers a much-improved approach for determining oligomer distributions relevant to aggregation.

Taking the folding work of Paschek and coworkers as a reference [86], we used REMD to study the elongation six additional Aβ_7 peptides (wildtype) respective Arctic mutants (Aβ_{7g}-mutant) at atomic level in explicit aqueous solution. In the starting configuration of this study, the six monomeric Aβ_7 peptides were placed (in a randomly antiparallel mutual orientation) at a distance of about 1.45 nm around the center of the ordered Aβ_7 tetramer (Figure 9.1). The tetramer that served as a nucleus for further growth, was obtained in an initial constant pressure simulation of four peptides at 360 K after 20 ns (see chapter 6). All 10 peptides where immersed in 5900 SPC/E water molecules in a $5.8 \times 5.8 \times 5.8\,\mathrm{nm}^3$ cubic box and periodic boundary conditions were applied (Figure 9.1a). Identical conditions were applied for studying the mutant system: we replaced the six free Aβ_7 peptides by Aβ_{7g} peptides (keeping the Aβ_7 tetramer as nucleus) and charge-balanced the system by replacing six water molecules with equal number of Cl^- ions (Figure 9.1b). Before initiating the REMD simulation, an equilibration was run for about 1 ns at constant pressure without replica exchange.

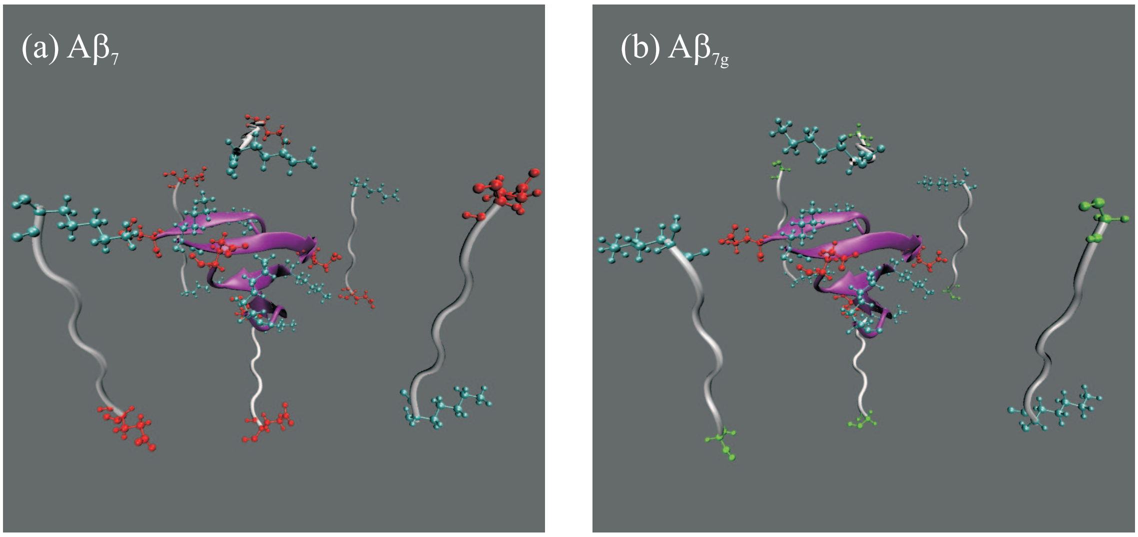

Figure 9.1: *(a) Aβ_7 peptide system (b) Aβ_{7g} peptide system : The initial ordered peptide tetramer is in purple. Additional free peptides (in white) were placed around 1.45 nm away from the center of mass of the initial ordered peptide aggregate as monomer peptides and became part of the peptide aggregate during simulations. Lys(+) shown in cyan, Glu(-) in red and Gly (mutant) in green.*

For REMD, 76 replicas, distributed over a temperature range from 285.0 to 606.3 K were used, in which multiple copies (or replicas) of identical systems were simulated in parallel at different temperatures. The temperature spacing between each of the replicas was chosen such that the energy distributions overlap sufficiently and the REMD-state exchange attempts are (on average) accepted with a 20 % probability. To initially set up the temperature-spacings, energy distributions were obtained from a preceding series of non-coupled short (0.5 ns) constant volume Molecular Dynamic simulations at similar density. The selected temperatures for all the replicas are 285.0, 287.4, 289.8, 292.3, 294.8, 297.3, 299.9, 302.5, 305.1, 307.7, 310.4, 313.1, 315.9, 318.6, 321.5, 324.3, 327.2, 330.2, 333.1, 336.2, 339.2, 342.3, 345.5, 348.7, 351.9, 355.2, 358.5, 361.9, 365.4, 368.8, 372.4, 376.0, 379.6, 383.4, 387.1, 391.0, 394.8, 398.8, 402.8, 406.9, 411.0, 415.3, 419.5, 423.9, 428.3, 432.8, 437.4, 442.0, 446.8, 451.6, 456.5, 461.4, 466.5, 471.6, 476.8, 482.1, 487.5, 492.9, 498.5, 504.1, 509.9, 515.7, 521.6, 527.6, 533.7, 539.8, 546.1, 552.5, 558.9, 565.4, 572.0, 578.7, 585.5, 592.4, 599.3 and 606.3 K.

State exchange attempts were successful with a probability of 0.05, leading to a time of about 1.6 ps for each replica between two state exchanges. The simulations and analysis were carried out with the modified GROMACS 3.2.1 [121] simulation program, to allow state-swapping moves. The OPLS-All Atom force field [125] was chosen to represent the peptide in GROMACS. The system is coupled to an external heat bath (Nose-Hoover-thermostat) with a relaxation time of 1.5 ps. The density is kept constant in the REMD sequence. The electrostatic interactions are treated by the smooth particle mesh Ewald summation [179] with a real space cutoff of 0.9 nm. A 2.0 fs timestep was used for all simulations. Constraints for the water molecules were solved using the SETTLE procedure, while the SHAKE-algorithm [103] was used for the polymer constraints. All the model parameters were kept the same in our mutation peptide studies. The entire simulation of 20 ns per replica adds up to a total simulation length of 1.5 μs.

9.1 Decamer of Aβ_7 peptides

From the REMD simulations, the solvent accessible surface area (SASA), the radius of gyration (R$_{gyr}$) and the average number of hydrogen bonds over the central hydrophobic core (CHC) region were extracted at 76 different temperatures. In the wildtype system, below 391 K, the R$_{gyr}$ of the peptide cluster decreases with increasing temperature, and starts to increase with temperature above 391 K (Figure 9.2a). The SASA showed a similar characteristic like that of R$_{gyr}$, reaching the lowest point at 398 K (Figure 9.2b). The maximum number of peptide–peptide hydrogen bonds

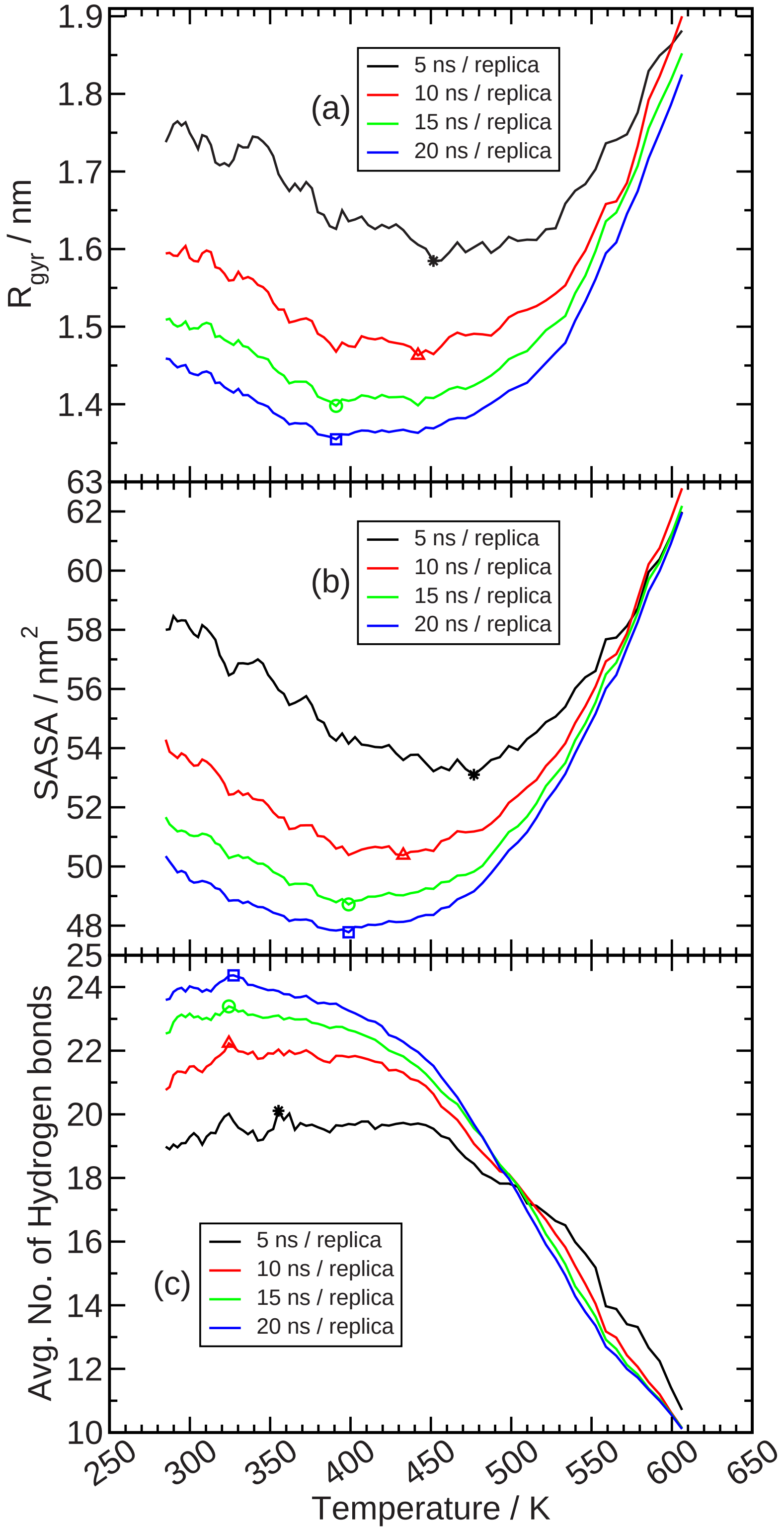

Figure 9.2: *Properties of the Aβ_7 peptide aggregates, averaged over different lengths of the simulation runs as a function of temperature. Lowest/highest values are marked. (a) Radius of gyration R_{gyr} (b) Solvent exposed hydrobobic area of Aβ_7 peptide aggregates (c) Average number of hydrogen bonds between the peptides main chain of Aβ_7 peptide aggregates.*

was observed already at around $\sim 330\,\mathrm{K}$ this number diminishes and reduced at higher temperatures (Figure 9.2c). Such a behavior could be explained as follows: At the lowest temperatures (above 285 K) the free peptides remain isolated hence the hydrogenbond interactions is low leading to high SASA and R$_{gyr}$ values. When the temperature range of 391 to 398 K is reached, the free peptides attain compact aggregate structure with the lowest SASA and R$_{gyr}$ values and a high number of hydrogenbond interactions. But the highest number of hydrogen bond interactions is reached already at 330 K, upto which the peptides were elongated to attain fibril growth. Above this temperature the twist angle of the β-sheet increases to shield the CHC, leading to the lowest SASA at 398 K. Interestingly, this temperature coincides with the position of the SASA minimum in the previous chapter obtained for the same system without replica exchange (chapter 8, Figure 8.10). From this we can conclude that the elongation process is dependent both on the peptide - peptide hydrogen bond interaction and the hydrophobic interactions. In other words the shift of the positions of the minima of R$_{gyr}$ and SASA compared to the maximum of the number of hydrogen bonds can be explained by the fact, that with increasing temperature the hydrogen bonds are weakened beyond 330 K, whereas the hydrophobic interaction strength still increases. While the hydrogen bonds tend to build a planar β-sheet structure, the increasing hydrophobic interaction produces more compact structures leading to a twist of the β-sheet. For this study the REMD simulations were averaged over the first 5, 10, 15 and the full 20 ns. The 15 and 20 ns simulations show the same positions of the extrema. Meaning, that between 15 and 20 ns the three properties have reached a steady state. Hence, 20 ns time, for each replica, was reasonable to study early aggregation.

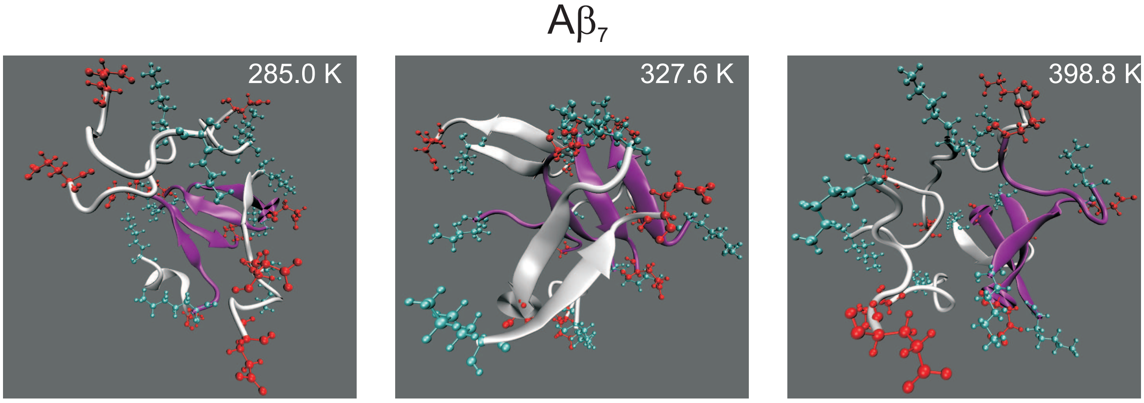

Figure 9.3: *Final snapshots of Aβ_7 peptides aggregation at three different temperatures. The initial ordered peptide tetramer is in purple, additional free peptides are shown in white, Lys(+) in cyan, Glu(-) in red.*

Final snapshots of the system at three different temperatures: 285 K - lowest temperature, 327.6 K - highest number of hydrogen bonds, 398.8 K lowest SASA, are displayed in Figure 9.3. At the lowest temperature the added monomers remain isolated and adopt a collapsed coil structure. At 327 K the added peptides show some more ordered structure which is reminiscent of β-sheets. At 398 K the peptides get organised into more micelle-like structures, in which the hydrophobic residues are more packed and the hydrophilic ends are exposed to the water (Figure 9.3). Figures 9.2 and 9.3 together show that the aggregated structures extend at intermediate temperatures rearranging from more β-like to more micelle-like structures and disintegrate at high temperatures.

9.2 Decamer of Aβ_{7g} peptides

In the mutant system, the R$_{gyr}$ of the peptide clusters were lower than in the wildtype system with a shifted position of the temperature minimum (Figure 9.4a). Also the SASA, calculated from the CHC, showed a very flat temperature dependence (Figure 9.4b). Also here, the minimum position is the shown as same as in the previous chapter, observed for the same system without replica exchange (chapter 8, Figure 8.10). This difference may be due to the hydrophobic interaction in water, since in the wildtype system the hydrophilic ends take a major role to protect the hydrophobic core. The maximum number of inter molecular peptide–peptide hydrogen bonds was observed to be higher than in the wildtype system. In contrast to the wildtype system, the highest number of hydrogen bonds was observed at the lowest temperature (Figure 9.4c). The R$_{gyr}$ and SASA of the hydrophobic core for the mutated peptides are lower than for the Aβ_7 peptides, because the loss of charge of the C-terminus in the Arctic mutation, effects the aggregation process.

In comparison to the wlidtype system, in the arctic mutation system the more ordered aggregates were formed at much lower temperatures (285 K). At higher temperatures, disordered droplet like aggregates were formed (Figure 9.5). In the mutated system the aggregated structures do not depend strongly on temperatures, as observed in wildtype system, but disintegrate into disordered structures at high temperatures (Figures 9.4 and 9.5). To demonstrate the convergence of the REMD simulations we used 20 ns simulation time for each replica to study the early aggregation. The behavior of this system was identical to the wildtype system when averaged over different lengths.

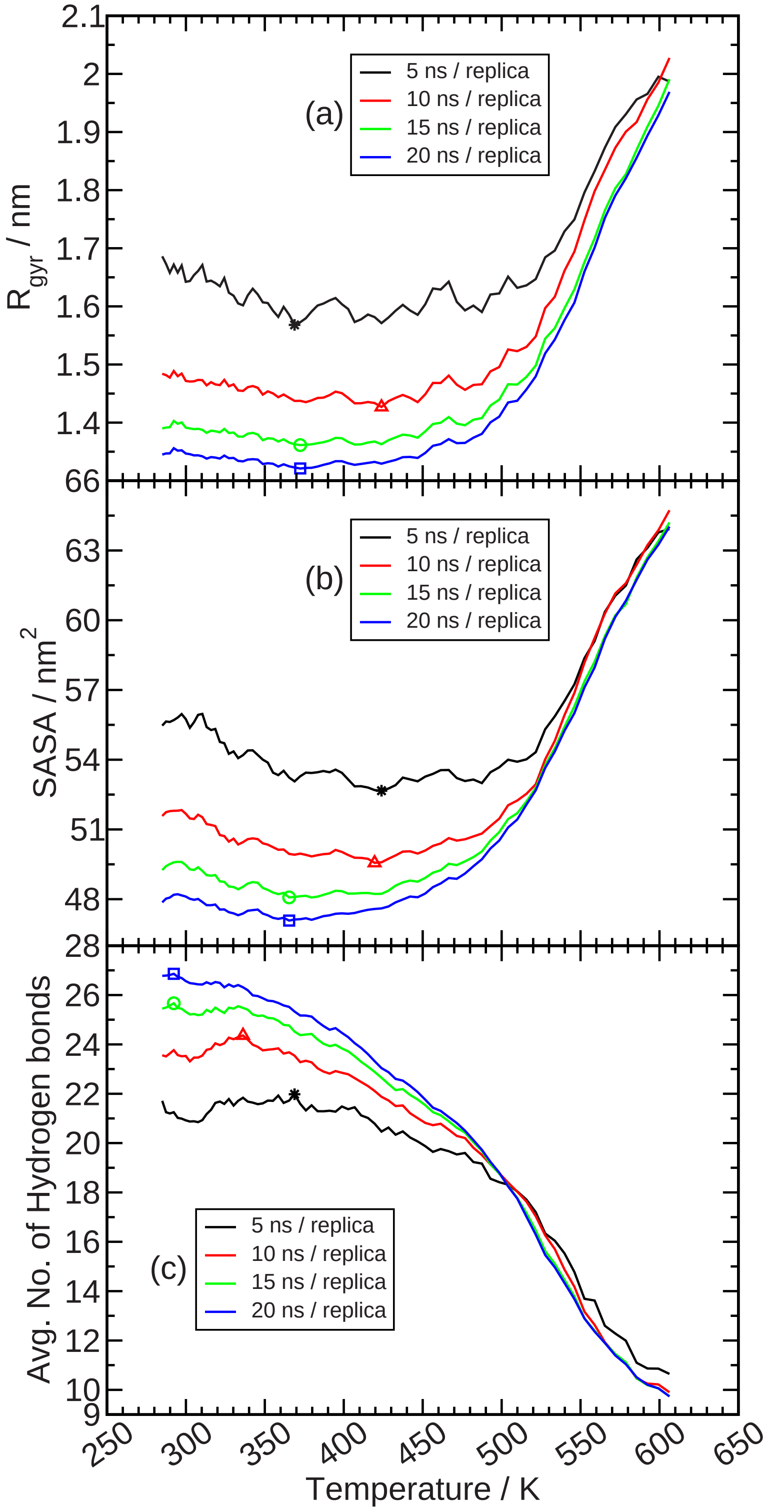

Figure 9.4: *Properties of the Aβ$_{7g}$ peptide aggregates, averaged over different lengths of the simulation runs as a function of temperature. Lowest/highest values are marked. (a) Radius of gyration R_{gyr} (b) Solvent exposed hydrobobic area of Aβ$_{7g}$ peptide aggregates (c) Average number of hydrogen bonds between the peptides main chain of Aβ$_{7g}$ peptide aggregates.*

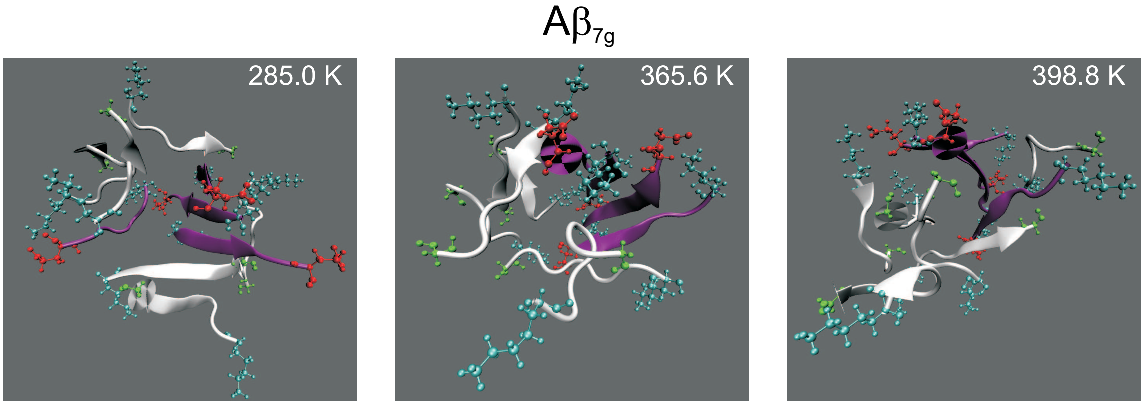

Figure 9.5: *Final snapshots of $A\beta_{7g}$ peptides aggregation at three different temperatures. The initial ordered peptide tetramer is in purple, additional free peptides are shown in white, Lys(+) in cyan, Glu(-) in red and Gly(mutant) in green.*

9.3 Conclusions

In contrast to the REMD simulations in [117] we used explicit water for the two systems, wildtype ($A\beta_7$) and mutant ($A\beta_{7g}$). Moreover we applied this technic to a larger system, consisting of a tetrameric nucleus and six free peptides, to study the fibril elongation process. In contrast to the earlier report [117] our model systems clearly develop temperature minima for R_{gyr}. This discrepancy can be explain by the lack of charge and explicit water in their simulation model, which is similar to our mutant system. Our mutant system which has a lower charge at C-terminus behaves more like the (uncharged) Meinke and Hansmann system, indicating the role of the charges to be a important driving force for aggregation. This is also evident from the previous observation by Gnanakaran and Garcia who applied REMD simulations on a two peptide system and found thus β-amyloid fragment dimers formed at 275 K due to strong electrostatic interactions between the charged groups whereas at 310 K strong hydrophobic interaction dominate in explicit water [116]. Our data clearly demonstrate that the β-sheet organisation significantly depends on temperature. Further our data demonstrate that $A\beta_7$ peptide aggregates organize into structures, in which hydrophobic regions are shielded from the aqueous environment at high temperatures.

In this chapter, we have studied the fibrils growth process by REMD simulations using an ordered aggregated tetramer as nucleus and six additional free $A\beta_7$ peptides or $A\beta_{7g}$ peptides in explicit water. Our results are in good agreement with the previous work done by Meinke et al. [117] and Gordon et al. [178]. We find that at lower temperatures the structure of the $A\beta_7$ peptide aggregates is largely determined by electrostatic interactions and hydrogen bonding. This leads to the formation of well ordered antiparallel β-sheet structures. With increasing temperature, hydrophobic interactions become more important, as indicated by the formation of stacked β-sheets, as well as less regular ordered collapsed clusters. Our results are consistent with the NMR studies showing that a hydrophobic cluster composed of Aβ_{17-21} (CHC) is involved in a hydrophobic path of peptide aggregation [62]. At the highest temperatures the aggregates are found to disintegrate due to the strong thermal motions. Aβ_{7g} peptide aggregates are largely determined by hydrophobic interactions and do not show a strong temperature dependence. These data indicate that hydrophobic interactions are a significant factor in determining the organization of β-sheets in aggregated structure. Other factors, such as charge interactions, electric dipoles, amphiphilicity and hydrogen bond geometry, may also be critical in determining aggregated structure. The addition of the peptides to an existing oligomer notably improved the peptide tendency to aggregate, which provides good templates for further elongation.

Summary

The temperature dependence of the structural and volumetric properties of amyloid β-peptides and their aggregates in liquid water are studied by molecular dynamics simulations. Analysis of the temperature dependence of water density in the hydration shell of peptides allowed a first estimation of the intrinsic thermal expansion coefficient of peptides and their aggregates in water. Upon heating, the full-length amyloid β(1-42) peptide (Aβ_{42}) transforms from an extended chain-like structure with a significant content of α-helices to a more compact and mainly disordered structure with noticeable content of β-structures. The apparent volume of Aβ_{42}, that is the change of total volume of the solution due to the presence of Aβ_{42}, shows a quite different temperature dependence below and above $T \approx 320$ K: α^{app}(Aβ_{42}) is about 1.5$\cdot10^{-3}$ K^{-1} at $T \leq 320$ K and about 0.6$\cdot10^{-3}$ K^{-1} at $T > 320$ K. The intrinsic thermal expansion coefficient of Aβ_{42} is found to be negative: α^{int}(Aβ_{42}) $\approx$ -0.8$\cdot10^{-3}$ K^{-1}. The negative thermal expansion coefficient of Aβ_{42} can be attributed to its rubber-like (entropic) elasticity and/or to the thermal breaking of intrapeptide hydrogen bonds upon heating, that provides higher packing of a peptide.

The fragment Aβ_{16-22} (Aβ_7) of Aβ_{42} shows quite different temperature-induced conformational changes. β-structures dominate at low temperatures, whereas, upon heating, both the helical content and the number of intrapeptide hydrogen bonds increase. At $T \leq 335$ K, the intrinsic thermal expansion coefficient α^{int} of Aβ_7 is close to zero (wild-type form) or slightly negative (pathogenic form, Arctic mutation: Aβ_{7g}). At higher temperatures, α^{int} is positive ($\approx$ 1.5$\cdot10^{-3}$ K^{-1}) for both studied forms of Aβ_7. A positive thermal expansivity of Aβ_7 at $T > 335$ K indicates the absence of a mechanisms, which may provide entropic elasticity of such a short peptide. An essential helical content and the stability of intrapeptide hydrogen bonds in a wide temperature range make the thermal expansivity of Aβ_7 peptides solid-like, i.e. positive.

The changes of the structural and volumetric properties of the Aβ_7 peptides upon aggregation are significant. Upon aggregation, the α-helical content and the num-

ber of intrapeptide hydrogen bonds decrease. The peptide surface exposed to water becomes more hydrophobic due to the peptide aggregation, as indicated by the decreasing density of the hydration water. This evidences the dominating role of electrostatic and hydrogen bonding interactions at the early stages of aggregation of the considered peptides. The intrinsic thermal expansivity of Aβ_7 peptide aggregates turns from positive to negative values with increasing number of peptides in the aggregate. This is accompanied by an increasing intrinsic density of the peptide aggregate, which in the case of a decamer aggregate, approaches that of Aβ_{42}. These results show the possibility to obtain the intrinsic thermal expansion coefficient α^{int} of biomolecules and their aggregates, which are found highly sensitive to their conformational and structural properties. This evidences, that studies of the intrinsic volumetric properties of peptides is a new promising tool, which may clarify the character of the conformational changes of peptides and their aggregates in liquid water.

In the fibril growth study of the wildtype peptide system at constant pressure and at different temperatures, six free Aβ_7 monomers were added to an ordered Aβ_7 tetramer nucleus. The additional peptides form anti-parallel hydrogen bonded dimers in the lower temperature range of 280–340 K. In the mid temperature range from 340 to 400 K, these dimers aggregate to form larger structures that resemble the amyloid fibrils: twisted β-sheets are formed from antiparallely oriented peptides and the initiation of a self assembled second layer is observed. In the higher temperature range (from 400 to 460 K) the twist angle between the monomers increases, probably to protect the hydrophobic residues from water.

The same study, when applied to a mutant system with six free Aβ_{7g} peptides added to the same Aβ_7 tetramer nucleus did not show any twist between the peptides and did not show a strong temperature dependence. Interestingly the Aβ_{7g} peptide system formed mixed β-sheet structures with parallel and antiparallel pair orientation. This results from the loss of charge at the C-terminus, by the substitution of the negatively charged glutamic acid (E) by a glycine (G) at position 22 (E22G: Arctic mutation). The same behavior was conformed in heterogeneous (each 3 free Aβ_7 and Aβ_{7g} peptides added to the Aβ_7 tetramer) system: Aβ_7 and Aβ_{7g} peptides are like to form antiparallel and mixed β-sheets. The temperature dependent behavior of the Aβ_7 and Aβ_{7g} peptide aggregates was confirmed in a REMD study at constant volume. Aβ_7 peptide aggregates largely form antiparallel β-sheets by electrostatic interactions and show a strong temperature dependence. The Aβ_{7g} peptide aggregates largely determine droplet like structures, formed by hydrophobic interactions, and do not show a strong temperature dependence.

Zusammenfassung

Mittels molekulardynamischer Simulationsrechnungen wurde die Temperaturabhängigkeit struktureller und volumetrischer Eigenschaften von Amyloid-β-Peptiden und deren Aggregaten in Wasser untersucht. Eine Analyse der Temperaturabhängigkeit der Dichte des Hydrathüllen-wassers der Peptide ermöglichte erstmalig eine Abschätzung des intrinsischen thermischen Ausdehnungskoeffizienten der Peptide und deren Aggregate in wässriger Lösung. Das vollständige Amyloid-β(1-42)-Peptid (Aβ_{42}) wandelt sich bei Erwärmung von einer ausgedehnten Kette mit signifikanter α-helikaler Struktur in eine kompaktere und ungeordnetere Struktur mit deutlichen β-Strukturelementen um. Das scheinbare Volumen von Aβ_{42}, also die Änderung des Gesamtvolumens der Lösung durch die Anwesenheit von Aβ_{42}, zeigt ein unterschiedliches Temperaturverhalten unterhalb und oberhalb von $T \approx 320$ K: α^{app}(Aβ_{42}) ist etwa $1.5 \cdot 10^{-3}$ K^{-1} bei $T \leq 320$ K und etwa $0.6 \cdot 10^{-3}$ K^{-1} bei $T > 320$ K. Der intrinsische thermische Ausdehnungskoeffizient von Aβ_{42} ist negativ: α^{int}(Aβ_{42}) $\approx$ -$0.8 \cdot 10^{-3}$ K^{-1}. Der negative thermische Ausdehnungskoeffizient von Aβ_{42} beruht entweder auf gummielastischem (entropischem) Verhalten oder wird durch das thermische Aufbrechen von Intrapeptid-H-Brücken verursacht, was zu einer dichteren Packung des Peptids führt.

Das Fragment Aβ_{16-22} (Aβ_7) des Aβ_{42}-Peptids zeigt ganz andere temperaturinduzierte Veränderungen. β-Strukturen dominieren bei tiefen Temperaturen, bei Erwärmung nehmen helikale Strukturen und intramolekulare H-Brücken zu. Bei Temperaturen $T \leq 335$ K ist der intrinsische thermische Ausdehnungskoeffizient α^{int} fast null bei Aβ_7 (wild type) und leicht negativ für Aβ_{7g} (Arktische Mutation). Bei höheren Temperaturen ist α^{int} positiv ($\approx 1.5 \cdot 10^{-3}$ K^{-1}) bei beiden untersuchten Peptiden. Ein positiver thermischer Ausdehnungskoeffizient von Aβ_7 bei $T > 335$ K zeigt das Fehlen eines Mechanismus, der eine entropische Elastizität eines so kleinen Peptids bewirken könnte. Ein wesentlicher helikaler Strukturanteil und die Stabilität intramolekularer Wasserstoffbrücken in einem weiten Temperaturbereich führen zu dem festkörperähnlichen (positiven) Ausdehnungskoeffizienten des

Aβ_7-Peptids.

Bei der Aggregation der Aβ_7-Peptide treten signifikante Veränderungen der strukturellen und volumetrischen Eigenschaften auf. Der α-helikale Strukturanteil und die Zahl der intramolekularen Wasserstoffbrücken nimmt deutlich ab. Die Oberfläche der Peptide, welche dem Wasser zugewandt ist, wird bei der Aggregation hydrophober. Dies wird aus der abnehmenden Dichte des Hydratwassers ersichtlich. Auch die wichtige Rolle der elektrostatischen und H-Brücken-Wechselwirkungen im frühen Stadium der Aggregation der betrachteten Peptide wird deutlich. Der intrinsische thermische Ausdehnungskoeffizient der Aβ_7-Aggregate verschiebt sich mit zunehmender Aggregatgröße von positiven zu negativen Werten. Parallel dazu vergrößert sich die intrinsische Dichte der Aggregate und nähert sich bei dem Dekamer der intrinsischen Dichte des Aβ_{42}. Diese Untersuchungen zeigen einerseits, dass es möglich ist, aus Simulationen den intrinsischen thermischen Ausdehnungskoeffizienten α^{int} von Biomolekülen und deren Aggregaten zu berechnen. Andererseits liefert die hohe Sensitivität von α^{int} bezüglich konformativer und struktureller Eigenschaften ein vielversprechendes neues Werkzeug zur Aufklärung konformativer Veränderungen von Peptiden und deren Aggregation in wässriger Lösung.

In der Studie zum Fibrillenwachstum des Wildtype-Peptidsystems bei konstantem Druck und verschiedenen Temperaturen, wurden sechs freie Aβ_7-Monomere zu einem System hinzugefügt, welches einen geordneten Aβ_7-Tetramer als Wachstumskeim enthielt. Die hinzugefügten Peptide bilden bei den tiefen Temperaturen von 280 bis 340 K innerhalb der Simulationszeit antiparallele Wasserstoff-verbrückte Dimere. Im mittleren Temperaturbereich zwischen 340 und 400 K aggregieren diese Dimere zu größeren Strukturen, die denen der Amyloid-Fibrillen ähneln: verdrillte β-Blätter werden aus antiparallel orientierten Peptiden gebildet und die Ausbildung einer selbstassemblierten zweiten Schicht beginnt. Im höheren Temperaturbereich zwischen 400 und 460 K vergrößert sich der Verdrillungswinkel, wahrscheinlich, um einen zu großen hydrophoben Kontakt zu Wasser zu vermeiden.

Dieselbe Untersuchung an einem System mit sechs hinzugefügten Mutantenpeptiden Aβ_{7g} (zu dem gleichen Aβ_7-Keim) zeigte keinerlei Verdrillung zwischen den Peptiden und keine starke Temperaturabhängigkeit. Interessanterweise bilden die Aβ_7-Peptide auch gemischte β-Blattstrukturen mit parallelen und antiparallelen Paaranordnungen. Dies resultiert aus dem Ladungsverlust am C-Terminus durch die Substitution der negativ geladenen Glutaminsäure (E) durch Glycin (G) an der Position 22 (E22G: Arktische Mutanten). Das gleiche Verhalten wird auch in einem weiteren heterogenen System beobachtet, wo drei Aβ_7- und drei Aβ_{7g}-Peptide hinzugefügt wurden. Hier bilden die Peptide sowohl parallele als auch antiparallele Paare. Die Temperaturabhängigkeit der Peptidaggregate konnte durch REMD-Simulationen bestätigt werden. Die Aβ_7-Peptide bilden im Wesentlichen wegen der elektrostatischen Wechselwirkungen antiparallele β-Blätter und zeigen starke Temperaturabhängigkeit. Die Aβ_{7g}-Peptide bilden viel ungeordnetere, tropfenähnliche Strukturen, im Wesentlichen aufgrund hydrophober Wechselwirkungen und zeigen keine starke Temperaturabhängigkeit.

Bibliography

[1] Tigran V. Chalikian. Volumetric properties of proteins. *Ann. Rev. Biophys. Biomol. Struct.*, 32(1):207–235, 2003.

[2] Seemann H., Winter R., and Royer C. A. Volume, expansivity and isothermal compressibility changes associated with temperature and pressure unfolding of staphylococcal nuclease. *J. Mol. Biol.*, 307:1091–1102, 2001.

[3] Revanur Ravindra, Catherine Royer, and Roland Winter. Pressure perturbation calorimetic studies of the solvation properties and the thermal unfolding of staphylococcal nuclease. *Phys. Chem. Chem. Phys.*, 6:1952 – 1961, 2004.

[4] Mitra L., Smolin N., Ravindra R., Royer C., and Winter R. Pressure perturbation calorimetric studies of the solvation properties and the thermal unfolding of proteins in solution—experiments and theoretical interpretation. *Phys. Chem. Chem. Phys.*, 8:1249 – 1265, 2006.

[5] Nicolini C., Ravindra R., Ludolph B., and Winter R. Characterization of the Temperature- and Pressure-Induced Inverse and Reentrant Transition of the Minimum Elastin-Like Polypeptide GVG(VPGVG) by DSC, PPC, CD, and FT-IR Spectroscopy. *Biophys. J.*, 86(3):1385–1392, 2004.

[6] Hiebl M. and Maksymiw R. Anomalous temperature dependence of the thermal expansion of proteins. *Biopolymers*, 31:161–167, 1991.

[7] Brovchenko I., Krukau A., Smolin N., Oleinikova A., Geiger A., and Winter R. Thermal breaking of spanning water networks in the hydration shell of proteins. *J. Chem. Phys.*, 123(22):224905, 2005.

[8] Brovchenko I., Krukau A., Oleinikova A., and Mazur A. K. Water percolation governs polymorphic transitions and conductivity of DNA. *Phys. Rev. Lett.*, 97(13):137801, 2006.

[9] Brovchenko I., Krukau A., Oleinikova A., and Mazur A. K. Water clustering and percolation in low hydration DNA shells. *J. Phys. Chem. B*, 111(12):3258–3266, 2007.

[10] Krukau A., Brovchenko I., and Geiger A. Temperature-induced conformational transition of a model elastin-like peptide GVG(VPGVG)$_3$ in water. *Biomacromolecules*, 8:2196–2202, 2007.

[11] Ellis R. J. and Pinheiro J. T. Medicine: Danger – misfolding proteins. *Nature*, 416:483–484, 2002.

[12] Cohen F. E. and Kelly J. W. Therapeutic approaches to peptide misfolding diseases. *Nature*, 426(18/25):905–909, 2003.

[13] Dobson C. M. Peptide folding and misfolding. *Nature*, 426(18/25):884–890, 2003.

[14] Dobson C. M. Principles of protein folding, misfolding and aggregation. *Semin. Cell Dev. Biol.*, 15:3–16, 2004.

[15] Lomakin A., Chung S. D., Benedek G. B., Kirschner D. A., and Teplow D. B. On the nucleation and growth of amyloid beta-protein fibrils: detection of nuclei and quantitation of rate constants. *Proc. Natl. Acad. Sci. USA*, 93:1125–1129, 1996.

[16] Teplow D. B. Structural and kinetic features of amyloid β-protein fibrillogenesis. *Amyloid Int. J. Exp. Clin. Invest*, 5:121–142, 1998.

[17] Lansbury P. T. Jr. A reductionist view of alzheimer's disease. *Acc. Chem. Res.*, 29:317–321, 1996.

[18] Lomakin A., Teplow D. B., Kirschner D. A., and Benedek G. B. Kinetic theory of fibrillogenesis of amyloid β-protein. *Proc. Natl. Acad. Sci. USA*, 94:7942–7947, 1997.

[19] Esler W. P., Stimson E. R., Jennings J. M., Vinters H. V., Ghilardi J. R., Lee J. P., Mantyh P. W., Maggio J. E., Dyda F., Reed J., and Tycko R. Alzheimer's disease amyloid propagation by a template-dependent dock-lock mechanism. *Biochemistry*, 39:6288–6295, 2000.

[20] Kusumoto Y., Lomakin A., Teplow D. B., and Benedek G. B. Temperature dependence of amyloid β-protein fibrillization. *Proc. Natl. Acad. Sci. USA*, 95:12277–12282, 1998.

[21] Harper J. D. and Lansbury P. T. Models of amyloid seeding in alzheimer's disease and scrapie: mechanistic truths and physiological consequences of the time-dependent solubility of amyloid proteins. *Annu. Rev. Biochem.*, 66:385–407, 1997.

[22] Massi F. and Straub J. E. Energy landscape theory for alzheimer's amyloid β-peptide fibril elongations. *Proteins*, 42:217–229, 2001.

[23] Necula M., Kayed R., Milton S., and Glabe C. G. Small Molecule Inhibitors of Aggregation Indicate That Amyloid β Oligomerization and Fibrillization Pathways Are Independent and Distinct. *J. Biol. Chem.*, 282(14):10311–10324, 2007.

[24] Nilsberth C., Westlind-Danielsson A., Eckmann C. B., Condron M. M., Axelman K., Forsell C., Stenh C., Luthman J., Teplow D. B., Younkin S. G., Näslund J., and Lannfelt L. The 'arctic app mutation (e693g) causes alzheimer's disease by enhanced aβ protofibril formation. *Nat. Neurosci.*, 4(9):887–893, 2001.

[25] Tjernberg L. O., Näslund J., Lindqvist F., Johanson J., Karlström A. R., Thyberg J., Terenius L., and Nordstedt C. Arrest of β-amyloid fibril formation by a pentapeptide ligand. *J. Biol. Chem.*, 271:8545–8548, 1996.

[26] Lashuel H. A., Hartley D. M., Petre B. M., Wall J. S., Simon M. N., Walz T., and Lansbury Jr P. T. Mixtures of wild-type and a pathogenic (e22g) form of aβ40 in vitro accumulate protofibrils, including amyloid pores. *J. Mol. Biol.*, 332:795–808, 2003.

[27] Favrin G., Irb*ä*ck A., and Mohanty S. Oligomerization of amyloid aβ_{16-22} peptides using hydrogenbonds and hydrophobicity forces. *Biophys. J.*, 87:3657–3664, 2004.

[28] Balbach J. J., Ishii Y., Antzutkin O. N., Leapman R. D., Rizzo N. W., Dyda F., Reed J., and Tycko R. Amyloid fibril formation by $a\beta_{16-22}$, a seven residue fragment of the alzheimer's β-amyloid peptide, and structural characterization by solid state nmr. *Biochemistry*, 39:13748–13759, 2000.

[29] Petty S. A. and Decatur S. M. Experimental evidence for the reorganization of β-strands within aggregates of the aβ_{16-22} peptide. *J. Am. Chem. Soc.*, 127(39):13488–13489, 2005.

[30] Frenkel D. and Smit B. *Understanding Molecular Simulation — From Algorithms to Applications.* Academic Press, San Diego, 2nd edition, 2002.

[31] Branden C. and Tooze J. *Introduction to protein structure.* Routledge, New York, 2nd edition, 1999.

[32] Nelson D. L. and Cox M. M. *Lehninger Principles of Biochemistry.* Worth publishers, New York, third edition, 2000.

[33] Murphy R. M. and Kendrick B. S. Protein misfolding and aggregation. *Biotechnology Progress*, 2007.

[34] Hart P. J. Pathogenic superoxide dismutase structure, folding, aggregation and turnover. *Curr. Opin. Chem. Biol.*, 10:131–138, 2006.

[35] Chi E. Y., Krishnan S., Randolph T. W., and Carpenter J. F. Physical stability of proteins in aqueous solution: Mechanism and driving forces in nonnative protein aggregation. *Pharm. Res.*, 20:1325–1336, 2003.

[36] Lesk A. M. *Introduction to protein architecture.* Oxford University Press, 2001.

[37] Ramachandran G. N., Ramakrishnan C., and Sasisekharan V. Stereochemistry of polypeptide chain configurations. *J. Mol. Biol.*, 7:95–9, 1963.

[38] Onuchic J. N., Luthey-Schulten Z., and Wolynes P. G. Theory of protein folding: The energy landscape perspective. *Annual Review of Physical Chemistry*, 48(1):545–600, 1997.

[39] Dill K. A. and Chan H. S. From levinthal to pathways to funnels. *Nature Struct. Biol.*, 4:10–19, 2003.

[40] Dobson C. M., Sali A., and Karplus M. Peptide folding: A perspective from theory and experiment. *Angew. Chem. Int. Ed.*, 37(7):868–893, 1998.

[41] Leach A. R.. *Molecular Modelling: Principles and Applications.* Pearson Education Ltd.,, 2nd edition, 2001.

[42] Sunde M. and Blake C. C. F. From the globular to the fibrous state: protein structure and structural conversion in amyloid formation. *Q. Rev. Biophys.*, 31:1–39, 1998.

[43] Stefani M. and Dobson C. Protein aggregation and aggregate toxicity: new insights into protein folding, misfolding diseases and biological evolution. *J. Mol. Med.*, 81:678–699, 2003.

[44] Malinchik S. B, Inouye H., Szumowski K. E., and Kirschner D. A. Structural analysis of alzheimer's β (1–40) amyloid: Protofilament assembly of tubular fibrils. *Biophys. J.*, 74:537–545, 1998.

[45] Chiti F. and Dobson C. M. Protein misfolding, functional amyloid, and human disease. *Annu. Rev. Biochem.*, 75:333–366, 2006.

[46] Nelson R. and Eisenberg D. Structural models of amyloid-like fibrils. *Advances in protein chemistry*, 73:235–282, 2006.

[47] Bucciantini M., Giannoni E., Chiti F., Baroni F., Formigli L., Zurdo J., Taddei N., Ramponi G., Dobson C. M., and Stefani M. Inherent toxicity of aggregates implies a common mechanism for protein misfolding diseases. *Nature*, 416:507–511, 2002.

[48] Selkoe D. J. Folding proteins in fatal ways. *Nature*, 426(18/25):900–904, 2003.

[49] Selkoe D. J. Amyloid β-protein and the genetics of alzheimer's disease. *J. Biol. Chem.*, 271:18295–18298, 1996.

[50] Makin O. S. and Serpell L. C. Structures for amyloid fibrils. *FEBS Journal*, 272:5950–5961, 2005.

[51] Azheimer A. Über eine eigenartige erkrankung der hirnrinde. *Allg. Z. Psychiatr.*, 64:146–148, 1907.

[52] Gaggelli E., Kozlowski H., Valensin D., and Valensin G. Copper homeostasis and neurodegenerative disorders (alzheimer's, prion, and parkinson's diseases and amyotrophic lateral sclerosis). *Chemical Reviews*, 106(6):1995–2044, 2006.

[53] Walsh D. M., Lomakin A., Benedek G. B., Condron M. M., and Teplow D. B. Amyloid beta-Protein Fibrillogenesis. DETECTION OF A PROTOFIBRILLAR INTERMEDIATE. *J. Biol. Chem.*, 272(35):22364–22372, 1997.

[54] Lansbury P. T., Costa P. R, Griffiths J. M., Simon E. J., Auger M., Halverson K. J, Kocisko D. A., Hendsch Z. S., Ashburn T. T., Spencer R. G. S., Tidor B., and Griffin R. G. Structural model for the β-amyloid fibril based on interstrand alignment of an antiparallel-sheet comprising a c-terminal peptide. *Nature Struct Biol*, 2:990–998, 1995.

[55] Bitan G., Kirkitadze M. D., Lomakin A., Vollers S. S., Benedek G. B., and Teplow D. B. Amyloid β-protein (Aβ) assembly: Aβ40 and Aβ42 oligomerize through distinct pathways. *Proc. Natl. Acad. Sci.*, 100(1):330–335, 2003.

[56] Fezoui Y. and Teplow D. B. Kinetic Studies of Amyloid β-Protein Fibril Assembly differential effects of α-helix stabilization. *J. Biol. Chem.*, 277(40):36948–36954, 2002.

[57] Tomaselli A. S., Esposito V., Vangone P., van Nuland N. A., Bonvin A. M., Guerrini R., Tancredi T., Temussi P.A., and Picone D. The α-to-β conformational transition of alzheimer‘s aβ_{1-42} peptide in aqueous media is reversible: a step by step conformational analysis suggests the location of β conformation seeding. *J. ChemBioChem*, 7:257–267, 2006.

[58] Serpell L. C. Alzheimer's amyloid fibrils: structure and assembly. *Biochim. Biophys. Acta / Molecular Basis of Disease*, 1502:16–30, 2000.

[59] Gursky O. and Aleshkov S. Temperature-dependent β-sheet formation in β-amyloid aβ_{1-40} peptide in water: uncoupling β-structure folding from aggregation. *Biochim. Biophys. Acta / Protein Structure and Molecular Enzymology*, 1476:93–102, 2000.

[60] Jarvet J., Damberg P., Bodell K., GoranEriksson L. E., and Graslund A. Reversible random coil to *beta*-sheet transition and the early stage of aggregation of the a$beta_{12-28}$ fragment from the alzheimer peptide. *J. Amer. Chem. Soc.*, 122(18):4261–4268, 2000.

[61] Danielsson J., Jarvet J., Damberg P., and Graslund A. The alzheimer β-peptide shows temperature-dependent transitions between left-handed 31-helix, β-strand and random coil secondary structures. *FEBS Journal*, 272(15):3938–3949, 2005.

[62] Zhang S., Iwata K., Lachenmann M. J., Peng J. W., Li S., Stimson E. R., Lu Y. -a., Felix A. M., Maggio J. E., and Lee J. P. The alzheimer's peptide a[beta] adopts a collapsed coil structure in water. *J. Struct. Biol.*, 130:130–141, 2000.

[63] Zagorski M. G. and Barrow C. J. Nmr studies of amyloid β-peptides: proton assignments, secondary structure, and mechanism of an α-helix .fwdarw. .beta.-sheet conversion for a homologous, 28-residue, n-terminal fragment. *Biochemistry*, 31(24):5621–5631, 1992.

[64] Terzi E., Holzemann G., and Seelig J. Reversible random coil-beta-sheet transition of the alzheimer β-amyloid fragment (25-35). *Biochemistry*, 33:1345–1350, 1994.

[65] Balbach J. J., Petkova A. J., Olyer N. A., Antzutkin O. N., Gordon D. J., Meredith S. C., and Tycko R. Superamolcular structure in full length alzheimer's β-amyloid fibrils; evidnce for parallel β-sheet organization from solid state nmr. *Biophys. J.*, 83:1205–1216, 2002.

[66] Johansson A. S., Berglind-Dehlin F., Karlsson G., Edwards K., Gellerfors P., and Lannfelt L. Physiochemical characterization of the alzheimer's disease-related peptides aβ1–42arctic and aβ1–42wt. *FEBS Journal*, 273:2618–2630, 2006.

[67] Sahlin C., Lord A., Magnusson K., Englund H., Almeida C. G., Greengard P., Nyberg F., Gouras G. K., Lannfelt L., and Nilsson L. N. G. The arctic alzheimer mutation favors intracellular amyloid-β production by making amyloid precursor protein less available to α-secretase. *Journal of Neurochemistry*, 101(3):854–862, 2007.

[68] Van Nostrand W. E., Melchor J. P., Cho H. S., Greenberg S. M., and Rebeck G. W. Pathogenic Effects of D23N Iowa Mutant Amyloid beta-Protein. *J. Biol. Chem.*, 276(35):32860–32866, 2001.

[69] Kirschner D. A., Inouye H., Duffy L. K., Sinclair A., Lind M., and Selkoe D. J. Synthetic Peptide Homologous to β Protein from Alzheimer Disease Forms Amyloid-Like Fibrils in vitro. *Proc. Natl. Acad. Sci. USA*, 84(19):6953–6957, 1987.

[70] Huang T. H. J., Fraser P. E., and Chakrabartty A. Fibrillogenesis of alzheimer aβ peptides studied by fluorescence energy transfer. *J. Mol. Biol.*, 269, 1997.

[71] Burkoth T. S., Benzinger T. L. S., Urban V., Morgan D. M., Gregory D. M., Thiyagarajan P., Botto R. E., Meredith S. C., and Lynn D. G. Structure of the β-amyloid$_{10-35}$ fibril. *J. Am. Chem. Soc.*, 122(33):7883–7889, 2000.

[72] Benzinger T. L. S., Gregory D. M., Burkoth T. S., Miller-Auer H., Lynn D. G., Botto R. E., and Meredith S. C. Two-dimensional structure of β-amyloid$_{10-35}$ fibrils. *Biochemistry*, 39(12):3491–3499, 2000.

[73] Benzinger T. L. S., Gregory D. M., Burkoth T. S., Miller-Auer H., Lynn D. G., Botto R. E., and Meredith S. C. Propagating structure of Alzheimer's β-amyloid$_{10-35}$ is parallel β-sheet with residues in exact register. *Proc. Natl. Acad. Sci. USA*, 95(23):13407–13412, 1998.

[74] Klimov D. K. and Thirumalai D. Dissecting the assembly of aβ_{16-22} amyloid peptides into antiparallel β-sheets. *Structure*, 11:295–307, 2003.

[75] Klimov D. K., Straub J. E., and Thirumalai D. Aqueous urea solution destabilizes $A\beta_{16-22}$ oligomers. *Proc. Natl. Acad. Sci. USA*, 101(41):14760–14765, 2004.

[76] Ma B. and Nussinov R. Stabilities and conformations of alzheimer's β-amyloid peptide oligomers ($a\beta_{16-22}$, $a\beta_{16-35}$, and $a\beta_{10-35}$): sequence effects. *Proc. Natl. Acad. Sci. USA*, 99:14126–14131, 2002.

[77] Santini S., Mousseau N., and Derreumaux P. In silico assembly of alzheimer's $a\beta_{16-22}$ peptide into β-sheets. *J. Am. Chem. Soc.*, 126(37):11509–11516, 2004.

[78] Santini S., Wei G., Mousseau N., and Derreumaux P. Pathway complexity of alzheimer's $a\beta_{16-22}$ peptide assembly. *Structure*, 12:1245–1255, 2004.

[79] Nguyen P. H., Li M. S., Stock G., Straub J. E., and Thirumalai D. Monomer adds to preformed structured oligomers of Aβ-peptides by a two-stage dock-lock mechanism. *Proc. Natl. Acad. Sci. USA*, 104(1):111–116, 2007.

[80] Kamihira M., Oshiro Y., Tuzi S., Nosaka Y. A., Saito H., and Naito A. Effect of electrostatic interaction on fibril formation of human calcitonin as studied by high resolution solid state $_{13}$c nmr. *J. Biol. Chem.*, 278:2859–2865, 2003.

[81] Tarus B., Straub J. E., and Thirumalai D. Dynamics of asp23-lys28 salt-bridge formation in aβ_{10-35} monomers. *J. Am. Chem. Soc.*, 128(50):16159–16168, 2006.

[82] Dima R. I. and Thirumalai D. Exploring protein aggregation and self-propagation using lattice model: Phase diagram and kenetics. *Protein Sci.*, 11:1036–1049, 2002.

[83] Rohrig U. F., Laio A., Tantalo N., Parrinello M., and Petronzio R. Stability and Structure of Oligomers of the Alzheimer Peptide Aβ_{16-22}: From the Dimer to the 32-Mer. *Biophys. J.*, 91(9):3217–3229, 2006.

[84] Broome B. M. and Hecht M. H. Nature disfavors sequences of alternating polar and non-polar amino acids: implications for amyloidogenesis. *J. Mol. Biol.*, 296:961–968, 2000.

[85] Sgourakis N. G., Yan Y., McCallum S. A., Wang C., and García A. E. The alzheimer's peptides aβ40 and 42 adopt distinct conformations in water: A combined md / nmr study. *J. Mol. Biol.*, 368:1448–1457, 2007.

[86] Paschek D., Nymeyer H., and García A. E. Replica exchange simulation of reversible folding/unfolding of the trp-cage miniprotein in explicit solvent: On the structure and possible role of internal water. *J. Struct. Biol.*, 157:524–533, 2007.

[87] Attig N., Binder K., Grubmüller H.., and Kremer K. *Computational Soft Matter: From Synthetic Ploymers to Proteins*, volume 23. NIC Directors, Germany, 2004.

[88] van Gunsteren W. F., Weiner P. K., and Wilkinson A. J. *Computer simulation of biomolecular systems, theoretical and experimental applications, Vols. 1 – 3*. Kluwer, Dordrecht, 1989.

[89] Hansmann U. H. E. Parallel tempering algorithm for conformational studies of biological molecules. *Chem. Phys. Lett.*, 281:140–140, 1997.

[90] Sugita Y. and Okamoto Y. Replica-exchange molecular dynamics method for protein folding. *Chem. Phys. Letters*, 314:141–151, 1999.

[91] Verma A. *Development and application of a free energy force field for all atom protein folding*. PhD thesis, Universität Dortmund, 2007.

[92] Schlick T. *Molecular Modeling and Simulation: An Interdisciplinary Guide*. Springer Verlag, New York, 2002.

[93] Alder B. J. and Wainwright T. E. Phase transition for a hard-sphere system. *J. Chem. Phys.*, 27:1208–1209, 1957.

[94] Alder B. J. and Wainwright T. E. Studies in md. i. gerneral method. *J. Chem. Phys.*, 31:459–466, 1959.

[95] Rahman A. Correlations in the motion of atoms in liquid argon. *Phys. Rev. A*, 136:405–411, 1964.

[96] Stillinger F. H. and Rahman A. Improved simulation of liquid water by molecular dynamics. *J. Chem. Phys.*, 60:1545–1557, 1974.

[97] McCammon J. A., Gelin B. R., and Karplus M. Dynamics of foldrd proteins. *Nature (Lond.)*, 267:585–590, 1977.

[98] Villa E., Balaeff A., and Schulten K. Structural dynamics of the lac repressor–dna complex revealed by a multiscale simulation. *Proc. Natl. Acad. Sci. USA*, 102:6783–6788, 2005.

[99] Almlof M., Aqvist J., Smalas A. O., and Brandsdal B. O. Probing the Effect of Point Mutations at Protein-Protein Interfaces with Free Energy Calculations. *Biophys. J.*, 90(2):433–442, 2006.

[100] Knecht V., Mark A. E., and Marrink S. J. Phase behavior of a phospholipid/fatty acid/water mixture studied in atomic detail. *J. Am. Chem. Soc.*, 128:2030–2034, 2006.

[101] Periole. X. and Mark A. E. Convergence and sampling efficiency in replica exchange simulations of peptide folding in explicit solvent. *J. Chem. Phys.*, 126:014903–014914, 2007.

[102] Allen M. P. and Tildesly D. J. *Computer simulation of liquids.* Clarendron Press, Oxford, 1987.

[103] Ryckaert J. P., Ciccotti G., and Berendsen H. J. C. Numerical integration of the cartesian equations of motions of a system with constraints: Molecular dynamics of n–alkanes. *J. Comp. Phys.*, 23:327–341, 1977.

[104] Nosé S. A molecular dynamics method for simulating in the canonical ensemble. *Mol. Phys.*, 52:255–268, 1984.

[105] Mitsutake A., Sugita Y., and Okamoto Y. Generalized-ensemble algorithms for molecular simulations of biopolymers. *Biopolymers*, 60:96–123, 2001.

[106] Marinari E. and Parisi G. Simulated tempering: A new monte carlo scheme. *Europhys. Lett.*, 19:451–458, 1992.

[107] Snow C. D., Sorin E. J., Rhee Y. M., and Pande V. S. How well can simulation predict protein folding kinetic and thermodynamics? *Ann. Rev. Biophys. Biomol. Struct.*, 34:43–69, 2005.

[108] Zhou R. H., Berne B. J., and Germain R. The free energy landscape for beta hairpin folding in explicit water. *Proc. Natl. Acad. Sci. USA*, 98:14931–14936, 2001.

[109] Sugita Y., Kitao A., and Okamoto Y. Multidimensional replica-exchange method for free-energy calculations. *Chem. Phys.*, 113:6042–6051, 2000.

[110] Rhee Y. M. and Pande V. S. Multiplexed replica exchange molecular dynamics method for protein folding simulation. *Biophys. J.*, 84:775–86, 2003.

[111] Paschek D. *Volume, Temperature (V,T) Replica Exchange Molecular Dynamics with the GROMACS 3.2.1 Simulation Package.* http://ganter.chemie.uni-dortmund.de/ pas/, 2004.

[112] Paschek D., Gnanakaran S., and García A. E. Simulations of the pressure and temperature unfolding of an α-helical peptide. *Proc. Natl. Acad. Sci. USA*, 102:6765–6770, 2005.

[113] Paschek D. and García A. E. Reversible temperature and pressure denaturation of a protein fragment: A replica exchange molecular dynamics simulation study. *Phys. Rev. Letters*, 93:238105–238108, 2004.

[114] García A. E. and Onuchic J. N. Folding a protein in a computer: an atomic description of the folding/unfolding of protein a. *Proc. Natl. Acad. Sci. USA*, 100:13898–13903, 2003.

[115] García A. E. and Sanbonmatsu K. Y. Exploring the energy landscape of a hairpin in explicit solvent. *Proteins*, 42:345–354, 2001.

[116] Gnanakaran. S., Nussinov. R., and García A. E. Atomic-level description of amyloid β-dimer formation. *J. Am. Chem. Soc.*, 128:2158–2159, 2006.

[117] Meinke J. H. and Hansmann U. H. E. Aggregation of β-amyloid fragments. *J. Chem. Phys.*, 126:014706–014711, 2007.

[118] Burri R. R., Paschek D., and Geiger A. Remd simulations of aβ_{16-22} peptide aggregation in explicit solvent. *From Computational Biophysics to Systems Biology (CBSB07), Proceedings of the NIC Workshop 2007, NIC Series*, (36):91–94, 2007.

[119] Berendsen H. J. C., van der Spoel D, and van Drunen R. Gromacs: A message-passing parallel molecular dynamics implementation. *Comp. Phys. Comm.*, 91:43–56, 1995.

[120] van der Spoel D, Lindahl E., Hess B., Groenhof G., Mark A. E., and Berendsen H. J. C. Gromacs: Fast, flexible and free. *J. Comp. Chem.*, 26:1701–1718, 2005.

[121] Lindahl E., Hess B., and van der Spoel D. Gromacs 3.0: A package for molecular simulation and trajectory analysis. *J. Mol. Model.*, 7:306–317, 2001.

[122] van der Spoel D., Lindahl E., Hess B., van Buuren A. R., Apol E., Meulenhoff P. J., Tieleman D. P., Sijbers T. M., Feenstra K. A., van Drunen R., and Berendsen H. J. C. *Gromacs User Manual version 3.2.* www.gromacs.org, 2004.

[123] Cornell W. D., Cieplak P., Bayly C. I., Gould I. R., Merz Jr K. M., Ferguson D. M., Spellmeyer D. C., Fox T., Caldwell J. W., and Kollman P. A. A second generation force field for the simulation of proteins, nucleic acids and organic molecules. *J. Am. Chem. Soc.*, 117:5179–5197, 1995.

[124] MacKerell Jr A. D., Bashford D., Bellot M., Dunbrack Jr R. L., Evanseck J. D., Field M. J., Fischer S., Gao J., Guo H., Ha S., Joseph-McCarthy D., Kuchnir L, Kuczera K, Lau F. T. K., Mattos C, Michnick S, Ngo T, Nguyen D. T., Prodhom B., Reiher III W.E., Roux B, Schlenkrich M, Smith J. C., Stote R., Straub J., Watanabe M., Wiorkiewicz-Kuczera J., Yin D., and Karplus M. An

all-atom empirical potential for molecular modeling and dynamics of proteins. *J. Phys. Chem. B*, 102:3586–3592, 1998.

[125] Jorgensen W. L., Maxwell D. S., and Tirado–Rives J. Development and testing of the opls all–atom force field on conformational energetics and properties of organic liquids. *J. Am. Chem. Soc.*, 118:11225–11236, 1996.

[126] van Gunsteren W. F., Bakowies D., Baron R., Chandrasekhar I., Christen M., Daura X., Gee P., Geerke D. P., Glättli A., Hünenberger P. H., Kastenholz M. A., Oostenbrink C., Schenk M., Trzesniak D., van der Vegt N. F. A., and Yu H.B. Biomolecular modeling: Goals, problems, perspectives. *Angew. Chem. Int. Ed.*, 45:4064–4092, 2006.

[127] Jorgensen W. L. and Tirado–Rives J. The opls potential functions for proteins. energy minimizations for crystals of cyclic peptides and crambin. *J. Am. Chem. Soc.*, 110:1657–1666, 1988.

[128] Kaminski G. A., Friesner R. A., Tirado-Rives J., and Jorgensen W. L. Evaluation and reparametrization of the opls-aa force field for proteins via comparison with accurate quantum chemical calculations on peptides. *J. Phys. Chem. B*, 105:6474–6487, 2001.

[129] Schuler L. D. and Van Gunsteren W. F. On the choice of dihedral angle potential energy functions for n-alkanes. *Mol. Simul.*, 25:301–320, 200.

[130] Barker J. A. and Watts R. O. Structure of water; a monte carlo calculation. *Chemical Physics Letters*, 3:144–145, 1969.

[131] Rahman A. and Stillinger F. H. Molecular dynamics study of liquid water. *The Journal of Chemical Physics*, 55(7):3336–3359, 1971.

[132] Paschek D. Temperature dependence of the hydrophobic hydration and interaction of simple solutes: An examination of five popular water models. *The Journal of Chemical Physics*, 120(14):6674–6690, 2004.

[133] Guillot B. A reappraisal of what we have learnt during three decades of computer simulations on water. *Journal of Molecular Liquids*, 101:219–260, 2002.

[134] Vega C., Sanz E., and Abascal J. L. F. The melting temperature of the most common models of water. *The Journal of Chemical Physics*, 122(11):114507, 2005.

[135] Berendsen H. J. C., Grigera J. R., and Straatsma T. P. The missing term in effective pair potentials. *Journal of Physical Chemistry*, 91(24):6269–6271, 1987.

[136] Jorgensen W. L., Chandrasekhar J., Madura J. D., Impey R. W., and Klein M. L. Comparison of simple potential functions for simulating liquid water. *J. Chem. Phys.*, 79(2):926–935, 1983.

[137] Mahoney M. W. and Jorgensen W. L. A five-site model for liquid water and the reproduction of the density anomaly by rigid, nonpolarizable potential functions. *The Journal of Chemical Physics*, 112(20):8910–8922, 2000.

[138] Horn H. W., Swope W. C., Pitera J. W., Madura J. D., Dick T. J., Hura G. L., and Head-Gordon T. Development of an improved four-site water model for biomolecular simulations: Tip4p-ew. *The Journal of Chemical Physics*, 120(20):9665–9678, 2004.

[139] Bernal J. D. and Fowler R. H. A theory of water and ionic solution, with particular reference to hydrogen and hydroxyl ions. *The Journal of Chemical Physics*, 1(8):515–548, 1933.

[140] Daura X., Gademann K., Jaun B., Seebach D., van Gunsteren W. F., and Mark A. E. Peptide folding: When simulation meets experiment. *Angew. Chem. Int. Ed.*, 38(1/2):236–240, 1999.

[141] Larson S. M., Snow C. D., Shirts M., and Pande V. S. Folding@home and genome@home: Using distributed computing to tackle previously intractable problems in computational biology.

[142] Duan Y. and Kollman P. A. Pathways to a protein folding intermediate observed in a 1-microsecond simulation in aqueous solution. *Science*, 282:740–744, 1998.

[143] Daura X., Jaun B., Seebach D., van Gunsteren W. F., and Mark A. E. Reversible peptide folding in solution by molecular dynamics simulation. *J. Mol. Biol.*, 280:925–932, 1998.

[144] Schaefer M., Bartels C., and Karplus M. Solution conformations and thermodynamics of structured peptides: molecular dynamics simulation with an implicit solvation model. *J. Mol. Biol.*, 284:835–848, 1998.

[145] Feig M. and Brooks C. L. Recent advances in the development and application of implicit solvent models in biomolecule simulations. *Curr. Opin. Struct. Biol.*, 14:217–224, 2004.

[146] Gupta P., Hall C. K., and Voegler A. C. Effect of denaturant and protein concentrations upon protein refolding and aggregation: A simple lattice model. *Protein Sci*, 7(12):2642–2652, 1998.

[147] Nguyen H. D. and Hall C. K. Spontaneous fibril formation by polyalanines; discontinuous molecular dynamics simulations. *J. Am. Chem. Soc.*, 128(6):1890–1901, 2006.

[148] Jang H., Hall C. K., and Zhou Y. Thermodynamics and stability of β-sheet complex: Molecular dynamic simulations on simplified off-lattice protein models. *Protein Sci.*, 13:40–53, 2004.

[149] Wu C., Lei H., and Duan Y. Elongation of ordered peptide aggregate of amyloidogenic hexapeptide nfgail observed in molecular dynamics simulations with explicit solvent. *J. Am. Chem. Soc.*, 127:13530–13537, 2005.

[150] Tiana G., Simona F., Broglia R. A., and Colombo G. Thermodynamics of β-amyloid fibril formation. *J. Chem. Phys.*, 120(17):8307–8317, 2004.

[151] Gsponer J., Haberthur U., and Caflisch A. The role of side-chain interactions in the early steps of aggregation: Molecular dynamics simulations of an amyloid-forming peptide from the yeast prion Sup35. *Proc. Natl. Acad. Sci.*, 100(9):5154–5159, 2003.

[152] Hwang W., Marini D. M., Kamm R. G., and Zhang S. Supramolecular structure of helical ribbons self-assembled from a β-sheet peptide. *J Chem Phys*, 118:389–397, 2003.

[153] Zanuy D., Ma B., and Nussinov R. Short peptide amyloid organization: Strabilities and conformations of the islet amyloid peptide nfgail. *Biophys J*, 84:1884–1894, 2003.

[154] Ma B. and Nussinov R. Molecular dynamics simulations of alanine rich β-sheet oligomers: Insight into amyloid formation. *Protein Sci*, 11:2335–2350, 2002.

[155] Xu Y., Shen J., Luo X., Zhu W., Chen K., Ma J., and Jiang H. Conformational transition of amyloid β-peptide. *Proc. Nat. Acad. Sci.*, 102(15):5403–5407, 2005.

[156] Baumketner A., Bernstein S. L., Wyttenbach T., Bitan G., Teplow D. B., Bowers M. T., and Shea J. E. Amyloid β-protein monomer structure: A computational and experimental study. *Protein Sci*, 15(3):420–428, 2006.

[157] Lindahl E., Hess B., and van der Spoel D. Gromacs 3.0: A package for molecular simulation and trajectory analysis. *J. Mol. Model.*, 7:306–317, 2001.

[158] Reynolds P. J., Stanley H. E., and Klein W. Ghost fields, pair connectedness, and scaling: exact results in one-dimensional percolation. *Journal of Physics A: Mathematical and General*, 10(11):L203–L209, 1977.

[159] Bauchspiess K. R. One-dimensional site percolation on a finite lattice. *Z. für Physik B Cond. Matt.*, 37:333–337, 1979.

[160] Oleinikova A., Brovchenko I., Smolin N., Krukau A., Geiger A., and Winter R. Percolation transition of hydration water: from planar hydrophilic surfaces to proteins. *Phys. Rev. Lett.*, 95(24):247802, 2005.

[161] Oleinikova A. and Brovchenko I. Percolation transition of hydration water in biosystems. *Mol. Phys.*, 104:3841–3855, 2006.

[162] Skvor J., Nezbeda I., Brovchenko I., and Oleinikova A. Percolation transition in fluids: Scaling behavior of the spanning probability functions. *Phys. Rev. Lett.*, 99(12):127801, 2007.

[163] Coniglio A. and Klein W. Clusters and ising critical droplets: a renormalisation group approach. *J. Phys. A: Math. and Gen.*, 13(8):2775–2780, 1980.

[164] Brovchenko I., Geiger A., and Oleinikova A. Liquid-liquid phase transitions in supercooled water studied by computer simulations of various water models. *J. Chem. Phys.*, 123:044515, 2005.

[165] Brovchenko I., Geiger A., and Oleinikova A. Water in nanopores: Ii. the liquid-vapour phase transition near hydrophobic surfaces. *J. Phys.: Cond. Matt.*, 16(45):S5345–S5370, 2004.

[166] Binder K. Critical behaviour at surfaces. *Phase Transitions and Critical Phenomena, C. Domb, J.L. Lebowitz (eds), London: Academic Press*, 8:1–144, 1983.

[167] Brovchenko I., Geiger A., and Oleinikova A. Surface critical behavior of fluids: Lennard-jones fluid near a weakly attractive substrate. *Eur. Phys. J. B*, 44:345–358, 2005.

[168] Frauenfelder H., Hartmann H., Karplus M., Kuntz I. D., Kuriyan J., Parak F., Petsko G. A., Ringe D., Tilton R. F., and et al. Thermal expansion of a protein. *Biochemistry*, 26(1):254–261, 1987.

[169] Hoeve C. A. J. and Flory P. J. The elastic properties of elastin. *J. Amer. Chem. Soc.*, 80(24):6523–6526, 1958.

[170] Nakajima A. and Scheraga H. A. Thermodynamic study of shrinkage in fibers made from insulin. *J. Amer. Chem. Soc.*, 83(7):1585–1589, 1961.

[171] Loeb G. and Scheraga H. A. The thermally-induced transition in fibrin. *J. Amer. Chem. Soc.*, 84(2):134–142, 1962.

[172] Mandelkern L. Contractile processes in fibrous macromolecules. *Ann. Rev. Phys. Chem.*, 15(1):421–448, 1964.

[173] Debenedetti P. G. Supercooled and glassy water. *J. Phys.: Cond. Matt.*, 15:R1669–R1726, 2003.

[174] Whiting H. *A Theory of Cohesion, Harvard University, Cambridge*, 1884.

[175] Roentgen W. C. *Annalen der Physik und Chemie*, 45:91, 1892.

[176] Soreghan B., Kosmoski J., and Glabe C. Surfactant properties of alzheimer's aβ peptides and the mechanism of amyloid aggregation. *J. Biol. Chem.*, 269:28551–28554, 1994.

[177] Pauling L. and Corey R. Configuration of polypeptide chains with favored orientation around single bonds: two new pleated sheets. *Proc. Natl. Acad. Sci. USA*, 37:729–739, 1951.

[178] Gordon D. J., Balbach J. J., Tycko R., and Meredith S. C. Increasing the amphiphilicity of an amyloidogenic peptide changes the β-sheet structure in the fibrils from antiparallel to parallel. *Biophys. J.*, 86:428–434, 2004.

[179] Essmann U., Perera L., Berkowitz M. L., Darden T. A., Lee H., and Pedersen L. G. A smooth particle mesh Ewald method. *J. Chem. Phys.*, 103:8577–8593, 1995.

Curriculum Vitae

Personal data

Full Name: Raghunadha Reddy Burri
Birth Date: 28th February, 1978
Birth Place: Guntur (India)
Permanent Address: Karalapadu, Piduguralla, Guntur, Andhra Pradesh, India - 522314
Temporary Address: Adalbertstrasse, 149, 44149 Dortmund, Germany

Education

- **Doctoral student** (April 2004 - until now)
  Department of Physical Chemistry, Technical University of Dortmund, Germany.
- **PostGraduate(Masters) in Bioinformatics** (2002 - 2003)
  Cologne University Bioinformatics Center, University of Köln, Germany.
- **Bachelor of Engineering (B.E.) in Chemical Engineering** (1996 - 2000)
  Madras University, Tamil Nadu, India.

Experience

- **Master Preparatory** (November 2003 - April 2004)
  University of Dortmund, Dortmund, Germany.
- **Practical Courses** (November 2002 - September 2003)
  1. Max Delbrück Center for Molecular Medicine (MDC), Berlin, Germany.
  2. Interdisziplinäres Zentrum Für Bioinformatics, University of Leipzig, Leipzig, Germany.
- **Process Engineer** (June 2000 - February 2002)
  Spansules Pharmatech Pvt. Ltd., Hyderabad, Andhra Pradesh, India.